Development of Novel Methodologies for the Electrodeposition of Polypyrrole-based Films in Controlled Morphologies with Potential Application in Nitrate Sensing.

NUI MAYNOOTH

Ollscoil na hÉireann Má Nuad

Conor P. McCarthy, B.Sc

Department of Chemistry

National University of Ireland Maynooth

2013

Thesis Submitted to the National University of Ireland in Fulfilment of the Requirements for the Degree of Doctor of Philosophy

Supervisors: Dr. Bernadette E. Alcock-Earley and Prof. Carmel B. Breslin

Head of Department: Dr. John C. Stephens

Chapter 1: Introduction and Literature Review

Chapter 2: Experimental

Chapter 3: The Facile Template-Free Electrochemical Polymerisation and Characterisation of Poly [*N*-(2-cyanoethyl)pyrrole Nanowires

Chapter 4: The Electrochemical Deposition of Poly [*N*-(2-cyanoethyl)pyrrole] Microtubes and Microcontainers using an Acoustically Formed Emulsion

Chapter 5: The Electrodeposition of Copper Micro/Nano Structures at Polypyrrole and Poly[*N*-(2-cyanoethyl)pyrrole Polymers for the Electrochemical Detection of Nitrate

Chapter 6: Conclusions

Declaration

I hereby certify that this thesis has not been submitted before, in whole or part, to this or any other university for any degree, and is, except where stated otherwise, the original work of the author.

Signed:_____

Conor McCarthy

Acknowledgements

First, I would like to thank my supervisor Dr Bernadette Alcock-Earley for her support and guidance over the last 4 years. To Prof. Carmel Breslin, whom I completed my 4th year project with many years ago which was the start of my interest in Electrochemistry, thanks for your guidance and insightful discussions over the years. Also, for your help when applying for the research stay in Norway, your input was vital. To Dr. Denise Rooney, thanks for your training on how to organise, structure, write and submit high quality papers. Most importantly, the best ways to respond to reviews in a serious and comprehensive manner. I have learned a tremendous amount in the last 2 years and will always remember scrambling from your office to find a reference for some 'hand wavey' science I had conjured up! I would like to thank the Environmental Protection Agency for funding this project (STRIVE programme) and for SFI for providing access to the Tyndall National Institute through the National Access Programme.

To my side kick and companion for this entire trip, Lynn Gary, thanks for all the fun times, chats and craic over the years it would not have been the same without you. You are a very generous and kind person who has the very special ability to ask the most difficult 'fundamental' chemistry questions. To my gym buddy, cook and full time collaborator, Niall (Joseph) McGuinness, we had some serious fish in the lab over the years, we always found some way of taking the mick and it was a great laugh. All those late nights and long hours paid off, from applying to NAP, working on the papers, to our constant discussions about electrochemistry. You are a true academic and an excellent chemist, I have learned a lot from you. Writing my thesis to the sounds of your tapping feet while waiting for you "to just save this" was tremendous banter.

To the love buzz Roisin O Fla and housemate and general sci-fi enthusiast John Murphy, cheers for all the craic. You both had a very strong work ethic and determination to get finished. I particularly took solace from the phrase "when you're tired don't be tired" when working the 12 hour days towards the end. To all the other post grads and post docs and the 1o'clockers in the chemistry dept. there are too many to name but your all good horses.

To Dr. Gillian Hendy and Dr. Eimear Ryan who offered their help proof reading large amount of my thesis, particularly at short notice, your help was very much appreciated and will not be forgotten. To Dr. Enrico Andreoli, Dr Valeria Annibaldi, Dr. Richard Dolye and Dr Johnny Colleran thanks for comments on the papers and helpful electrochemistry

discussions over the years. To all the technical staff at NUIM, thanks for all your assistance and support. In particular, thanks to Mr.Noel Williams for his constant support with the SEM and fixing the many technical problems which arose. Also thanks for your help with designing the many SEM electrodes and stages over the years and for constructing the water contact angle apparatus. To Karen Herdmann for her help with the copper experiments and for doing an excellent 4th year project and producing some excellent work.

In Norway thanks to my supervisor Edel Sheridan for a great experience and helping me settle in! To my German comrades Markus and Tobi thanks for all the great times, fishing trips and snowboarding excursions. I think it is safe to say we will never get on a boat together again but I'm glad we survived.

To the battery group, Morten and Carl Erik thanks for your help and cringe women/battery jokes. To all the lads on the football team thanks for all the craic I still have my award for 'best blunder' stuck to my wall.

At the Tyndall National Institute, Cork, thanks to Pat, Nikolay and Mircea for your expertise and hard work and to Paul Roseingrave for organising everything. To Anne Shanahan in DIT thanks for giving us a lot of your time for the Raman experiments.

To the 'oul pair', your scientific input into this project was poor, however keeping me well fed and properly transported was infinitely more valuable, thanks very much.

To my closest allies and fellow celtic tiger babies from laurel lodge thanks for reminding me that Maynooth is a very small place and I can't go around wearing jeans all my life.

Abstract

In this thesis the novel electrochemical deposition of poly[N-(2-cyanoethyl)pyrrole] (PPyEtCN) into nanowire and microtube morphologies is reported. Cyclic and pulsed electrochemical techniques were employed to electrodeposit copper micro and nano particles at PPyEtCN and polypyrrole (PPy) surfaces. A PPy nanowire/copper modified electrode was investigated for its effectiveness as an electrochemical sensor for the detection of the nitrate ion.

To produce PPyEtCN in a nanowire morphology a facile, one step, electrochemical method was employed, which did not require the use of any templates or surfactants. Using optimised conditions the nanowires nucleated to give a homogeneous film across the electrode surface, with lengths of approximately 2 μm and diameters of 150 nm. Evidence is presented to support an instantaneous 3-D nucleation and growth mechanism. Structural information on the nanowires was obtained using vibrational spectroscopy which reveals the polaron as the main charge carrier within the polymer matrix.

To fabricate novel vertically aligned open and closed-pore microstructures of PPyEtCN, an electrodeposition procedure was developed using an emulsion in a co-solvent mixture. Adsorbed toluene droplets were employed as soft templates to direct polymer growth. The microstructures only grew in the presence of both ClO_4^- and $H_2PO_4^-$ doping ions, due to a slower rate of polymer propagation in this electrolyte. Two sonication methods (probe and bath) were used to form the emulsion, producing significantly different microstructure morphologies. Control over microtube diameter was achieved by simply altering the emulsion sonication time or the amount of toluene added to form the emulsion. Electrochemical characterisation indicated the PPyEtCN microtube morphology had an increased electrochemical response compared to its bulk counterpart. TEM analysis of individual closed-pore microtubes identified a hollow interior at the base within which the toluene droplet was encapsulated. This cavity may be used to entrap other compounds making these materials useful in a range of applications. The methodology was also applied to form microstructures of poly(3,4-ethylenedioxythiophene) and PPy.

Electrodeposition of copper crystals at PPy and PPyEtCN was performed using constant potential and cyclic voltammetry techniques. For potentiostatic deposition, the concentration of copper and the magnitude of the overpotential were altered to control the deposited crystal habit. Using a negative potential of -0.200 V, the evolution of a dendrite morphology was followed using microscopy. This morphology had an increased surface area due to the copper branching extending into the electrolyte. PPy nanowire/copper electrodes were developed by altering the speed and cycle number of the cyclic deposition procedure. This was an accurate means of controlling the shape and size of the deposits. Varying the scan rate from 100 to 900 mV/s resulted in the size of the copper deposits changing from μm to nm. Sensing experiments revealed that the PPy/copper electrode was not as sensitive as a glassy carbon/copper electrode due to interference from residual carbonate ions remaining within the polymer matrix; however, it was observed to be more stable over repeated cycling due to a charge transfer interaction between the copper and pyrrole nitrogen.

Chapter 1

Introduction and Literature Review

1.1 Introduction

The work presented in this thesis is focused on the electrochemical deposition of polymer and metal nanomaterials at electrode surfaces. The research topic dealing with the design of nanomaterials by employing electrochemical techniques has developed rapidly in the last decade.[1-3] This is due to a strong understanding of the electrochemical processes that occur at electrode surfaces which enables fabrication of a range of nanomaterials.[4] These materials have wide technological importance as the various compositions and morphologies have applications in areas such as solar cells, memory, and sensor devices.[5-8] Furthermore, employing nanostructured materials has led to increases in efficiencies compared to the typical 'bulk' materials.[9] In the field of polymer science, nanomaterials have proven to be attractive candidates as electrochemical sensors due to the higher sensitivities and faster redox chemistry they can achieve.[10-12] For this reason the development of novel, facile and template free methods to produce polymeric and metallic nanomaterials is a research goal with strong merit and importance.

In this introductory chapter, the fundamental processes involved in electrodepositing polypyrrole (PPy) are discussed in terms of the structural and electronic characteristics. This is followed by analysis of the most relevant and up-to-date literature accounts relating to PPy nanostructuring, particularly focusing on nanowires and hollow microtubes/containers. Similarly, the latest developments within the fields of substituted PPy and copper electrodeposition are discussed with reference to the most significant work in the literature.

1.2 Objectives and Achievements

The objectives of this research was to firstly develop a means of fabricating novel morphologies of the functionalised poly[*N*-(2-cyanoethyl)pyrrole] (PyEtCN) monomer. In Chapter 3, the growth of PPyEtCN nanowires is investigated with the aim of controlling the morphology by a template free method. This work is extended in Chapter 4 to developing an emulsion polymerisation solution to grow various hollow morphologies of PPyEtCN.

Secondly, pulsed and cyclic electrochemical techniques were investigated for their ability to control the electrodeposition of copper microparticles at polypyrrole (PPy) surfaces for nitrate sensing, this is presented in Chapter 5. These electrodeposition techniques were also attempted at the novel PPyEtCN polymers.

The main achievements of this work have been identified as (i) the electrochemical synthesis of novel PPyEtCN nanowires at an electrode surface by a template-free method; (ii) the development of an mechanistic understanding of the nanowire formation process using in–depth characterisation by electrochemistry, microscopy and spectroscopy; (iii) the successful design of a new emulsion polymerisation methodology to prepare hollow and closed microstructures of PPyEtCN, and extending it for use with other monomers; (iv) the controlled electrodeposition of copper dendrite microstructures at PPy bulk surfaces; (v) development of several morphologies of copper nano/micro particles at PPy nanowires using a cyclic electrodeposition routine and (vi) the testing of polymer-metal hybrid materials for their ability to electrochemically reduce the nitrate ion in aqueous solution. A proportion of this work was accepted for publication in the peer reviewed journals of *Electrochemistry Communications*[13] and *Macromolecules.*[14]

1.3 Polypyrrole (PPy)

Polymers are most easily recognised for their use as common plastics (poly(vinylidene chloride)) and textiles (polyesters) which have many uses in today's world. Conducting polymer (CP) materials however, are a type of polymer which are intrinsically conducting. Also called 'synthetic metals' they have the ability to carry an electrical current and can be formed in solution or at electrode surface. Their development was accredited to Heeger, MacDiarmid and Shirakawa who won the Nobel Prize in Chemistry in 2000 for their work.[15] Polypyrrole (PPy) is one of the most extensively studied conducting polymers due to its facile preparation and attractive range of properties, including redox activity,[16] ion exchange capabilities[17] and biocompatibility.[18] The redox properties of PPy can be controlled by an electrical potential stimulus; as a result it has been successfully applied in a wide variety of applications such as supercapacitors,[19] actuators,[20] biosensors,[21] drug delivery[22] and corrosion protection.[23]

1.3.1 Structural and Electronic Properties of Polypyrrole

Materials can be classified into three broad categories as insulators, semiconductors or conductors, depending on their ability to conduct electricity. The overlap of electronic states in these materials produces electronic bands. The valence electrons overlap to from the valence band while the electronic levels above these are called the conduction band. The gap which exists between these two bands is called the bandgap, E_g. The energy required to excite an electron into the conduction band from the valence band determines whether a material will be conducting or insulating, or a value in-between. A large value, say 10.0 eV, will typically result in an insulating material, while a value 1.0 eV will allow excitation of the electrons into the conduction band. Generally, conducting polymers, including PPy, have a band gap above 1.0 eV making them semiconducting (3.16 eV for PPy).[24] These three electronic configurations are depicted in Figure 1.1.

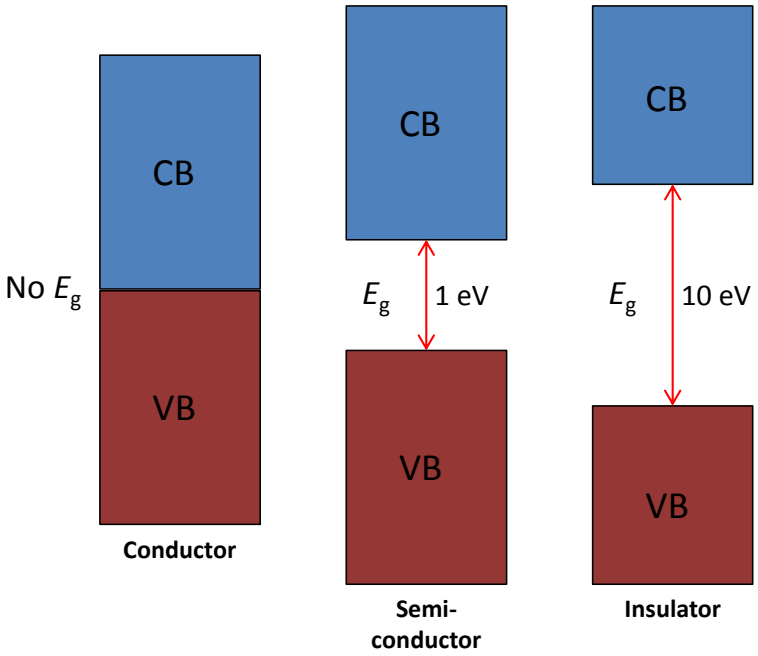

Figure 1.1. The difference in energy between the valence band (VB) and conduction band (CB) for a conductor, semiconductor and insulator.

PPy is a black insoluble material which was first electrochemically synthesised in 1969 by Dall'Ollio *et al.*[25] The poor mechanical and electrical properties did not give rise to any further developments for another 10 years when Diaz *et al.*[26] produced a homogeneous and conducting film. Typically, PPy is synthesised by the anodic oxidation of the monomer which polymerises through connecting σ-σ bonds, as shown in Figure 1.2. Its unique electrical properties arise from the delocalised π-electron overlap which extends over several recurrent monomer units. In order to extend the conjugation along the polymer chain the individual Py monomer units must be coplanar, Figure 1.3. Bond formation at the 2 and 5 positions (α-coupling) is preferred over the 3 and 4 positions (β-coupling) on the monomer backbone. This is due to polymerisation at the β position decreasing conductivity by breaking planarity and linearity of the PPy chains.[27]

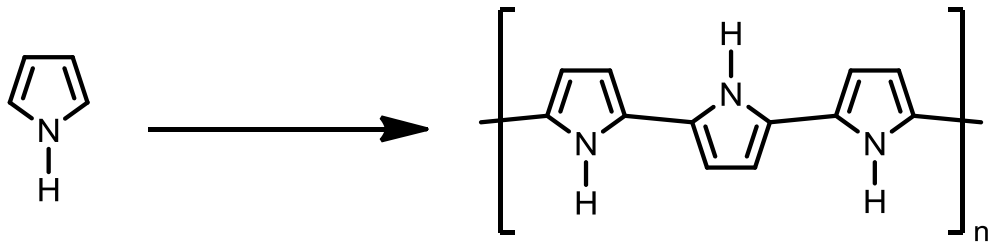

Figure 1.2. The pyrrole monomer and polypyrrole polymer with reoccurring monomer units, shown here in the reduced form.

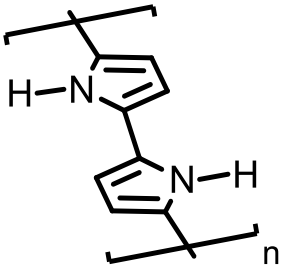

Figure 1.3. The coplanarity of the PPy monomer units leading to extensive π electron overlap.

PPy is only electroactive and conducting in its oxidised state. This conductivity is achieved by the oxidation (or reduction in some cases) of the polymeric backbone to create charge carrier entities,[24] Figure 1.4. These charges also cause a relaxation of the geometry of the polymer to give a more energetically favourable conformation. The entities created, called polaron and bipolarons, are capable of movement along the polymer backbone and are associated with the incorporation of a counterion to balance the charge generated. In electrochemistry, these counterions are commonly called ‘dopants’, which is a term borrowed from inorganic semiconductors in solid state physics. In this thesis the term ‘dopant’ is used in place of the term ‘counterion’ as it has been adopted into the literature in all electrochemical journals and is commonly used. However, it is clear that these ‘dopants’ are not involved in supplying electron density to the materials to increase their conductivity, but rather encourage charge carriers by stabilising them within the polymer backbone.

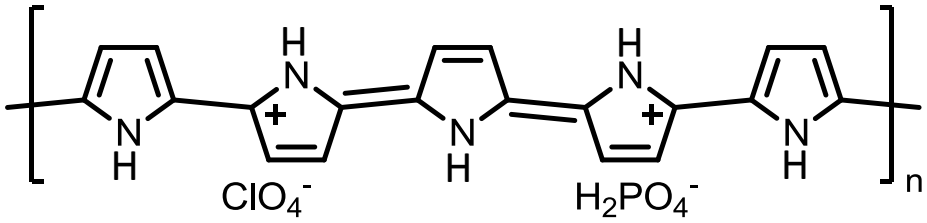

Figure 1.4. PPy in its doped state with a bipolaron stabilised by ClO_4^- and $H_2PO_4^-$ anions.

Dopants are usually incorporated at the time of polymerisation by diffusing from the bulk electrolyte and physically entering the polymer lattice. During doping the polymer will undergo a structural distortion from the volumetric strain (and shrink on dopant expulsion). Since dopants balance the opposite charge on the polymer backbone they can be expelled by applying a reversed electrical impulse to the polymer. This allows polymers to exchange dopants depending on the electrolytes in which they are immersed. Furthermore, a range of dopants can be employed from small anions (ClO_4^-) to large polyelectrolytes such as poly(styrene sulfonic acid). Since many attributes of CPs depend on the dopants incorporated, different film characteristics can be obtained by altering the dopant.

The proportion of dopant incorporated into the polymer per monomer unit is termed the 'doping level' and is directly related to the conductivity of the polymer. The maximum doping level for PPy with a ClO_4^- dopant is one dopant per 3.3 monomer units.[24] In some cases this means that 20 to 40 mol% of the entire polymer can be made up of dopants, depending on the synthesis conditions.[28] Therefore, it is reasonable to expect that the characteristics and morphology of the resultant polymer film will depend heavily on the nature and concentration of the doping anion in the electrolyte solution. The subsequent size, hydrophobicity and flux of the dopant leads to changes in the porosity and microstructure of the film[29] and also its morphology.[30-31]

1.3.2 Polymerisation Mechanism

A range of techniques have been developed to polymerise PPy including chemical and electrochemical. In this thesis, only electrochemical deposition using a constant anodic potential will be discussed. Benefits of this method include the absence of a catalyst, direct deposition onto an electrode surface and control over the thickness.[32]

The Py monomer consists of a 5 member ring structure which is aromatic. The carbon and nitrogen atoms all have sp^2 hybridisation, which generates a 6π electron system. The resonance forms indicate a partial positive charge at the nitrogen position since the lone pair is delocalised into the Py ring, Figure 1.5. The inclusion of the heteroatom stabilises the structure and creates a dipole moment.[32] The stable forms of the resonate structures are at (2) and (4) in Figure 1.5. This is due to the presence of the positive and negative charges in close proximity.[33] The stability of the negative charge at the 2 and 5 position on the Py backbone is the property that produces the σ-σ linkages at these sites during polymerisation.

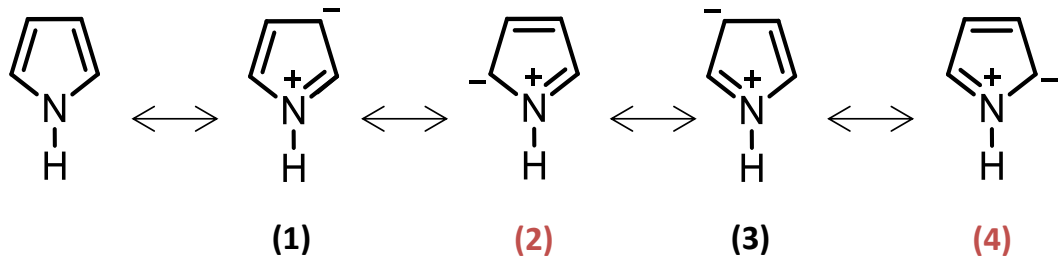

Figure 1.5. The resonance structures of PPy showing the most stable forms highlighted in red.

The electrochemical polymerisation of PPy proceeds in several steps,[24] Figure 1.6. Firstly, it is initiated by applying an anodic potential to the electrode which oxidises the Py monomer and forms a radical cation. These radical cations combine with the loss of two protons forming the radical dimer. The concentration of radical cations is much larger than neutral monomers in the vicinity of the electrode. This drives the coupling reaction. The radical dication then loses two protons to become a neutral dimer. This is then further oxidised to form the radical dimer. The radical dimer then combines with radical monomers and this process repeats to build up the polymer layers. Chain growth is terminated by reaction with water or other nucleophilic

groups. It would appear from Figure 1.6 that the resultant trimer is in the neutral state. However, this is not the case since the stability of the radical cation increases with the number of monomers in the polymer chain. This increases the delocalisation and subsequently lowers the oxidation potentials of the PPy chain compared to the monomer. This leads to the polymer bearing an overall charge after polymerisation. This charge is then balanced by the dopant counterions as described previously.[24]

Many factors affect the Py polymerisation reaction namely: the solvent, nature of electrode, concentration and nature of dopants and pH of the electrolyte. These have significant consequences on the final morphology and conductivity of the deposited polymer.[34] These factors are examined in detail in Chapter 3 and 4 for the experiments involving PPyEtCN and are related to the morphology of the resultant polymer films formed.

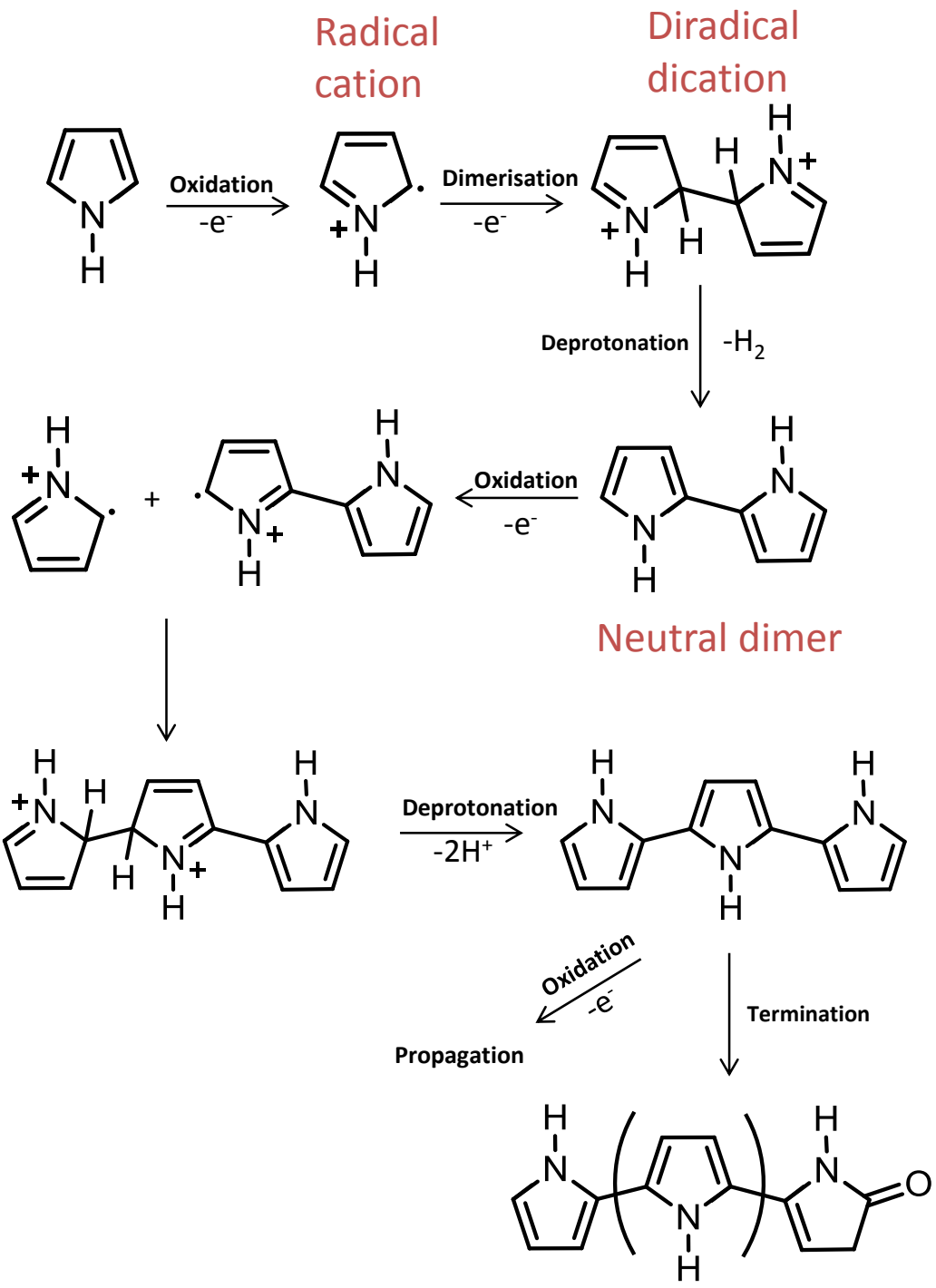

Figure 1.6. The steps involved in the oxidation and polymerisation of Py leading to the radical cation, diradical dication and neutral dimer. Propagation or termination are the final steps in the reaction.

1.3.3 Overoxidation Mechanism

Overoxidation has been described as the nucleophilic attack of the polymer chains by nucleophilic species when the applied potential is higher than the oxidation potential of the polymer.[35] It is possible to overoxidise the PPy backbone by holding the polymer-modified electrode at a high oxidising potential, or polarising for long times. This is due to the fact that PPy has a lower oxidation potential compared to the Py monomer which means that overoxidation is an unavoidable consequence of film growth when nucleophilic species such as water are present.[28] Overoxidation is generally seen as an undesirable process as it degrades the conjugation along the polymer backbone to a point it becomes irreversibly reduced.[28, 36-37] Furthermore, as shown in Figure 1.7, the dopant anion is ejected during overoxidation and the polymer loses its electroactivity. Furthermore, chemical defects, such as oxygen in the form of carbonyl and carboxyl groups, are incorporated onto the Py backbone at the β positions.[38] This is why the overoxidation process is more apparent in basic solutions due to the higher availability of OH^- species.[39] This is discussed in Chapter 5 where basic polymerisation solutions are employed to polymerise PPy nanowires. This process is also recurrent in Chapter 3 as the substituted PPyEtCN monomer employed is particularly susceptible to overoxidation.

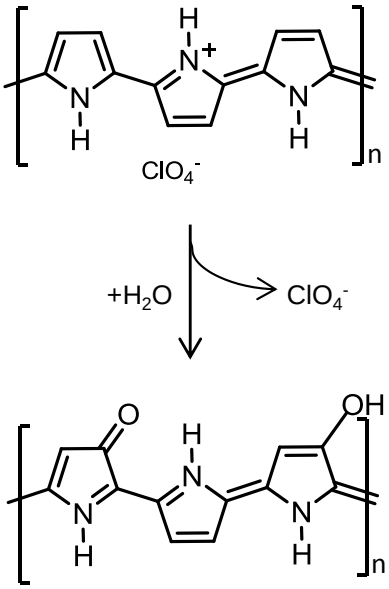

Figure 1.7. The overoxidation process involved at a PPy polymer going from doped to undoped state using the perchlorate anion as an example.

1.3.4 Nanostructuring

In recent years there has been extensive research into developing PPy into nanowires and nanotubes.[40] This is due to the enhanced electrical, structural and electrochemical properties they possess compared to the classic bulk morphology.[12] As discussed in Section 2.1, the diffusion of dopant ions to the polymer surface is an important component of the conductivity within polymer systems. This process is usually the rate determining step when polymers are switched between redox states. Most CP films will take several hundred milliseconds to undergo this process. Researchers have strived to overcome this problem by employing nanowire and nanotube morphologies which have a greater surface area and therefore a larger surface interaction with the electrolyte. This leads to a shorter diffusion length for the dopant ions as depicted in Figure 1.8. Furthermore, PPy nanowires have a much greater stability since they are more capable than bulk films of dealing with the strain of swelling and contracting, which causes polymer degradation. [41]

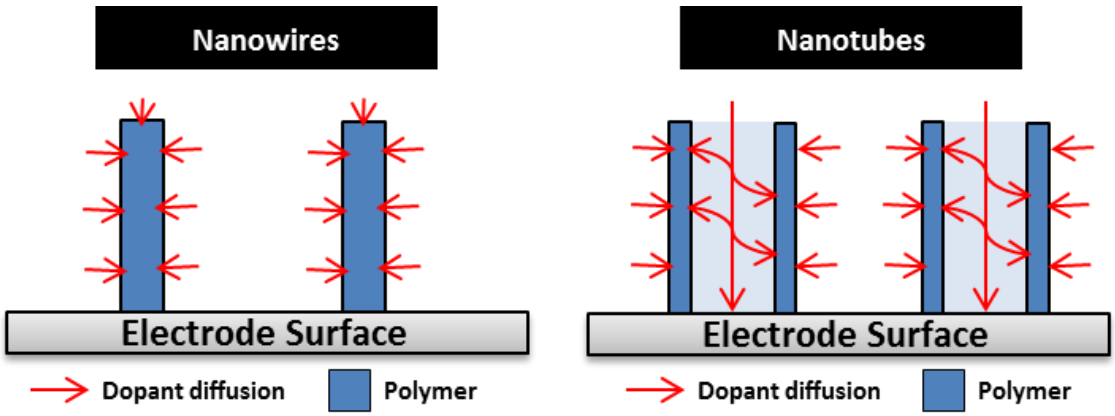

Figure 1.8. The dopant diffusion properties of a nanowire and nanotube polymer film.

The standard method typically used to produce polymer (and metallic) nanomaterials is the 'hard template' approach. First proposed by Martin *et al.*[42-43] for PPy and polyaniline, this is where a porous aluminium template is used to direct polymer growth. The monomer simply diffuses into the pores and polymerises on the walls of the template forming tubes. As polymerisation continues the tubes fill to form nanowires. The resultant wires are limited to the diameter of the template used; therefore several templates must be purchased (or fabricated) to obtain several

nanowire diameters, increasing costs.[44] Post synthesis steps to dissolve the template can be harsh on the polymer and cause it to degrade.

There is a growing interest in preparing PPy nano/microstructures employing facile template-free or soft-template electrochemical approaches.[45-47] The advantage of these methodologies is that the steps to construct and then subsequently dissolve the hard templates are not required. Furthermore, the morphology of the polymer formed can be controlled by simply altering the electrochemical conditions. In recent years there has been a large increase in the number of research groups involved in the preparation of template-free electrodeposition methods. Several authors have developed facile, reproducible and environmentally friendly methods of producing PPy nanowires. Researchers of note include Dongtao Ge and co-workers who have made advances using hierarchical polymeric materials with various surface wettabilities[48] and developed a range of applications for PPy nanowires;[49-51] Catherine Debemmie-Chouvy and co-workers who made efforts to elucidate the nanowire polymerisation mechanism,[52-53] and Jiyong Huang and co-workers who developed several methods of producing PPy nanowire arrays. [41, 54-57]

In terms of the nanowire morphology different compounds have been employed to direct the polymerisation at an electrode surface. These can be grouped into three specific categories: a surfactant soft-template, employing a biomolecule or the use of a pH buffered electrolyte. For the surfactant soft-template method an acidic compound such as camphorsulfonic or pyrenesulfonic acid is added into the polymerising electrolyte.[58] The surfactant molecules and Py monomer form micelles in solution, which limit polymerisation in radial directions. PPy growth then only occurs at the tips, forming nanowires, Figure 1.9.

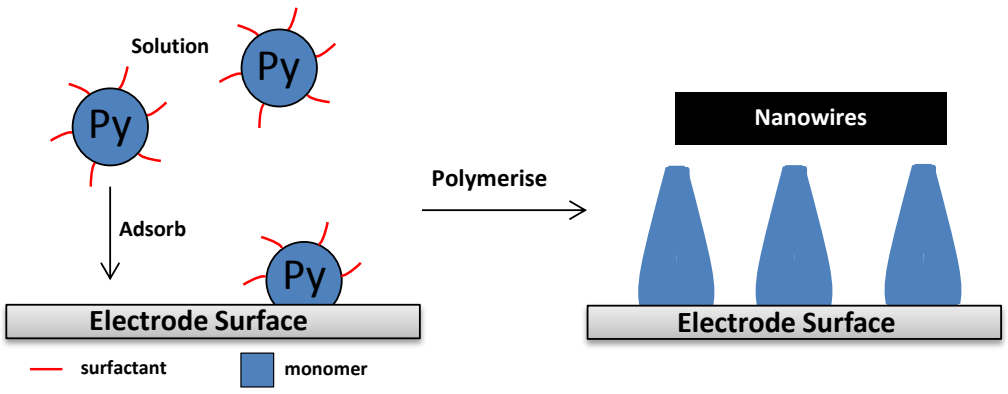

Figure 1.9. Soft-template assisted growth using an acidic surfactant.

Using biomolecules such as heparin, starch or gelatin the morphology of the pyrrole deposits can be directed into a wire morphology.[59-61] This method allows for adsorption of the Py monomer at specific active sites on the biomolecule chain through hydrogen bonding with either –COOH, $–NH_2$ or $–SO_3$ groups. Since the biomolecules are typically in a chain shape conformation, the Py polymerises along these chains adopting the morphology.[59] In this way the biomolecules act as soft templates. An example polymerisation using heparin as the biomolecule is outlined in Figure 1.10. [60]

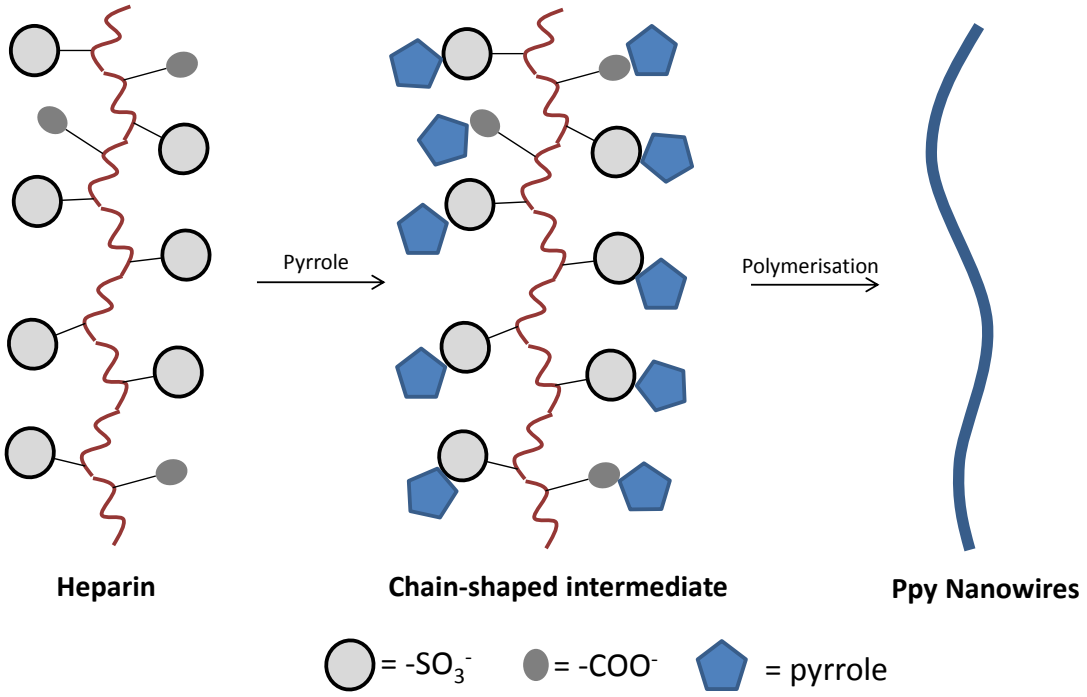

Figure 1.10. Possible mechanism for the formation of PPy nanowires using heparin in the polymerisation solution. [60]

In the third methodology a buffer electrolyte is used to keep the pH of the polymerisation solution stable as the polymerisation reaction proceeds.[41] Since H^+ ions are generated at the electrode surface from PPy deprotonation, they cause a decrease in the local pH at the electrode surface. It is also known that acidic conditions favour an increased rate of polymer polymerisation.[62] Therefore, employing these basic anions to 'mop up' the free protons, Figure 1.11, reduces the decrease in pH and allows the polymer to grow in a slower and more ordered

fashion. As will be discussed further in this thesis, various reports in the literature have proven that to produce nanowire morphologies a slow and controlled reaction rate must be obtained.[63-64] The acid surfactant and pH buffer methodologies were attempted in this work to produce PPy and substituted PPy nanowires. The latter methodology is outlined in Chapter 3 and Chapter 5 for substituted PPy and PPy respectively.

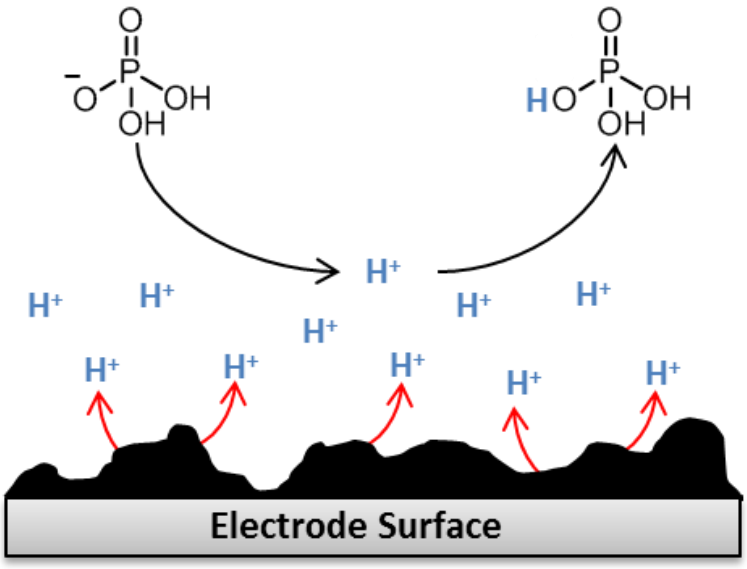

Figure 1.11. Diagram representing the generation of H^+ ions during polymerisation of Py. $H_2PO_4^-$ anions 'mop up' these free protons reducing the pH at the electrode.

1.3.5 Hollow-container and Hollow-tube Morphologies

1.3.5.1 Hollow-containers

Similar to PPy nanowires there has been a surge of interest in PPy hollow tube and containers in recent years.[21, 65-70] This is due the range of attractive properties of encapsulation and subsequent release which they possess,[45, 63, 71] not possible for solid polymer materials. The container morphologies are capable of storing specific molecules within their core and then releasing them when an external stimulus is applied.[72] This allows the possibility to fabricate effective drug delivery systems or using them as nanoreactors.[73-76]

A successful approach, to develop closed micro-container morphologies, was made by Maciej Mazur who has added several significant contributions to the field. He developed an elegant means of synthesising hollow PPy capsules using oil droplets as hosts to dissolve chemical compounds, while also being a surface for Py polymerisation.[77] This chemical polymerisation occurred at the surface of the oil droplets and allowed the subsequent release of entrapped fluorescent dyes by controlling the hydration of polymer shell. Mazur and co-workers developed a mechanism for this polymerisation based on the Py monomer transferring into the organic phase where it is more soluble, this confines the polymerisation reaction onto the oil droplet surface.[78] Entrapment of the fluorescent dyes allowed for spectroscopic methods to probe the oil droplets.[79] Finally, by inverting the oil-in-water to a water-in-oil emulsion a wide range of drug delivery applications became available.[80] The development of these PPy materials as host-guest systems highlights the practical implications of developing CP hollow microcontainers. Development of this oil droplet technique to produce hollow containers at an electrode surface, controlled by electrochemical means, rather than chemical, is presented in Chapter 4.

1.3.5.2 Hollow-tubes

Using an electrochemical approach has also been developed to produce hollow open structured PPy materials with the advantage that they are attached to an electrode surface. The ‘pioneering and brilliant’ work by Shi and co-workers places them at the forefront of the CP microtube field. Their critical review on CP nanomaterials

synthesised by electropolymerisation, is a comprehensive and accurate assessment of current procedures and applications associated with hollow microstructures.[81] In their work they developed a 'soap bubble' method which uses the decomposition of water to generate bubbles on the working electrode.[82-84] These O_2 bubbles are stabilised by a surfactant and become soft templates for polymer growth, as highlighted an a excerpt from work by Parakhonskiy *et al.*,[71] Figure 1.12. The onset oxidation potential for decomposition of water was lower at PPy compared to a bare stainless steel electrode; therefore PPy had a catalytic effect on the bubble formation process. The 'bubbles mechanism' was confirmed by dynamic light scattering measurements which showed the generated bubbles and polymer microstructures were comparable in size.[85] By generating different sized bubbles at the electrode, the size and shape of the resultant microstructures could be accurately controlled.

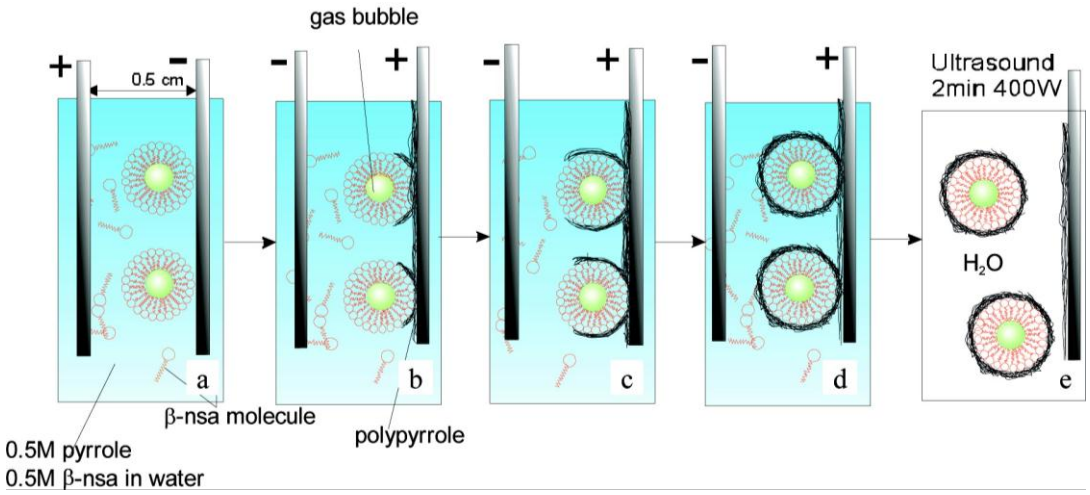

Figure 1.12. Generation of a gas bubble at a working electrode which forms a template for hollow PPy tubes/containers using naphthalene sulfonic acid electrolyte.

A recent progression in the formation of CPs has seen the use of sonication techniques. The electrolyte solution is agitated by acoustic energy which produces a stable emulsion between the insoluble monomer and the solvent solution. The effect of this process on the EDOT monomer has been studied at length by Atobe and co-workers.[86-89] Shi and co-workers developed this monomer droplet process to produce microcups.[90-91] In Chapter 4 we investigate the monomer droplet process for the polymerisation PPyEtCN polymers and finally develop a toluene emulsion solution produced by sonication. These polymerisation solutions were then used to generate hollow polymeric structures at an electrode surface.

1.4 Substituted Polypyrrole

While the nano/micro morphologies of conducting polymers have been comprehensively studied, very little work has been performed with their covalently functionalised counterparts. The development of functionalised conducting polymers in controlled morphologies was highlighted as an important future research area by Shi and co-workers in their review on nanostructured conducting polymers.[81] A number of other studies have been reported using electrochemical or chemical approaches to form microstructures of *N*-functionalised PPy. Examples of note include the electrodeposition of poly(*N*-Methylpyrrole) (PPyMe) microstructures in a 'doughnut' morphology using a H_2 bubble template carried out by Teixeira-Dias *et al.*[92] and the development of PPyEtCN and PPyMe microspheres through chemical oxidation on polystyrene core particles by Alemán and co-workers.[93-94] Electrodes modified with covalently functionalised conducting polymers have been utilised in sensor applications as the moieties at the substituted position enable supramolecular interactions with other molecules. [95-96] For example, PPyEtCN modified electrodes have been used bind specific antibodies for the fabrication of biosensors[97] and in the electrochemical sensing of dopamine.[96] They have also been used for the immobilisation of DNA[98-99], enzymes and other molecules for applications in bio-sensing.[100-103] Alternatively, the functional group can be chemically modified in order to covalently attach a wide range of species to the polymer surface which include carbon nanotubes,[104] biomolecules[105] or fluorinated alkyl chains.[106] Therefore, the benefit of using these monomers is substantial, developing them into nanostructured morphologies will expose their unique abilities further. Some examples of the more commonly studied *N*-substituted Py monomers are shown in Figure 1.13.

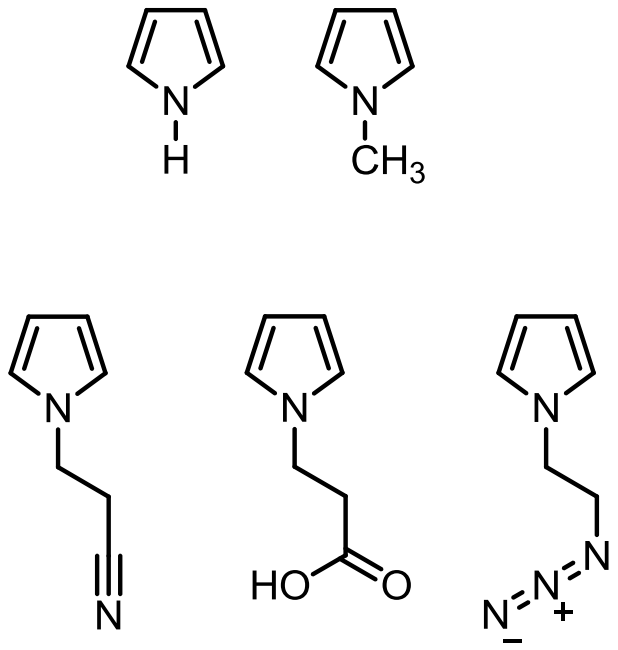

Figure 1.13. From top left to bottom right the chemical structures for pyrrole, *N*-methylpyrrole, *N*-(cyanoethyl)pyrrole, *N*-(carboxyethyl)pyrrole and *N*-(azidoethyle)pyrrole.

There are very few studies on the electrochemical (or chemical) polymerisation of substituted PPy in a nanoscale morphology. Dongtao *et al.* made a nanowire composite film by coating PPy with (carboxyethyl) pyrrole.[107] The most commonly studied of the PPy derivatives is poly(*N*-methylpyrrole) (PPyMe).[108-115] Some chemical[94, 116] and electrochemical[92, 117] synthesis of nanostructured substituted polymer films have been reported. These structures have been successfully used as dopamine and morphine sensors.

In this thesis only the poly(cyanoethyl)pyrrole polymer is studied and methods to produce nanowire and microtube morphologies are discussed. However, using these same procedures described in Chapter 3, employing the poly(azidoethyl)pyrrole polymer, it was also possible to use this functionalised polymer to attach a ferrocene moiety through a 1,3 copper catalysed azide-alkyene cycloaddition (CuCAAC), as shown in Figure 1.14, from unpublished work.[118] This proves that post-functionalisation of the substituted nanowire morphologies is possible. Although *N*-substituted polypyrrole has been employed for sensor applications, there are few studies on the preparation of these polymers in the nanowire morphology. Moreover, these studies have utilised either a template approach or coated already grown polypyrrole nanowires with the functionalised polypyrrole.[107]

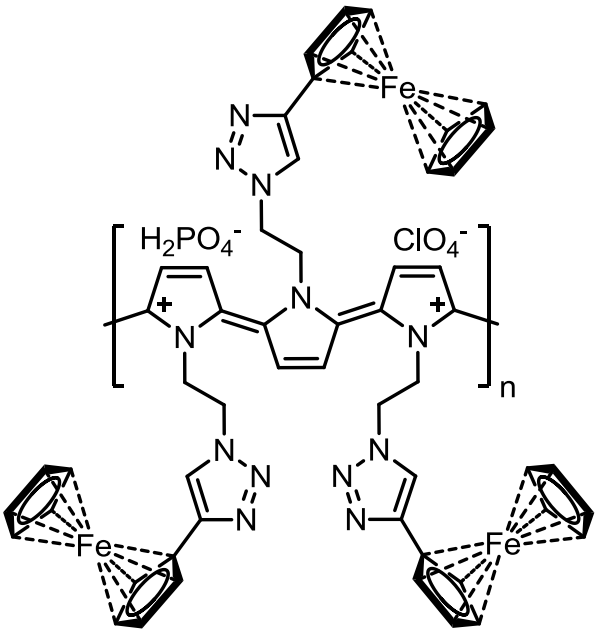

Figure 1.14. The poly(azidoethyl)pyrrole polymer doped ClO_4^- and $H_2PO_4^-$, with a ferrocene molecule chemically attached by the CuCAAC reaction.

1.4.1 Poly[*N*-(2-cyanoethyl)pyrrole] (PPyEtCN)

N-(cyanoethyl)pyrrole has been somewhat understudied in terms of its morphology formed from electrochemical deposition. The Alemán group have performed extensive structural and electronic characterisation of this particular monomer.[119-120] Recently they successfully produced a hollow morphology using a hard template chemical synthesis.[93] To date there have been no reports of the synthesis of this polymer in a nano morphology despite its proven application as a dopamine sensor[93, 96], immunosensor,[121] and for immobilising antibodies.[97] Since this polymer is commonly used as a sensor material, it is seen as the 'next step' to produce it in a nanowire morphology. For this reason we have chosen to develop methods to electrochemical deposit PPyEtCN nanowires by a template free method.

The PPyEtCN polymer is observed to have a similar conductivity to that of PPyMe, which is about 5.5 x 10^{-3} Scm^{-1}. This is significantly smaller than the unsubstituted monomer analogues which are typically 5 times more conducting. It was also observed that this monomer underwent an overoxidation process by the incorporation of carbonyl groups at the β-position which would reduce the degree of conjugation

further and encourage polymer chains to form with irregularities, Figure 1.15. [119] Interestingly, these linkage defects can generate distortions in adjacent chains leading to further linkage errors. Therefore, the formation of conjugation defects (α-β and β-β linkages) at early stages of polymer growth can have a much more detrimental effect on the stereoregularity and stacking of the polymer chains compared to the same defect occurring at a later stage.[32] It was also reported that due to the steric interactions involved with the cyano moiety that the π-π interaction between monomer units was reduced and the polymer consisted of highly cross linked structure with a terminating carbonyl terminating group, [120] Figure 1.16. These factors also explain the reason why PPyEtCN has a higher oxidation potential compared to PPy. Subsequently, electropolymerising a conducting and useful PPyEtCN film is a task which has inherent difficulties.

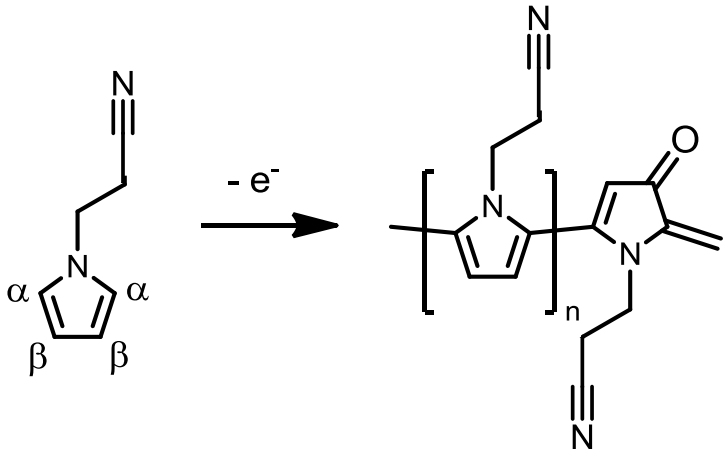

Figure 1.15. Structure of the PPyEtCN monomer showing the positions and the resultant polymer after polymerisation with the terminal carbonyl group.

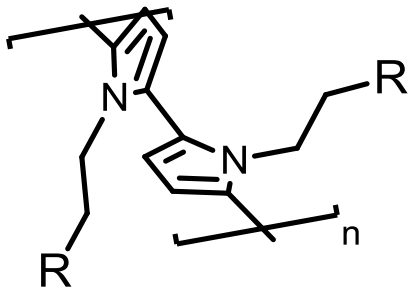

Figure 1.16. Structure of an N substituted monomer which has lower planarity of the π system due to steric clashing.

1.5 Copper Electrodeposition

The electrodeposition of copper at an electrode surface is a vast area of research. Generally, a reductive potential is applied to the working electrode which reduces the metal ion in solution and causes it to deposit on the electrode surface. It offers advantages such as low temperature, low cost and high control.[122] The electrodeposited materials remains in good electrical contact with the substrate which makes them easily integrated into electrical devices. The high level of understanding surrounding the underlying electrochemistry[4] has produced a significant amount publications on the topic. As the morphology is a function of the applied potential, copper concentration and temperature, a large array of morphologies have been developed[123] such as honeycomb,[124] sphere,[125] dendrite,[126] octahedral,[127] nanowire,[128] flower[129] and nanoparticle.[130]

Some of the more prominent researchers in the field are Choi and co-workers, who have a range of publications[131-135] and review articles[136-137] relating to the development of electrochemical deposition of Cu_2O structures in controlled morphologies. They have developed a means of controlling the crystal habit (visible external shape) by selectively hindering growth rates at certain facets of the copper crystal. This produces a vast number of branched and octahedral shapes as shown in Figure 1.18.[123] They describe the formation of copper crystal habits as always growing fastest at the higher energy faces, therefore low energy faces (100) (such as cube) will end up the predominant morphology, Figure 1.17. In their experiments they used SO_4^- and sodium dodecylsulfate to stabilise the high energy (111) faces and limit the formation of (100). This understanding was employed in Chapter 5 to investigate the production of specific crystal structures at PPy surfaces.

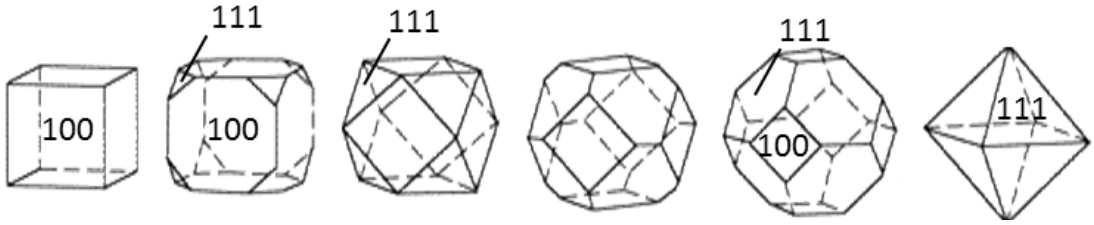

Scheme 1.17. Orientations of different crystal surfaces.

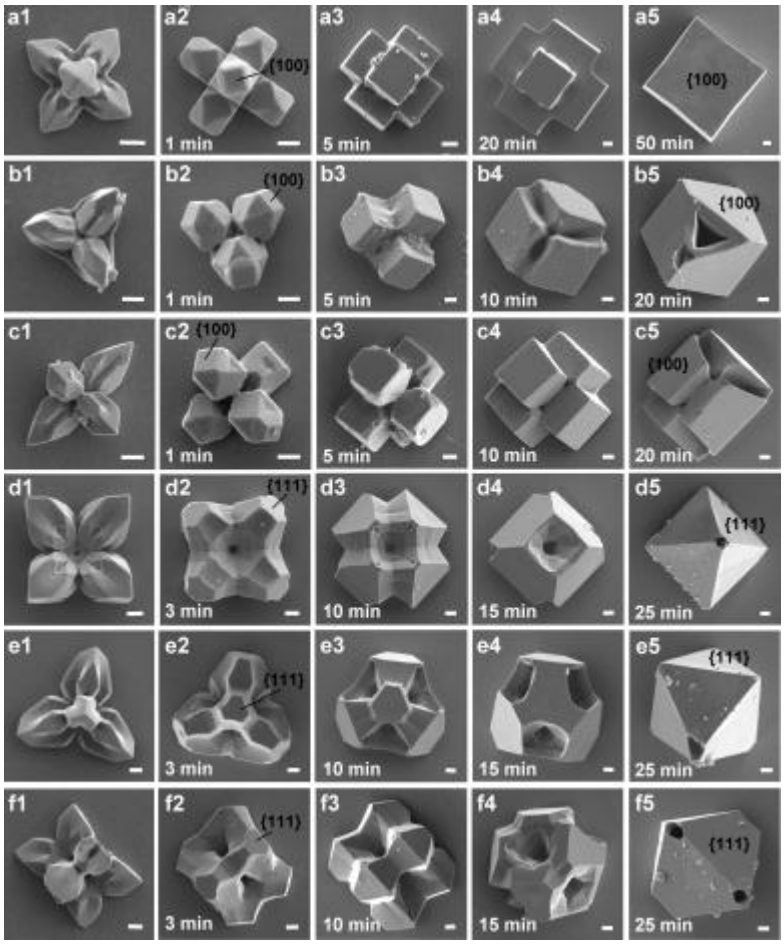

Figure 1.18. The array of copper crystal habits produced by Choi and co-workers[123] which highlights the versatility of electrodeposition techniques.

There are many benefits to employing a CP as a substrate material to electrodeposit copper.[138] Leung *et al.*[139-140] have shown that the polymer thickness has a drastic effect on the number of nucleation sites and size of the copper deposits. This shows that the PPy substrate itself can be used to affect the final deposit morphology. The different surface species of copper can be identified at an electrode by cyclic voltammetry, as shown in Figure 1.19[141]. Here, different peaks are identified as the potential is switched from oxidative to reductive segments of the voltammogram, which signifies the formation of a new copper species at a GC electrode.

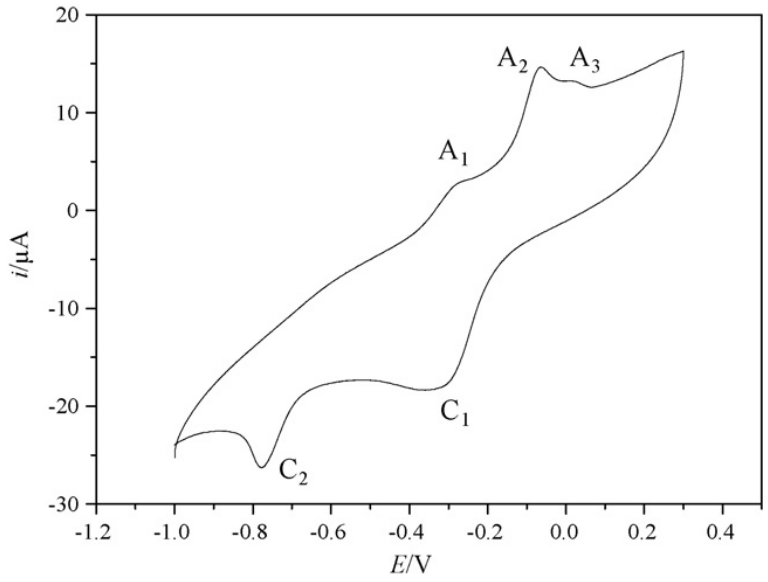

Figure 1.19. Copper deposition process at a GC electrode in a 0.100 M NaOH solution.

The peak labels A_1-A_3 and C_1-C_2 are given as:[141]

Peak A_1: $Cu + OH^- - e^- \rightarrow CuOH$

$2CuOH \rightarrow Cu_2O + H_2O$

Peak $A_2(A_3)$: $CuOH + OH^- - e^- \rightarrow CuO + H_2O$

$Cu_2O + 2OH^- - 2e^- \rightarrow 2CuO + H_2O$

Peak C_1: $CuO + H_2O - e^- \rightarrow CuOH + OH^-$

$2CuO + H_2O - 2e^- \rightarrow Cu_2O + 2OH^-$

Peak C_2: $CuOH - e^- \rightarrow Cu + OH^-$

$Cu_2O + H_2O - 2e \rightarrow 2Cu + 2OH^-$

This can be used to identify which copper species will be generated when an applied constant potential is used. Work is presented in Chapter 5 which focuses on varying the reductive potential to generate copper deposits of different morphologies. In this work the aim was to produce Cu_2O copper materials, therefore potentials more reductive than -0.200 V were not employed (see Figure 1.19).

1.5.1 Copper Electrodeposition at Polypyrrole Substrates

It has been proposed that PPy polymers can act as an intermediate for the electrodeposition of copper species. This is because Cu(I) ions are inserted into the polymer matrix and have a role in the charge compensation of the polymer backbone. The PPy surface is first reduced to Ppy^0 and these sites subsequently transfer charge to the copper ion, Figure 1.20.[142] Interestingly, at a PPy surface a Cu(I)-PPy complex is formed when an reduction potential is applied, Figure 1.21, with a strong interaction with the pyrrolyium nitrogen. It also leads to copper being deposited on the surface and inside the polymer matrix.[143] The formation of Cu(II)-PPy or Cu(0)-PPy complexes is not suggested in this process.

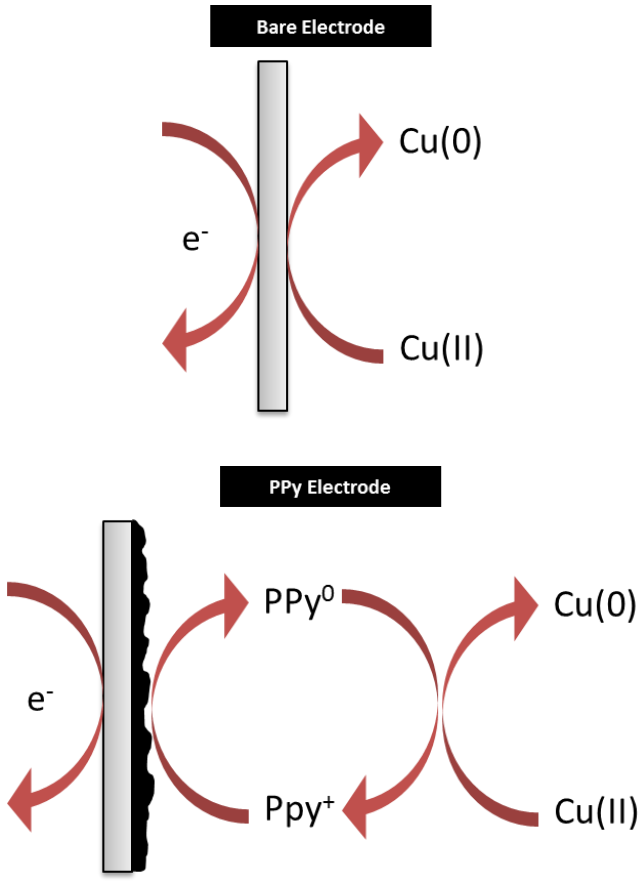

Figure 1.20. The electrochemical reduction of copper at a bare electrode and a PPy modified electrode.

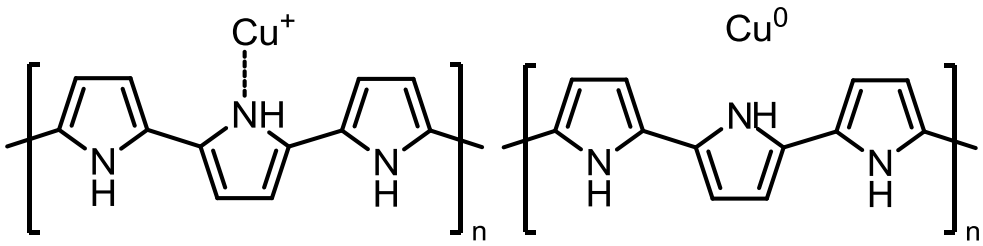

Figure 1.21. Valence copper (left) and elemental copper (right) obtained during the electrochemical reduction of Cu(II) at a PPy surface.

Wang and Liu have done extensive research on the interaction of copper with PPy. They showed that because of this interaction the intrinsic conductivity of the PPy was increased.[144-145] This is due to copper locating at the Py nitrogen and donating electrons into the PPy backbone.[144] They also showed that PPy-Cu(I) was more stable than PPy when exposed to an oxygen atmosphere for 50 days, again citing the electron transfer from copper to Py as the reason for the stability enhancement.[146] Liu and co-workers later described the interaction of the Cu(I) species as strong enough to remain bound to PPy even when an anodic potential was applied.[147] Therefore, PPy has the ability to stabilise Cu(I) species.

The ability to encourage the formation of Cu(I) species has an implication for the development of photo-electrochemical and photovoltaic devices.[134, 148] Furthermore, controlling the morphology of the Cu(I) deposits has the ability to increase the efficiency of such devices.[136, 149] Using PPy as a substrate material to stabilise Cu(I) species and improve its conductivity has benefits as a practical nanocomposite. To investigate this, the copper materials developed in Chapter 5 were investigated as possible electrochemical sensors for the nitrate ion.

1.6 Nitrate Sensing

The determination of nitrate levels and their subsequent removal plays an important role in water analysis. In recent years there has been considerable interest in nitrate pollutants with the introduction of the Nitrates Directive (1991/676/EC) and the EU Water Framework Directive (WFD) (200/60/EC). Nitrates are a common ground water contaminant in irrigation waters and in heavily populated areas. Over exposure can lead to a host of medical problems (the nitrate safe limit is set at 30 mg/L i.e. 800 μM); for example nitrates can combine with amines to form toxic and carcinogenic nitrosamines. Also, nitrates in the form of fertilisers can cause eutrophication of water.[150] This is seen as the main threat to surface water quality, which is the over-abundant growth of plant and algae arising from excess nutrients in the water. These nutrients then consume the available dissolved oxygen in the water killing aquatic life. In agriculture, higher productivity over the past fifty years was accompanied by a significant increase in the use of inorganic nitrogen and phosphate fertilisers.[151] Ireland has a significant problem due to high levels of agricultural land use which is a large source of unwanted nitrates, Figure 1.22. The "Water Quality in Ireland 2006 – Key Indicators of the Aquatic Environment" which was published in October 2007 describes "eutrophication of rivers, lakes and tidal waters to be the main threat to surface waters with agricultural run-off and municipal discharges being the key contributors." It also refers to agricultural run-off as being the main threat to the quality of the groundwater resource.

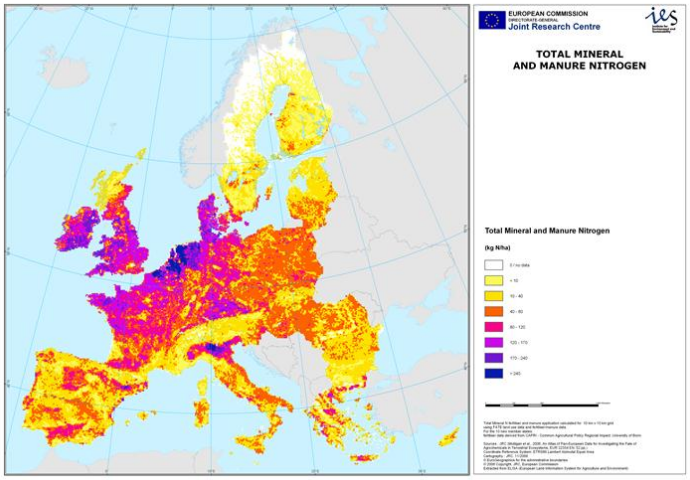

Figure 1.22. Total nitrogen application, manure and chemical fertilizer (source : JRC, Mulligan et al., 2006).

Increasing concern about the rising concentration of nitrate in groundwater has resulted in intensive research in the area of denitrification of drinking water.[152] These factors combined with the fact that Ireland is required to meet the WFD, which requires 'good water status' for all European waters by 2015. Irelands monitoring policy was mentioned specifically within the WFD document as being below par compared to other member states, as shown from Figure 1.23. It was also highlighted that rivers, lakes and ground waters had more than a 60% chance of failing to meet the WFD agreement by 2015,[153] Figure 1.24. Therefore Ireland, due to its large agricultural practises and low monitoring policy, is in need of good quality and accurate nitrate sensing technologies.

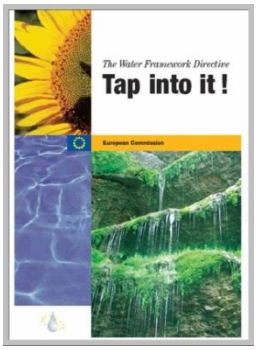

"By the end of 2003, all Member States, with the exception of Ireland, had, albeit some rather belatedly, established one or more action programmes on their territory. Ireland finally established its programme in 2006."

"Member States (except Spain, Greece and Ireland) provided details on their monitoring programme regarding frequency."

Figure 1.23. Quotes from the WFD relating to the monitoring programmes in Ireland.

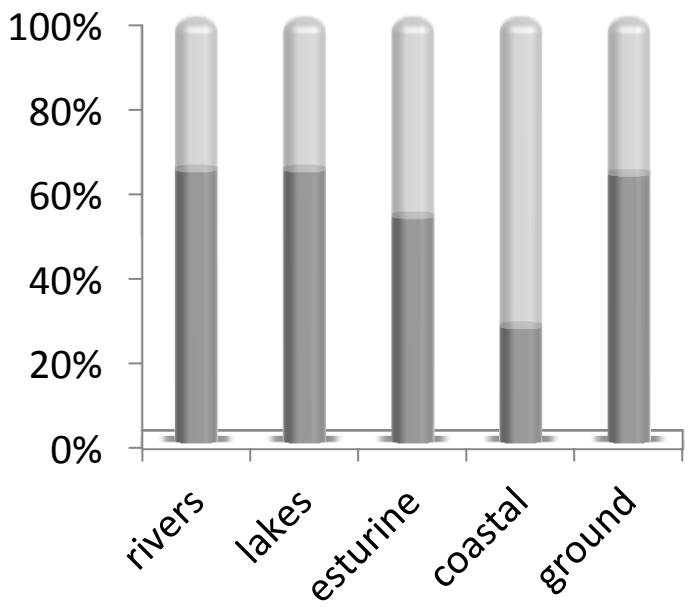

Figure 1.24. The percentage of water bodies in Ireland at risk of failing to meet the WFD good water targets.

1.6.1 Current Research in Electrochemical Nitrate Sensors

There is significant research interest in developing methods to detect nitrate by using electrochemistry.[154-156] This is due to the flexible, inexpensive, possibility of miniaturisation and in-situ measurement associated with these sensors.[157] The trend of employing nanomaterials to increase the sensor response has also been developed for nitrate electrochemical sensors.[158-160] The nitrate reduction reaction may occur by the reaction:

$$NO_3^- + H_2O + 2e^- \rightarrow NO_2^- + 2OH^-$$

Further reduction of nitrate to ammonia is also possible by the reaction:

$$NO_2^- + 5H_2O + 6e^- \rightarrow NH_3 + 7OH^-$$

It is known that the nitrate reduction reaction is a multistep reduction reaction which is controlled kinetically rather than by diffusion, proceeding by the following reactions:[161]

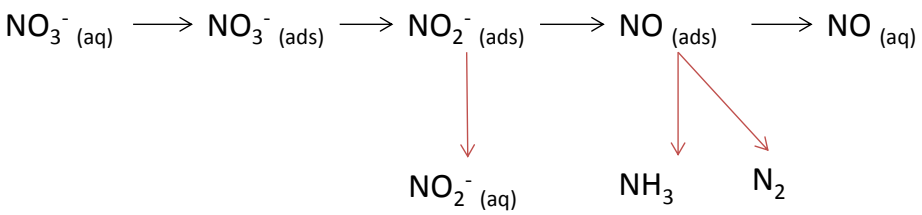

Several metals have been investigated for their ability to catalyse the nitrate reduction reaction such as iron and silver.[162-163] The most actively studied metal for nitrate electroreduction is copper.[164] Several electrochemical methods have been produced to use copper as a nitrate sensor. It has been shown that nitrate undergoes an adsorption step before it can be electrochemically reduced. This has been observed to happen by the reaction:

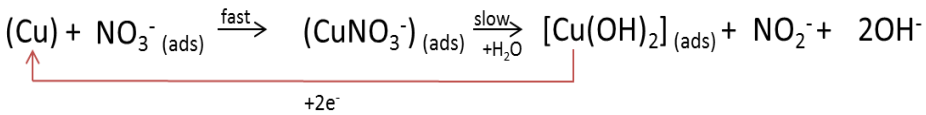

Gabriela Badea [165] studied the nitrate electroreduction in alkaline media at a copper electrode and proposed that copper promotes intermediate nitrate species formation because the bond length of Cu-Cu (1.32 Å) is similar to the bond length of N-N (1.4 Å). Roue *et al.*[166], using similar conditions, found that the nitrate electroreduction reaction was an adsorption process strongly dependant on the applied potential. This nitrate adsorption step which precedes electroreduction was further demonstrated by Casella and Gatta.[167]

Several authors have reported using electrochemically deposited copper, over a copper electrode, as an effective nitrate sensor, as it has been observed to catalyse the reduction of nitrate.[168] Bertotti *et al.*[169] developed a means of replenishing the copper surface by dissolution and redeposition of copper species at a copper wire. Compton *et al.*[170-171] showed that copper deposits at carbon and boron doped diamond were capable of distinguishing between the reduction of nitrate and nitrite. Therefore, there are clear advantages to developing a sensor based on electrodeposited copper particularly if nanostructuring can be employed. This is discussed in Chapter 5 where the combination of PPy nanowires and copper electrodeposited micro and nanoparticles are tested for their ability to detect the nitrate ion.

1.7 References

1. Singh, T.; Pandya, D. K.; Singh, R. *Appl. Surf. Sci.* **2013,** *270*, 578-583.
2. Jiao, S.-H.; Xu, D.-S.; Xu, L.-F.; Zhang, X.-G. *Wuli Huaxue Xuebao* **2012,** *28*, 2436-2446.
3. Bedioui, F.; Nyokong, T.; Zagal, J. H. *Int. J. Electrochem.* **2012**, 405825, 2 pp.
4. Milan Paunovic, M. S. *Fundamentals of Electrochemical Deposition*. Wiley: **2006**; p 52.
5. Dong, S.; Chen, X.; Zhang, X.; Cui, G. *Coord. Chem. Rev.* **2013,** *257*, 1946-1956.
6. Veloso, A. J.; Cheng, X. R.; Kerman, K. *Biomaterials* **2012,** *45*, 3-40.
7. Kumar, H.; Rajan, S.; Shukla, A. K. *Sci. Prog.* **2012,** *95*, 283-314.
8. Kois, J.; Bereznev, S.; Gurevits, J.; Volobujeva, O. *Mater. Lett.* **2013,** *95*, 110-113.
9. Oja, S. M.; Wood, M.; Zhang, B. *Anal. Chem.* **2013,** *85*, 473-486.
10. Janaky, C.; Visy, C. *Anal. Bioanal. Chem.* **2013,** *405*, 3489-3511.
11. Mazloum-Ardakani, M.; Sheikh-Mohseni, M. A.; Abdollahi-Alibeik, M.*J. Mol. Liq.* **2013,** *178*, 63-69.
12. Cho, S. I.; Lee, S. B. *Acc. Chem. Res.* **2008,** *41*, 699-707.
13. McCarthy, C. P.; McGuinness, N. B.; Alcock-Earley, B. E.; Breslin, C. B.; Rooney, A. D. *Electrochem. Commun.* **2012,** *20*, 79-82.
14. McCarthy, C. P.; McGuinness, N. B.; Carolan, P. B.; Fox, C. M.; Alcock-Earley, B. E.; Breslin, C. B.; Rooney, A. D. *Macromolecules* **2013,** *46*, 1008-1016.
15. Stevenson, R. *Chem. Br.* **2000,** *36*, 26-28.
16. Johanson, U.; Marandi, M.; Tamm, T.; Tamm, J. *Electrochim. Acta* **2005,** *50*, 1523-1528.
17. Dziewonski, P. M.; Grzeszczuk, M. *J. Phys. Chem. B* **2010,** *114*, 7158-7171.
18. George, P. M.; Lyckman, A. W.; LaVan, D. A.; Hegde, A.; Leung, Y.; Avasare, R.; Testa, C.; Alexander, P. M.; Langer, R.; Sur, M. *Biomaterials* **2005,** *26*, 3511-3519.
19. Dubal, D. P.; Lee, S. H.; Kim, J. G.; Kim, W. B.; Lokhande, C. D. *J. Mater. Chem.* **2012,** *22*, 3044-3052.
20. Kaneto, K.; Takashima, W. *J. Phys.: Conf. Ser.* **2012,** *358*, 012002/1-012002/6.
21. Kathuroju, P. K.; Jampana, N. *IEEE Trans. Instrum. Meas.* **2012,** *61*, 2339-2345.

22. Sharma, M.; Waterhouse, G. I. N.; Loader, S. W. C.; Garg, S.; Svirskis, D. *Int J Pharm* **2013,** *443*, 163-8.

23. Annibaldi, V.; Rooney, A. D.; Breslin, C. B. *Corros. Sci.* **2012,** *59*, 179-185.

24. Chandrasekhar, P. *Conducting Polymers, Fundamental and Applications*. Kluwer Academic Publishers: **1999**.

25. Dall'Olio, A.; Dascola, G.; Varacca, V.; Bocchi, V. *C. R. Acad. Sci., Paris, Ser. C* **1968,** *267*, 433-5.

26. Diaz, A. F.; Kanazawa, K. K.; Gardini, G. P. *Chem. Commun.* **1979,** *0*, 635-636.

27. Jang, J.; Oh, J. H.; Li, X. L. *J. Mater. Chem.* **2004,** *14*, 2872-2880.

28. Saunders, B. R.; Fleming, R. J.; Murray, K. S. *Chem. Mater.* **1995,** *7*, 1082-94.

29. Sabouraud, G.; Sadki, S.; Brodie, N. *Chem. Soc. Rev.* **2000,** *29*, 283-293.

30. Silk, T.; Hong, Q.; Tamm, J.; Compton, R. G. *Synth. Met.* **1998,** *93*, 59-64.

31. Silk, T.; Hong, Q.; Tamm, J.; Compton, R. G. *Synth. Met.* **1998,** *93*, 65-71.

32. Roncali, J. *Chem. Rev.* **1992,** *92*, 711-738.

33. Sayyah, S. M.; Abd, E.-R. S. S.; El-Deeb, M. M. *J. Appl. Polym. Sci.* **2003,** *90*, 1783-1792.

34. Ko, J. M.; Rhee, H. W.; Park, S. M.; Kim, C. Y. *J. Electrochem. Soc.* **1990,** *137*, 905-909.

35. Saunders, B. R.; Fleming, R. J.; Murray, K. S. *Chem. Mater.* **1995,** *7*, 1082-94.

36. Li, Y.; Qian, R. *Electrochimica. Acta.* **2000,** *45*, 1727-1731.

37. Qian, R.; Qiu, J. *Polymer Journal* **1987,** *19*, 157-172.

38. Ozkorucuklu, S. P.; Sahin, Y.; Alsancak, G. *Sensors* **2008,** *8*, 8463-8478.

39. Debiemme-Chouvy, C.; Tran, T. T. M. *Electrochem. Commun.* **2008,** *10*, 947-950.

40. Long, Y.-Z.; Li, M.-M.; Gu, C.; Wan, M.; Duvail, J.-L.; Liu, Z.; Fan, Z. *Prog. Polym. Sci.* **2011,** *36*, 1415-1442.

41. Huang, J.; Wang, K.; Wei, Z. *J. Mater. Chem.* **2010,** *20*, 1117-1121.

42. Martin, C. R. *Acc. Chem. Res.* **1995,** *28*, 61-68.

43. Penner, R. M.; Martin, C. R. *J. Electrochem. Soc.* **1986,** *133*, 2206-7.

44. Qu, L.; Shi, G.; Yuan, J.; Han, G.; Chen, F. E. *J. Electroanal. Chem.* **2004,** *561*, 149-156.

45. Wang, J.; Xu, Y.; Yan, F.; Zhu, J.; Wang, J. *J. Power Sources* **2011,** *196*, 2373-2379.

46. Al-Mashat, L.; Debiemme-Chouvy, C.; Borensztajn, S.; Wlodarski, W. *J. Phys. Chem. C* **2012,** *116*, 13388-13394.

47. Zang, J.; Li, C. M.; Bao, S.-J.; Cui, X.; Bao, Q.; Sun, C. Q. *Macromolecules* **2008,** *41*, 7053-7057.

48. Ge, D.; Huang, S.; Qi, R.; Mu, J.; Shen, Y.; Shi, W. *ChemPhysChem* **2009,** *10*, 1916-1921.

49. Ge, D.; Ru, X.; Hong, S.; Jiang, S.; Tu, J.; Wang, J.; Zhang, A.; Ji, S.; Linkov, V.; Ren, B.; Shi, W. *Electrochem. Commun.* **2010,** *12*, 1367-1370.

50. Meng, F.; Shi, W.; Sun, Y.; Zhu, X.; Wu, G.; Ruan, C.; Liu, X.; Ge, D. *Biosens. Bioelectron.* **2013,** *42*, 141-147.

51. Ru, X.; Shi, W.; Huang, X.; Cui, X.; Ren, B.; Ge, D. *Electrochim. Acta* **2011,** *56*, 9887-9892.

52. Al-Mashat, L.; Debiemme-Chouvy, C.; Borensztajn, S.; Wlodarski, W. *J. Phys. Chem. C* **2012,** *116*, 13388-13394.

53. Debiemme-Chouvy, C. *Electrochem. Commun.* **2009,** *11*, 298-301.

54. Huang, J.; Quan, B.; Liu, M.; Wei, Z.; Jiang, L. *Macromol. Rapid Commun.* **2008,** *29*, 1335-1340.

55. Huang, J.; Wang, K.; Wei, Z. Method and electrolyte for fabricating nanoscale polypyrrole electrode, and application thereof to supercapacitor. CN101635201A, 2010.

56. Huang, J.; Wei, Z.; Chen, J. *Sens. Actuators, B* **2008,** *B134*, 573-578.

57. Huang, J.; Luo, X.; Lee, I.; Hu, Y.; Cui, X. T.; Yun, M. *Biosens. Bioelectron.* **2011,** *30*, 306-309.

58. Lu, G.; Li, C.; Shi, G. *Polymer* **2006,** *47*, 1778-1784.

59. Ge, D.; Mu, J.; Huang, S.; Liang, P.; Gcilitshana, O. U.; Ji, S.; Linkov, V.; Shi, W. *Synth. Met.* **2011,** *161*, 166-172.

60. Shi, W.; Liang, P.; Ge, D.; Wang, J.; Zhang, Q. *Chem. Commun.* **2007**, 2414-2416.

61. Shi, W.; Ge, D.; Wang, J.; Jiang, Z.; Ren, L.; Zhang, Q. *Macromol. Rapid Commun.* **2006,** *27*, 926-930.

62. Zhou, M.; Heinze, J. *J. Phys. Chem. B* **1999,** *103*, 8443-8450.

63. Huang, J.; Quan, B.; Liu, M.; Wei, Z.; Jiang, L. *Macromol. Rapid Commun.* **2008,** *29*, 1335-1340.

64. Liang, L.; Liu, J.; Windisch, J. C. F.; Exarhos, G. J.; Lin, Y. *Angew. Chem. Int., Ed.* **2002,** *41*, 3665-3668.

65. Jang, J.; Yoon, H. *Chem.Commun.* **2003**, 720-721.

66. Zhou, C.; Han, J.; Guo, R. *J. Phys. Chem. B* **2008,** *112*, 5014-5019.

67. Gonzalez, M. B.; Saidman, S. B. *Electrochem. Commun.* **2011,** *13*, 513-516.

68. Shen, Y.; Wan, M. *J. Polym. Sci., Polym. Chem.* **1999,** *37*, 1443-1449.

69. Orinakova, R.; Filkusova, M. *Synth. Met.* **2010,** *160*, 927-931.

70. Kim, S. W.; Cho, H. G.; Park, C. R. *Langmuir* **2009,** *25*, 9030-9036.

71. Parakhonskiy, B.; Andreeva, D.; Möhwald, H.; Shchukin, D. G. *Langmuir* **2009,** *25*, 4780-4786.

72. Bajpai, V.; He, P.; Dai, L. *Adv. Funct. Mater.* **2004,** *14*, 145-151.

73. Caruso, F.; Trau, D.; Moehwald, H.; Renneberg, R. *Langmuir* **2000,** *16*, 1485-1488.

74. Shchukin, D. G.; Sukhorukov, G. B.; Price, R. R.; Lvov, Y. M. *Small* **2005,** *1*, 510-513.

75. Daehne, L.; Leporatti, S.; Donath, E.; Moehwald, H. *J. Am. Chem. Soc.* **2001,** *123*, 5431-5436.

76. Langer, R. *Science* **1990,** *249*, 1527-33.

77. Mazur, M. *Langmuir* **2008,** *24*, 10414-10420.

78. Kępińska, D.; Blanchard, G. J.; Krysiński, P.; Stolarski, J.; Kijewska, K.; Mazur, M. *Langmuir* **2011,** *27*, 12720-12729.

79. Kubacka, D.; Krysiński, P.; Blanchard, G. J.; Stolarski, J.; Mazur, M. *J. Phys.Chem. B* **2010,** *114*, 14890-14896.

80. Kijewska, K.; Blanchard, G. J.; Szlachetko , J.; Stolarski, J.; Kisiel, A.; Michalska, A.; Maksymiuk, K.; Pisarek, M.; Majewski, P.; Krysiński, P.; Mazur, M. *Chem.–Eur. J.* **2012,** *18*, 310-320.

81. Li, C.; Bai, H.; Shi, G. *Chem. Soc. Rev.* **2009,** *38*, 2397-2409.

82. Qu, L.; Shi, G. *Chem. Commun.* **2003**, 206-207.

83. Qu, L.; Shi, G.; Chen, F. E.; Zhang, J. *Macromolecules* **2003,** *36*, 1063-1067.

84. Qu, L.; Shi, G. *J. Polym. Sci., Polym. Chem.* **2004,** *42*, 3170-3177.

85. Qu, L.; Shi, G.; Yuan, J.; Han, G.; Chen, F. E. *J. Electroanal. Chem.* **2004,** *561*, 149-156.

86. Asami, R.; Fuchigami, T.; Atobe, M. *Langmuir* **2006,** *22*, 10258-10263.

87. Asami, R.; Atobe, M.; Fuchigami, T. *J. Am. Chem. Soc.* **2005,** *127*, 13160-13161.

88. Atobe, M.; Ishikawa, K.; Asami, R.; Fuchigami, T. *Angew. Chem., Int. Ed.* **2009,** *48*, 6069-6072, S6069/1-S6069/3.

89. Atobe, M.; Tsuji, H.; Asami, R.; Fuchigami, T. *J. Electrochem. Soc.* **2006,** *153*, D10-D13.

90. Gao, Y.; Zhao, L.; Bai, H.; Chen, Q.; Shi, G. *J. Electroanal. Chem.* **2006,** *597*, 13-18.

91. Gao, Y.; Zhao, L.; Li, C.; Shi, G. *Polymer* **2006,** *47*, 4953-4958.

92. Teixeira-Dias, B.; Alemán, C.; Estrany, F.; Azambuja, D. S.; Armelin, E. *Electrochim. Acta 56*, 5836-5843.

93. Fabregat, G.; Alemán, C.; Casas, M. T.; Armelin, E. *J. Phys. Chem. B* **2012,** *116*, 5064-5070.

94. Marti, M.; Fabregat, G.; Estrany, F.; Alemán, C.; Armelin, E. *J. Mater. Chem.* **2010,** *20*, 10652-10660.

95. Khan, W.; Kapoor, M.; Kumar, N. *Acta Biomaterialia* **2007,** *3*, 541-549.

96. Fabregat, G.; Córdova-Mateo, E.; Armelin, E.; Bertran, O.; Alemán, C. *J. Phys. Chem. C* **2011,** *115*, 14933-14941.

97. Um, H.-J.; Kim, M.; Lee, S.-H.; Min, J.; Kim, H.; Choi, Y.-W.; Kim, Y.-H. *Talanta* **2011,** *84*, 330-334.

98. Li, X.; Xia, J.; Zhang, S. *Analytica Chimica Acta* **2008,** *622*, 104-110.

99. Peng, H.; Soeller, C.; Vigar, N.; Kilmartin, P. A.; Cannell, M. B.; Bowmaker, G. A.; Cooney, R. P.; Travas-Sejdic, J. *Biosens. Bioelectron.* **2005,** *20*, 1821-1828.

100. Sen, G. S.; Uygun, A.; Tilki, T. *J. Macromol. Sci., Part A: Pure Appl. Chem.* **2010,** *47*, 681-688.

101. Li, X.; Wang, Y.; Yang, X.; Chen, J.; Fu, H.; Cheng, T. *Trends in Anal. Chem,* **2012,** *39*, 163-179.

102. Aytaç, S.; Kuralay, F.; Boyacı, İ. H.; Unaleroglu, C. *Sens. Actuators, B* **2011,** *160*, 405-411.

103. Percec, S.; Skidd, G.; Zheng, M. *J. Polym. Sci., Part A: Polym. Chem.* **2009,** *47*, 6014-6024.

104. Sravendra, R.; Niranjan, K.; Jae Whan, C.; Young Ho, K. *Nanotechnology* **2008,** *19*, 495707.

105. Kwon, O. S.; Park, S. J.; Jang, J. *Biomaterials* **2010,** *31*, 4740-4747.

106. Shida, N.; Ishiguro, Y.; Atobe, M.; Fuchigami, T.; Inagi, S. *ACS Macro Letters* **2012,** *1*, 656-659.

107. Jiang, H.; Zhang, A.; Sun, Y.; Ru, X.; Ge, D.; Shi, W. *Electrochim. Acta* **2012,** *70*, 278-285.

108. Raso, M. A.; Gonzalez-Tejera, M. J.; Carrillo, I.; Sanchez, d. l. B. E.; Garcia, M. V.; Redondo, M. I. *Thin Solid Films* **2011,** *519*, 2387-2392.

109. Arjomandi, J.; Safdar, S.; Malmir, M. *J. Electrochem. Soc.* **2012,** *159*, E73-E81.

110. Teixeira-Dias, B.; Alemán, C.; Estrany, F.; Azambuja, D. S.; Armelin, E. *Electrochim. Acta* **2011,** *56*, 5836-5843.

111. Redondo, M. I.; Sanchez, d. l. B. E.; Garcia, M. V.; Gonzalez-Tejera, M. J. *Prog. Org. Coat.* **2009,** *65*, 386-391.

112. Kadam, S. B.; Datta, K.; Ghosh, P.; Shirsat, M. D. *Int. J. Polym. Mater.* **2011,** *60*, 233-243.

113. Atta, N. F.; El-Kady, M. F.; Galal, A. *Anal. Biochem.* **2010,** *400*, 78-88.

114. González-Tejera, M. J.; de la Blanca, E. S.; Carrillo, I.; Redondo, M. I.; Raso, M. A.; Tortajada, J.; García, M. V. *Synth. Met.* **2005,** *151*, 100-105.

115. González-Tejera, M. J.; Garcá-a, M. V.; SÃnchez de la Blanca, E.; Redondo, M. I.; Raso, M. A.; Carrillo, I. *Thin Solid Films* **2007,** *515*, 6805-6811.

116. Kim, J.-Y.; Kim, J.-T.; Song, E.-A.; Min, Y.-K.; Hamaguchi, H.-o. *Macromolecules* **2008,** *41*, 2886-2889.

117. Aradilla, D.; Estrany, F.; Armelin, E.; Alemán, C. *Thin Solid Films* **2010,** *518*, 4203-4210.

118. McGuinness, N. B.; McCarthy, C. P.; Rooney, A. D. *Unpublished work*.

119. Aradilla, D.; Estrany, F.; Armelin, E.; Oliver, R.; Iribarren, J. I.; Alemán, C. *Macromol. Chem. Phys.* **2010,** *211*, 1663-1672.

120. Aradilla, D.; Torras, J.; Alemán, C. *J. Phys. Chem. B* **2011,** *115*, 2882-2889.

121. Ouerghi, O.; Senillou, A.; Jaffrezic-Renault, N.; Martelet, C.; Ben Ouada, H.; Cosnier, S. *J. Electroanal. Chem.* **2001,** *501*, 62-69.

122. Zhou, Y.; Switzer, J. A. *Scr. Mater.* **1998,** *38*, 1731-1738.

123. Siegfried, M. J.; Choi, K.-S. *Angew. Chem., Int. Ed.* **2005,** *44*, 3218-3223.

124. Shin, H.-C.; Dong, J.; Liu, M. *Adv. Mater.* **2003,** *15*, 1610-1614.

125. Zheng, J. Y.; Jadhav, A. P.; Song, G.; Kim, C. W.; Kang, Y. S. *Thin Solid Films* **2012,** *524*, 50-56.

126. Qiu, R.; Cha, H. G.; Noh, H. B.; Shim, Y. B.; Zhang, X. L.; Qiao, R.; Zhang, D.; Kim, Y. I.; Pal, U.; Kang, Y. S. *J. Phys. Chem. C* **2009,** *113*, 15891-15896.

127. Huang, Y.-F.; Shih, H.-S.; Lin, C.-W.; Xu, P.; Williams, D. J.; Ramos, K. J.; Hooks, D. E.; Wang, H.-L. *Crystal Growth & Design* **2012,** *12*, 1778-1784.

128. Daltin, A.-L.; Addad, A.; Chopart, J.-P. *J. Cryst. Growth* **2005,** *282*, 414-420.

129. Tang, S. C.; Meng, X. K. *Sci. China, Ser. E: Technol. Sci.* **2009,** *52*, 2709-2714.

130. Huang, L.; Lee, E.-S.; Kim, K.-B. *Colloids Surf., A* **2005,** *262*, 125-131.

131. Siegfried, M. J.; Choi, K.-S. *J. Am. Chem. Soc.* **2006,** *128*, 10356-10357.

132. Siegfried, M. J.; Choi, K.-S. *J. Electrochem. Soc.* **2007,** *154*, D674-D677.

133. Siegfried, M. J.; Choi, K.-S. *Angew. Chem., Int. Ed.* **2008,** *47*, 368-372.

134. McShane, C. M.; Choi, K.-S. *J. Am. Chem. Soc.* **2009,** *131*, 2561-2569.

135. Siegfried, M. J.; Choi, K.-S. *Adv. Mater.* **2004,** *16*, 1743-1746.

136. Choi, K.-S. *J. Phys. Chem. Lett.* **2010,** *1*, 2244-2250.

137. Choi, K.-S. *Dalton Trans.* **2008**, 5432-5438.

138. Tsakova, V. *J. Solid State Electrochem.* **2008,** *12*, 1421-1434.

139. Sarkar, D. K.; Zhou, X. J.; Tannous, A.; Louie, M.; Leung, K. T. *Solid State Commun.* **2003,** *125*, 365-368.

140. Zhou, X. J.; Harmer, A. J.; Heinig, N. F.; Leung, K. T. *Langmuir* **2004,** *20*, 5109-5113.

141. Le, W.-Z.; Liu, Y.-Q. *Sens. Actuators, B.* **2009,** *141*, 147-153.

142. Tian, Y.; Li, Z.; Xu, H.; Yang, F. *Separation and Purification Technology* **2008,** *63*, 334-340.

143. Hepel, M.; Chen, Y.-M.; Stephenson, R. *J. Electrochem. Soc.* **1996,** *143*, 498-505.

144. Liu, Y. C.; Hwang, B. J. *Thin Solid Films* **1999,** *339*, 233-239.

145. Liu, Y. C.; Hwang, B. J. *J. Electroanal. Chem.* **2001,** *501*, 100-106.

146. Liu, Y.-C.; Hwang, B. J. *Thin Solid Films* **2000,** *360*, 1-9.

147. Liu, Y.-C.; Yang, K.-H.; Ger, M.-D. *Synth. Met.* **2002,** *126*, 337-345.

148. Mandke, M. V.; Pathan, H. M. *J. Electroanal. Chem.* **2012,** *686*, 19-24.

149. Mao, Y.; He, J.; Sun, X.; Li, W.; Lu, X.; Gan, J.; Liu, Z.; Gong, L.; Chen, J.; Liu, P.; Tong, Y. *Electrochimica Acta* **2012,** *62*, 1-7.

150. Prüsse, U.; Hähnlein, M.; Daum, J.; Vorlop, K.-D. *Catalysis Today* **2000,** *55*, 79-90.

151. Eurpean Communities Council, Nitrates Directive **1991**.

152. Environmental Protection Agency, H. S. E. *Joint Position Paper, Nitrates in Drinking Water*; Ireland, **2010**.

153. Agency, E. P. *Water Quality in Ireland 2006 - Key Indicators of the Aquatic Environment*; **2007**.

154. Armijo, F.; Goya, M. C.; Reina, M.; Canales, M. J.; Arevalo, M. C.; Aguirre, M. J. *J. Mol. Catal. A: Chem.* **2007,** *268*, 148-154.

155. Carpenter, N. G.; Pletcher, D. *Anal. Chim. Acta* **1995,** *317*, 287-93.

156. Ojani, R.; Raoof, J.-B.; Zarei, E. *Electrochim. Acta* **2006,** *52*, 753-759.

157. Bendikov, T. A.; Kim, J.; Harmon, T. C. *Sens. Actuators, B* **2005,** *B106*, 512-517.

158. Tian, Y.; Wang, J.; Wang, Z.; Wang, S. *Synth. Met.* **2004,** *143*, 309-313.

159. Tian, Y.; Wang, J.; Wang, Z.; Wang, S. *Sens. Actuators, B* **2005,** *B104*, 23-28.

160. Aravamudhan, S.; Bhansali, S. *Sens. Actuators, B* **2008,** *B132*, 623-630.

161. de, V. A. C. A.; van, S. R. A.; van, V. J. A. R. *J. Mol. Catal. A: Chem.* **2000,** *154*, 203-215.

162. Chen, Y.-X.; Chen, S.-P.; Chen, Q.-S.; Zhou, Z.-Y.; Sun, S.-G. *Electrochim. Acta* **2008,** *53*, 6938-6943.

163. Fajerwerg, K.; Ynam, V.; Chaudret, B.; Garcon, V.; Thouron, D.; Comtat, M. *Electrochem. Commun.* **2010,** *12*, 1439-1441.

164. Reyter, D.; Chamoulaud, G.; Belanger, D.; Roue, L. *J. Electroanal. Chem.* **2006,** *596*, 13-24.

165. Badea, G. E. *Electrochim. Acta* **2009,** *54*, 996-1001.

166. Reyter, D.; Belanger, D.; Roue, L. *Electrochim. Acta* **2008,** *53*, 5977-5984.

167. Casella, I. G.; Gatta, M. *J. Electroanal. Chem.* **2004,** *568*, 183-188.

168. Solak, A. O.; Gulser, P.; Gokmese, E.; Gokmese, F. *Mikrochim. Acta* **2000,** *134*, 77-82.

169. Paixao, T. R. L. C.; Cardoso, J. L.; Bertotti, M. *Talanta* **2007,** *71*, 186-191.

170. Davis, J.; Moorcroft, M. J.; Wilkins, S. J.; Compton, R. G.; Cardosi, M. F. *Analyst* **2000,** *125*, 737-742.

171. Ward-Jones, S.; Banks, C. E.; Simm, A. O.; Jiang, L.; Compton, R. G. *Electroanalysis* **2005,** *17*, 1806-1815.

Chapter 2

Experimental

2.1 Introduction

The main aim of the research is concerned with the fabrication and characterisation of micro/nano materials synthesised on electrode substrates. These materials are composed of semi-conducting polymeric and metallic building blocks. Hybrid mixtures of polymer and metal have also been developed.

The polymer materials investigated were polypyrrole (PPy) and poly[*N*-(2-cyanoethyl)pyrrole] (PPyEtCN) doped predominantly with the ClO_4^- anion. A range of structures were assembled including nanowire, hollow microtube and microcontainer. The aspect ratio and final morphology of these materials was controlled by a template free electrochemical method. Copper oxide was electrodeposited within these polymeric materials as discrete micro and nano particles. Due to the microscopic nature of these materials and novel methodology followed in their production, in-depth surface characterisation was needed to examine their respective morphologies. This was performed using extensive microscopy including SEM and TEM. The chemical structures and doping levels of the polymer films were investigated by employing Raman, FTIR, and EDX spectroscopies, while contact angle measurements revealed their surface wettability. These composite materials were investigated as potential candidates for the electroreduction of the nitrate ion in aqueous systems.

All details relating to synthesis, characterisation and application of the PPy, PPyEtCN and PPy/PPyEtCN -Cu composites are given in the following sections together with a short description of each applied experimental technique.

2.2 Experimental Procedures

2.2.1 Chemicals and Solutions

All chemicals were purchased from Sigma-Aldrich and were of analytical grade. Pyrrole and *N*-(2-cyanoethyl)pyrrole were distilled under vacuum using a krugelrohr and stored under nitrogen at -40 ^{o}C. For polymerisation the monomer was pipette into solutions of deionised water and ethanol in various mixtures. The dopant salts, typically $LiClO_4$, $(NH_4)H_2PO_4$ and Na_2CO_3, were added with vigorous stirring until dissolved. For the preparation of PPyEtCN microstructures, toluene was added to the electrolyte solution after the addition of the dopant salts and then sonication was performed. The electrolytes used for the electrochemical characterisation of the polypyrrole films consisted of 0.100 M $LiClO_4$ or 0.005 M $K_3[Fe(CN)_6]$ in 0.100 M KCl. Copper electrochemical deposition was performed in solutions of $CuCl_2$ or $CuSO_4$ with supporting electrolytes of H_2SO_4, NaCl or Na_2SO_4. For select experiments high purity nitrogen and oxygen gases, supplied by BOC, were passed through these solutions for 20 min. Solution pH was measured using an Orien Model 720A pH meter, which was calibrated with buffer solutions of pH 4.0 and 7.0, respectively, prior to use. These buffer solutions were obtained from Sigma-Aldrich.

2.2.2 The Electrochemical Cell Set-up

The vast majority of the materials developed and characterised in the present work were prepared electrochemically. Experiments were performed using a Solatron 1285 potentiostat at room temperature. A standard three electrode cell was employed using Pt mesh as counter electrode, while the working electrode was typically a glassy carbon (GC) rod embedded in a Teflon holder using an epoxy resin. The counter electrodes were brushed regularly with silicon carbide based abrasive paper (Buheler P2500) then heated over a naked flame until bright red. They were then sonicated in distilled milli-Q water and ethanol for 300 s, respectively. All potentials were measured against a saturated calomel electrode (SCE) reference. When not in use, the reference electrode was stored in a saturated solution of potassium chloride (KCl), to prevent the porous frit at the tip of the electrode from drying out. This

electrode was rinsed with distilled water between experiments to avoid contamination of electrolyte solutions with KCl. A scheme of the electrochemical setup that was used is shown in Figure 2.1. The electrochemical cell was a glass cylinder of 10 or 20 mL volume and had a Teflon lid with openings for each of the electrodes. The three electrodes were immersed in the electrolyte solution and were connected to a potentiostat, which was controlled by computer.

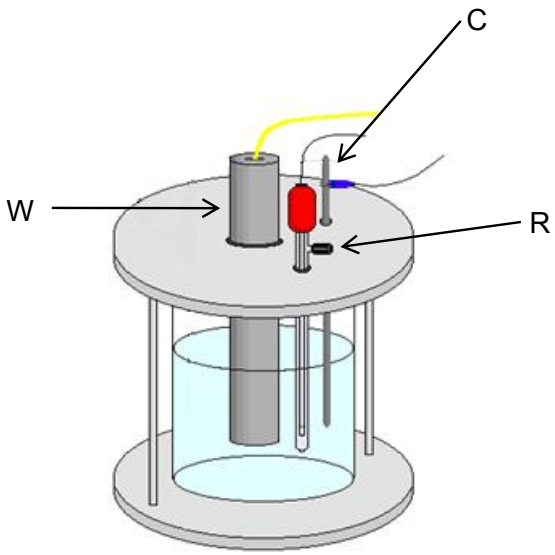

Figure 2.1: Schematic of the cell set-up used for electrochemical measurements.

2.2.2.1 Preparation of the Working Electrodes

The metals in each of the working electrodes were supplied by GoodFellow in rod form and cut into lengths of 3 cm. Copper wire was attached to the base of the metal working surface using a conducting silver epoxy resin. This resin was cured under a heat lamp to guarantee a high conductivity and solid adhesion. The quality of the electrical contact was verified with a multimeter to ensure that the resistance between the surface of the electrodes and the connection to the potentiostat was lower than 1 Ω A. A non-conducting epoxy resin was then used to seal the electrode within a Teflon holder. A schematic representation of the electrode assembly is shown in Figure 2.2.

Prior to each experiment the exposed electrode surface was hand polished using Buehler MetaDi monocrystalline diamond suspension and a Buehler polishing microcloth. The samples were polished to a smooth finish with successively finer diamond grades ranging from 30 µm to 1 µm with a minimum of 300 s polishing performed per diamond grade. The electrodes were then rinsed with distilled water and sonicated for 300s in an ultrasonic bath in between each polish grade. The electrodes were finally sonicated in ethanol and water, respectively, before use. The sonication process was performed to remove any diamond paste which had adhered to the surface during polishing. To replenish the surface of the electrode between each experiment a Buehler METASERV grinder polisher with Buehler SiC grinding paper (Grit P 2500) was used and then the polishing steps were repeated.

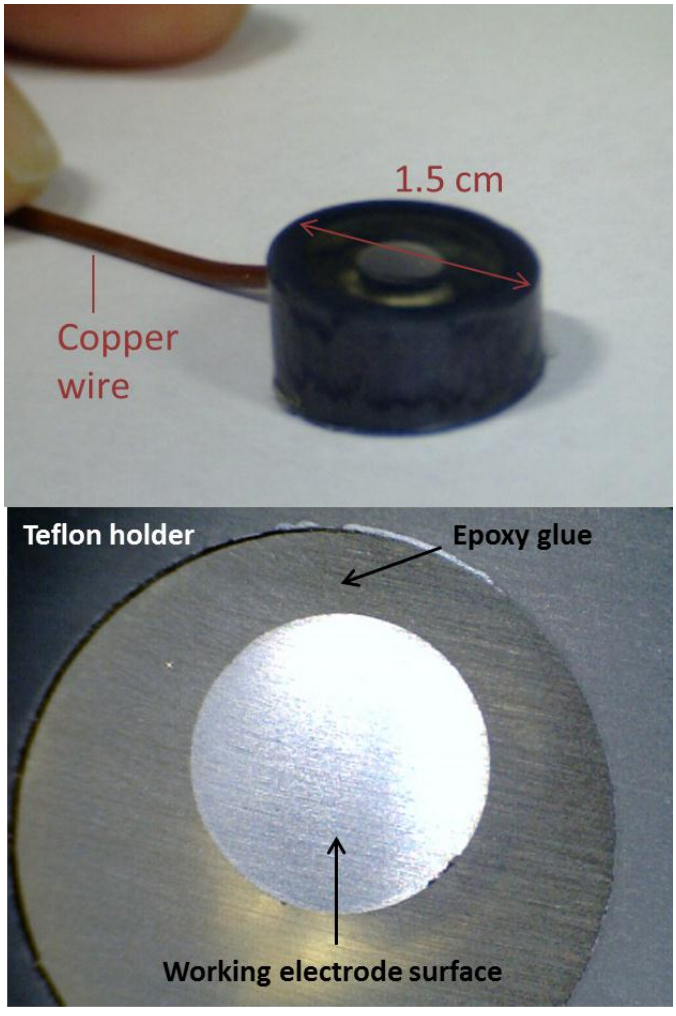

Figure 2.2. Images of working electrode with identification of the working surface, epoxy resin glue and Teflon holder.

Due to the large amount of SEM analysis performed during these studies a customised SEM stage and electrode casing were designed with the technical assistance of Mr. Noel Williams. The 'screw electrodes' were fabricated by using a very short length Teflon rod and engraving a screw thread using an M12 die, Figure 2.3a. Then on a circular aluminium plate the opposing screw thread was fabricated from a sheet of alluminum, Figure 2.3b. As can be seen in Figure 2.3c the electrodes were then screwed tightly into the aluminium stage. This stage was capable of holding up to 8 electrodes simultaneously. This permitted a large number of samples to be put in the vacuum and pumped down over 24 hours, leading to better vacuum as the chamber was not opened for sample exchanging. Furthermore, to analyse the adjacent electrode, the stage was rotated exactly 45° removing the need to manually 'find' the next sample which can be a time consuming process. Most significantly, since the electrodes were tightly fixed into place there was no drift or movement of the electrode which causes serious problems when recording high magnification images. Finally, the electrodes could be confidently tilted to 90° without the risk of detachment from the stage.

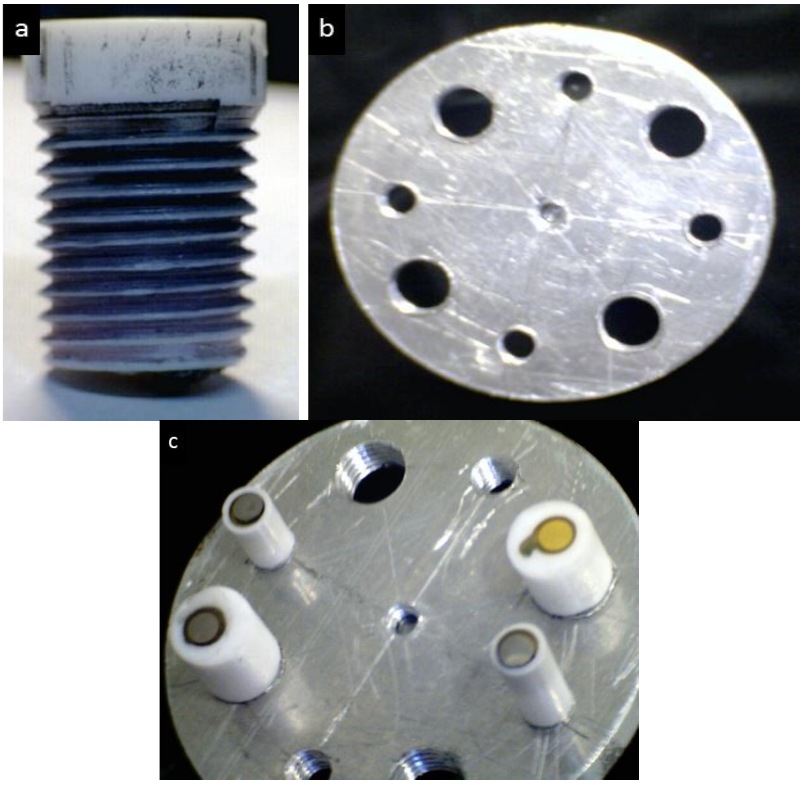

Figure 2.3. Images of the customised screw SEM electrode produced (a), corresponding aluminium SEM stage (b) and electrodes fixated onto the stage (c).

2.2.3 Polymer Electropolymerisation

2.2.3.1 Electropolymerisation of *N*-(2-cyanoethyl)pyrrole Bulk and Nanowire Polymers

Bulk PPyEtCN films were obtained using 0.750 M PyEtCN monomer in 0.100 M $LiClO_4$ employing a constant applied potential of 0.850 V. For the production of PPyEtCN nanowires, the monomer (0.750 M) was dissolved in EtOH (3 ml) while both $LiClO_4$ (0.020 M) and $(NH_4)H_2PO_4$ (0.300 M) were dissolved in H_2O (7 ml). The two solutions were mixed, stirred for 10 min and finally a potential of 0.850 V was applied for set times between 10 to 3600 s.

2.2.3.2 Electropolymerisation of N-(2-cyanoethyl)pyrrole Hollow Microtubes and Microcontainers

In a typical experiment $LiClO_4$ (0.020 M) and $(NH_4)H_2PO_4$ (0.100 M) were dissolved in a water/ethanol (7:3) solution. Toluene (80 µL) and PPyEtCN monomer (0.056 M) were added to 10 mL of this solution by micropipette. This suspension was shaken vigorously and then sonicated using a probe sonicator (Bandelin Sonoplus HD2200, MS72 tip) for 1 minute at 20% of maximum power or the suspension was stirred vigorously and then sonicated in an ultrasonic bath (Fisher Scientific FB 15048) for 1 minute.

2.2.3.3 Electropolymerisation of Bulk and Nanowire Pyrrole Polymers

Bulk PPy films were obtained using 0.150 M Py monomer in 0.100 M $LiClO_4$ at 0.850 V. In a typical experiment to produce PPy nanowires the Py monomer (0.150 M) was dissolved deionised water. $LiClO_4$ (0.100 M), Na_2CO_3 (0.100 M) and $NaHCO_3$ (0.300 M) were added. The solution was stirred until all components were dissolved. Potentials ranging from 0.700 to 0.900 V vs. SCE were applied until a set charge was reached, typically 0.04 C/cm^2.

2.2.4 Electrochemical Deposition of Copper Structures

Copper micro/nanomaterials were electrochemically deposited on PPy and PPyEtCN bulk and nanowire films. The following sections describe the electrochemical procedures that were employed.

2.4.1.1 Employing Constant Potential

All experiments relating to the preparation of copper deposition using constant potential were performed by Karen Herdman during her 4th year undergraduate research project. Using this method copper microstructures were electrodeposited at PPy bulk and PPyEtCN bulk and nanowire films. The electrode was immersed in a 0.050 M $CuSO_4$/0.050 M Na_2SO_4 solution and a constant cathodic potential ranging from -0.105 to -1.200 V was applied for times ranging from 10 to 600 s. The polymer-Cu films were then washed with water and dried by N_2 flow before further characterisation.

2.4.1.2 Employing Cyclic Voltammetry

Cyclic voltammetry (CV) was employed to electrodeposit copper micro/nano structures at PPy nanowire films. The electrode was immersed in a 0.050 M $CuCl_2$/H_2SO_4 solution and cycled between set potentials of 0.100 and -0.400 V for between 10 and 320 cycles. The scan rate was varied from 50 to 900 mV/s depending on the size of deposits desired. The polymer-Cu films were then washed with water and dried by N_2 flow before further characterisation.

2.2.5 Polymer Characterisation

2.2.5.1 Microscopy

For the majority of the SEM and EDX analyses a Hitachi S-3200-N with a tungsten filament electron was employed. This has a maximum magnification of 200,000x and resolution of 3.5 nm. This microscope was equipped with Oxford Instrument INCA x-act EDX system with silicon drift detector. Two other SEMs were employed at the Tyndall National Institute, Cork and operated by Patrick Carolan and Vince Lodge as part of the National Access Programme Grant (NAP project 353). Lower magnification work was carried out with a Hitachi S-4000 with cold cathode field emission electron source (FESEM), maximum magnification 300,000x and resolution 1.5 nm. This microscope was equipped with Princeton Gamma Technology Avalon 8000 EDX system with liquid nitrogen cooled Li(Si) detector. A FEI Nova NanoSEM 630 ultra-high resolution with field emission gun (FEG), maximum magnification 1,000,000x and a resolution of 1 nm was also employed for higher resolution measurements. This microscope was equipped with Oxford Instrument X-MAX 80 large area Si diffused detector.

For all analysis the electrodes were prepared by firstly drying with a N_2 flow and then placed in the sputter coater under vacuum for 30 minutes to remove any residual solvent. The chamber was allowed to pump to 0.1 mB before sputtercoating was performed under argon using an Au/Pd target. A thickness monitor was employed to obtain a coating of 15 nm. Electrically conducting copper tape was adhered to the working area of the electrode and connected to an earthed metal, usually the aluminium holder. This reduced the build-up of incident electrons gathering at the surface of the sample, known as charging. Depending on the thickness and conductivity of the sample, and the magnification required, the electrons were accelerated between 5 and 30 kV. For high resolution imaging the beam current was limited to 10 uA to greater resolve fine nanostructures combined with a working distance of 5 mm and the smallest aperture (4) was used to reduce the occurrence of ‘off axis’ electrons. To reduce charging effects and increase the overall electron count at the detector the stage was tilted by at least 45°. For cross section imaging the stage was tilted to 90° and the dynamic focus mode was engaged. To expose the

under layers of polymer between the surface and the substrate a surgical blade was employed to make incisions in various directions across the polymer. This was performed before the sputter coating procedure. Images were recorded at a medium rastering rate with a resolution of 1024 x 766 pixels and analysed using ImageJ software.

For EDX analysis and elemental mapping the working distance was brought to 15 mm since the detector is poised at an incident angle compared to the secondary electron detector. The detector was moved from the stationary position and extended to its maximum distance. Typically the voltage was maintained at 20 kV with a beam current of 70 μA. The stage was not tilted. To allow the maximum amount of incident electrons to penetrate the sample the largest aperture was employed (aperture '0'). Spectra were analysed using Inca software. The Infra-red camera was switched off as it creates noise within the X-ray detector.

TEM was performed at the Tyndall National Institute, Cork, using a JEOL 2010 with a LaB6 filament operating at 200 kV, operated by Patrick Carolan. Samples were prepared by growing a minimum of 10 polymers and removing them from the substrate using a surgical blade. The loose polymers were then sonicated in ethanol for 10 minutes to generate single nanowires free from the polymer bulk layer. Several drops of this solution were pipette onto a TEM grid and allowed to evaporate. Images were analysed using ImageJ software.

Light microscopy measurements were performed on the monomer solutions by pipetting them onto glass slides. The toluene emulsion mixtures were also analysed and were prepared with the addition of a red dye (Sudan IV, 0.005% wt) which was added to the toluene before its addition to the emulsion solution. This allowed the droplets to be more easily identified. Several drops of this solution were pipetted onto a glass slide and images were recorded using an Olympus BX161 optical microscope with Cell^{F} analysis software. Urszula Migas performed all transmission microscopy analysis.

2.2.5.2 Spectroscopy

Raman measurements were performed with a Reinshaw inVia reflex Raman Microscope using an Argon ion laser (514 nm) with a beam spot of 1.1 μm at the Tyndall National Institute, Cork, operated by Mircea Modreanu. For studies employing the 473, 660 and 785 nm laser lines a LabRAM high resolution Raman spectrometer using solid state diode laser (100 mW) was employed at the Focus Institute at the Dublin Institute of Technology, operated by Anne Shanahan. The polymer samples were directly analysed on the electrode surfaces, using GC, Au or Pt. For GC electrodes gold nanoparticles were placed on the surface to encourage a surface enhancement effect (SERS). To analyse the Py and PPyEtCN monomers several drops were dissolved in an NMR tube using ethanol and analysed accordingly. The 'starting materials' used to electropolymerise the polymers were also made into KBr disks and analysed, including $LiClO_4$, $(NH_4)H_2PO_4$ and ethanol. 'Blank' KBr disks were used as a reference material. FTIR spectra were obtained using a Perkin Elmer 2000 FTIR spectrometer. Samples were developed by grinding the polymers into KBr and producing disks under high pressure clamp.

2.2.5.3 Contact Angle

Contact angle experiments were performed at the Tyndall National Institute by Eileen Hurley and employed a static water droplet of 1.00 μL using an OCA 20 from Dataphysics Instruments. The polymers were analysed on the electrode substrate and an n = 3 was obtained by drying the polymers between each experiment. Analysis of the resultant droplets was performed using ImageJ software with the 'dropsnake' add-on software.

2.3 Experimental Techniques

2.3.1 Electrochemistry

The two fundamental observables of any electrochemical system are the current (*I*) and potential (*E*), with the current being the flow of charge and the driving force being the potential. A typical electrochemical experiment consists of controlling one of the two observables while recording the evolution of the other. The response of the electrochemical system to the external perturbation is influenced by many variables such as the nature and concentration of the materials.

2.3.1.1 Potentiostatic Techniques (Chronoamperometry)

This electrochemical technique involves applying a constant potential to the working electrode and monitoring the resultant current, *I*, with respect to time, *t*. These plots are typically called transients to emphasise their time dependence. The electrical potential at the working electrode is instantaneously stepped from a resting value where no electrolysis occurs to a value where conversion of reactants begins.[1-2] The potential can be applied for a fixed period of time or until a desired charge is reached. Chronoamperometry was used in the formation of PPy and PPyEtCN polymers at the working electrode. An anodic potential was applied to oxidise the monomer units which polymerised and deposited on the surface of the electrode. The resultant current was proportional to the rate of polymerisation occurring at the electrode surface.[3] This method was also used in the deposition of the copper microstructures by maintaining a constant reductive current to produce insoluble copper species which nucleate on the electrode surface, Equation 2.1.[4]

$$M^{z+}_{solution} + ze \rightarrow M_{lattice} \qquad (2.1)$$

Sometimes it is more informative to plot the charge (*Q*) passed through the electrochemical cell as a function of the time, this technique is called chronocoulometry. The charge can be calculated at any time from the integral of the current; relating the experimental observation to the charge is particularly useful when considering the overall extent of the redox process instead of its instantaneous

rate (i.e. the current). The total charge passed after an electrode reaction can be related to the thickness of a polymer deposit or to the total amount of copper deposited at an electrode.

The shape of the current profile is dependent on several factors such as the concentration of reactants, applied potential, mass transfer and kinetic parameters. For the experiments detailed in this thesis, only the current responses related to the electrodeposition at an electrode surface will be considered. The nucleation and growth of electrodeposits is a vast topic that has been studied in considerable detail both experimentally and theoretically. The special case of the potentiostatic current-time transient for two and three -dimensional nucleation with diffusion controlled growth has been modelled by Scharifker and Hills.[5] Their models outline two theoretical diagnostic relationships, one for the instantaneous nucleation (i.e. where all the growing nuclei are formed at the same time during electrodeposition), and one for the progressive nucleation (i.e., new nuclei develop during the growth period). The two non-dimensional relationships are provided for progressive and instantaneous 2-D and 3-D nucleation as Equations 2.2 – 2.4.

$$\frac{j}{j_{\max}} = \left(\frac{t}{t_{\max}}\right) \exp\left\{-\frac{2}{3}\left(\frac{t^3 - {t_{\max}}^3}{{t_{\max}}^3}\right)\right\} \qquad (2.2)$$

$$\frac{j}{j_{\max}} = \left(\frac{t}{t_{\max}}\right) \exp\left\{-\frac{1}{2}\left(\frac{t^2 - {t_{\max}}^2}{{t_{\max}}^2}\right)\right\} \qquad (2.3)$$

$$\left(\frac{j}{j_{\max}}\right)^2 = \frac{1.2254}{\left(\frac{t}{t_{\max}}\right)}\left\{1 - \exp\left[-2.3367\left(\frac{t}{t_{\max}}\right)^2\right]\right\}^2 \qquad (2.4)$$

$$\left(\frac{j}{j_{\max}}\right)^2 = \frac{1.9542}{\left(\frac{t}{t_{\max}}\right)}\left\{1 - \exp\left[-1.2564\left(\frac{t}{t_{\max}}\right)\right]\right\}^2 \qquad (2.5)$$

The general current response for the potentiostatic nucleation and growth of electrodeposits taking into account the effect of nuclei overlapping is shown in **Error! Reference source not found.** 2.4.[4] The current free from overlapping effects (I_{free}) increases linearly with time in the case of instantaneous nucleation, and as t^2 in the case of progressive nucleation. For the area designated I_{free} the growth of the nuclei are independent of each other. This assumption is only valid for the initial stages of growth. Succeeding stages of growth causes the diffusion zones to overlap. Overlap zones lead to a reduced concentration of depositing material and results in nuclei not growing freely as the separate nuclei impinge on each other.[4] This creates a reduced growth rate and causes the current response to drop.

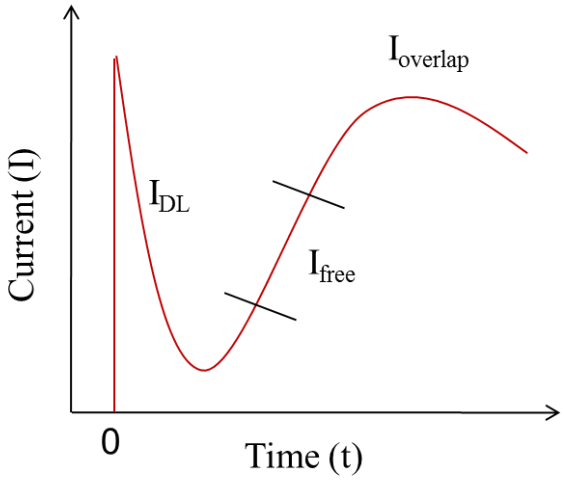

Figure 2.4. The diffusion controlled amperometric response after a potential perturbation is displayed with sections highlighted for the current associated with the double layer charging, I_{DL}. The current associated with nucleation and growth without overlapping diffusional zones, I_{free} and finally response at the peak maximum due to the nuclei diffusional zones overlapping, $I_{overlap}$.

2.3.1.2 Cyclic Voltammetry

Cyclic voltammetry is the primary electroanalytical study performed in electrochemistry as it reveals information about the nature of the electrode and the reactions taking place at it. Cyclic voltammetry is a dynamic electrochemical technique wherein the applied potential is ramped at a scan rate of υ between two chosen potential limits. The initial applied potential, E_i, is swept to a vertex potential, E_v, where the scan is reversed and swept back to the final potential, E_f. This process

is cyclic and is typically repeated a number of times to observe the evolution of an electrochemical reaction occurring at the electrode surface. The generation of a peak current maximum is due to the constant increase of the electrical potential forcing the reaction, for example, of A undergoing an electron transfer to B as shown by Equation 2.5.

$$A(aq) - e^{-}(m) \Leftrightarrow B(aq) \tag{2.5}$$

Where (aq) relates to a species in solution and (m) is electrons produced or accepted by the electrode. The process of the formation of an anodic peak potential for Equation 2.5 is shown in Figure 2.5. Here, the peak current maximum has been magnified while the rest of the CV has been excluded. It can be seen at point (1) there is no current flowing as the applied potential is not great enough to induce electron transfer.[1] As the potential is brought to higher anodic values the oxidation of A to B begins with a corresponding flow of current, point (2). As the potential is made even more anodic the current continues to rise as more A is converted to B with greater efficiency, until a peak maximum is reached and the current then begins to diminish, point (3).[1] The decrease in current arises as the larger positive electrode potential more efficiently consumes the available concentration of reactant A. The remaining current is controlled by how quickly fresh A can diffuse from the bulk solution. Simply put the electrode depletes the reactants close to the electrode surface, this depletion zone becomes thicker as electrolysis proceeds so A must diffuse from further distances. This leads to lower currents being recorded after the maximum which decay further as electrolysis proceeds and the diffusion zone thickens.

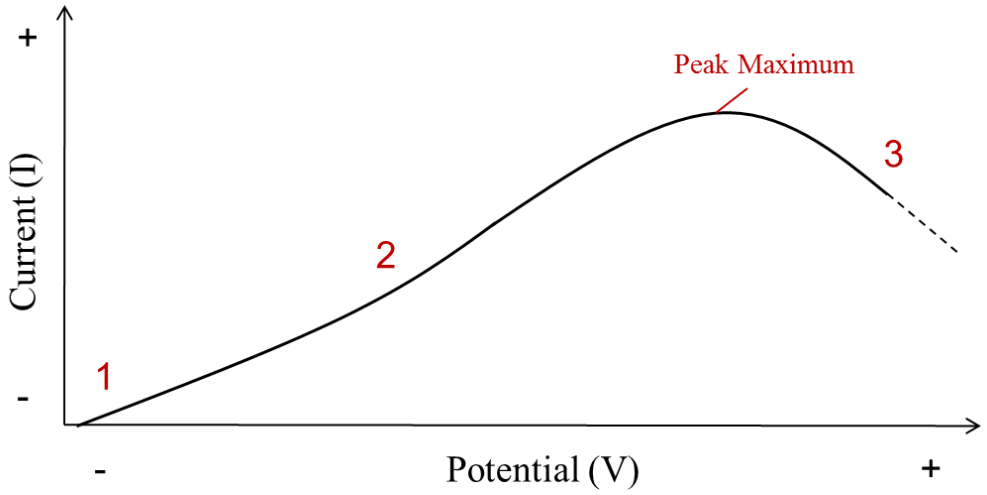

Figure 2.5. The process of formation of a peak current maximum employing an increasing oxidising potential, similarly obtain using a CV. Current response corresponds to a hypothetical electrochemical reaction of A being oxidised to B as shown by Equation 2.5.

There are four main CV responses that depend on the reversibility of the redox process and whether the redox species adsorbed to the electrode surface, Figure 2.6. Each response is characterised by a different shape and symmetry surrounding the generated peak maximum, which is described by three key parameters, the peak current (i_p), the peak potential (E_p) and the potential width at half peak ($|E_p - E_{p/2}|$). The dependence of each parameter on the potential scan rate, υ, allows for the full characterization of the electrochemical system and highlights the reversibility of the A/B reaction from Equation 2.5. The terms 'reversible' and 'irreversible' are commonly used in electrochemistry and refer to limiting cases according to whether the electrode kinetics are fast or slow. Intermediate behaviours are termed quasi-reversible.

Reversible	Irreversible
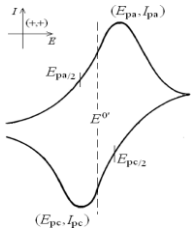	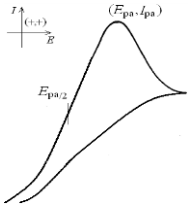
$I_p \propto \upsilon^{1/2}$	$I_p \propto \upsilon^{1/2}$
E_p independent of υ	$\lvert E_p \rvert$ increases as υ increases
$\lvert E_p - E_{p/2} \rvert = 59/n$ mV	$\lvert E_p - E_{p/2} \rvert = 48/\alpha n$ mV
Quasi-reversible	**Adsorption***
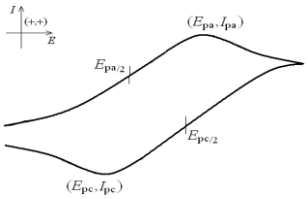	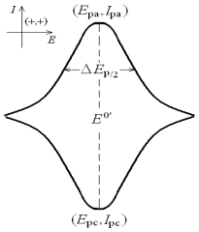
I_p not proportional to $\upsilon^{1/2}$ as υ increases	$I_p \propto \upsilon$
$\lvert E_p \rvert$ increases as υ increases	E_p independent of υ *
$\lvert E_p - E_{p/2} \rvert = 26\Delta(\Lambda, \alpha)$ mV *	$\Delta E_{p/2} = 90/n$ mV
	* For reversible adsorption.

Figure 2.6. Cyclic voltammograms with their respective peak current and potential characteristics showing degree of reversibility. The integer, *n*, is the number of electrons involved in the redox process, and α is the corresponding transfer coefficient. All potential widths at half-peak are expressed at 298 K.

2.3.2 Surface Analysis

2.3.2.1 Scanning Electron Microscopy

The aim of electron microscopy is the imaging of objects at the nanoscale level. The essential feature of a microscope is the interaction between the material being studied and waves, visible electromagnetic waves in the case of optical microscopy, and high-energy electrons in the case of electron microscopy. The wavelength of visible light (~550 nm) is the limiting factor of the maximum resolution achievable by optical microscopes. For electron microscopes a voltage (kV) is applied to an electron gun causing electrons to eject from a tungsten filament and accelerate down an optic column. A higher applied voltage generates electrons with higher energy and shorter wavelength, Equation 2.6.[6] The observable resolution obtained by a microscope, *d*, between two small adjacent particles is proportional to the wavelength of the incident beam, λ ($d \propto \lambda$), An electron beam accelerated at 80 kV is has a wavelength of 0.004 nm.[4] Therefore, higher resolutions are obtained using higher accelerating voltages.

$$\lambda = \left(\frac{1.5}{V}\right)^{1/2} \tag{2.6}$$

The scanning electron microscope (SEM) consists of an electron-optical column mounted on a vacuum chamber. The electron gun placed on top of the column is typically a thermoionic cathode made of tungsten that emits electrons when heated. The electrons are pushed down into the columns by an accelerating voltage ranging from 1 to 30 kV. The sample is contained in a specimen chamber which has a pressure of 10^{-3} – 10^{-5} Pa (~ 10^{-7} mmHg). This is to reduce the occurrence of the electrons colliding with other molecules once fired from the gun. The specimen is placed on a stage that can be moved with accurate precision along the x, y, and z axis, with rotation and tilting also possible. Image generation at an electron microscope results from two processes. The first is the elastic scattering as the beam penetrates the specimen. This, in turn, results in backscattered electrons (BSE) with negligible energy loss and scattering angles larger than 90°. The inelastic scattering which results from the deep interaction of the incident electrons with the nuclei and electrons of the material and generates other signals with substantial energy loss transferred to the sample. Secondary electrons (SE), Auger electrons, X-Ray

emission and cathodoluminescence belong to this group. The incident beam has a characteristic penetration volume in the sample and each signal originates from a different part of it, Figure 2.7a. The BSE electrons have high energy (> 50 eV) enough to emerge from underneath the sample surface. The SE electrons are of low energy (< 50 eV) and consequently carry topographical information of the surface of the sample and are therefore the predominantly used electron source. The depth to which they can penetrate the sample is determined by the accelerating voltage and elemental composition of the sample, Figure 2.7b.

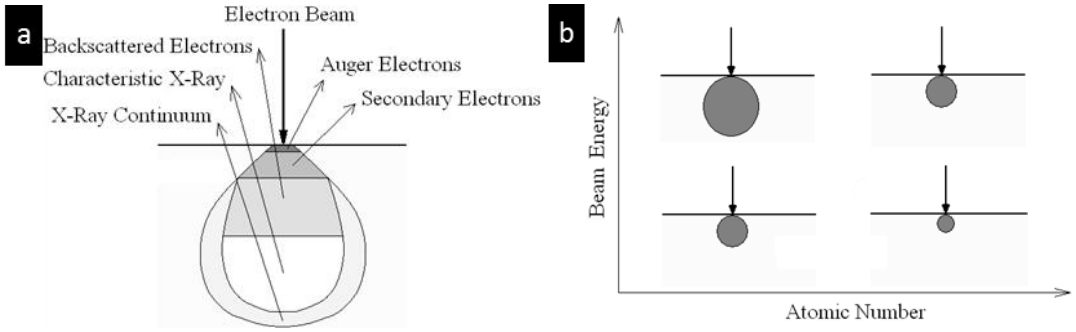

Figure 2.7 Schematic representation of electron-material interactions in the SEM. The volume of interaction of the electron beam with the sample surface and corresponding areas from which different signals originate (a). Size of the electron interaction volume as a function of atomic number of the elements in the sample and the energy of the electron beam (b).

The information and content of electron-generated images is restricted by both instrumental and operational limits. The basis of obtaining good quality images is a balance between keeping a high level of brightness while encouraging the highest resolution by employing the lowest beam current (spot size). These are opposing processes since a low beam current leads to low brightness. The operator has a significant influence on the generation of artefacts during the preparation and manipulation of the samples. Therefore, understanding the chemical makeup of the sample to be analysed can allow the operator to adjust the settings to accommodate non-conducting or dense materials. In the case of polymer materials it is possible that beam damage can change the morphology during imaging.[7] Therefore employing low accelerating voltages is an important consideration.

The most important aspect of imaging non conducting samples such as polymers is the reduction of surface charging phenomena. This occurs when the electrons

injected into the sample accumulate on the surface and deflect the incident electron beam, Figure 2.8. Samples are typically coated with a thin layer of noble metals, e.g., Au/Pd (15 nm) to increase the conductivity of the sample and decrease the electron build-up on the surface. The advantage of using Au/Pd over Au is that having two different atom species discourages epitaxial growth of the other and produces a more homogeneous coating.[7] Other methods of reducing charging effects are to ensure complete drying of the sample by extensive vacuum drying, tilting the stage, reducing the beam current and accelerating voltage. To produce high quality images using the tungsten filament it is imperative to eliminate all charging effects by correct sample preparation and imaging conditions. However, while employing these techniques to reduce charging it is most likely that a significant loss of brightness will develop, therefore proper saturation of the filament and correct alignment of the beam is essential. It is important to weigh up possible charging effects against the reduction in resolution and brightness when trying to minimise these effects. This further highlights the critical importance in understanding the sample properties and performing correct sample preparation. This combined with a strong understanding of how to control the intensity of the electron beam will deliver a superior level of image resolution during SEM operation.

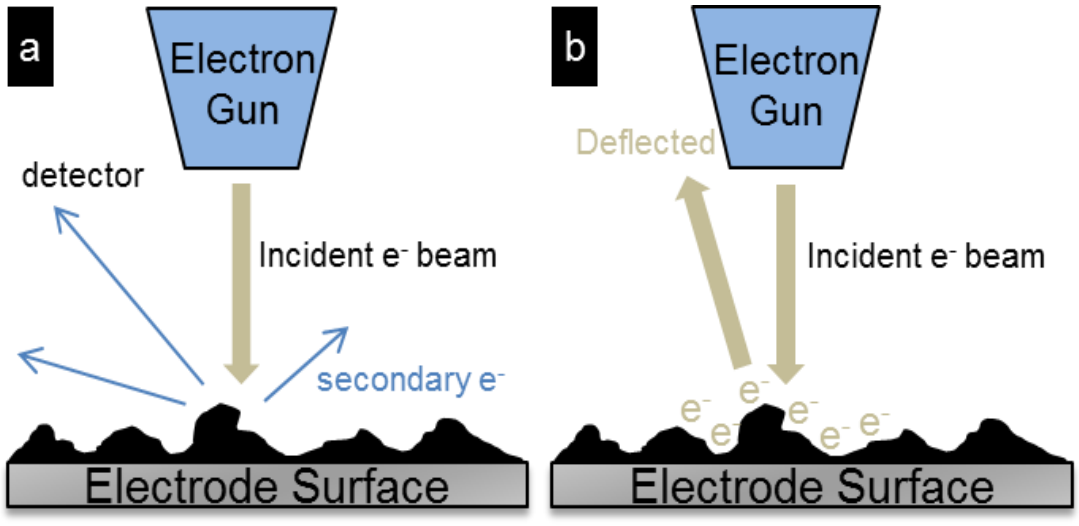

Figure 2.8. SEM analysis of a sufficiently conducting sample which produces secondary electrons in a high yield (a) and a non-conducing sample which facilitates the build-up of electrons and deflection of the incident beam (b).

2.3.2.2 Transmission Electron Microscopy

Transmission electron microscopy (TEM) performs under the same principles as SEM. However the electrons are accelerated to a much greater speed (typically 200 kV) and are narrowly focused using electromagnetic lenses and metal apertures. A benefit of the TEM is that the chamber to insert the sample is separate from the filament chamber and other compartments, therefore the pump down time is relatively shorter compared to an SEM, Figure 2.9. As the electrons attain much greater speeds their wavelength is significantly smaller and hence the resolution is much greater. The ability to penetrate through the sample material is also a characteristic of the higher energy electrons produced by TEM. Due to this penetration the electron beam is highly dependent on the properties of the sample, including density and composition. One drawback of the TEM is that if the samples are too thick the electrons will be scattered or absorbed by the material rather than being transmitted. The TEM provides a scattering contrast when the composition or thickness of the sample varies between different regions.[8] Thicker regions of the sample scatter a greater number of the incident electrons so this area of the TEM image will appear dark. Regions of higher atomic number, metals for instance, also give rise to a higher contrast due to an increase in the amount of elastic scattering. It is also possible to obtain an electron diffraction pattern of the sample as the electrons will be diffracted by the atomic planes in the sample.[8]

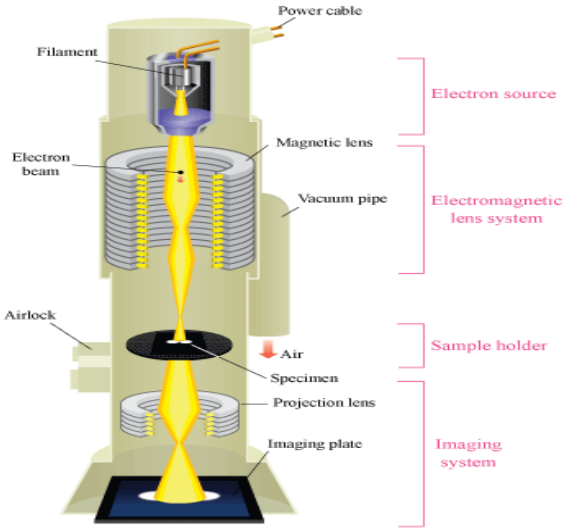

Figure 2.9. The main components of the TEM showing the generation and control of the electron beam.

2.3.2.3 Focused Ion Beam

The Focused Ion Beam (FIB) performs exactly like an electron microscope except it uses ions instead of electrons to interact with the sample for milling and deposition capabilities. As ions are much larger than electrons they cannot easily penetrate within individual atoms as electrons do. Instead, they break chemical bonds within the sample since their mass is similar to that of the sample atom. They transfer their energy to that atom and remove it from its matrix.[9] This leads to a milling process occurring at the surface of the sample at a rate of typically a few μm^3/nC depending on the elements present within the sample. Gallium (Ga) ions are chosen as ejection particles as they are a very convenient atom to construct a gun with limited heating. The Ga ions are also heavy enough to mill most other elements and can be accelerated up to 150 keV. The micro-machining capabilities of the FIB can be used to produce a deep and exposed cross sectional area of the sample. Analysing these areas allows the study of the layered structure within the sample.

A gas phase chemical precursor can be adsorbed on top of the sample and then converted to a metal deposit by the ion beam bombardment. Gas precursors of W, Pt, Au, Al and Cu have been successfully implemented to deposit the corresponding metals. The precursor of Pt metal is trimethyl(methylcyclopentadienyl)platinum(IV) and after ion beam bombardment generates a solid deposit with an average composition of about 45:24:28:3 - Pt:C:Ga:O. The Pt metal layer can be deposited as a superficial protective layer before performing the milling of the sample. This was performed on all the polymer FIB samples in this thesis.

2.3.2.4 Contact Angle

The surface wetting of materials is measured by its water contact angle (CA). Using a static water droplet placed on a surface, the angle formed by the drop at a three phase boundary where the solid, liquid and vapour intersect is measured. A surface is deemed hydrophilic when the angle is less than 90° and hydrophobic when greater than 90°. Surfaces with values between 150° and 180° are called superhydrophobic while values below 50° are superhydrophilic, Scheme 2.3. Generally, a rougher surface leads to an increase in the surface hydrophobicity. Examples of hydrophobic

and hydrophilic surfaces are shown in Figure 2.10. Industry strives to create surfaces which are extremely hydrophobic since they have self-cleaning properties. It has been shown from studying the lotus leaf that having a hierarchical structure promotes hydrophobicity which enables self-cleaning. The wettability of nano materials are therefore scrutinised as possible hydrophobic materials.

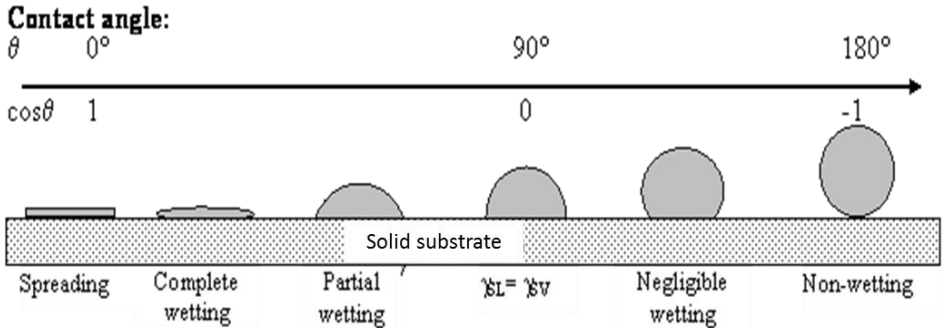

Scheme 2.3. The contact angle in relation to the water droplet and wetting state.

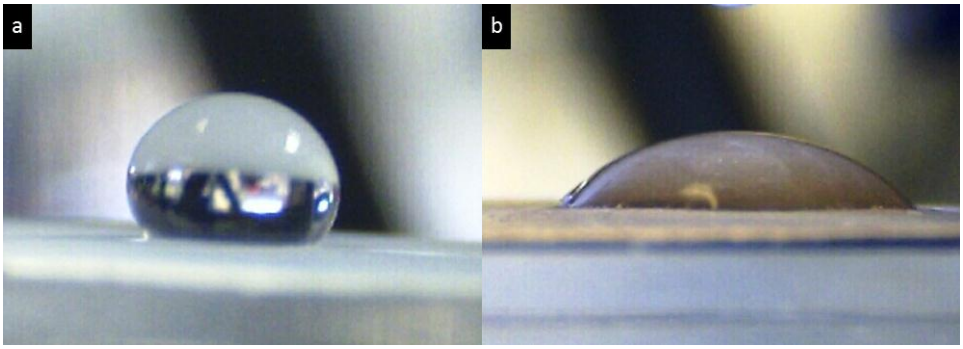

Figure 2.10. Examples of hydrophobic (a) and hydrophilic (b) surfaces measured using the static water droplet method.

For measurement of CA a droplet of water is placed on the material to be analysed. The resultant angle between the tangent to the liquid-fluid interface and the tangent to the solid surface at the contact line between the three phases is known as the CA. The CA (θ) is given by Youngs equation 2.7 taken from Figure 2.11.[10]

$$cos\ \theta = \frac{(\gamma_{sa} - \gamma_{sl})}{\gamma_{la}} \qquad (2.7)$$

When performing surface CA measurements it is important to keep the size of the droplet employed larger than the dimensions of the structures on the surface.[11] Since the CA experiments in this thesis were performed on the microtubular polymer

morphology, a droplet size of 1 μl was employed which corresponds to a spherical diameter of 0.5 mm. This ensured the droplet diameter was much larger than the microtubes so the resultant contact angle was not affected by local distortion on the surface caused by the microtubes.

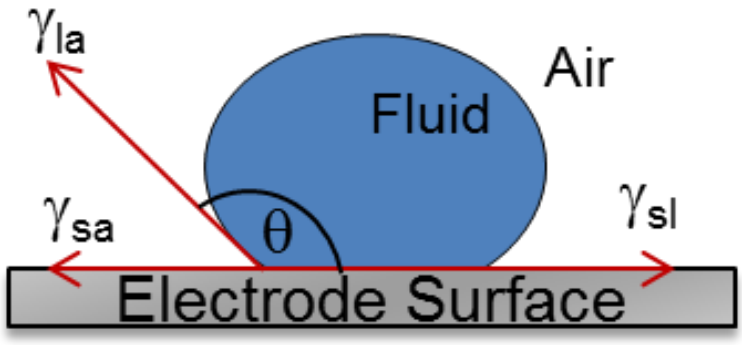

Figure 2.11. Diagram of a static water droplet on a surface highlighting the contact angle and parameters leading to its calculation.

2.3.3 Spectroscopy

Spectroscopy is the study of the interaction of electromagnetic radiation with matter e.g light, radio waves or X-rays.[12] The electrically charged nuclei and electrons within molecules interact with the oscillating electric and magnetic fields of the incident light and adsorb the energy carried within it.

2.3.3.1 Energy Dispersive X-Ray Spectroscopy (EDX)

Energy Dispersive X-ray spectroscopy (EDX) is used in combination with SEM analysis as X-rays are generated when electrons are bombarded at the sample. EDX allows the localised micro-elemental analysis of approximately 1-2 μm of the material under investigation.[6]

A characteristic X-ray signal of each element within the sample is produced when the incident electrons interact with an inner shell electron of the sample. This results in the ejection of an inner shell electron of the sample. This leaves the atom in an excited state; this hole is then replaced by an outer shell electron which undergoes a

transition to fill this vacancy, since it has a higher energy compared to the inner shell. This leads to a spectrum being generated which is characteristic of the only the elements present in the sample. The transitions involved in the characteristic X-ray emission are labelled after the shell which contained the initial vacancy (K, L, M, N), Figure 2.12. and then by the shell from which the electron was replaced (α, β or γ).[6] Transitions of electrons immediately after the emptied level are α and the following levels are β and γ in order of increasing energy.

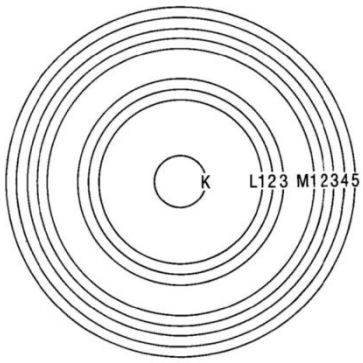

Figure 2.12. Diagram of the labelling of inner atomic electron shells.

An X-ray continuum is also generated through the deceleration of the incident electrons with the coulombic field of the atomic core which forms a continuous background signal which is present in all EDX spectra (also referred as Bremsstrahlung or X-ray continuum). This background has much lower intensity than the elemental peaks and so does not hinder the identification of the main characteristic X-rays. The resolution of the EDX probe is given by the size of the volume of interaction between the electron beam and the sample and depends on the beam current and accelerating voltage. This is important since the incident electrons may produce X-rays from areas outside the original area of interest due to varying penetration depths of the electron at different beam conditions. Furthermore, the EDX qualitative and quantitative analysis is affected by the surface roughness, Figure 2.13. The beam undergoes scattering once it enters the sample and generates X-rays within the sample. The interaction of the BSE electrons with the surrounding zones of the probed point (the beam spot) can cause the emission of X-rays that add to the signal belonging to the point of analysis. Therefore, using a low electron

accelerating voltage can limit the amount of scattering involved and limit the depth of electron injection into the sample.

A quantitative EDX analysis is produced only when high-quality flat-polished sample surfaces are used and the results performed after a known standard (cobalt in most cases) has been used as a calibration.[9] The sample must then be analysed with the same beam intensity used for the standard. Semi-quantitative analysis is possible by comparison of relative peak heights from the sample and a standard of know composition measured under the same conditions. Generally, when analysing a sample of unknown composition employing 20 kV is preferable as at least one series from every element will be excited. Since the polymer materials are of a finite thickness it is important to choose the correct kV as it is possible to obtain X-rays from the underlying substrate at high accelerating voltages.

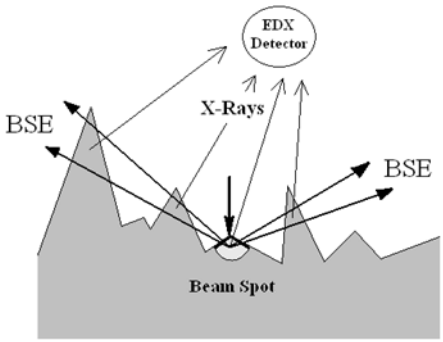

Figure 2.13. Schematic illustration of the effect of the surface roughness on the detection of the X-ray signals

2.3.3.2 Infrared Spectroscopy

In Infrared (IR) spectroscopy, light of all different frequencies is passed through a sample and the intensity of the transmitted light is measured at each frequency.[12] The sample to be analysed is mixed with opaque salts such as KBr or NaCl which are transparent to the IR radiation. A material absorbs the IR energy as it passes through it based on the vibrational motion of atoms inside the material. This absorption provides a means of identification of the groups and species present in the material as every group has a characteristic frequency (band) of absorption. In order for a molecule to be IR active it must be associated with a change in the dipole moment. The dipole moment in the material arises from the asymmetrical distribution of the

positive and negative charges.[13] Symmetry is the fundamental property of materials that distinguishes whether a vibrational mode is IR active. In order to be active, the displacement of the charge distributions must break any original element of symmetry present in the material. The IR absorption intensity is proportional to the square of change of dipole moment, it follows that the probability of IR transitions is greater for vibrations with larger dipole moment change.

In covalent bonds the nuclei can vibrate around an average position. A simple representation of a diatomic molecule is shown in Figure 2.14 where a symmetric stretching vibration can be observed. It is also possible for asymmetric modes to occur. The energy involved in this vibration depends on the length of the bond and mass of the atoms in the bond. As well as stretching, molecules can also bend (or wag, twist or rock) as shown for a polyatomic molecule such as water, Figure 2.15. An N-atomic molecule has 3N-5 normal modes of vibration if it is linear and 3N-6 if it is non-linear.[14]

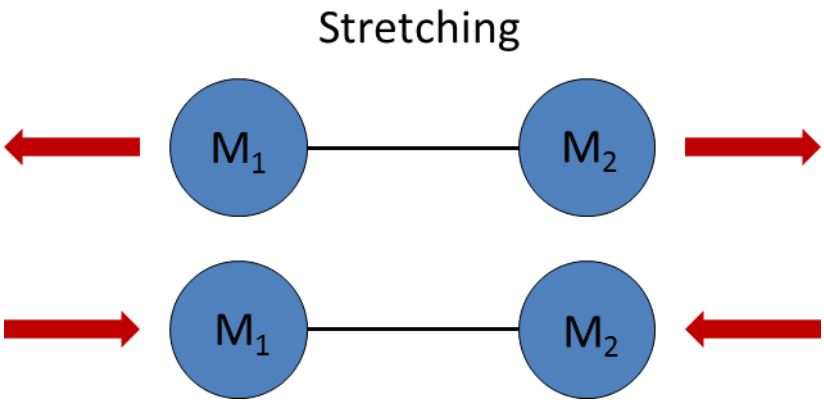

Figure 2.13. A diatomic molecule undergoing a stretching vibration

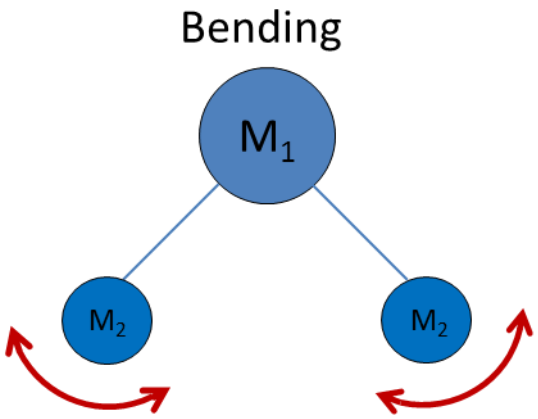

Figure 2.15. A polyatomic molecule undergoing a bending mode.

The Fourier transform (FT) is a mathematical operation that relates two functions defined in domains with reciprocal units. Given a signal s(*a*) in the generic domain *a*, its Fourier transform S(*b*) is another signal in the domain *b* with unit reciprocal to *a*, i.e. [*b*] = 1/[*a*]. The most common case is the FT of a signal from the time (s) to the frequency (s^{-1}) domain, but in the case of infrared spectroscopy the transformation of the signal is from the spatial (cm) to its reciprocal (cm^{-1}) domains.

2.3.3.3 Raman Spectroscopy

Raman spectroscopy is based on the inelastic scattering of monochromatic radiation rather than observing transmitted light which is the basis of IR spectroscopy. Vibrational transitions occur both in IR and Raman spectroscopy. The main differences between the two are the energy of the incident radiation and the nature of the radiation-material interaction. Light of a single frequency, usually a monochromatic laser beam, must be employed for Raman experiments.[12] Treating radiation with frequency ν as consisting of a stream of particles called photons, having a an energy of hν, where h which is Planck's constant.[15] After undergoing collisions and exchanging energy with a molecule, a photon is scattered away with an energy that is either lower or higher than its original energy. The energy difference is characteristic of the material. The energy absorbed during a Raman scattering brings the molecule from its ground state to a generic 'virtual state' different than any energy level of the molecule. This energy is then either scattered in all directions known as Rayleigh scattering, or shifted by a certain value higher or lower than the incident light, called Raman scattering. Radiation scattered with a frequency lower and higher than that of the incident beam is known as Stokes (S) and anti-Stokes (A) radiation respectively. Stokes radiation is generally more intense than anti-stokes radiation.[8]

The IR and normal Raman transitions are shown in Figure 2.16. The IR transition requires a smaller and exact amount of energy compared to the Raman transitions. The Rayleigh scattering (R) is the elastic scattering of the incident photon. The Stokes (S) and anti-Stokes (A) lines corresponding to the transition of the molecule

between different vibrational levels within the same electronic ground state, E_0. In the case of the Stokes line the starting vibrational level is the ground state, the ending is a vibrational level at higher energy (absorption). In the case of the anti-Stokes line, the starting vibrational level is above the ground state, the ending is the ground level (emission). The population of the vibrational levels above the ground level is low at ambient temperature (Boltzmann distribution).

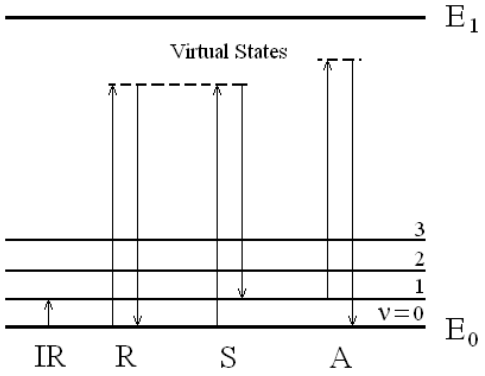

Figure 2.16 Infrared and normal Raman energy transitions within the same molecular electronic level, E_0. The infrared (IR) transition corresponds to the absorption of the incoming radiation with energy matching the separation between the vibrational levels 0 and 1 (ν is the vibrational quantum number). The Rayleigh scattering (R) is the absorption and emission of radiations of the same energy. The Raman scattering Stokes (S) and anti-Stokes (A) lines are produced by the absorption and emission of vibrational energy upon the interaction with the incoming radiation.

The polarizeability of a molecule is important for understanding Raman spectroscopy. When a molecule is put into an electric field it undergoes a distortion, with the positively charged nuclei being attracted towards the negative pole of the field and the electrons to the positive pole.[15] This separation of charge causes an electric dipole moment to occur in the molecule. The molecule can now be called polarised. The magnitude of this polarisation is given by Equation 2.8, where the dipole moment μ depends on the magnitude of the applied electric field and the ease of which the molecule is distorted.

$$\mu = \alpha E \tag{2.8}$$

The rate of change of the polarizability in a molecule, and consequently its Raman activity, is strongly dependent on the molecular symmetry as seen for the IR transitions. Some vibrations are inherently weak in IR and strong in Raman, and vice

versa. In general, covalent bonds are strong in Raman (e.g. C–C, C=C and C≡C), whereas polar bonds are strong in IR (e.g. O–H, N–H and C=O).

Considering the nature of the IR and Raman phenomena, the measurement of the effect of two processes are performed in different ways. The samples are irradiated with beams of infrared energy for IR and of UV-Vis energy for Raman. The resulting absorption in the IR is detected in line with the beam source, whereas the scattered Raman energy is detected at a right angle with the beam source. Raman scattering is a very weak process (low probability process) and only one of 10^8 incident photons results in Raman scattering, for this reason the measurement must be performed with very high energy sources like lasers; consequently sample deterioration is one of the limitations of Raman spectroscopy. This sample degradation was observed in some samples of polymer in this thesis, therefore a low power laser intensity was employed.

Two other important phenomena must be considered when recording a Raman measurement, these are the Resonance Raman scattering (RR) and the Resonance Fluorescence (RF). The RR occurs when the incident radiation brings the molecule to a virtual energy level of the exited electronic state. This phenomenon happens when the frequency of incident radiation is in the range of an electronic transition of the molecule. In this particular situation the Raman bands originating from this particular electronic transition are enhanced by a factor of 10^3 to 10^5. The RF occurs when the molecule is exited exactly to a discrete level of the exited electronic state. It follows that the molecule decays via a radiationless transition and then emits radiation. This radiation can interfere with the Stokes bands, and in such a case it is useful to examine the anti-Stoke emission.

2.4 References

1. Fisher, A. C. *Electrode Dynamics*. Oxford Universtiy Press: Oxford, **1996**.
2. Monk, P. M. S. *Fundamentals of Electroanalytical Chemistry*, **2001**.
3. Chandrasekhar, P. *Conducting Polymers, Fundamental and Applications*. Kluwer Academic Publishers: **1999**.
4. Milan Paunovic, M. S. *Fundamentals of Electrochemical Deposition*. Wiley: **2006**; p 52.
5. Scharifker, B.; Hills, G. *Electrochim. Acta* **1983,** *28*, 879-889.
6. Instruments, O. *INCAEnergy Applications Training Course*, Oxford, **2009**.
7. Joseph Goldstein, D. N., David Joy, Charles Lyman, Patrick Echlin, Eric Lifshin, Linda Sawyer, and Joseph Michael, *Scanning Electron Microscopy and X-Ray Microanalysis*, Springer: New York, **2007**.
8. Egerton, R. F. *Physical Principles of Electron Microscopy*, Springer: **2005**.
9. Company, F. Focused Ion Beam Technology, Capabilities and Applications, Company, F., Ed. Oregon, **2005**.
10. Liu, Y.; Choi, C.-H. *Colloid Polym Sci* **2012**, 1-9.
11. Yong Chae, J.; Bharat, B. *Nanotechnology* **2006,** *17*, 4970.
12. Bertolucci, D. C. H. a. M. D. *Symmetry and Spectroscopy An introduction to Vibrational and electonic spetroscopy*. Dover Publications: New York **1978**.
13. Colthup, N. B. Infrared Spectroscopy, In *Encyclopedia of Physical Science and Technology - Analytical Chemistry*, 3rd ed.; Elsevier: **2001**.
14. Hollas, J. M., *Modern Spectroscopy*. John Wiley and Sons: New York, **1987**.
15. Banwell, C. N. *Fundamentals of Molecular Spectroscopy*. McGraw-Hill Book Company Limited: UK, **1972**.

Chapter 3

The Facile Template-Free Electrochemical Polymerisation and Characterisation of Poly[*N*-(2-cyanoethyl)pyrrole] Nanowires.

3.1 Introduction

Polypyrrole (PPy) is one of the most extensively studied conducting polymers (CP) due to its facile preparation and its attractive range of properties, including redox activity,[1] ion exchange capabilities[2] and biocompatibility.[3] However, there is currently much interest in using functionalised monomers to generate conducting polymers as novel materials, in particular, as biosensors.[4-7] When the functional group on the substituted pyrrole contains a terminal cyano group, supramolecular interactions between that group and other molecules are possible. Indeed, poly[*N*-(2-cyanoethyl)pyrrole] (PPyEtCN) modified electrodes have been used to immobilise specific antibodies for the fabrication of biosensors [8-9] and in the electrochemical sensing of dopamine.[10] In this work, the reason for investigation of these polymers was to employ them as possible candidates to enhance the electrochemical reduction of the nitrate ion. Developing them into the nanowire morphology would increase the sensor response significantly.

In recent years a number of authors have reported template-free electrochemical methods for the formation of PPy nanowires.[11-12] These nanowires possess a higher surface area and shorter diffusion lengths than the analogous bulk materials, providing the wires with more attractive properties.[13] Although *N*-substituted PPy has been employed for sensor applications, there are few studies on the preparation of these polymers in the nanowire morphology. Moreover, these studies have utilised either a template approach or coated already grown PPy nanowires with the functionalised PPy.[14-15] In this chapter, the work presented is focused on the synthesis of novel PPyEtCN nanowires which, to the best of our knowledge, is the first report of a one-step preparation of *N*-substituted polypyrrole nanowires using a facile template-free electrochemical approach.

3.2 Results and Discussion

3.2.1 Preliminary Studies on the Solvent and Salt System for the Electrochemical Growth of PPyEtCN Nanowires

PPy nanowires are generally grown in aqueous solutions using either a phosphate or carbonate electrolyte combined with a $LiClO_4$ salt. As the pyrrole (Py) monomer is reasonably soluble in aqueous systems there are no solubility issues when growing PPy nanowires. The PyEtCN monomer however, has limited solubility in water and PPyEtCN, or any *N*-substituted PPy monomer, is typically polymerised using acetonitrile as the solvent.[8, 16-19] This makes the deposition of PPyEtCN in the nanowire morphology extremely difficult as the standard morphology directing components, which are mainly acids or inorganic salts,[20-21] are not fully soluble in organic media. It is possibly due to these solubility issues that PPyEtCN nanowires have not been reported in the literature to date.

A mixed solvent system, consisting of aqueous and organic components, was studied in an attempt to overcome the limited solubility of the PyEtCN monomer in water. This mixture would account for the low solubility of the morphology directing salts in organic media by maintaining a large water content. To the best of our knowledge this approach has never been attempted for the formation of PPy or PPyEtCN nanowires and for this reason a new experimental system was designed. The first part of this study was focused on establishing the composition of an organic and aqueous solvent system in which the PyEtCN monomer was sufficiently soluble. Once these conditions were achieved, using the minimum organic content, the solvent mixture was combined with various salts to give a high concentration of the morphology directing agents. This would facilitate an efficient electropolymerisation reaction as these salts also perform as dopants to balance charge generation within the polymer backbone. Ethanol was selected as the organic component, while distilled water was used as the aqueous phase. These results are presented and discussed in Sections 3.2.1.1 and 3.2.1.2.

3.2.1.1 The Influence of the Organic Component on the Solubility and Electropolymerisation Rate of the Monomer

In order to get efficient growth of a conducting polymer it is necessary to have a sufficient concentration of the monomer in solution, otherwise diffusion of the monomer to the surface may be limited, leading to slow polymerisation. During the formation of the polymer, the monomer is consumed rapidly at the electrode surface and this monomer must be replenished from the bulk electrolyte.[22] A constant growth rate is only maintained provided a sufficient concentration of the monomer is available.[23] For this reason a 0.100 M or greater concentration of the monomer is typically used in the formation of PPy nanowires.[24-26] Due to PyEtCN being insoluble in aqueous systems the amount of organic content in the polymerisation solution was critical. However, to grow the nanowire morphology the concentration of the salts, which are only soluble in the aqueous phase, was equally as important. Good solubility of these salts was essential in the formation of the PPyEtCN nanowires. Therefore, our goal was to achieve a minimum amount of ethanol within the mixed solvent system which would solubilise 0.100 M of the monomer, leaving a high aqueous content to dissolve the salts.

Experiments were carried out in order to measure the solubility of the monomer as a function of the ethanol content. The composition of the co-solvent system was varied from 5 to 90% ethanol with the addition of 0.100 M PyEtCN monomer. The solutions were inspected using an optical microscope with a x200 optical zoom to ascertain the extent of monomer solubility. The images were recorded following the addition of PyEtCN at room temperature with vigorous stirring for approximately 300 s. The results are presented in Figure 3.1. At 5% ethanol content a large amount of the insoluble monomer was observed at the bottom of the vial, indicating very poor solubility. At the higher ethanol contents of 10, 15 and 20%, the solubility improved slightly, however ‘globules’ of the monomer were still clearly evident dispersed throughout the solution. Even with vigorous stirring and sonication, or with gentle heating, only a partial increase in monomer solubility was obtained. However, these measures were only temporary and the monomer precipitated from the solution once the heating or sonication effects had dissipated. Very good solubility of the monomer was achieved with a 30% ethanol mixture, as highlighted in Figure 3.1.

Although the 30% ethanol solution was clear by visual inspection it was possible that the monomer had formed a nanoemulsion. This has been observed by other researchers dealing with the aniline monomer using sonication as their means of agitation.[27] These solutions contain nano sized droplets of insoluble material which are stable over a long period of time. Inspection of our solutions over several days (sealed to prevent ethanol evaporation) revealed that the monomer did not revert back to its 'globular' undissolved state. It is possible that the nucleation of our nanowires may follow a monomer droplet mechanism facilitated by monomer nano droplets.[28]

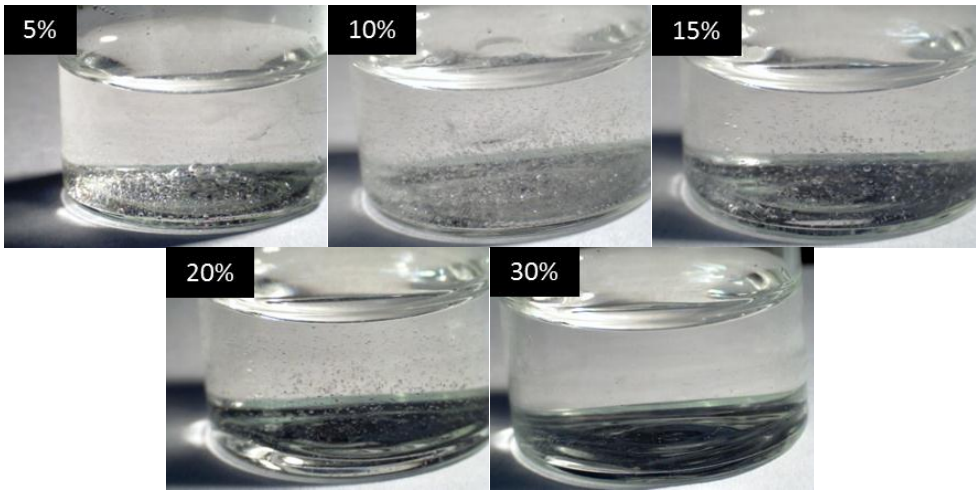

Figure 3.1. Optical microscope images of 0.100 M PPyEtCN in solutions with increasing amounts of ethanol including 5, 10, 15 20 and 30%. Remainder of solution made up with distilled water. Images recorded after vigorous stirring at room temperature.

The influence of the ethanol content on the oxidation potential of the PyEtCN monomer, and the subsequent rate of the electropolymerisation reaction, was studied by cyclic voltammetry (CV). A GC electrode was immersed in a 0.005 M PyEtCN solution with the addition of 0.100 M $LiClO_4$ and cycled from 0.000 to 1.600 V. Under these conditions only the bulk polymer was deposited at the electrode surface. However, a good understanding of the effects of ethanol on the electropolymerisation reaction is important in formulating conditions for depositing the PPyEtCN nanowires. With this knowledge the formation of PPyEtCN nanowires with tunable lengths and diameters can be achieved, similar to that observed for other polymer nanowires.[29-32] The bulk PPyEtCN was deposited using CV as this technique can be used to monitor the oxidation potential of the monomer. This is not the primary

technique used when depositing CP nanowires due to the formation of compact polymer layers. This occurs as the oxidative growth potential is periodically discontinued as the potential is switched to reductive parts of the voltammogram.[23] For this reason this technique has rarely been used in the formation of wire morphologies, although CV can be employed with surfactants to produce microtubes.[33] Representative data for the polymerisation of 0.100 M PyEtCN in various solutions with differing ethanol contents from 30, 50, 70 and 90% are shown in Figure 3.2. These concentrations are considerably higher than the 30% minimum value described earlier, but with the additional increase in ethanol interesting trends can be observed. From the data shown in Figure 3.2 it can be seen that the ethanol content had a significant influence on the formation of the bulk PPyEtCN, affecting both the oxidation potential of the monomer and the rate of electropolymerisation. With each addition of ethanol to the solution, the oxidation potential shifted to lower overpotentials, but lower peak currents were also observed. For example, in the 90% ethanol solution, the onset of the monomer oxidation was seen at approximately 1.000 V, while the current increased to give a peak potential at about 1.200 V. This peak potential increased to 1.400 V in the presence of 30% ethanol. Interestingly, in the 90% ethanol solution, a second peak current is observed at 1.500 V which was most likely due to overoxidation process occurring since the monomer has a lower oxidation potential in this mixture.

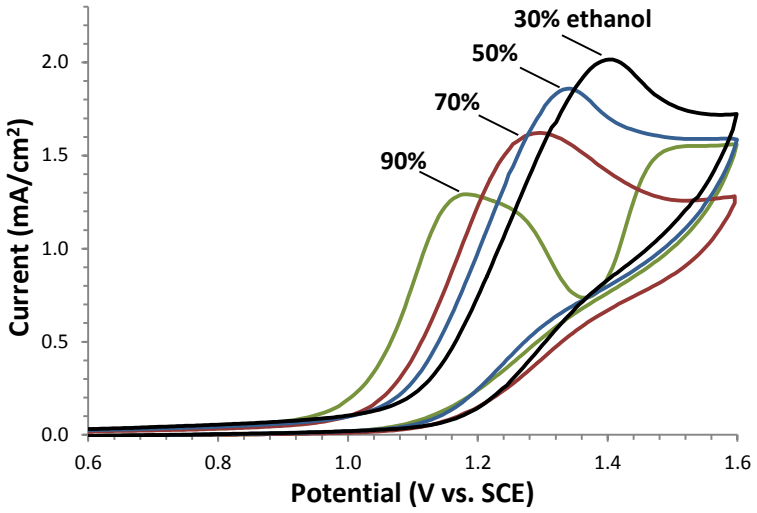

Figure 3.2. Cyclic voltammograms at a GC electrode in 0.100 M $LiClO_4$ with 0.005 M PyEtCN monomer cycled from 0.000 to 1.600 V at 50 mV/s in 30, 50, 70 and 90% ethanol solutions.

Linear relationships were observed between the ethanol concentration and the peak oxidation potential (E_p) (R^2 value of 0.979) and peak current (I_p) (R^2 value of 0.978), as shown in Figure 3.3a and 3.3b respectively. These plots illustrate that adding more ethanol to the reaction system made the monomer oxidation more favourable and produced an onset oxidation wave with a steeper gradient. This was consistent with the increasing solubility of the monomer in the higher ethanol-containing solutions. Although good solubility of the monomer was observed in a 30% ethanol solution, due to the high water content the composition of the solvent mixture at the electrode-solution interface may be somewhat different, with a higher water content compared to the bulk solution. This is due to the electrode surface having a high affinity for the adsorption of water molecules.[34] This, in turn, would give lower concentrations of the soluble monomer and account for the higher oxidation potentials, Figure 3.2.

Comparatively, when the I_p were examined the opposite trend was noticed. Again, a linear plot was observed when the I_p was plotted as a function of the ethanol content. However, as more ethanol was added the I_p values decreased, as shown in Figure 3.3. As the current recorded is proportional to the rate of the reaction,[35] this indicated that the rate of the electropolymerisation reaction was increased at lower ethanol contents, even though the solubility and effective concentration of the monomer was decreased at this ethanol concentration (30%). This trend was somewhat unusual, but can be explained in terms of the differences in dielectric constants of water and ethanol, the solubility of the monomer and the solubility of the electrolyte salts. Furthermore, the solvation of the anions and monomer will vary in different solvent solutions. It is well known that ethanol has a lower dielectric constant compared to water (24[36] and 80[37], respectively, at 25 ^{o}C). This, combined with the solubility variations, can have substantial effects on the formation of the polymer, including the rate of growth, the nucleation at the surface, the adherence of the film, and the surface coverage.[38-39] As the ethanol content was increased, the dielectric constant of the solvent decreased and this appeared to reduce the rate of the electron transfer. With the higher dielectric constant, the coulombic repulsion between the radical cations was reduced and consequently this facilitated radical-radical coupling and higher rates of electropolymerisation.[40]

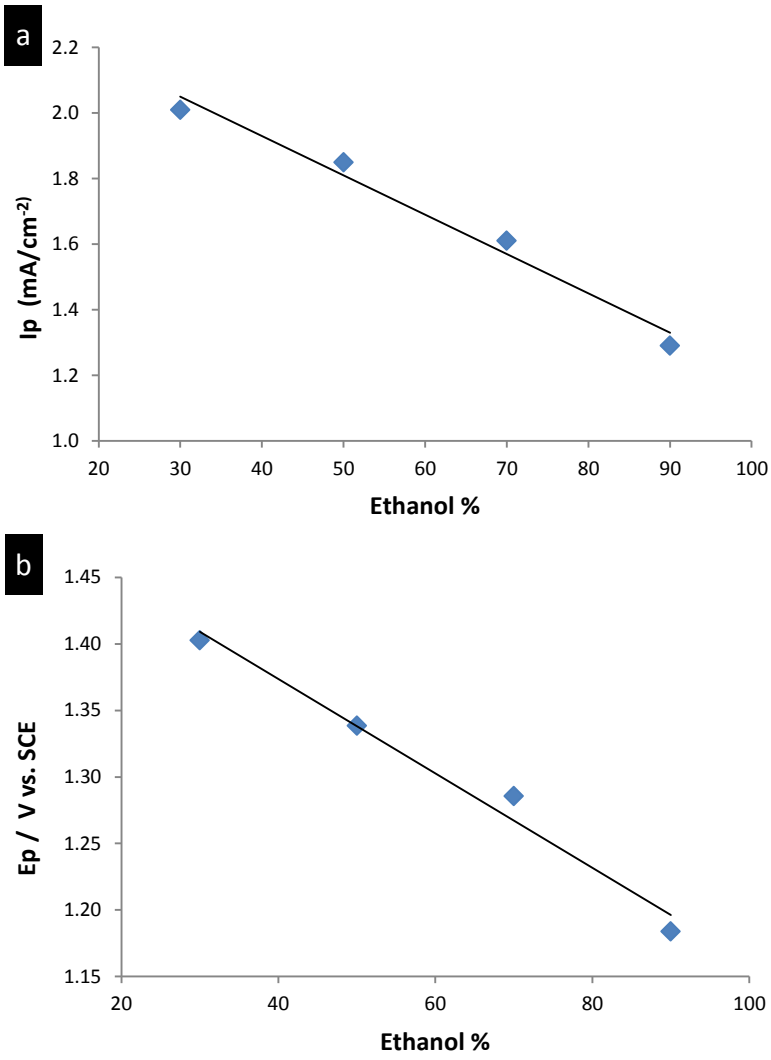

Figure 3.3. Peak current (I_p) (a) and peak potential (E_p) (b) plotted as a function of % ethanol. All experiments were performed at a GC electrode with 0.005 M PPyEtCN and 0.100 M $LiClO_4$.

These results are similar to the marked effect water has on the electropolymerisation of pyrrole in acetonitrile, where the addition of water increases the rate of electropolymerisation, improves the adherence of the film to the electrode and enhances the conductivity of the film.[41] The occurrence of this 'water effect' has been investigated by many authors and different conclusions have been developed. These effects have been explained in terms of variations in the dielectric constant of water and acetonitrile, where the dielectric constant of acetonitrile (33)[42] is similar to that of ethanol. Contrary to this, it has also been suggested that the addition of water reduces the solubility of oligomers and this leads to faster deposition of the film onto the electrode.[43] It has also been proposed that protons released during polymerisation produce oligomers in front of the electrode surface which reduce subsequent

electropolymerisation, while water is able to scavenge or 'mop up' these excess protons since it is more basic than the monomer.[44] This would account for the significant reduction in the peak currents observed in Figure 3.2 as less water is available to perform these actions. Indeed, the high ethanol content, while increasing the solubility of the monomer, may also give rise to enhanced solubility of the oligomers and poor rates of polymer formation.

The slower polymerisation rate recorded in higher concentrations of ethanol was further confirmed by inspection of charge time plots produced from simple potentiostatic growths using 0.100 M $LiClO_4$ and 0.100 M PPyEtCN monomer, Figure 3.4. These charge time plots were recorded at 1.100 V and as evident from Figure 3.2, this corresponds to a potential where oxidation of the monomer occurs. Potentials higher than 1.100 V were not employed as this led to overoxidation of the polymer. This overoxidation process is described elsewhere in Chapter 1, Section 1.2. Briefly, it is well known that holding the polymer-modified electrode at a high potential, or polarising for long times, breaks the conjugation along the polymer backbone to a point it becomes irreversibly reduced.[22, 45-46] This is due to the fact that PPy has a lower oxidation potential compared to the Py monomer which means that overoxidation is an unavoidable consequence of film growth when nucleophilic species such as water are present.[22] Subsequently, this process can be reduced by using lower overpotentials or employing shorter oxidation times during polymerisation.

Figure 3.4 shows charge vs. time plots for PPyEtCN polymers grown in 30, 50 and 100% ethanol solutions. From this data it can be confirmed that the ethanol content had a significant effect on the charge consumed. The rate of polymer formation using 100% ethanol was significantly slower, even though the monomer was highly soluble in this solution. For the solutions with 30% and 50% ethanol it was seen that the charge was much larger. The total charge consumed was 0.66, 0.58 and 0.17 C/cm^2 for the 30, 50 and 100% ethanol-containing solutions, respectively. It was also evident from Figure 3.4 that the charge increased in a linear manner with time for the 30% and, to a somewhat lesser extent, for the 50% ethanol contents. Again, this was consistent with an increase in the rate of film formation at the lower ethanol contents. However, with the 100% ethanol solution, this linear increase was not observed, and the rate of growth plateaued over the 100 s period, leading to a low rate of polymer

formation at the electrode. These data are in good agreement with the cyclic voltammograms shown in Figure 3.2.

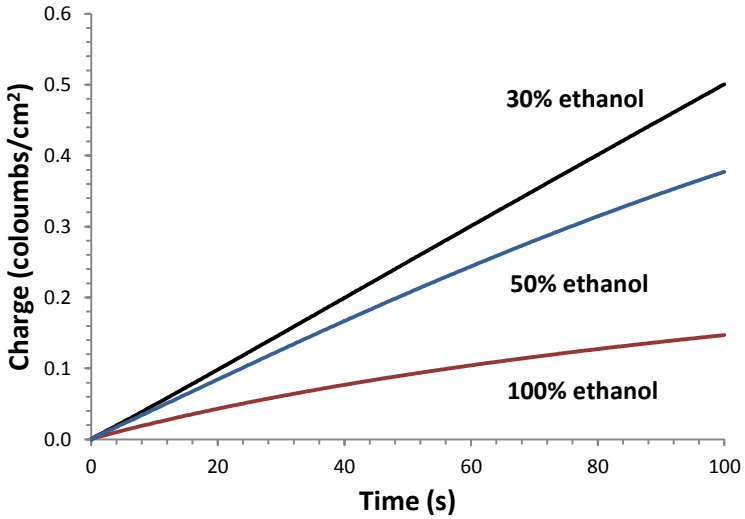

Figure 3.4. Charge-time plot recorded at a GC electrode for the polymerisation of 0.100 M PyEtCN monomer at 1.100 V in 0.100 M $LiClO_4$ with in 30, 50 and 100% ethanol.

These significant differences in the polymerisation rates will have a major effect on the resultant polymer film which is formed. It is known that the rate of electropolymerisation affects the porosity and thickness of the final deposited polymer films.[22] This can also have an effect on the overall surface coverage of the electrode, with the faster growing polymers typically covering the entire electrode uniformly. Indeed, this effect was observed in the higher ethanol-containing solutions which had slower growth rates. Typical micrographs are presented in Figure 3.5 for the polymer deposited from a 50% ethanol solution, producing polymer only at isolated sites on the surface. Very poor surface coverage was observed, with nucleation of the polymer in a patchy and uneven manner across the substrate. In addition, the adhesion of the polymer to the electrode surface was relatively poor. Adhesion was measured by a crude but effective method; by covering the electrode with sellotape and visually inspecting the amount of polymer on the tape after removal.

From these experiments it was clear that the minimum amount of ethanol required to dissolve 0.100 M PyEtCN monomer was 30%. Although higher ethanol contents enhanced the solubility and lowered the oxidation potential of the monomer, as

shown in Figure 3.2, they gave rise to a significant reduction in the rate of electropolymerisation and to the formation of patchy polymer deposits, Figure 3.5. Conversely, the solution with a 70% water/30% ethanol solution (water/ethanol (7:3)) allowed for a consistently high rate of growth and was capable of dissolving a sufficient concentration of monomer. It has been reported that controlling the kinetics of polymerization, during electrochemical deposition, is the key to growing conducting polymers in an ordered morphology.[47-48] In these studies the applied current density was reduced in a stepwise fashion to allow for fast initial nucleation followed by slow propagation yielding uniformly oriented conducting polymer nanowires/tubes. Therefore, the experiments outlined in this section are important for understanding the rate of polymerisation within our chosen co-solvent system.

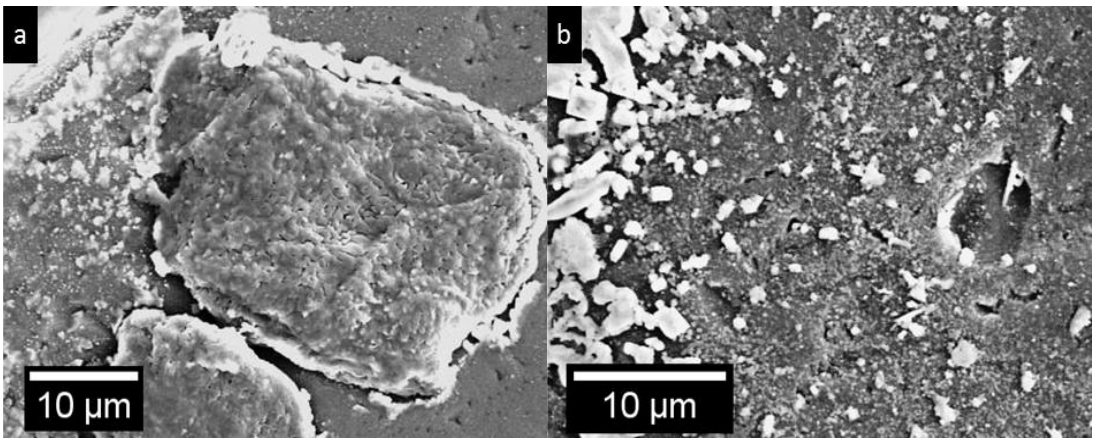

Figure 3.5. SEM micrographs of the patchy PPyEtCN deposited at 1.100 V from 0.100 M PyEtCN and 0.100 M $LiClO_4$ in 50% ethanol/50% water.

To grow nanowires only a limited range of electrolytes are capable of generating the wire morphology. These electrolytes direct growth through hydrogen bonding or control of the solution pH.[11-12] The solubility of these species in the ethanol water mix is equally as important as the monomer solubility. The results presented and discussed in Section 3.2.1.2 are focussed on the choice of morphology directing salts which remained soluble in the ethanol-water mix and still produced the nanowire morphology. The dopant and salts that were chosen and discussed in the next section were limited to the water/ethanol (7:3) solution, as this concentration was required for monomer solubility.

3.2.1.2 Influence of the Nature and Concentration of the Electrolyte Salts

From the literature it is known that PPy nanowires can be grown using either a phosphate or carbonate system with a small amount $LiClO_4$.[49-50] In other cases an acidic medium such as camporsulphonic[20] or pyrenesulphonic[31] acid have been used. In the present study the former methodology was chosen for the PyEtCN system as it was successfully used to grow PPy nanowires. The work discussed in Chapter 5 shows that using this methodology it is possible to control the morphology of the polymer films produced in a reproducible manner.

The first set of salts investigated involved the carbonate-based system. Wang *et al.*[51] employed a carbonate and bicarbonate mixture which was successfully used to control the wire diameter by altering the carbonate ratios. They observed the nanowire diameter decreased from 120 to 50 nm when the ratio of bicarbonate to carbonate was changed from 5:1 to 1:5. For the PPyEtCN system caesium carbonate was chosen (with sodium bicarbonate) as it has a high solubility in polar solvents and has some solubility in organic media.[52] The solubility of the salt systems in the solvent mixture was judged using a light microscope. Using the same mole ratios of each component (1 Cs_2CO_3: 3 $NaHCO_3$: 1 $LiClO_4$) and starting at a reasonably low total salt concentration of 0.125 M, the concentrations of the salts were increased incrementally. The main goal was to achieve the highest possible content of carbonate in the polymerisation solution to direct growth, without forming salt precipitates or compromising the solubility of the PyEtCN monomer. The solubility of the monomer was also dependent on the salt concentrations and as they increased, the solubility of the monomer decreased. Table 3.1 shows the concentrations and the solubility limits of the reagents investigated when added to the water/ethanol (7:3) solution in the presence of 0.100 M PyEtCN. It was evident from this data that the highest concentrations at which solubility was still maintained was 0.039 M Cs_2CO_3, 0.117 M $NaHCO_3$ and 0.039 M $LiClO_4$. Concentrations higher than these resulted in a precipitation of the salts as a white residue at the bottom of the vial. However, with sonication, the solution containing 0.040 M Cs_2CO_3, 0.121 M $NaHCO_3$ and 0.040 M $LiClO_4$, to give a total salt concentration of 0.201 M, was sufficiently soluble.

Table 3.1. Concentrations of Cs_2CO_3, $NaHCO_3$ and $LiClO_4$, and the observed solubility in the water/ethanol (7:3) solution. The concentration ratio was maintained at 1:3:1 for all samples.

Cs_2CO_3/M	$NaHCO_3$/M	$LiClO_4$/M	Solubility
0.025	0.075	0.025	Soluble
0.031	0.093	0.031	Soluble
0.037	0.112	0.037	Soluble
0.039	0.117	0.039	Soluble
0.040	0.121	0.040	Slightly
0.043	0.131	0.043	Insoluble
0.050	0.150	0.050	Insoluble

The solution containing 0.039 M Cs_2CO_3, 0.117 M $NaHCO_3$ and 0.039 M $LiClO_4$ and 0.100 M PyEtCN was polymerised at 1.100 V in an attempt to form PPyEtCN nanowires. The corresponding current-time and charge-time plots are presented in Figure 3.6. It was clear from the current transient response that the current decayed rapidly to a very low value. This is indicative of a slow rate of deposition occurring at the electrode surface. Furthermore, the charge-time plot (Figure 3.6 inset), although showing an initial increase in charge, reaches a limiting charge of about 25 mC at 30 to 100 s, indicating little or no further film formation of polymer at longer times. These slow rates of electropolymerisation were explained in terms of the pH of the solution which was measured as 9.48. This corresponds to a relatively high concentration of OH^- ions in solution, which are known to terminate propagation of pyrrole chains, leading to the formation of an overoxidised polymer.[45] Indeed, the data presented in Figure 3.6 are consistent with the formation of an insulating polymer. Further electropolymerisation upon this insulating layer occurs at a very slow rate due to the slow rate of electron transfer through the insulating polymer layers.

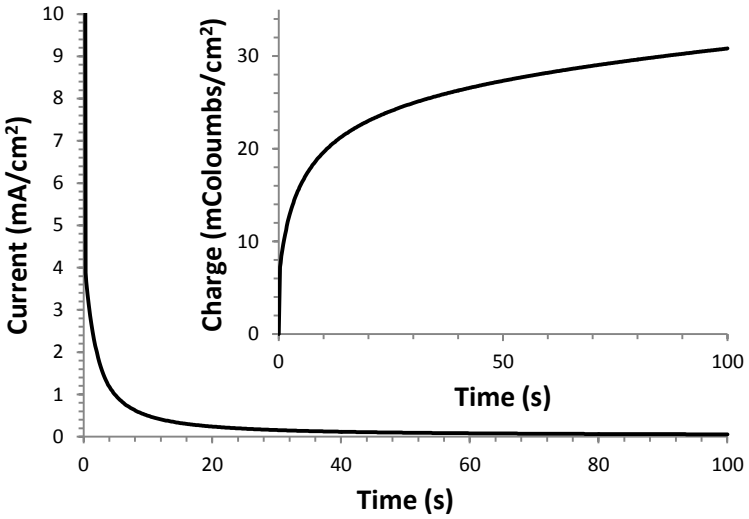

Figure 3.6. Current-time and charge-time transients recorded for the electropolymerisation of PyEtCN at 1.100 V, in 0.100 M PyEtCN, 0.039 M Cs_2CO_3, 0.117 M $NaHCO_3$ and 0.039 M $LiClO_4$ in water/ethanol (7:3) solution at a GC electrode.

These alkaline conditions were very unfavourable for growing polymers. After many unsuccessful attempts at forming the wire morphology, with variation of the applied potential, salt concentrations and the electropolymerisation period, an alternative approach was taken. The pH of the solution was reduced by employing a phosphate-based electrolyte. This electrolyte was very similar in many respects to the carbonate system as described earlier. Some authors have used it as a buffer system to control the pH of the solution and subsequently the morphology PPy nanowires.[11, 53] More recently, it has been shown that by simply adding $H_2PO_4^-$ to $LiClO_4$, a PPy nanowire morphology can be obtained.[12]

Similar to the carbonate system a range of salts were investigated to ascertain their ability to dissolve in the water/ethanol (7:3) solution. As discussed previously, solubility was the main factor in choosing which salt to follow in a more in-depth study. The salts chosen were NaH_2PO_4, KH_2PO_4 and $(NH_4)H_2PO_4$. Good solubility was observed with the phosphate salt concentrations of 0.200 M and 0.07 M $LiClO_4$ in the presence of 0.100 M PyEtCN. The KH_2PO_4 displayed more promise in terms of the morphology of the polymer, as some nodules or the beginning of wires appeared after electropolymerisation, as shown in Figure 3.7a. While the morphology of this polymer was essentially wire-like, the extremely short and thin nature of the wires prododuces a very low aspect ratio. It is also obvious from this SEM micrograph that there was minimal spacing between each individual wire, reducing

the advantageous increased surface area that separated wires possess. As a more positive growth potential was applied these nodules disappeared and a 'hills and valleys' type morphology was observed as shown in Figure 3.7b. This morphology was not isolated to PPyEtCN polymers and was also dominant for azidoethylpyrrole ($PPyEtN_3$) polymer films grown at elevated potentials.[54] This was a characteristic of the substituted monomers as the 'hills and valleys' morphology was not observed in un-substituted PPy experiments. It was observed by SEM and CV (not shown) that this type of morphology tended to crack and become brittle during electrochemical characterisation, due to the swelling and contraction which takes place when dopants and solvent move in and out of the polymer matrix.[55] This indicates that the PPyEtCN monomer was limited to a narrow potential range for growing stable and useable polymer films, with 1.20 V deemed as the maximum value.

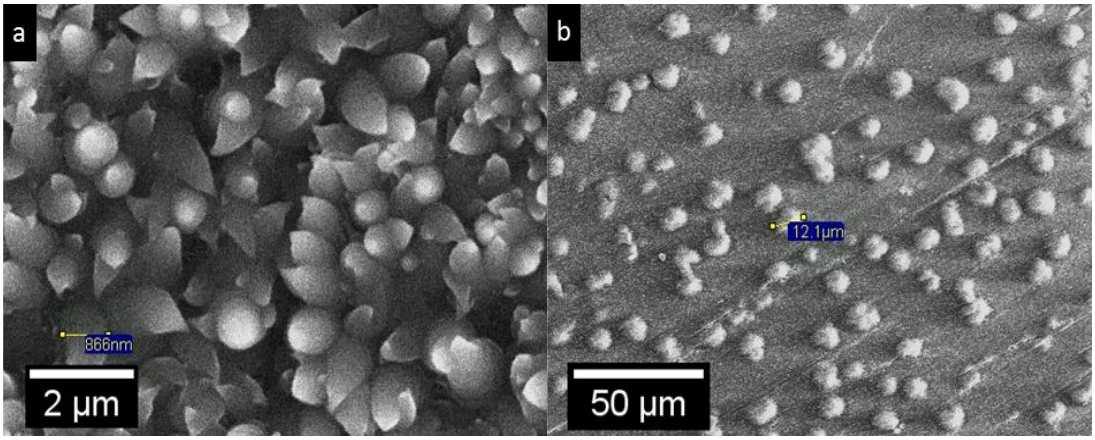

Figure 3.7. SEM micrographs PPyEtCN formed at (a) 0.90 V and (b) 1.20 V at a GC electrode using 0.070 M $LiClO_4$, 0.200 M KH_2PO_4 with 0.100 M PyEtCN in a water/ethanol (7:3) solution.

In Figure 3.8a and 3.8b respectively, the current-time and charge-time plots recorded in the water/ethanol (7:3) solution for both 0.200 M KH_2PO_4 and 0.200 M $(NH_4)H_2PO_4$ dissolved in 0.070 M $LiClO_4$ with 0.100 M PyEtCN are displayed. These profiles are overlaid with that recorded for the alkaline Cs_2CO_3 system, described previously in Table 3.1. It is clear that the pH of the solution has a significant influence on the rate of polymer formation and the shape of the current-time transients. In any polymerisation experiment, on application of the potential to the electrode there is an initial charging current which arises from the charging of the double layer.[34] This charging current decays rapidly, depending on the conductivity

of the solution. In the Cs_2CO_3 system the current continued to decay, indicating a low rate of electropolymerisation. However, a stabilised current transient was seen with the phosphate solutions and this indicated a much higher rate of polymer formation, Figure 3.8a. This was also evident in Figure 3.8b where near linear charge-time plots can be seen. Unfortunately the short term solubility of KH_2PO_4 in the water/ethanol (7:3) solution gave rise to the precipitation of the salt during the electropolymerisation period. Therefore the more soluble $(NH_4)H_2PO_4$ was selected as the source of the phosphate anions for further experimentation.

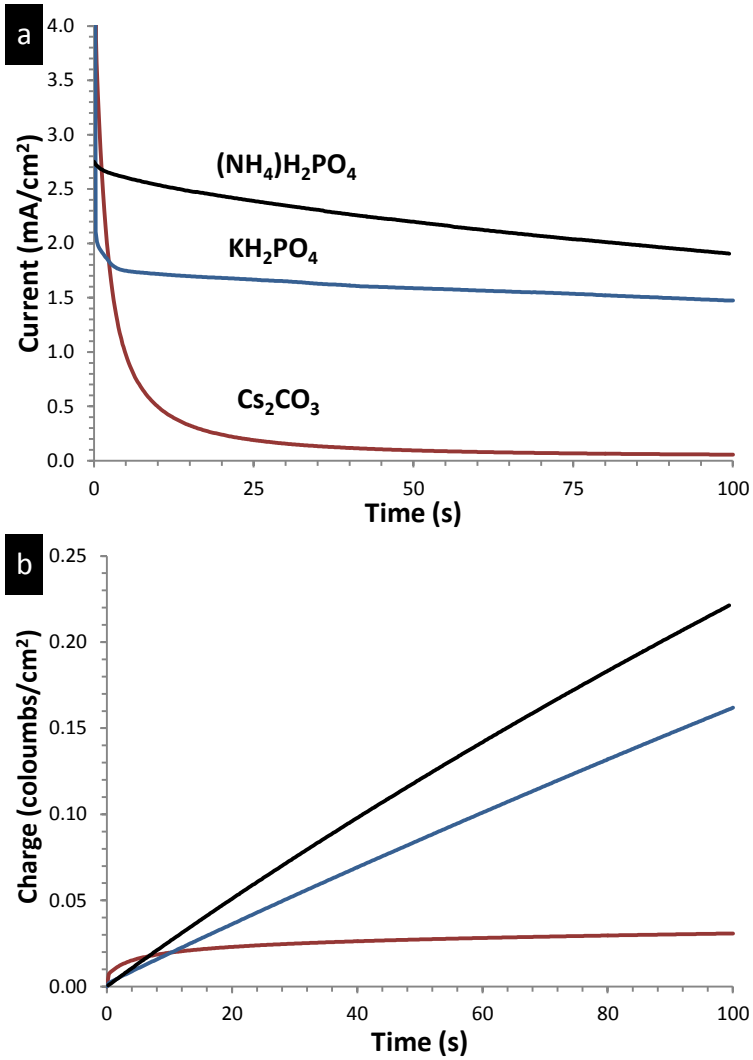

Figure 3.8. Current-time (a) and charge-time (b) plots recorded at GC in 0.100 M PyEtCN in a water/ethanol (7:3) solution in the presence of 0.070 M $LiClO_4$ in 0.200 M $(NH_4)H_2PO_4$, 0.200 M KH_2PO_4 and 0.390 M Cs_2CO_3 electrolytes containing 0.039 M $LiClO_4$.

Good solubility was observed using $(NH_4)H_2PO_4$ and the solution was stable for periods exceeding 1 h. As shown in Figure 3.8a, the currents recorded in the presence of $(NH_4)H_2PO_4$ were indicative of a high rate of growth and the charge consumed surpassed both the KH_2PO_4 and Cs_2HCO_3 systems, Figure 3.8b. Precipitation was not observed during polymerisation, and this potentially increased the growth rate due to a better availability of dissolved dopants in solution. Additionally, the pH of this phosphate solution was measured as 4.97, which was considerably more favourable for the formation of the polymer, compared to the alkaline conditions of the carbonate solution (pH 9.48). It is known that polymer growth rates are greatly increased in more acidic solutions.[56] Furthermore, basic solutions can promote hydroxyl groups from solution being inserted into the polymer over the dopant anions.[57] Therefore, a lower pH is preferred for successful polymerisation. However, a very low pH can weaken conductivity due to the acid catalysed formation of nonconjugated trimers and should be avoided.[58] Optimisation of pH has even been shown to favour more uniform polymers with fewer defects.[59] These reports highlight the importance of maintaining the correct pH during polymer formation.

The benefit of now having the monomer and morphology directing salt soluble in the same solvent system meant that a range of experimental parameters could be varied to optimise the formation of the nanowires. The concentration of the monomer, the applied potential and the electropolymerisation period were varied in the water/ethanol (7:3) solution with 0.300 M $(NH_4)H_2PO_4$ and 0.070 M $LiClO_4$. In Table 3.2 the results are summarised and it was clear that no polymer growth occurred at low monomer concentrations, nodules were formed in the higher monomer-containing solutions, while micro-wires and long micro-wires were formed with a monomer concentration of 0.075 M.

Table 3.2. The polymer morphology as a function of monomer concentration, applied potential and growth time. Polymerisation performed at a GC electrode with 0.300 M $(NH_4)H_2PO_4$ and 0.070 M $LiClO_4$ in water/ethanol (7:3).

Monomer/M	Potential/V	Time/s	Polymer
0.100	0.800	100	Very thin
	0.850	250	Nodules
	0.900	250	Nodules
	0.850	3600	Micro-wires
0.075	0.850	3600	Micro-wires
	0.850	7200	Long micro-wires
0.050	0.850	3600	No growth
	0.950	3600	Very thin

Further variations in the monomer concentration, applied potential and concentration of the phosphate salt had little effect on the morphology of the nodules or wires. By reducing the $LiClO_4$ concentration to 0.020 M and maintaining the other experimental parameters, at 0.850 V, 0.075 M PyEtCN for 1 h, wires in the nanoscale dimension were formed successfully, as shown in Figure 3.9. Here, the nanowires were produced as a homogeneous and uniform film over the entire electrode. This was an unexpected result as the role of ClO_4^- in the formation of polymer wires has not been discussed in the literature. Although the ClO_4^- is present at very low concentrations it is an essential 'ingredient' in the formation of the nanowire morphology. Indeed, the wires did not form when the ClO_4^- was not present, or added at higher concentrations, such as 0.100 M $LiClO_4$. Since ClO_4^- preferentially inserts into the nanowires as dopant (Section 3.2.3.4), it has a large impact on the growth rate achieved. If there was too much ClO_4^- the polymer chains propagated very fast and the resultant polymer was an amorphous bulk layer. Similar to the composition of the solution, the concentration of $LiClO_4$ was directly related to the rate of polymer growth and, as discussed previously, this is key to forming polymers in an ordered nanowire morphology. This is discussed further in the next section, where the dopant ratios are varied to ascertain the effect each component has on the nanowire morphology, along with other factors which affect morphology such as substrate, co-solvent mixture and polarisation time. Indeed, the theme of polymer

deposition rate connects these parameters together and highlights their obvious effect on the morphology of the PPyEtCN polymers.

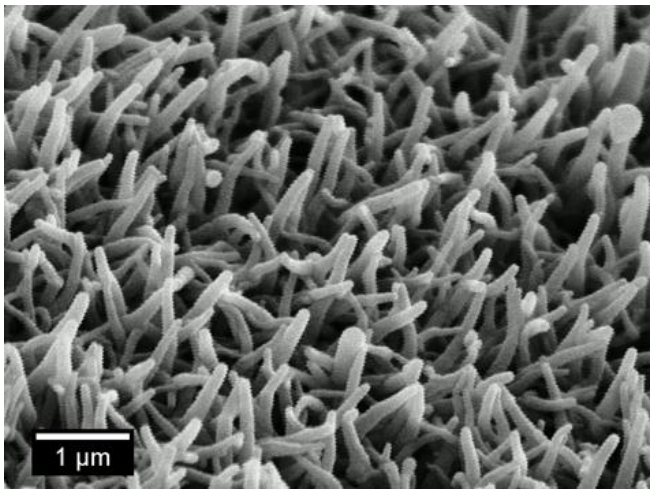

Figure 3.9. PPyEtCN nanowires grown with 0.020 M $LiClO_4$, 0.300 M $(NH_4)H_2PO_4$ and 0.075 M PyEtCN at 0.850 V for 1 h at a polished GC electrode in water/ethanol (7:3) solution.

3.2.2. Optimising Nanowire Growth Conditions

The preliminary studies discussed in Section 3.2.1 outline a set of standard conditions required to create a homogeneous and uniform nanowire film. Specifically these were a 70% water/30% ethanol (water/ethanol (7:3)) solution using a high concentration of $(NH_4)H_2PO_4$ with a minor amount of $LiClO_4$. It is also important to be able to demonstrate control over the nanowire growth and final aspect ratio as seen in the literature.[11-12, 25, 29, 60] Further investigations were required to ascertain whether it was possible to achieve this control using the novel co-solvent system described above. Certain parameters, critical to the nanowire morphology, were examined to verify if this control was possible. The chosen parameters were the substrate material, dopant ratios, electropolymerisation time and co-solvent mixture. Since this section is aimed at understanding the key factors in obtaining the nanowires, it must be noted that electropolymerisation potential will not be discussed in this section to reduce repetition as it has previously been mentioned in Section 3.2.1. However, it is still regarded as a critical factor for controlling the nanowire morphology.

3.2.2.1 Influence of Substrate

The nature of the electrode substrate can have a substantial effect on the mechanism of electropolymerisation. It has been shown that the substrate can alter the manner in which polymers are formed and even affect the final morphology. [23] These changes are due to different affinities of analytes for different metal surfaces or to variations in kinetics at each electrode. Currently, there is no information in the literature on the effect various substrates have on the electropolymerisation of bulk PPyEtCN. Therefore, metal and carbon electrodes were used to investigate the growth of PPyEtCN nanowire polymers.

It was observed that preparation of the substrate for electrochemical deposition of bulk PPy and PPyEtCN was not critical to polymer formation. Contrary to this, the surface preparation for PPy and PPyEtCN nanowires was critical. In order to obtain reproducible nanowire growth it was necessary to outline a new polishing procedure to ensure each of the electrode surfaces were brought to a high standard of finish. This procedure is outlined in Chapter 2, Section 2.3.1. Furthermore, this regime was more detailed and thorough than what is currently performed in the literature for mechanical polishing.[21, 31, 50, 61-66] Comparing unpolished (Figure 3.10a) and polished (Figure 3.10b) electrode surfaces shows the positive effect these extensive cleaning procedures have on the electrode surface. Clearly, the unpolished electrode surface remains dull while the polished surface has obtained a mirror finish.

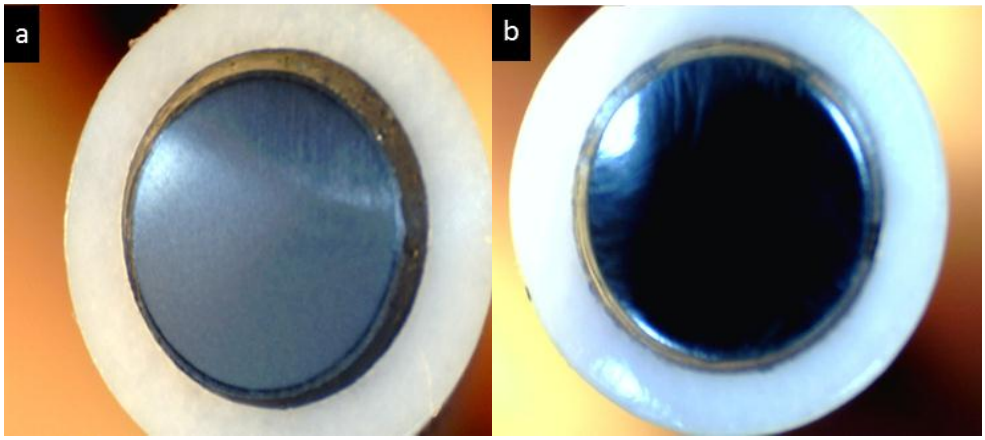

Figure 3.10. GC electrode surfaces (a) unpolished and (b) polished using successive diamond paste polishing procedure with sonication cleaning between each step.

Some authors have focused specifically on substrate cleaning methods, highlighting its importance.[65, 67] It is also common for electrochemical post-polishing routines to be employed to activate the surface [68-71] or for acid pretreatment to ensure a reproducible finish.[49, 51] These processes are valid means of increasing electron transfer and producing extremely clean electrode surfaces. While some of these methods were attempted in this work, the harsh acidic conditions used were detrimental to the epoxy coating which surrounds the electrodes and drastically reduced their overall lifetime. For this reason only mechanical polishing was employed in the work described here. Another method of ensuring a pristine substrate finish is to deposit metal layers on top of an inert substrate,[11, 72] this achieves a reproducible layer and removes the issues associated with mechanical polishing or human error. Similar to these procedures, our polishing routine produced a consistent and highly reproducible surface between successive experiments.

A uniform polymer film was necessary as inconsistent areas have a different electrochemical response and varying electrical conductivity compared to the bulk of the polymer.[73] The necessity of this cleaning regime was further realised when a metal substrate was used for polymerisation. As shown in Figure 3.11a and 3.11b, the polymer grew in straight ordered lines along the surface when using Au or Pt substrates, as highlighted by the red arrows. This is similar to how some authors have observed PPy to form when polymerised with surfactants.[74] In the PPyEtCN system however, the ordering was on a much larger scale which cannot be explained by a surfactant interaction. Furthermore, no surfactants were present within the electrolyte mixture. It is simply due to the malleability of the metal substrates which retain large indents from the harsh grinding they receive from removing the polymer layers between each experiment. The long scratches then formed areas which were high in surface defects. These defects had a higher surface energy which led to the polymer growing from these sites preferentially,[75] leading to much faster growth rate.[76-77] The growth rate was sufficiently fast in some areas to produce an array of random micro wires which had an uneven size distribution, shown in Figure 3.11c. While in the region of these microwires very few nanowires grew, with large gaps seen in between each micro structure, possibly due to the available monomer being consumed in the growth of the defect microstructures. It is also interesting to note

that far from these scratch sites a uniform nanowire morphology was predominant as shown in the inset of Figure 3.11a and 3.11b.

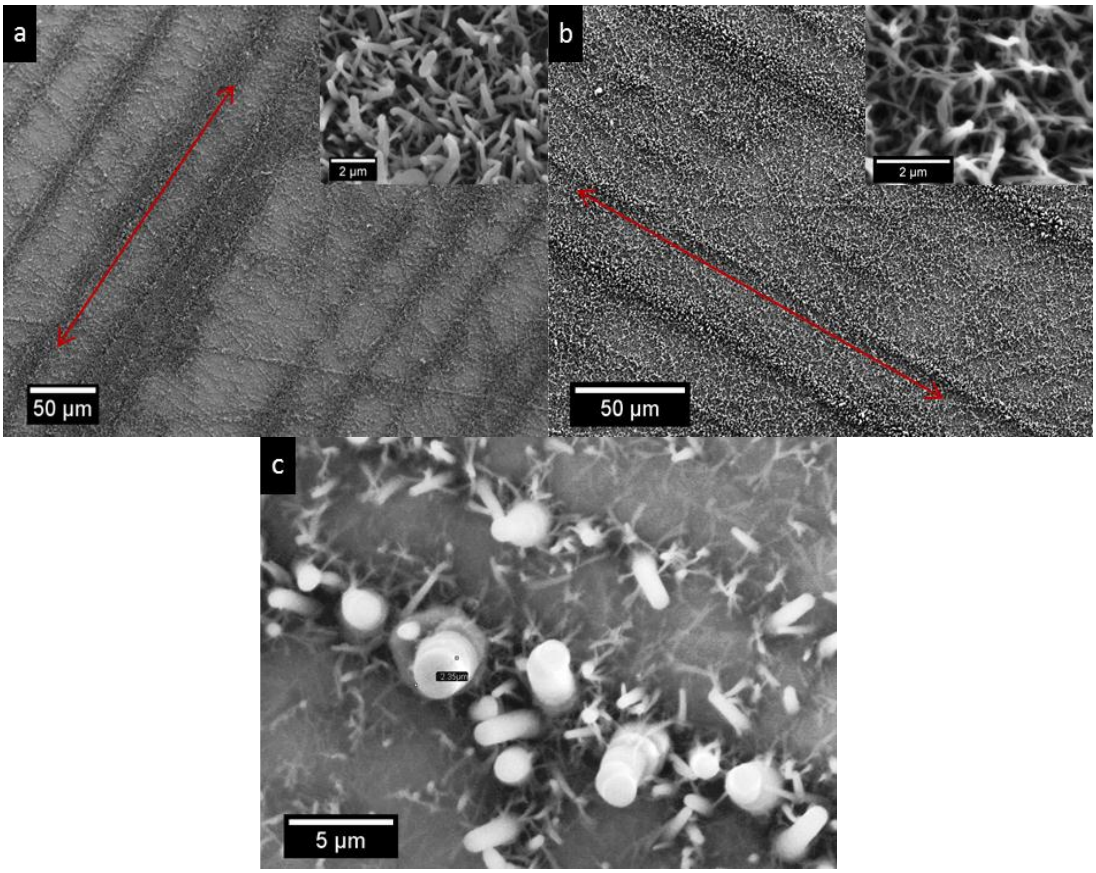

Figure 3.11. PPyEtCN polymers grown at 0.850 V for 1 hour with 0.300 M $(NH_4)H_2PO_4$, 0.020 M $LiClO_4$ in a water/ethanol (7:3) solution on (a) Pt and (b) Au, with magnification of unscratched areas inset and (c) high magnification image of a scratch defect area.

Conversely, GC substrates were brought to a mirror finish using the polishing procedure described previously. These surfaces were capable of producing a homogenous coating of PPyEtCN nanowires, as shown in Figure 3.12, free from the polymer ordering seen for the metal substrates. The nanowires were produced with a narrow distribution in their height and width. Another benefit of GC is that it is more inert compared to the metal substrates particularly when scanning to low reductive potentials where the hydrogen reduction reaction (HRR) can become an issue, as described in Chapter 5 Section 5.2.3. For this reason GC was used as the standard substrate for all PPyEtCN experiments. However, for some Raman experiments, Au

and Pt electrodes were employed to overcome some of the intense carbon vibrations associated with GC, as discussed in Section 3.2.3.3.2.

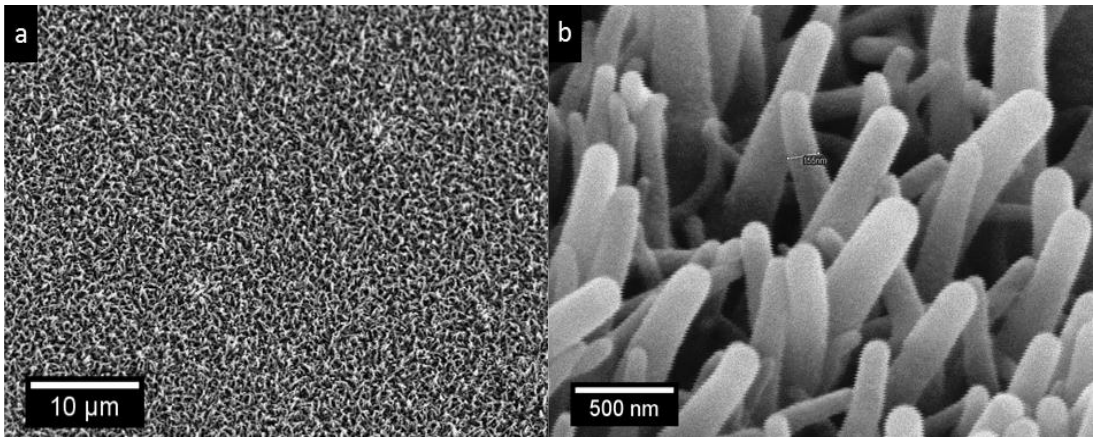

Figure 3.12. Low magnification (a) and high magnification (b) SEM micrographs of a nanowire film grown 0.850 V for 1 hour on a GC electrode using 0.020 M $LiClO_4$ and 0.300 M $(NH_4)H_2PO_4$ with 0.075 M PyEtCN in a water/ethanol (7:3) solution.

Comparison of the current vs. time plots for PPyEtCN nanowire films grown on Au, Pt and GC did not show any major differences (not shown). While it might be expected that an additional diffusion controlled peak would appear for the Au and Pt substrates, due to the fast growth of the micro wires along the scratch areas, this was not seen. This could be explained by reasoning that the local current passed at the defect sites was expected to be greater than the bulk electrode; in comparison the other areas of the electrode would record a lower current due to the slower consumption of monomer. This means that the global growth rate (or total I vs. t curve) across the entire electrode appeared to be a constant and uniform process since current is measured as an average of the entire electrode surface. However, by SEM analysis it was seen that both micro and nano wires had formed throughout by two different processes which could not be differentiated by the growth profiles.

The ability to form homogeneous and reproducible PPyEtCN nanowires was only obtained by employing a sufficiently polished GC electrode. These electrodes, which are constructed to be quite robust and stable, would most likely be used in long term sensing studies due to their cost of fabrication. However, as technology advances, most researchers have adopted to use electrodes known as ‘screen printed electrodes’ or SPE’s. These are plastic electrodes with the working, reference and counter

electrodes printed adjacent to each other in a small area. They are designed to be only used once and then discarded. This removes the need for regular calibration and stability measurements which have to be undertaken for long term use electrodes. These SPE's were purchased with a view to utilising them for growing the PPyEtCN nanowires and applying them in nitrate sensing. Several of the SPE's were analysed for their surface topography using SEM. It was observed that the surface layer of the electrodes were very amorphous and had a very high surface roughness. Therefore, the possibility of using these electrodes to electrodeposit the nanowires could not be undertaken, as highlighted by results from this section. Maintaining the standard epoxy electrodes, the next study was concerned with identifying the effect the concentration of the dopant anions had on the morphology of the nanowires.

3.2.2.2 Influence of Dopant Concentrations

As illustrated in Section 3.2.1.2, the nanowire growth was very sensitive to changes in the concentration of the minor dopant ClO_4^- even though the $H_2PO_4^-$ anion was in large excess in the electrolyte solution. It was found that a minimum concentration of the ClO_4^- anion was required to produce nanowires, which was 0.020 M. As illustrated in Figure 3.13a and 3.13b, any small changes below this concentration resulted in stark differences in morphology of the nanowires. At the lower ClO_4^- concentrations the wires appeared very short and 'curled' throughout the electrode. As the concentration was increased the wires started to straighten and become elongated. While there is no literature precedence for curled wires forming at low concentrations of dopant, some authors have shown that nanostructures can be formed with a helical pattern by employing chiral dopants that are strongly dependant on the ratio of monomer to dopant.[20, 78]

Similarly, $(NH_4)H_2PO_4$ was also seen to have a minimum concentration necessary for uniform nanowire growth. When changing the $H_2PO_4^-$ anion concentration the wires had much less morphological change compared to the ClO_4^- anion. Substantial morphological difference was only observed when the $H_2PO_4^-$ anion concentration was changed in 0.100 M increments. At lower concentrations the wires grew in a small short form with large spacing between each wire, shown in Figure 3.13c. A

critical concentration of 0.200 M was observed to be the minimum amount of phosphate required to form straight standing wires with a favourable aspect ratio, Figure 3.13d. However, at this concentration it was common for inconsistent gaps to form in the polymer at some parts of the electrode as shown in Figure 3.13d inset. At higher concentrations of phosphate (0.300 M) this issue was not apparent and homogeneous wires with reasonably uniform lengths and diameters were formed, Figure 3.12. This highlights the importance of the phosphate anion in the formation of the wires and how it can lead to ordered growth.

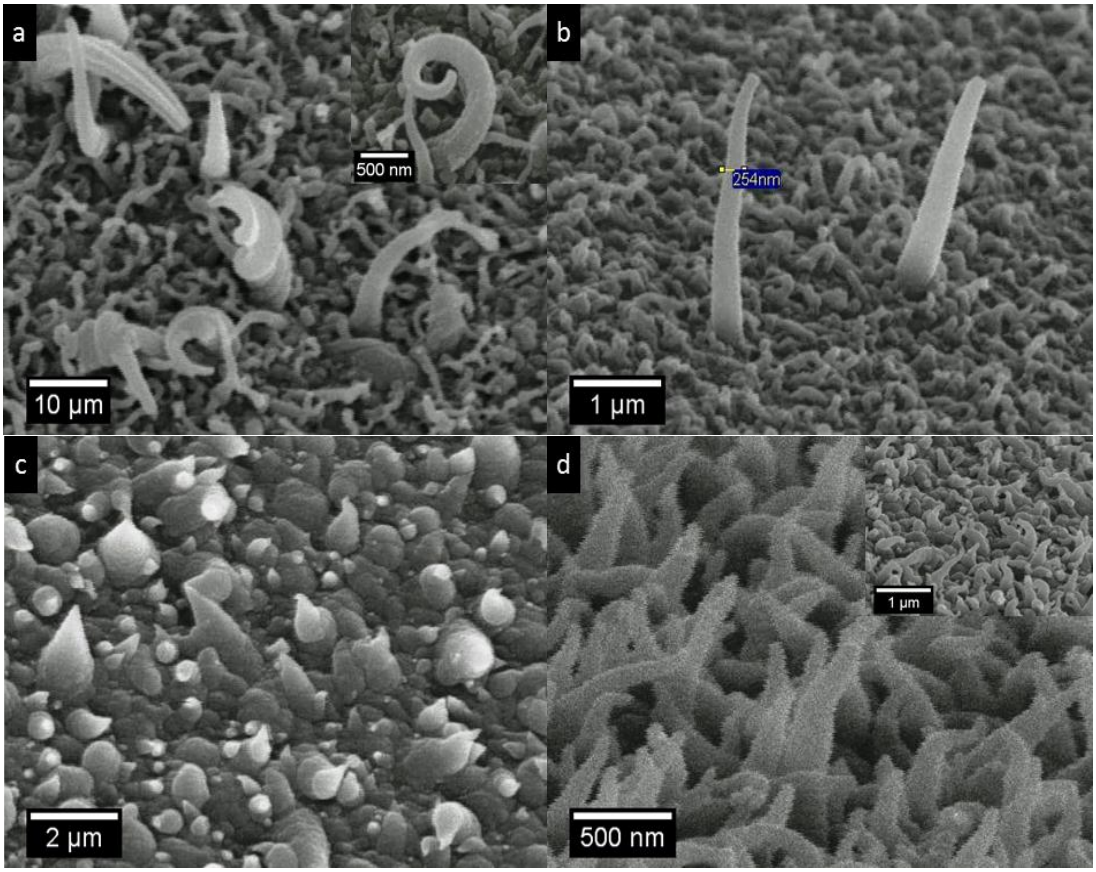

Figure 3.13. SEM micrographs showing PPyEtCN nanowires formed using $LiClO_4$ concentrations of (a) 0.012 M and (b) 0.015 M with 0.300 M $(NH_4)H_2PO_4$ in a water/ethanol (7:3) solution at 0.850 V with 0.075 M monomer. Concentrations of $(NH_4)H_2PO_4$ were changed from (c) 0.100 M and (d) 0.200 M at a concentration of 0.020 M $LiClO_4$.

While it was necessary to use these minimum concentrations of salts to obtain a uniform coverage of nanowires, it was also possible to change the relative ratios of these two components in relation to the monomer. This resulted in a range of

different structures forming and more importantly led to another way of controlling the morphology of the final nanowire film. A series of PPyEtCN films were grown using various amounts of both $LiClO_4$ and $(NH_4)H_2PO_4$ keeping the ratio of monomer constant. Although it is not possible to show all the individual SEM micrograph images, Table 3.3 summarises various ratios used and Figure 3.14 contains some of the respective images. The relative ratio of the salts used and the total excess phosphate compared to the perchlorate anion are displayed. The polymer film was then characterised using SEM and the dimensions of the wires (if any) and the overall coverage of the polymer have been tabulated.

Table 3.3. Polymers grown using different ratios of $LiClO_4$ and $(NH_4)H_2PO_4$ compared to the concentration of PyEtCN. The excess $(NH_4)H_2PO_4$ is tabulated along with resultant polymer dimensions and coverage. SEM micrograph locations A, B, C, D, E and F refer to micrographs in Figure 3.14, while other SEM are specifically located with Figure numbers. All polymers grown in a water/ethanol (7:3) solution at 0.850 V for 1 hour at a GC electrode. Colors blue, orange, green and red signify concentrations of reactants were too low, in the wrong ratio, optimal or too high to produce a uniform coverage of nanowires.

Ratios				Polymer		
PyEtCN	$LiClO_4$	$NH_4H_2PO_4$	Excess Phosphate	Dimension	Coverage	SEM
1	0.26	1.3	x5.0	Micro	Mixed	Fig 12c
1	0.26	2.6	x10.0	Micro	Mixed	A
1	0.26	3.3	x12.5	Nano	Mixed	
1	0.16	4.0	x25.0	Nano	Irregular	Fig 12a
1	0.20	4.0	x20.0	Nano	Irregular	Fig 12b
1	0.26	4.0	x15.4	Nano	Uniform	Fig 11
1	0.53	4.0	x7.5	Nano	Irregular	
1	0.26	5.3	x20.3	Nano	Uniform	B
1	0.26	6.6	25.4	Nano	Mixed	
1	0.53	6.6	12.5	Nano	Uniform	C
1	0.80	6.6	8.2	Nano	Uniform	D
1	1.30	6.6	5.1	Micro	Uniform	E
1	1.06	8.0	7.5	Random	Irregular	
1	0.80	10.6	13.2	Nano	Irregular	F

Table 3.14 gives insight into the role each salt plays in the nanowire formation. When the 'excess phosphate' column is examined with reference to the dimension and coverage of the film, a trend can be observed. A wire morphology with a good uniform coverage was produced over the entire electrode when this value was between 8 and 20, Figure 3.14b, 3.14c and 3.14d, while 15.4 was the optimal value. These idealised conditions are highlighted in green in Table 3.3. In some cases however, having this excess factor between 8 and 20 was not sufficient to produce a nanowire film with good consistency. Highlighted in blue, it was observed that if the $LiClO_4$ or $(NH_4)H_2PO_4$ overall concentration was too low, despite being in the correct ratio, the wires would form incoherently. As a general trend, and highlighted from the first 5 ratios in Table 3.3, when a low concentration of $(NH_4)H_2PO_4$ was used the wires would typically form as microwires, Figure 3.14a, due to the extra availability of perchlorate which is known to produce bulk polymers. Subsequently, nanowires were formed when a low concentration of perchlorate was used with a high excess of phosphate, but the coverage of the wires was patchy and irregular. Shown in orange in Table 3.3, are the experiments which had sufficient starting concentrations of both $LiClO_4$ and $(NH_4)H_2PO_4$ but the ratio of phosphate to perchlorate was not between 8 and 20, the value deemed as 'optimal'.

Similarly, as highlighted in red in Table 3.3, inconsistencies in the polymer formation were observed when the overall concentrations of the salts were excessively high. When a high concentration of phosphate was used or a high excess ratio (above 20), a uniform coverage of wires formed, however in certain sections of the electrode large deposits of polymer resembling pillar like structures were observed, Figure 3.14d and 3.14f inset. Even with a slightly elevated starting amount of phosphate, Figure 3.14d, a low collection of pillars appeared in a limited number of places. Conversely, employing a large starting concentration led to an array of these structures covering the entire electrode as evident in Figure 3.14f. They had a minor resemblance to the ordered microstructures outlined in Section 3.2.2.1 due to the substrate scratch effects, although they did not form in any ordered pattern. Furthermore, these areas were simply not sections which had grown at an accelerated rate but they also took on a new morphology, Figure 3.14f inset. Insoluble salt structures have been observed to produce an alternate morphology in different ratios of the water/ethanol solvent (discussed later in Section 3.2.2.4).

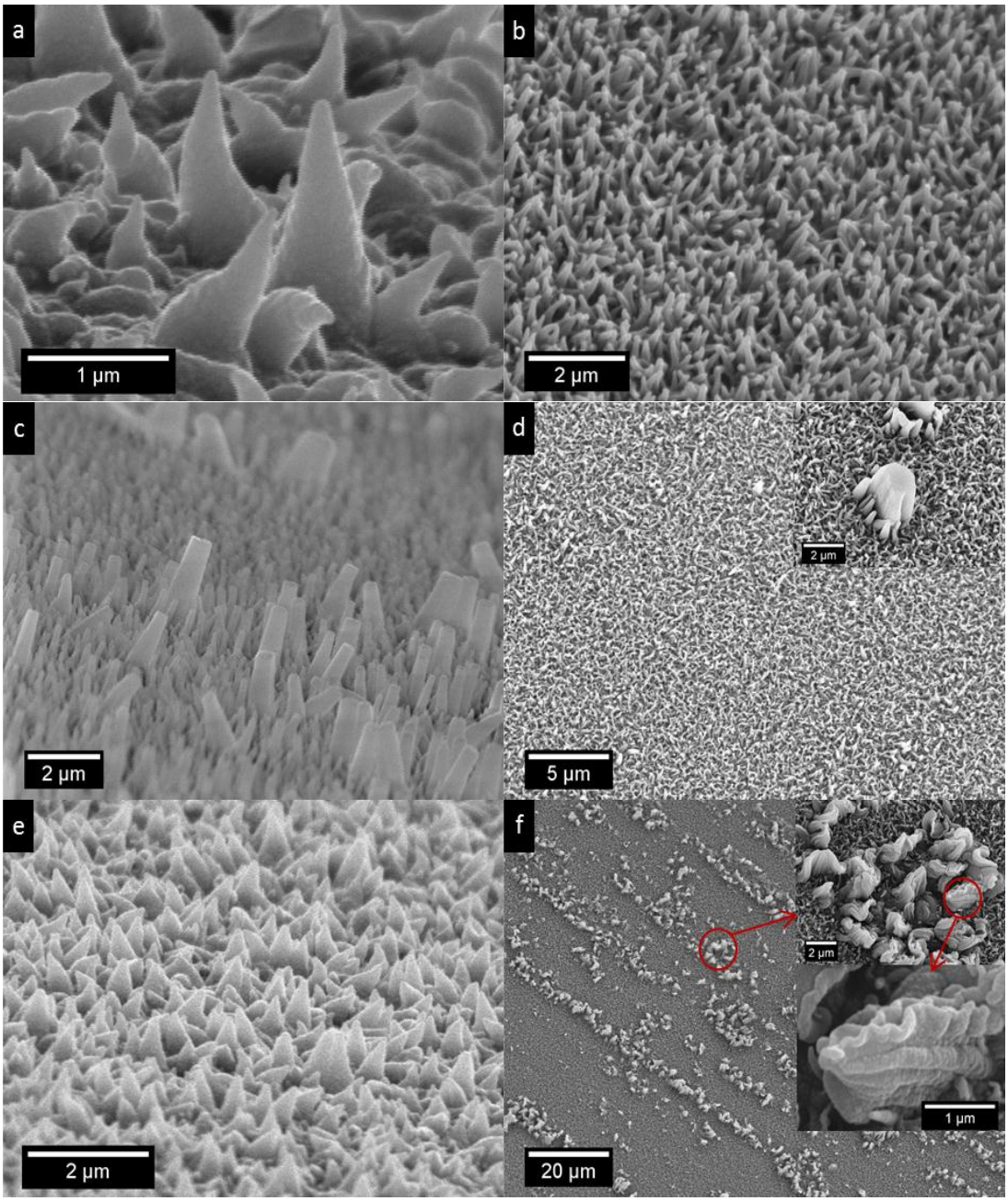

Figure 3.14. SEM micrographs of PPyEtCN polymers grown at 0.850 V for 1 hour in a water/ethanol (7:3) solution, (a) to (f) are the corresponding images from Table 3.3 and were grown at concentrations of $LiClO_4$ and $(NH_4)H_2PO_4$ specified within.

It can be concluded that maintaining the minimum concentrations of $LiClO_4$ (0.020 M) and $(NH_4)H_2PO_4$ (0.300 M) led to polymerisation of the nanowire morphology. Alteration of the dopant ratios in comparison to the monomer also had an impact on the final polymer morphology. It was clear that using concentrations

below these set values produced inconsistent and patchy growth while surpassing them has shown certain particular outcomes:

1) Excess ClO_4^-: greatly increased the probability of producing microwires over nanowires but favorably yields a uniform and homogeneous coverage of the instigated morphology.
2) Excess $H_2PO_4^-$: favors the final wire structures being in the nano dimensions but also introduces large columnar like structures which increase in surface coverage with higher concentrations.

While detailed examination of the ratios of nanowire (either PPy or Polyaniline) dopants has not been observed in the literature, several authors have highlighted the importance of dopant interactions during polymer formation.[12] For the most relevant and extensively studied example, PPy, 20 to 40 mol% of the entire polymer can be made up of dopants.[22] Therefore, it is reasonable to expect that the characteristics and morphology of the resultant polymer film will depend heavily on the nature and concentration of the doping anion in the electrolyte solution. The subsequent size, hydrophobicity and flux of the dopant leads to changes in the porosity and microstructure of the film[58] and also its morphology.[75, 79] The results presented here, for PPyEtCN monomer in the nanowire morphology, further support these reports and highlight the importance of understanding dopant/monomer interactions. Since their solubility was dependent on the composition of the solvent, the polymerisation co-solvent mixture was investigated next.

3.2.2.3 Varying the Co-solvent Mixture

Experiments were performed keeping concentration of monomer and electrolyte salts as described previously for the optimised nanowire growth, but the ratio of water and ethanol (within 10 ml) was altered. Very irregular polymers were formed from water/ethanol (9:1) solutions and water/ethanol (8.5:1) solutions due to solubility problems with the monomer. Interestingly, in the water/ethanol (8:2) solutions the polymer grew as large micro sized grains, Figure 3.15a. The exterior of these grains had crystalline-like shapes protruding through to the surface. In conjunction with

this, in certain areas, crystal like structures had formed on the polymer surface, Figure 3.15b.

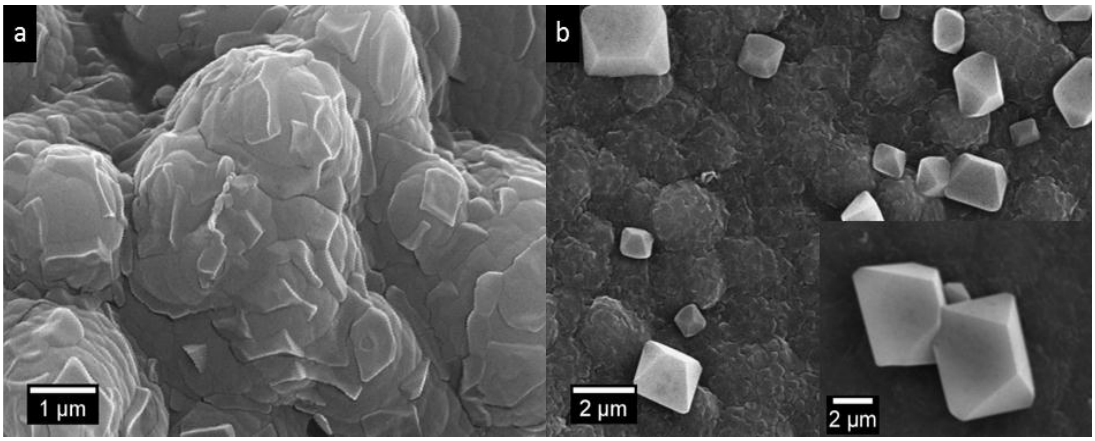

Figure 3.15. SEM micrographs of salt structures imbedded (a) and on top (b) of PPyEtCN polymers grown with 0.020 M $LiClO_4$, 0.300 M $(NH_4)H_2PO_4$ and 0.075 M PyEtCN at 0.850 V in a water/ethanol (8:2) solution.

EDX was used to identify their composition and were compared to a typical EDX of a nanowire polymer (Section 3.2.3.5). These specific crystalline sites had a very strong signal for chlorine, Figure 3.16a. Furthermore, as shown in Figure 3.16b and 3.16c once the electron beam was focused on these structures they visibly decomposed, shrank and collapsed, Figure 3.16d and 3.16e. This has not been observed for any of the other PPyEtCN polymer morphologies and signified that these crystalline structures were composed of hydrated salts.[80] Similar structures have been observed in the literature as a form of potassium salt.[81] Once the electron beam was focused on their exterior the heat from the incident electrons evaporated the water leading to their collapse. Therefore, it was clear that these objects were salt precipitates which had formed inside and on top of the surface of the polymer. This was due to the lower solubility of all components in the water/ethanol (8:2) solution which allowed a high concentration of salts to aggregate near the electrode surface during polymerisation.

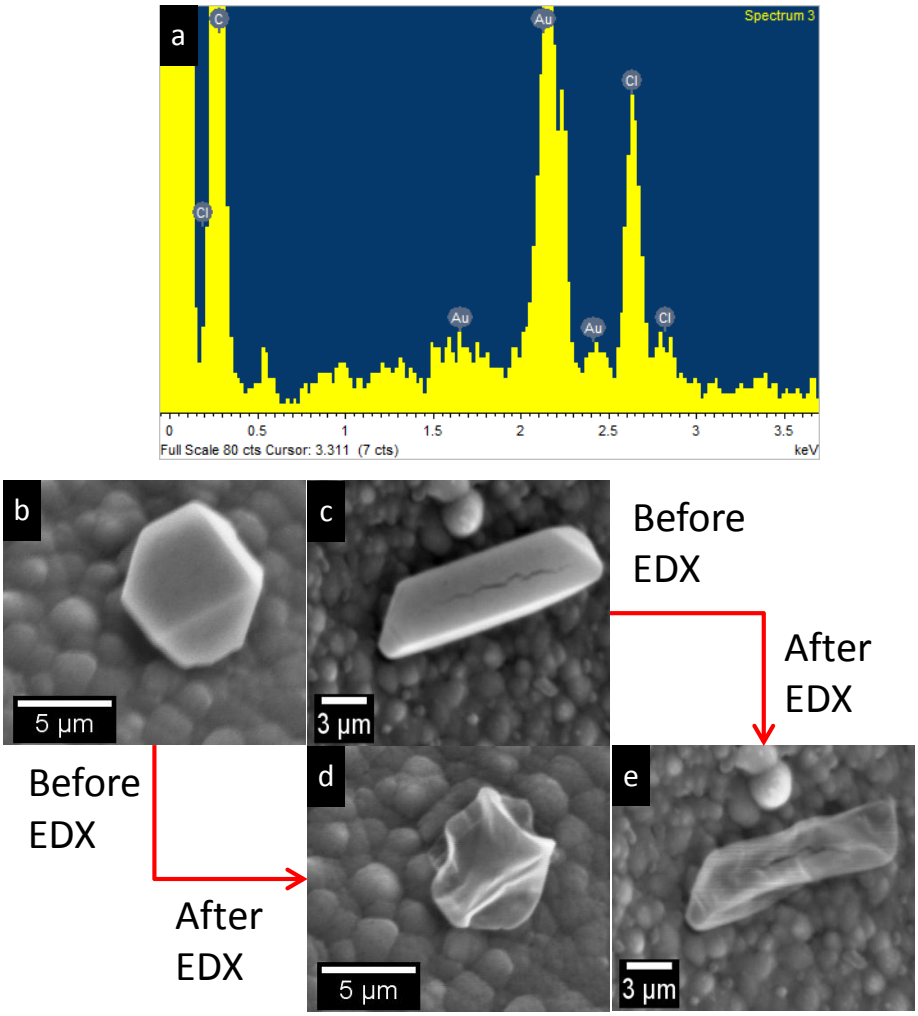

Figure 3.16. EDX spectra of salt structures imbedded in PPyEtCN polymers (a) grown with 0.020 M $LiClO_4$, 0.300 M $(NH_4)H_2PO_4$ and 0.075 M PyEtCN at 0.850 V in a water/ethanol (8:2) solution. Examples of salt structures before (b,c) and after EDX analysis (d,e) showing decomposition.

Reducing the monomer concentration from 0.075 to 0.038 M removed the formation of these salt precipitates in the water/ethanol (8:2) solutions and allowed the solubility of all other components to increase. Polymerisation in this solution produced nanowires which were 3 times longer (~ 3 µm, Figure 3.17a) to those formed in water/ethanol (7:3) solutions. As seen in Figure 3.17b, these nanowires had a tendency to wrap around each other at the tip possibly due to their long length making them less stable standing upright. Moreover, no salt structures were observed at any sites on the electrode confirming that the solubility of all components was maintained. These results highlight that this system is versatile in terms of wire formation as they can be produced at various solvent mixtures as long as each components solubility is maintained, reiterating the discussion in Section 3.2.1.

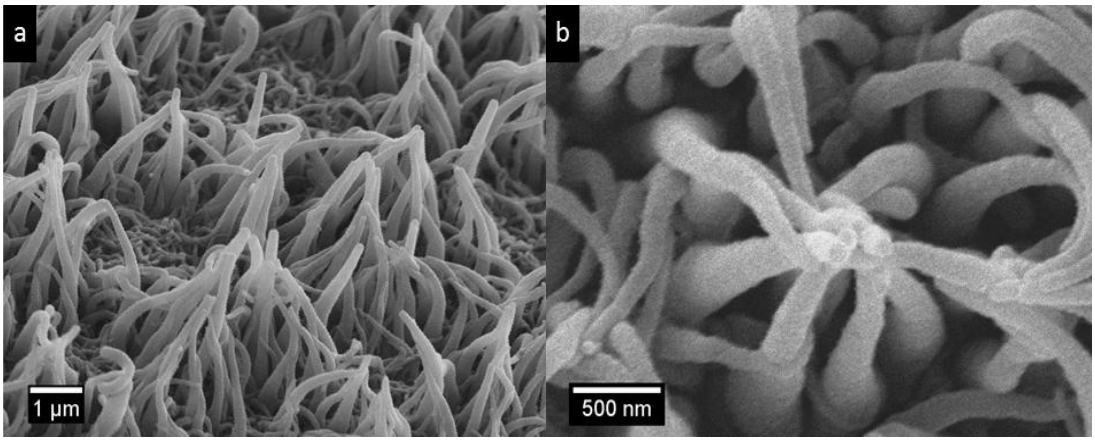

Figure 3.17. SEM images of PPyEtCN polymers grown with 0.020 M $LiClO_4$, 0.300 M $(NH_4)H_2PO_4$ and 0.038 M PyEtCN at 0.850 V in a water/ethanol (8:2) solution, (a) low magnification and (b) high magnification of the nanowire tips.

3.2.2.4 Influence of Polarisation Time

A study was performed to ascertain the effect of growth time on the length and diameter of the wires. FE-SEM micrographs recorded at various growth intervals revealed that both the diameter and length of the wires were easily controlled by varying the electropolymerisation period. As shown in Figure 3.18a, only nodules are evident after 30 s of growth. These indicated the beginning of the wire formation and were seen as circular tips protruding out of a base layer. After 5 min growth, nanowire formation was clearly evident and the wires had increased in length significantly but only become marginally thicker, Figure 3.18c. Finally in Figure 3.18d, long slightly tapered wires were obvious after 60 min of growth. This indicated that the polymerisation had mainly occurred at the tips of the wires, extending their lengths in the vertical direction. This was consistent with the formation of a 1-D structure. Other authors have observed similar trends when growing PPy or polyaniline nanowires by template free methods, with longer polarisation times generally leading to longer wires.[11-12, 29, 31]

Due to the FE-SEM high resolution, the rough nature of the surface of the wires can be seen. This resembles the cauliflower bulk growth which is commonly seen for PPy. By using top down and cross sectional SEM imaging, the diameter and length of the wires were accurately measured and plotted vs. polarisation time, Figure 3.19. To obtain confidence in the reproducibility of the measurements several wires were

measured at five different sites on the electrodes. The results correspond with similar data produced by C. Debiemmie-Chouvy, [12] where she showed a linear relationship between wire length and polarization time. In her paper she did not show data for individual wire diameters but rather set a specific range between 40 to 120 nm.[12] While the data presented here shows an increasing trend for nanowire length after 1200 seconds, it was linear within the same time frame of 700 seconds as reported by the above author. It is obvious from Figure 3.19 that while the length of the wires was greatly altered by growth time, the diameter of the wires varied significantly less with values of between 100 and 150 nm common for growth times increasing from 5 to 60 min.

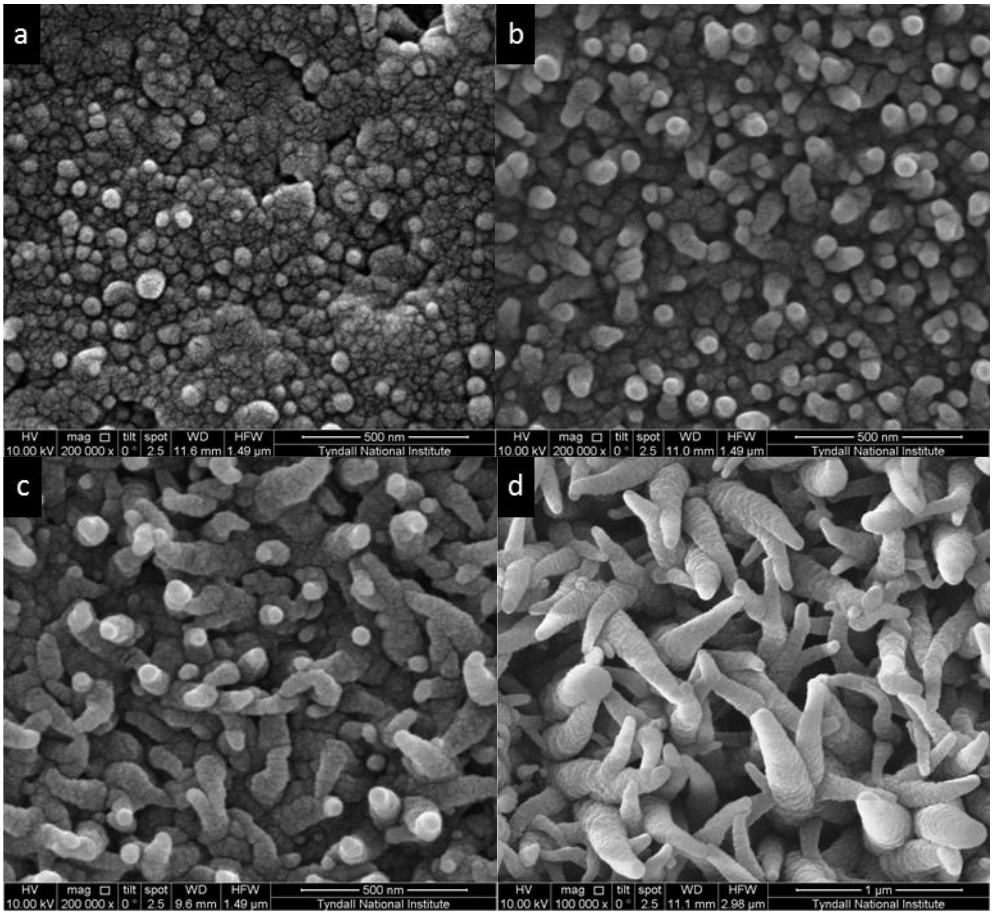

Figure 3.18. FE-SEM micrographs of PPyEtCN nanowires at different growth times of (a) 30 s, (b) 1 min, (c) 5 min and (c) 60 min. Nanowires grown using 0.85 V at a GC electrode with 0.020 M $LiClO_4$ and 0.300 M $(NH_4)H_2PO_4$ in a water/ethanol (7:3) solution.

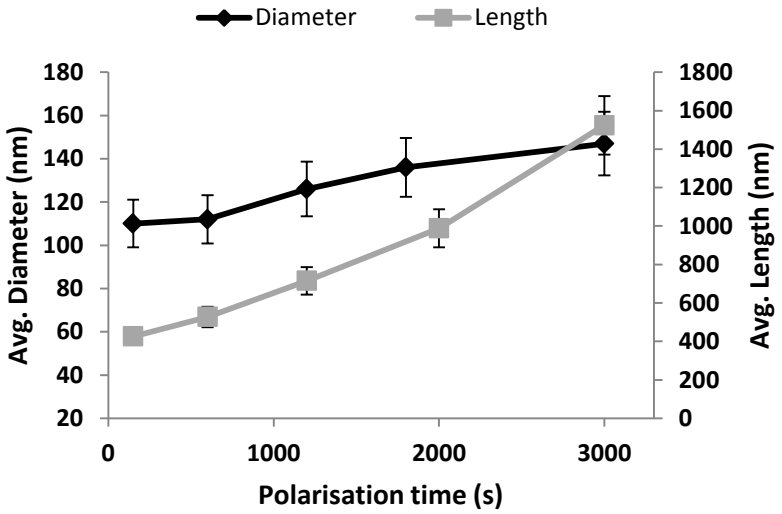

Figure 3.19. Polarisation time vs. average diameter and average length for PPyEtCN nanowires grown using 0.020 M $LiClO_4$, 0.300 M $(NH_4)H_2PO_4$ with 0.075 M PyEtCN in a water/ethanol (7:3) solution.

To understand the various electrochemical processes occurring at these different length nanowires, they were analysed electrochemically by cyclic voltammetry experiments. Typically, CPs undergo oxidation and reduction with the generation of polaron species across the polymer backbone. There is a redox chemistry associated with this as counterions, or dopants, flow from the electrolyte to balance these positively charged polarons.[23] Consumption of this dopant at the electrode generates a diffusion limited peak which increases in magnitude with increasing oxidation of the polymer backbone. A typical CV for PPy contains both an anodic and cathodic peak current due to the influx and expulsion of dopant anions.

The CVs for three different polymers, grown to 0.05, 0.07 and 0.12 mC/Cm^2, are displayed along with their charge transients, Figure 3.20. These charges correspond to polymerisation times of 100, 200 and 300 s respectively. The three profiles are superimposed on each other, Figure 3.20a, highlighting the reproducible nature of the growth process, allowing direct comparison of their CVs. Inspection of the CVs generated by these nanowires in a 0.100 M $LiClO_4$ solution reveals an anodic I_p at ~ 0.400 V which was due to the oxidation of the polymer, Figure 3.20b. For the cathodic I_p however, only a broad peak was observed. This would suggest a sluggish response from the nanowires to the reduction process. It may arise that due to the electrochemical switching of the polymer film being relatively slow at these scan

rates.[23] It was observed that as the thickness of the film was increased the peak shifted to more anodic potentials with an increase in the currents recorded. Since the currents at the oxidation and reduction of the polymer have increased, this would suggest a greater amount of dopant is interacting with the polymer. This may be due to the increased polymerisation time leading to longer nanowires, an observation confirmed by SEM micrographs, Figure 3.18. This suggest the nanowires have a greater surface area and possibly contain more electroactive sites within the polymer film.[23] However, the lack of an increase in capacitance within the polymer at non-faradaic regions (0.000 to 0.200 V), the quasi-reversibility of the redox process and lack of symmetry relating to the anodic and cathodic I_p requires further investigation.

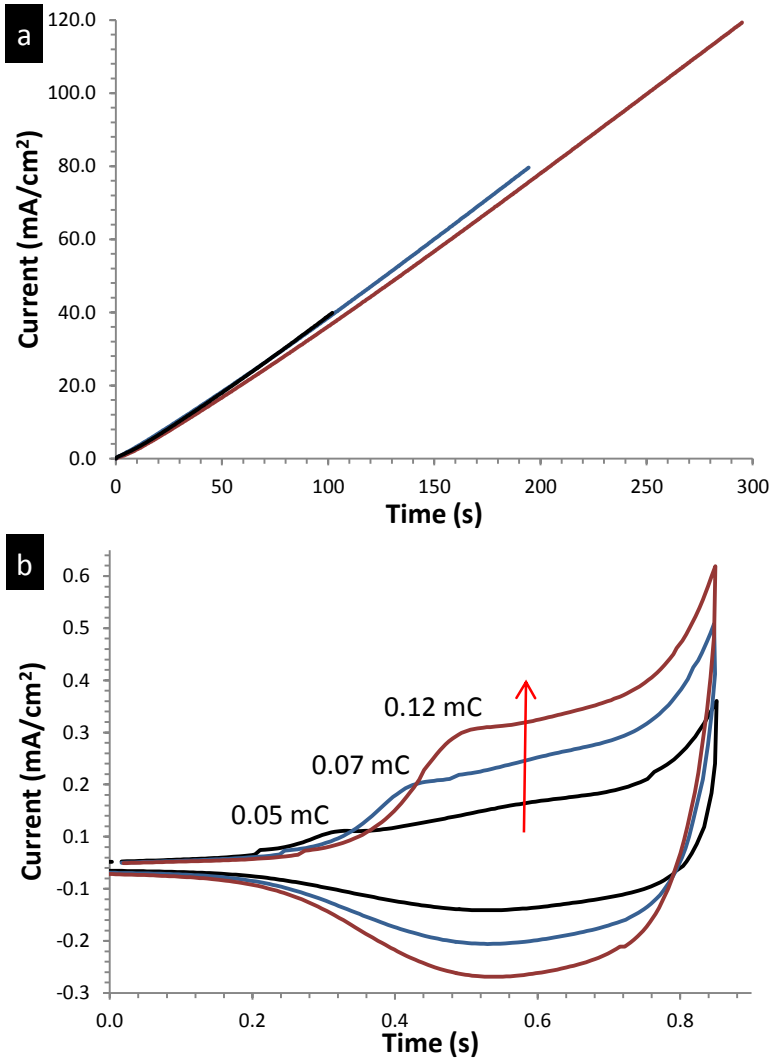

Figure 3.20. PPyEtCN nanowires grown to set charges of 0.05, 0.07 and 0.12 mC/cm^2 (a) and corresponding CVs cycled between 0.00 and 0.850 V at 50 mV/s in 0.10 M $LiClO_4$. Polymers grown 0.020 M $LiClO_4$, 0.300 M $(NH_4)H_2PO_4$ with 0.075 M PyEtCN in a water/ethanol (7:3) solution.

These experiments show that by controlling the polymerisation time it is easy to produce wires of desired lengths. It has clearly been demonstrated that these PPyEtCN nanowires can be controlled with similar accuracy as would be obtained from using a template method. Slight alterations to dopant and monomer concentrations combined with the correct polymerisation potential and time allows for a range of morphologies, diameters and lengths to be acquired. Displaying this level of control was vital for these wires to be useable in a range of applications. Furthermore, in conjunction with these morphological changes, the current response of the nanowires was observed to increase as the wires extended in length from the electrode surface. As the morphology of the nanowires had been successfully controlled, we next attempted to apply modeling equations to predict the nucleation process associated with the nanowires.

3.2.2.5 Modelling Nanowire Growth

Studies have shown that the preliminary stages of electrodeposition of CPs occur via diffusion controlled growth from nucleation sites.[82-83] By using the Sharifiker and Hills models the nucleation of the nanowires can be identified as either instantaneous or progressive in a 2-D or 3-D manner, Chapter 2, Equations 2.2 – 2.5. A typical current-time plot recorded during the electropolymerisation period is shown in Figure 3.21a. Dimensionless $(j/j_{max})^2$ vs. (t/t_{max}) and (j/j_{max}) vs. (t/t_{max}) plots were produced from these data and were compared to the theoretical 2-D and 3-D progressive and instantaneous models.[84] The resulting plots are shown in Figure 3.21b and 3.21c, and it is clear that for the early stages of growth the experimental data are consistent with the 3-D instantaneous phase of growth. Upon repeated experimentation we found that uniform nanowire films were only formed when the early stages of polymer growth followed the 3-D instantaneous growth model. This indicates that determining whether the polymer nanowires, which are 1-D structures, were able to form was determined at the point of nucleation. This would reiterate the discussion in Section 3.2.2.1, which highlights a clean and polished substrate as a prerequisite for successful nanowire polymerisation. A fractal or dirty electrode surface would encourage progressive growth as unequal sites for nucleation would exist.

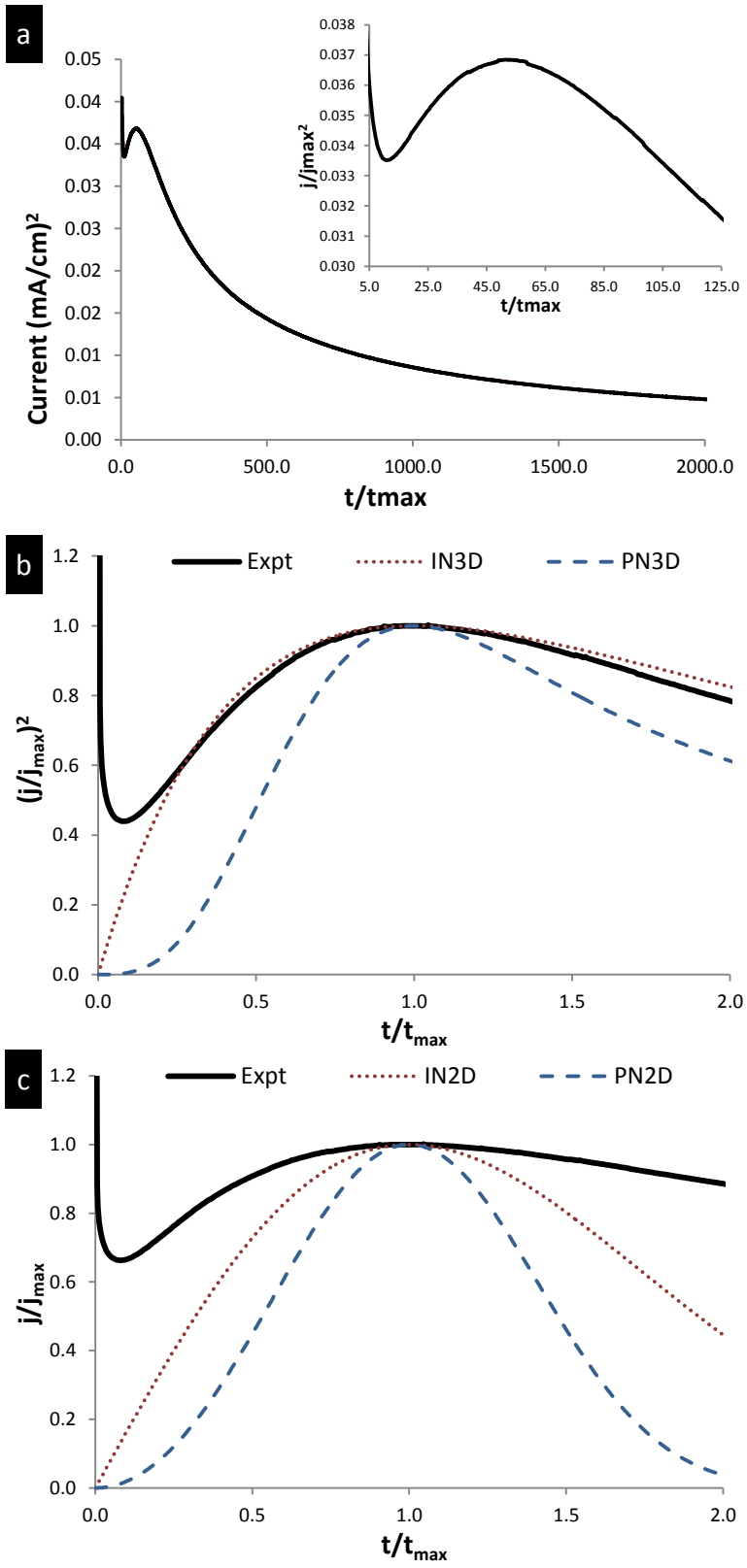

Figure 3.21. A typical current transient for the growth of PPyEtCN nanowires (a) with magnification of the I_p inset. Dimensionless plots of (a) $(j/j_{max})^2$ or (j/j_{max}) vs t/t_{max} compared with (b) 3-D instantaneous nucleation (IN3-D) and progressive nucleation (PN3-D) and (c) 2-D instantaneous nucleation (IN2-D) and progressive nucleation (PN2-D). Nanowires grown in 0.020 M $LiClO_4$, 0.300 M $(NH_4)H_2PO_4$ with 0.075 M PyEtCN in a water/ethanol (7:3) solution.

Cross-sections of the PPyEtCN films were obtained to experimentally verify the modeling results. These were performed by making incisions across the polymer surface using a surgical blade. As shown in Figure 3.22a, it was clear that the wires were attached together at the base by a layer of bulk polymer. It appears the polymer firstly nucleated on the surface in 3-D growth phase to give a bulk-like layer. Eventually this growth was followed by 1-D growth along the z-axis giving the wires extended lengths perpendicular to the substrate. The base layer was confirmed as the first layer of growth as it was present even at relatively shorter polymerisation times (150 s) where it had already reached 100 nm. Even with the longer polymerisation times, while 1-D growth was extending the tips, the base layer continued to grow, but at a slower rate. The layer was measured at ~ 500, 800 and 1150 nm for 15, 30 and 110 min of growth, respectively. The change from the 3-D to 1-D growth phase produced nanowires which had a thick base, as shown in Figure 3.22b. This effect was observed to a greater degree for the larger sized nanowires and was associated with the bulk layer growing.

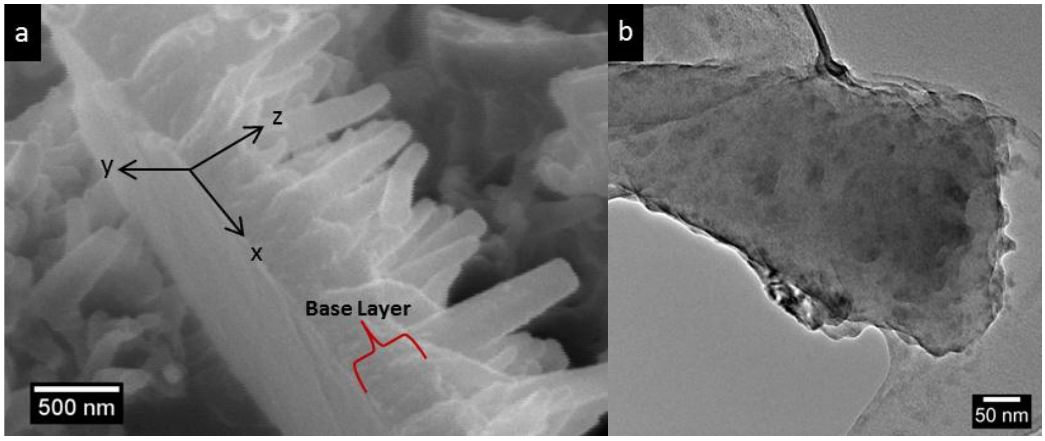

Figure 3.22. PPyEtCN nanowires grown using 0.020 M $LiClO_4$, 0.300 M $(NH_4)H_2PO_4$ with 0.075 M PyEtCN in a water/ethanol (7:3) solution. (a) SEM image of a cross section of a nanowire film showing the base layer, (b) TEM image of the base area of individual nanowire removed from the electrode surface.

The next step in this project was to characterise the chemical composition of the nanowires to confirm that the cyano functional group was intact and that the wires were in fact made of PyEtCN. This was critical to confirming that this was the first electrochemical deposition of PPyEtCN in the nanowire morphology.

3.2.3 Characterisation of the PPyEtCN Nanowires

To characterise the nanowires a number of techniques were employed including FTIR, Raman spectroscopy, TEM and EDX. The first surface characterisation technique employed was vibrational spectroscopy to investigate the cyano functional group and monomer backbone. High resolution TEM data was acquired to identify if the resultant morphology was a homogeneous solid material. Discussion concerning doping levels was revealed through Raman spectroscopy and EDX analysis.

3.2.3.1 Infra-red Spectroscopy

Direct evidence for the presence of the cyano group was obtained using FTIR spectroscopy. The polymer was mechanically removed from the electrode surface and ground into a KBr disk. A typical FTIR spectrum for a PPyEtCN nanowire film can be seen in Figure 3.23 along with a spectra of the PyEtCN monomer. Here the characteristic ν(C≡N) band at 2246 cm^{-1} can be clearly observed in both the monomer and polymer spectra. This band signifies that the cyano moiety has remained intact after polymerisation. The band at 1610 cm^{-1} arises due to the ν(C=C) stretching mode of the Py ring. Other bands observed at lower wavenumbers can be assigned to the phosphate and perchlorate anions which were in the electrolyte mixture. Specifically the band at 1088 cm^{-1} is due to the perchlorate anion favourably doping the polymer backbone over the phosphate anion which may be converted to the neutral phosphoric acid during polymerisation.[85] FTIR spectra were also obtained for both $LiClO_4$ and $(NH_4)H_2PO_4$ to confirm that thier bands were not mistaken for the 2246 cm^{-1} adsoption.

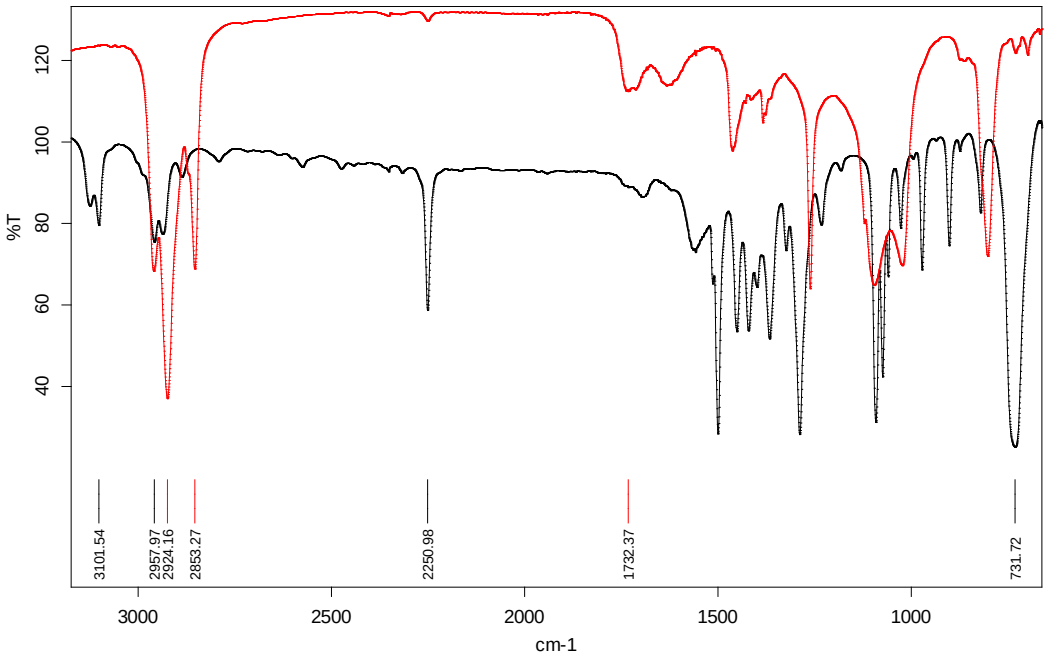

Figure 3.23. FTIR spectrum of PyEtCN monomer (black trace) and PPyEtCN nanowire polymer (red trace) in KBr, grown using 0.020 M $LiClO_4$, 0.300 M $(NH_4)H_2PO_4$ with 0.075 M PyEtCN water/ethanol (7:3) solution.

For the monomer, the strong sharp band observed at 732 cm^{-1} can be assigned to the C-H_α adsorption while the other bands at ~3100 $cm^{-1}$are attributed to aromatic C-H vibrations (both at the α and β positions).[86] This is expected for un-polymerised monomer as both α and β sites should contain a C-H bond, since it is not involved in C-C bonds with other monomer species, Scheme 3.2a. When polymerisation commences these protons are lost typically at the H_α sites, since α–α coupling is favored for the polymer chain conformation.[87] Polymers linked by these couples do not have the H_α band at 732 cm^{-1} present in FTIR spectra. Indeed, this was observed for the PPyEtCN nanowires as shown in Figure 3.23. However, it cannot be ruled out that the polymer linkages are formed by α–β or even β-β linkages producing a polymer with low stereoregularity.[88] This would lead to steric and conformation problems and produce a polymer of lower conductivity.[23, 38] This stems from a decrease in the overlap from π orbitals between the consecutive monomers due to a higher level of disorder in the polymer chains.[89] Interestingly, these linkage defects can generate distortions in adjacent chains leading to further linkage errors. Therefore, the formation of conjugation defects or α-β and β-β linkages at early stages of polymer growth can have a much more detrimental effect on the stereoregularity and stacking of the polymer chains compared to the same defects

occurring at a later stage.[38] This is compounded by the fact that that N-substituted pyrroles have low conductivity due to the steric clashing[90] which reduces planarity, Scheme 3.1. This would explain why PyEtCN has an electrical conductivity which is five times smaller than that of PEDOT.[91] Conversely, one advantage of having an *N*-substituent on the Py monomer is an increased environmental stability. This is due to the electron rich N-atom not coming under attack by oxidants which lead to degradation.[23]

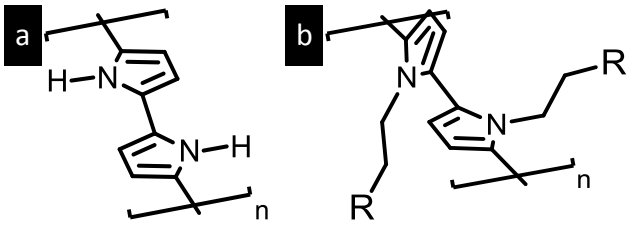

Scheme 3.1. Consecutive π overlap for (a) Py and (b) PyEtCN polymers.

Another explanation for the reduction in conductivity of the PPyEtCN nanowires was due to an incorporation of carbonyl groups at the β-position sites from overoxidation, Scheme 3.2b. Indeed a band was observed at 1708 cm^{-1} for the PPyEtCN nanowires which was indicative of a ν(C=O) stretching mode. Aradilla *et al.*[88, 91] observed a ν(C=O) band in the FTIR of bulk PPyEtCN. They proposed that this signal arose from the conversion of C−H moieties to carbonyls at the β positions of the pyrrole rings disrupting the conjugation of the polymer chains.

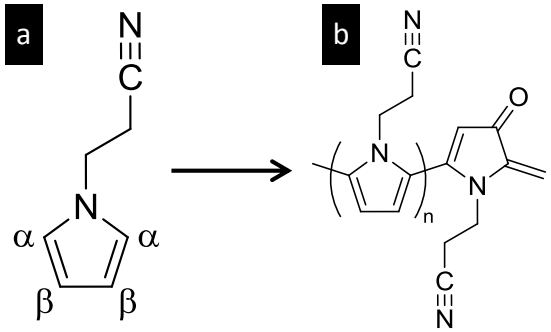

Scheme 3.2. C-H positions on the PyEtCN monomer (a) and polymerised PyEtCN with terminal carbonyl group (b).

This overoxidation process was also observed to occur for the liquid monomer while under ambient conditions without any solvent or electrolyte present. The monomer would turn yellow within 2-3 days if stored in a vial not purged with N_2. Furthermore, it was noticed (by visual inspection) that this process occurred at a much faster rate for PyEtCN compared to the Py monomer. This overoxidation process was confirmed by obtaining liquid IRs of the distilled PyEtCN and an overoxidised PyEtCN sample which had been left out in air for 1 week. The band at 1700 cm^{-1} was much larger for the oxidised monomer due to the C=O terminating groups, while all other bands remained the same (data not shown). It was likely that some of this solution also contained oligomers which had formed due to oxidation. In similar PPy and thiophene systems these oligomers have been shown not to partake in polymerisation as only the monomeric radical cation will initiate propagation,[23, 38] a fact proven by failed attempts to polymerise dimers and trimers of PPy directly. Therefore, the presence of oligomers should be minimised to produce high quality polymer films. The increase in concentration of oxidised groups as explained above highlights the importance of keeping the PyEtCN monomer under N_2 at all times once distilled.

When employing an *N*-substituted monomer it was important to confirm there was no partial loss or conversion of the substituted moiety. The Alemán group observed a small percentage of conversion of their cyano moiety into a nitrile group when chemically polymerising in a solution of $FeCl_3$.[86] Using $LiClO_4$ and an electrochemical approach the same conversion was not observed. Another possible method of conversion was chemical hydrolysis which transforms the cyano moiety into a carboxyl group. Other researchers observed this conversion with 5% KOH at 50 °C for 30 hours with stirring.[92] To ascertain whether our reaction conditions (water/ethanol (7:3) with 0.300 M $(NH_4)H_2PO_4$ and 0.020 M $LiClO_4$ at R.T.) were leading to this conversion, the monomer was added to the electrolyte mixture with stirring and an FTIR was taken over 30 min period in 5 min intervals. There was no decrease in the ν(C≡N) adsorption intensity over time. Moreover, there was no increase in the band at 1732 cm^{-1} which would signify an increase in C=O modes. Based on these experiments, and the fact that the base hydrolysis described above only saw a conversion of cyano to carbonyl of 14%,[92] it was clear that the cyano moiety was maintained at the PPyEtCN nanowires after polymerisation.

3.2.3.2 Transmission Electron Microscopy

SEM micrographs were capable of distinguishing the nanowire morphology from a bulk polymer film. However, there is a possibility that the wires were in fact hollow constructs at the center, either in part or throughout the entire structure. Therefore, it was important to inspect the interior density of the wire morphology on the nanoscale by employing high power TEM. A voltage of 200 kV was used to allow electrons to penetrate through the nanowires and highlight any changes in internal density by means of a contrast difference.[93]

TEM micrographs of different diameter PPyEtCN nanowires are shown in Figure 3.24. In Figure 3.24a and 3.24b, which are low and high magnification of the thinner nanowires, respectively, it can be seen that the entire length of the wires maintain the same contrast. This signifies a uniform density and a solid interior. Further confirmation of the solid character of the wires can be observed in Figure 3.24c. Here it is obvious that the electron beam has penetrated through the entire nanowire as the carbon holder can be seen underneath (highlighted by the red arrows). This means that it is possible for the TEM to distinguish the different internal densities within the nanowires. Furthermore, this micrograph clearly highlights the tapered morphology of the wires which have a much thicker diameter towards their base. This tapering effect was observed to occur to a greater extent for the larger wires and was evidence of the 3-D nucleation which initiated the polymer growth and formed a bulk layer under the wires. This base layer was observed to extend across the entire polymer film. It gave some stability to the nanowires by tethering them to the substrate and interconnecting them. Even after scraping the polymer from the electrode and sonicating it in ethanol for 15 min, small bundles of nanowires were still observable throughout the TEM grid, as shown in Figure 3.24d. The tip ends of the wires had a constant and uniform contrast as discussed previously but the base was a darker contrast. This signifies that the wires are bound at the bottom only due to the higher amount of polymer at this site.[94]

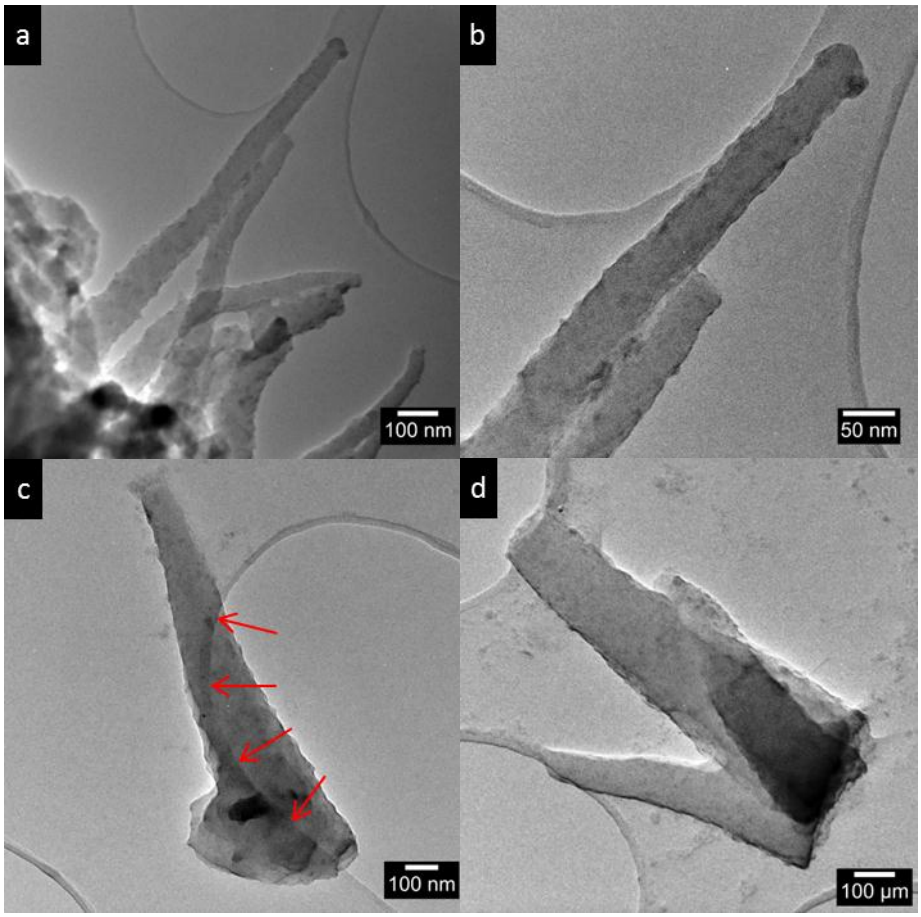

Figure 3.24. TEM micrographs of PPyEtCN nanowires at different diameters. Low and high magnification of a thinner nanowire (a) and (b). A thicker nanowire showing the tapering effect (c) and a bundle of nanowires tethered together (d). Nanowires grown using 0.850 V at a GC electrode with 0.020 M $LiClO_4$ and 0.300 M $(NH_4)H_2PO_4$ in a water/ethanol (7:3) solution.

3.2.3.3 Raman Spectroscopy

Raman spectroscopy is a powerful and unique tool which is capable of providing insight into the chemical structure of CP films. It can reveal information on the electrical properties of CPs by resolving the relative amounts of polaron and bipolaron species present within the polymer chains.[95] It is these charge carriers which lead to conductivity across the polymer backbone.[23] PPy has been extensively studied using Raman techniques, however, to date no Raman spectra have been reported in the literature for polymeric PPyEtCN. Therefore, it was advantageous to compare PPyEtCN and PPy spectra since they both contain Py as the monomer

repeating unit. Any difference between their spectra was then associated with the EtCN substituent and was characteristic of the PPyEtCN polymer.

A PPy polymer was grown using the same co-solvent mixture and oxidising potential as performed for the PPyEtCN, but without the 0.300 M $(NH_4)H_2PO_4$. A bulk morphology was employed as it was the most effective way of obtaining the typical stretching modes apparent for PPy. The Raman spectra of bulk PPy is shown in Figure 3.25. The main spectral bands from Figure 3.25 are tabulated in Table 3.4. These band assignments are comparable to what is commonly reported in the literature for PPy.[72, 89, 96] Furthermore, the Raman spectra for ethanol, $(NH_4)H_2PO_4$ and $LiClO_4$ were compared against the PPy and PPyEtCN Raman spectra to ensure that only the bands associated with the polymers were being investigated. The tabulated bands in Table 3.4 give the most information about the doping state and conjugation length within the polymer. Specifically, the ratio of the ν(C=C) mode at 1589 cm^{-1} and the skeletal band at 1514 cm^{-1} can be used to give a qualitative measure of the conjugation length within the polymer.[89] The 984 and 1053 cm^{-1} C-H deformations arise due to the cation and the 940 and 1083 cm^{-1} dication respectively and indicate the level of polaron and bipolaron species within the polymer.

Table 3.4. Position and assignment of adsorption bands for PPy polymers taken from the literature[72, 97] compared with a bulk PPy polymer grown in 0.100 M $LiClO_4$ from a water/ethanol (7:3)solution.

Position (cm^{-1})		Assignment
PPy Literature	PPy	
1595	1589	C=C stretch
1500	1514	Skeletal band
1380	1379	C-N stretch
1320	1322	Ring stretching
1255	1266	C-H in plane bending
1080	1082	C-H in plane bending DICATION
1050	1053	C-H in plane bending CATION
990	984	Ring deformation CATION
940	940	Ring deformation DICATION

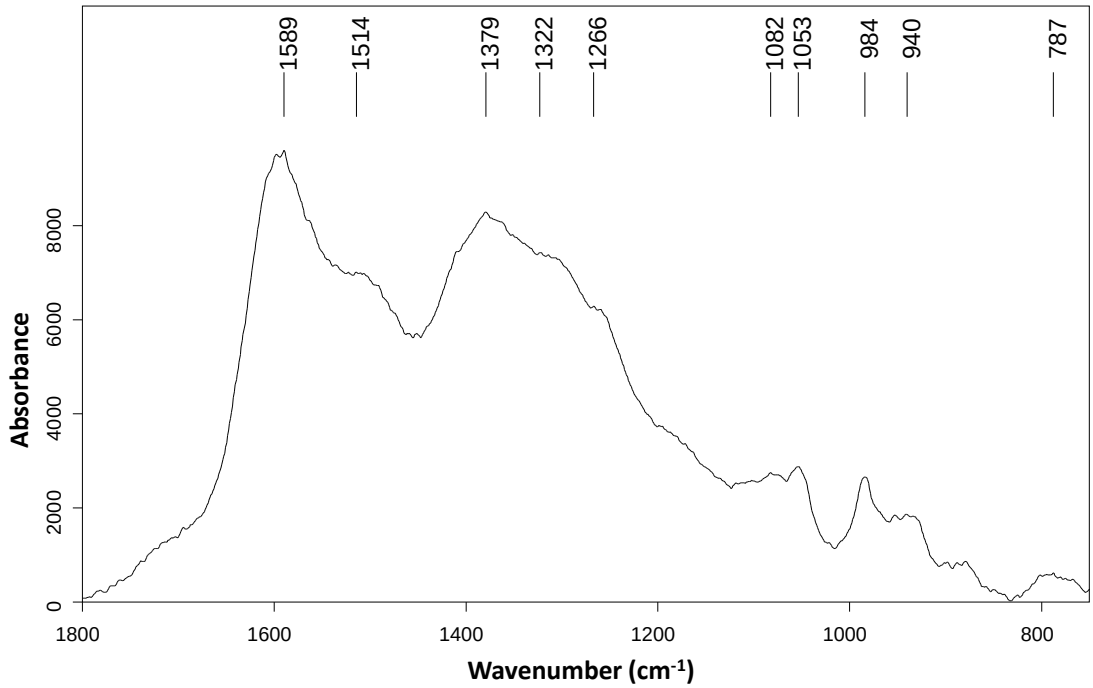

Figure 3.25. Raman spectrum at 660 nm of a PPy bulk polymer grown using at 0.850 V 0.100 M $LiClO_4$ in a water/ethanol (7:3) solution.

It is known that bipolarons are the main charge carriers leading to high levels of conductivity.[23] In Figure 3.25 however, the intensity of the bipolaron signals (940 and 1083 cm^{-1}) for PPy were not as predominant as what is reported in the literature.[72] The 984 and 1053 cm^{-1} C-H deformations due to the cation (polaron) are more intense than the 940 and 1083 cm^{-1}dication bands (bipolaron). Furthermore, the overall intensity of all these bands was weak in relation to the main ν(C=C) band at 1589 cm^{-1}. This suggests that the polymers synthesised in this study (both bulk PPy and PPyEtCN nanowires) had a reasonably lower conductivity compared to what is observed in the literature for PPy. [72, 89, 96] It was apparent that in the systems studied here there was a greater contribution to conductivity from polaron species.

This general decrease in intensity of the 940 – 1080 cm^{-1} bands and lack of bipolaron signal can be attributed to polymerising the monomer in an aqueous solution. This encourages nucleophilic attack leading to overoxidation and has a detrimental effect on polymer conjugation. It has been reported that PPy can lose its conductivity after exposure to an aqueous solution for as little as 0.5 h.[95] In conjunction, since the Raman experiments were performed at the Dublin Institute of Technology or at the Tyndall National Institute, 24 hours after their polymerisation, it is likely their

conductivity would have degraded significantly. This was most likely from residual solvent left within the polymer or from long exposure times to air.

Raman spectra were obtained for the PPyEtCN nanowires and compared to the bulk PPy films, Figure 3.26. It was observed that the PPyEtCN nanowires retain the characteristic bands from 1600 to 1320 cm^{-1} associated with the Py monomer unit from Table 3.4. A new band appeared at 1149 cm^{-1} which was only present in the spectra for the PyEtCN polymers and is most likely associated with the ethyl chain from the cyano moiety.[98] The other main difference was the band at 1707 cm^{-1} which was present due to the overoxidation of the polymer backbone. This has been reported by other authors as an unavoidable process associated with polymerisation of *N*-substituted monomers.[86, 98-99] This finding is consistent with the presence of a band at approximately 1705 cm^{-1} in FTIR spectrum which is indicative of a carbonyl stretching mode.

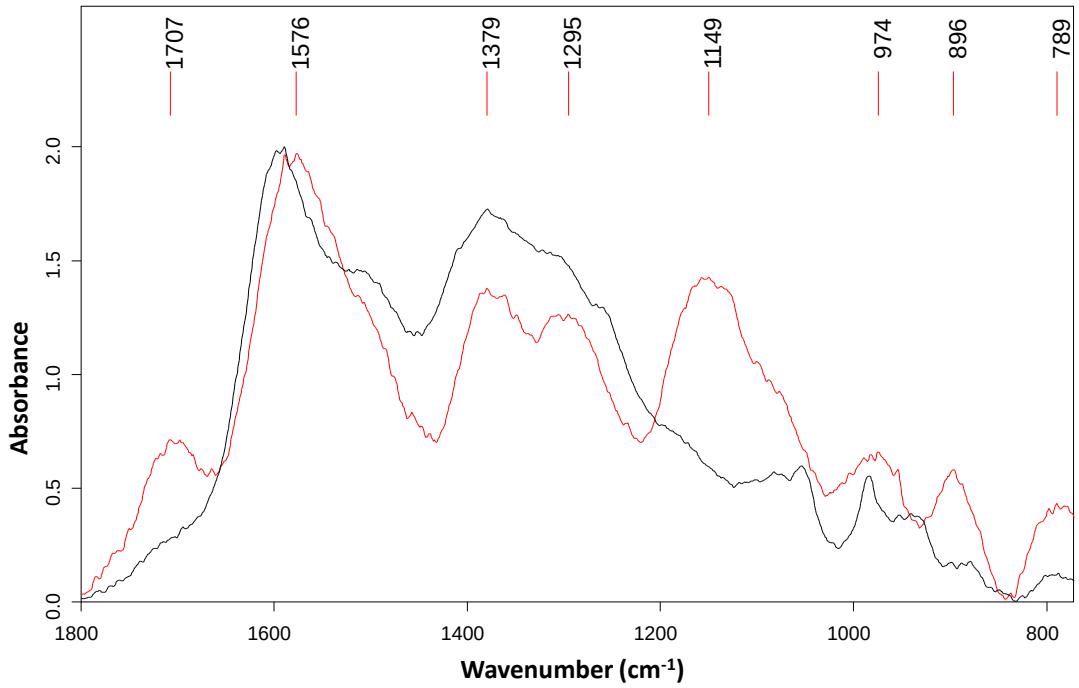

Figure 3.26. Raman spectrum at 660 nm of a PPy bulk polymer grown using at 0.850 V with 0.100 M $LiClO_4$ (Black trace) and PPyEtCN nanowire polymer grown using 0.020 M $LiClO_4$, 0.300 M $(NH_4)H_2PO_4$. with 0.075 M PyEtCN (red trace) in a water/ethanol (7:3) solution.

The bands for the PPyEtCN nanowires and PPy bulk polymers are presented and compared in Table 3.5. In general there was a shift in the frequency of most of the

bands for PPyEtCN nanowires compared to the bulk PPy synthesised under similar conditions, as shown in Table 3.5. As discussed previously the most intense band in the PPy spectrum was the ν(C=C) mode which typically arises in PPy systems at 1595 cm^{-1}.[96] This band is assigned as arising from the ν(C=C) modes of both oxidised and neutral Py units at 1610 and 1550 cm^{-1} respectively.[97] Its position and intensity are of particular interest. Liu and Hwang[95] performed a Raman study identifying oxidised and reduced species within PPy and highlighted that if a PPy film had a lower conductivity the C=C stretching modes would shift to higher frequencies. Tian *et al.*[100] reported similar results. For the PPyEtCN nanowires this band is shifted by 21 wavenumbers to a higher frequency of 1576 cm^{-1}. This signifies a reduced amount of conductivity within the PPyEtCN nanowires compared to the bulk PPy.

Table 3.5. Position and assignment of adsorption bands for PPy (bulk) and PPyEtCN (nanowire) polymers grown in water/ethanol (7:3) solutions. PPy had 0.100 M$LiClO_4$ and PPyEtCN nanowires had 0.020 M $LiClO_4$ and 0.300 M $(NH_4)H_2PO_4$ electrolyte mixture.

Position (cm^{-1})		Assignment
PPy (B)	PPyEtCN (N)	
	1707	C=O stretch
1597	1576	C=C stretch
1514	1499	Skeletal band
1379	1379	C-N stretch
1322	1295	Ring stretching
-	1149	C-H deformation
1266	-	C-H in plane bending
1083	~1075	C-H in plane bending DICATION
1054		C-H in plane bending CATION
984	974	Ring deformation CATION
940	-	Ring deformation DICATION

The lower conductivity of the PPyEtCN nanowires was further highlighted by inspection of bipolaron and polaron species at 940 and 980 cm^{-1}. Again as discussed previously, the PPy polymers displayed both bands, however only one broad band at 974 cm^{-1} was distinguishable in the PPyEtCN nanowire spectrum, Figure 3.26. Furthermore, the bands at 1050 and 1080 cm^{-1} were only observed as a small shoulder at 1075 cm^{-1} due to the strong intensity of the 1153 cm^{-1} band which obscured their identification. The lack of signal due to polaron and bipolaron species has also been observed for PPyMe microspheres produced chemically, these bands (1080cm^{-1} - 1040cm^{-1}, C-H in plane bending) did not appear due to a loss of symmetry associated with the PyMe molecule.[99] The measurement of conductivity from the intensity of the ν(C=C) band to that of the skeletal band at 1503 cm^{-1} were determined to be approximately 2.7 and 2.0 for the PPy and PPyEtCN systems respectively, further confirming the lower degree of conjugation in the PPyEtCN nanowire film. This is to be expected since it is commonly known that PPyEtCN has a much lower conductivity compared to PPy (5.5 x 10^{-3} and 20 S cm^{-1}, respectively).[91, 101]

It is known that addition of substituted groups at a PPy monomer can lead to steric interactions which result in a decrease in the overlap between π orbitals and hence shortens the mean conjugation length.[38] The combination of the high degree of overoxidation combined with the substituted group (the EtCN moiety) means that PPyEtCN nanowires produced may have a significantly lower electrical conductivity compared to conventional CPs studied in the literature (e.g PPy, PEDOT and PANi). These observations were further supported by UV-Vis results (not shown) performed on ITO which only displayed a strong band at 400 nm due to the π-π* transition. There was also only a weak band for the polaron excitation at 550 nm and no 'free carrier tail' (> 800 nm) associated with bipolaron generation, despite the clear electrochromic properties observed by optical microscope. As shown in Figure 3.27 the polymers were observed to transform from green (undoped) to red/yellow (doped) with increasing potential from 0.750 to 0.950 V, Figure 3.27a and 3.27b respectively. This trend could not be followed by UV-Vis at ITO electrodes due to the thinner nature of polymer required for light to transmit through the sample.

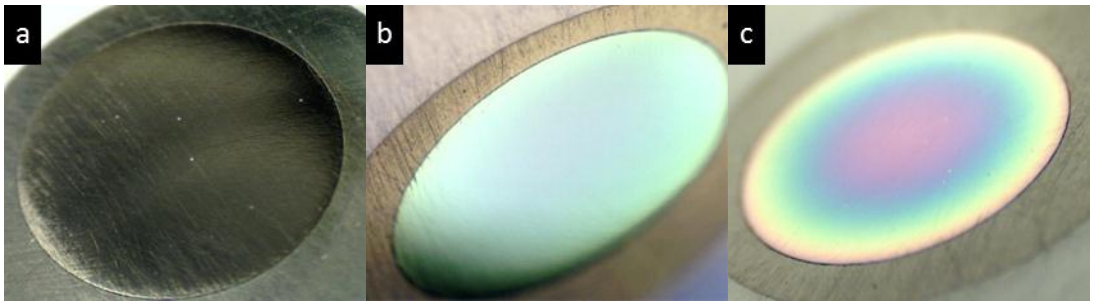

Figure 3.27. Optical microscope images of a bare GC electrode with no polymer (a) and GC electrodes with PPyEtCN nanowire polymers grown using 0.020 M $LiClO_4$, 0.300 M $(NH_4)H_2PO_4$ with 0.075 M PyEtCN in a water/ethanol (7:3) solution at 0.750 V (b) and 0.950 V (c).

3.2.3.3.1 Changing Laser Excitation

Since the PPyEtCN nanowires and PPy bulk polymer showed poor resolution for the polaron and bipolaron bands, attempts were made to increase the intensity of these Raman bands to gain more information about the polymer doping levels. Raman frequencies are not a function of the excitation source, however the resonance conditions of particular structures can become more dominant and shift to slightly different frequencies by changing the excitation wavelength.[102] In an attempt to resonate the bands associated with the polaron and bipolaron species two other laser wavelengths, 473 and 785 nm, were investigated along with the 660 nm already discussed.

When using the 473 nm laser line the resultant spectrum had very little intensity in the bands apart from the main C=C stretch, Figure 3.28. There were no signs of any resonance effects on any of the oxidised bands. The spectrum was void of any noticeable bands after ~ 1200 cm^{-1}, this means the polaron and bipolaron C-H in plane deformations were not identifiable. A similar decrease in intensity of the 940 – 1080 cm^{-1} region has been observed by Chen *et al.*[97] when using low wavelength excitation (514 nm) for examining PPy polymers. In their study they noticed that the 1080 cm^{-1} band was only a weak shoulder of the 1050 cm^{-1} band. Furthermore, this excitation did not display any changes in intensity of the polaron and bipolaron bands as the doping level increased. They concluded that the 514 nm was a very ineffective laser excitation for studying the doping levels within PPy.

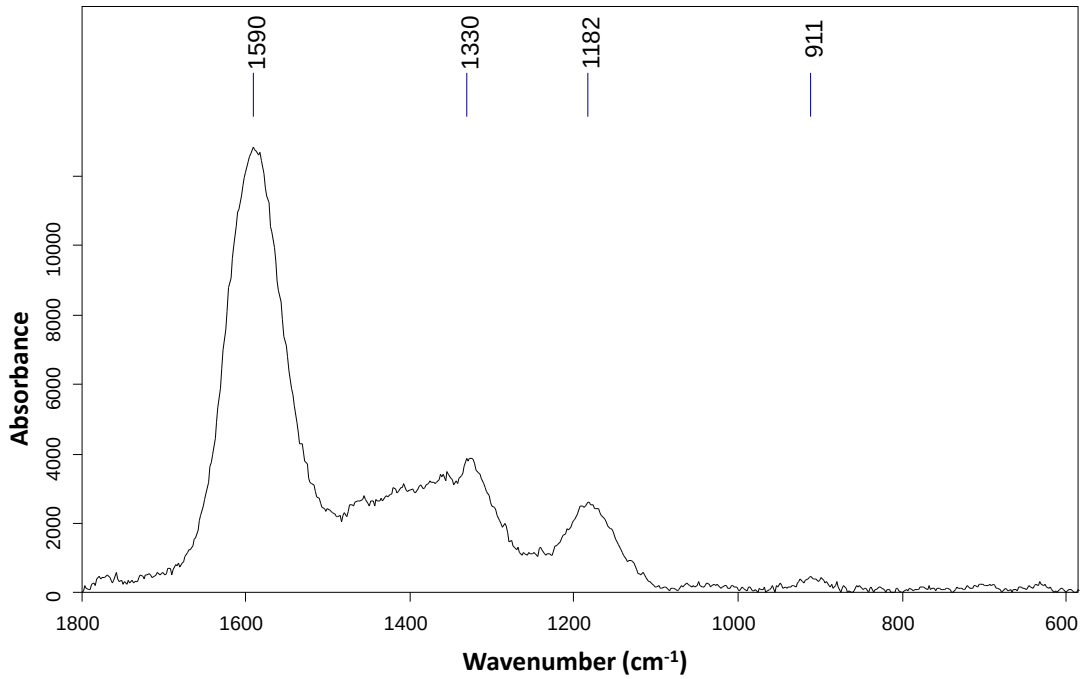

Figure 3.28. Raman spectrum of a PPyEtCN at 473 nm grown at 0.850 V using 0.020 M $LiClO_4$, 0.300 M $(NH_4)H_2PO_4$ with 0.075 M PyEtCN in a water/ethanol (7:3) solution.

Although the 473 nm excitation did not resonate any bands in the PPyEtCN nanowires, there were noticeable differences observed when using the 785 nm excitation wavelength. The polaron and bipolaron bands which are covered by the intense band at 1149 cm^{-1} in the 660 nm excitation could be more easily identified, as shown in Figure 3.29. A weak shoulder band in the region of 1073 cm^{-1} was present for the C-H deformation of the dication while 1040 cm^{-1} band associated with the cation was also observable. The other bands associated with the ring deformation were still only observed as a small band at ~950 cm^{-1}. These results were more resolved than the 660 nm excitation results discussed previously, implying the 785 nm laser line was more appropriate for revealing information about the conductivity within the PPyEtCN. This has also been observed by Chen *et al.*[97] where they saw an increase in resolution for the C-H deformation when using the high wavelength laser excitation (785 nm). The benefits of using the higher wavelength excitation can be observed from Figure 3.30, where the 785, 660 and 473 nm spectra for PPyEtCN nanowires are compared. When a GC electrode was employed for the Raman studies the spectra did not show any information for the polaron or bipolaron species. Using this substrate, studies were performed to see if employing surface enhanced Raman

scattering (SERS) could increase the detail observed in the Raman spectra for PPyEtCN nanowires. This is discussed in the next section.

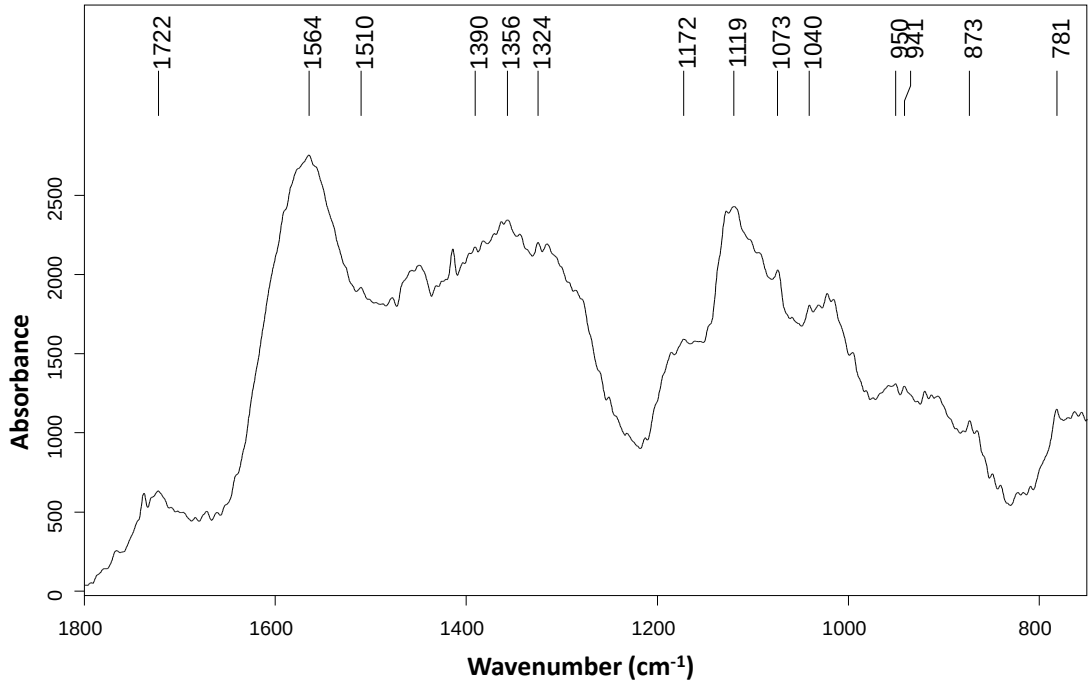

Figure 3.29. Raman spectrum of a PPyEtCN at 785 nm grown at 0.850 V using 0.020 M $LiClO_4$, 0.300 M $(NH_4)H_2PO_4$ with 0.075 M PyEtCN in a water/ethanol (7:3) solution.

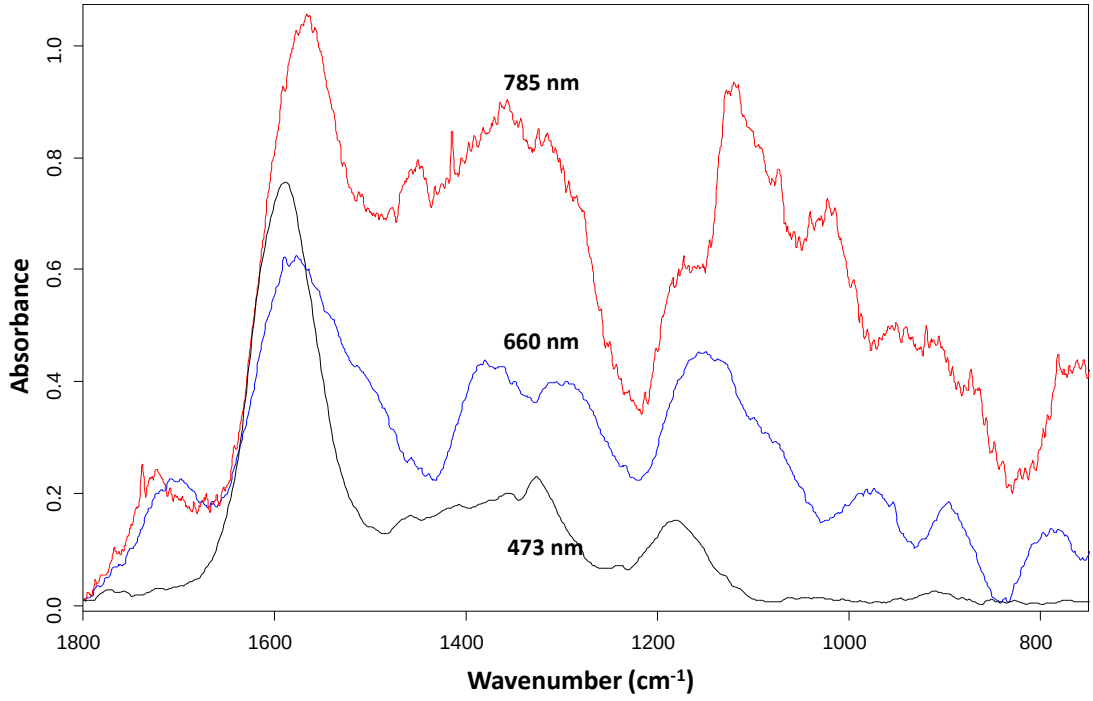

Figure 3.30. Raman spectrum of a PPyEtCN at 785 nm grown at 0.850 V using 0.020 M $LiClO_4$, 0.300 M $(NH_4)H_2PO_4$ with 0.075 M PyEtCN in a water/ethanol (7:3) solution.

3.2.3.3.2 Surface Enhanced Raman Scattering

Most authors performing Raman spectroscopy on CPs take advantage of surface enhanced Raman scattering (SERS) effects.[95, 97, 103-104] This significantly increases the signal intensity compared to a typical Raman spectrum by up to 300 times,[105] in some cases without SERS no spectrum bands due to the cation and dication are identifiable.[106] The enhancement has been ascribed to either an electromagnetic effect or a chemical effect, with the former being more understood.[105] The mechanism of the electromagnetic SERS enhancement is due to plasmon resonance on the surface of a metal which strengthen the local electric field.[107] This effect has been seen for roughened metal surfaces and for electrochemically or spray deposited metal nanoparticles. It arises in small metal nanoparticles when an oscillating electric field causes the conduction electrons to oscillate coherently as an electron cloud.[108] Large clusters of particles have been observed to give the greatest enhancement.[109]

The most common and simple method of employing SERS for the study of CPs is to use a gold substrate which has been roughened by oxidation-reduction cycles (ORC). As described previously, since our nanowires were very sensitive to the surface preparation it was difficult to form them reproducibly on a roughened surface, particularly on metals like Au or Pt. Irregular polymer growth of microwires occurred on surfaces not perfectly smooth. Chen *et al.*[97] also found that PPy deposited on a rough electrode was more irregular and porous compared to the compact smooth polymer deposits on polished electrodes. For this reason they avoided using substrates prepared for SERS. Liu *et al.*[106] reported that the SERS effect was generated at the interface of the Au substrate and polymer deposited on it. Once a thick amount of polymer was deposited on the substrate the Raman signal came from the bulk of the polymer and not from the interface, i.e. no SERS effect was obtained. In their Raman experiments with PPy they noticed a decrease in their SERS enhancement when the charge passed during polymer deposition exceeded 10 mC/cm^2. In our PPyEtCN experiments, for a typical 5 min polymerisation, the charge density passed was ~131 mC/cm^2. It is known that there is a direct relationship between increasing thickness and charge passed.[23] Since this thickness was required to generate reasonably long nanowires, it was unlikely that a substrate SERS effect

would be obtained using a substrate prepared by ORC as the nanowire polymers would be too thick.

As was described previously a GC substrate was employed to produce the PPyEtCN nanowires which allowed them to polymerise in a uniform fashion. Unfortunately, for the Raman analysis it became clear that the GC electrode was not an ideal candidate for use as a substrate material. The intensity of the spectrum peaks were very low compared to experiments performed on Pt or Au. Furthermore, a bare polished GC electrode has two strong bands at 1590 and 1360 cm^{-1} which makes it difficult to identify bands from the polymer close to these wavenumbers.[110] These strong bands were observed for the PPyEtCN nanowires grown on GC electrodes at the 473, 600 and 785 nm laser excitations which obscured other bands from being identified (data not shown).

In an attempt to gain more information from the Raman spectra at a GC substrate and to investigate the SERS effect, gold nanoparticles (Au NP) were added to the surface of the PPyEtCN nanowires by pipette and allowed to dry. The Au NP used were 100 - 200 nm in diameter and were citrate stabilised. The Raman spectrum of PyEtCN nanowires on a GC substrate with and without Au NPs can be seen in Figure 3.31. It was observed that adding the Au NPs onto the surface had a marked increase on the intensity of the bands above 800 cm^{-1}. The (C=C) band at 1595 cm^{-1} and the skeletal band have a much greater intensity and were more pronounced. This could be due to a SERS interaction of the NPs with the polymer as described above, or from a reduction of fluorescence leading to lower background signal. [111] In either case it is clear from the preliminary SERS results that to obtain high intesnsity Raman spectra using a GC electrode, that SERS is an effective tool for exposing Raman bands over the background signal.

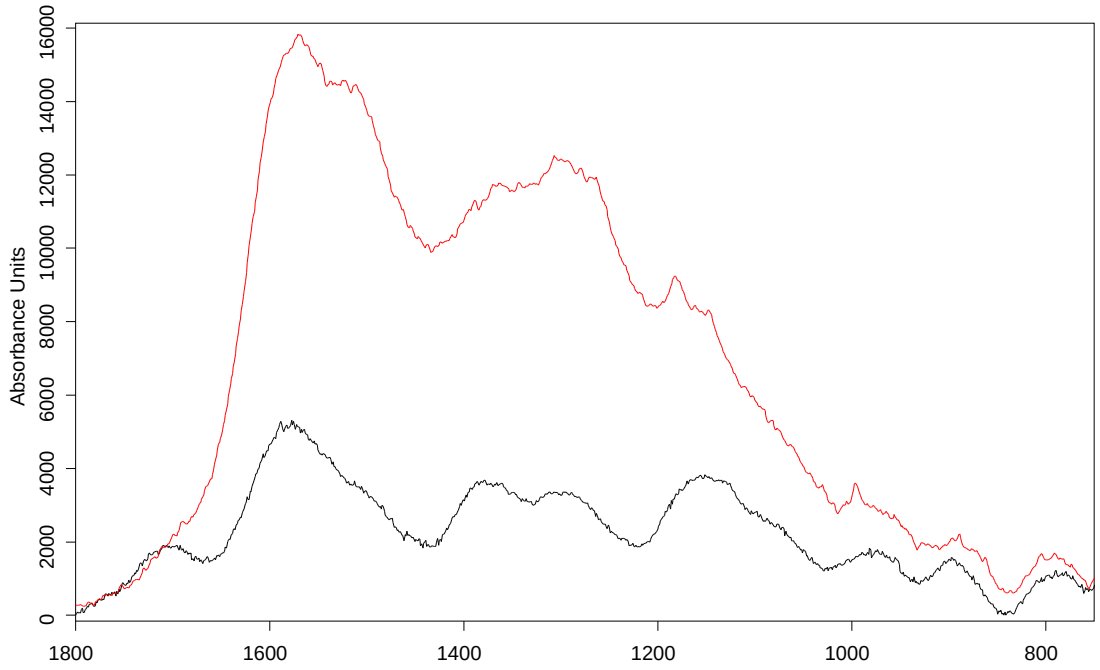

Figure 3.31. Raman spectrum of a PPyEtCN at 785 nm grown at 0.850 V using 0.020 M $LiClO_4$, 0.300 M $(NH_4)H_2PO_4$ with 0.075 M PyEtCN in a water/ethanol (7:3) solution.

3.2.3.4 Energy Dispersive X-Ray spectroscopy

The Raman results highlighted that the PPyEtCN was in an oxidised state with some polaron character. These polaron sites on the polymer backbone would be balanced by a dopant from the electrolyte solution. EDX analysis was performed to identify which of the salts in the polymerisation mixture was present in the polymer matrix.

The EDX analysis of a PPyEtCN nanowire film, Figure 3.32, revealed elemental signals for chlorine at *ca.* 2.6 and *ca.* 2.8 keV confirming the presence of perchlorate anion as dopant within the nanowire film. Elemental signals for phosphorus were observed at *ca.* 2.0 and *ca.* 2.2 keV. The phosphorus signals confirm that a certain amount of dihydrogen phosphate anion was also incorporated into the nanowire matrix during the electrochemical deposition of the nanowire film. This suggests that both ClO_4^- and $H_2PO_4^-$ were doping the polymer during polymerisation. The Au and Pd peaks are present due to the sputter coated layer added to the polymer surface to reduce charging effects.

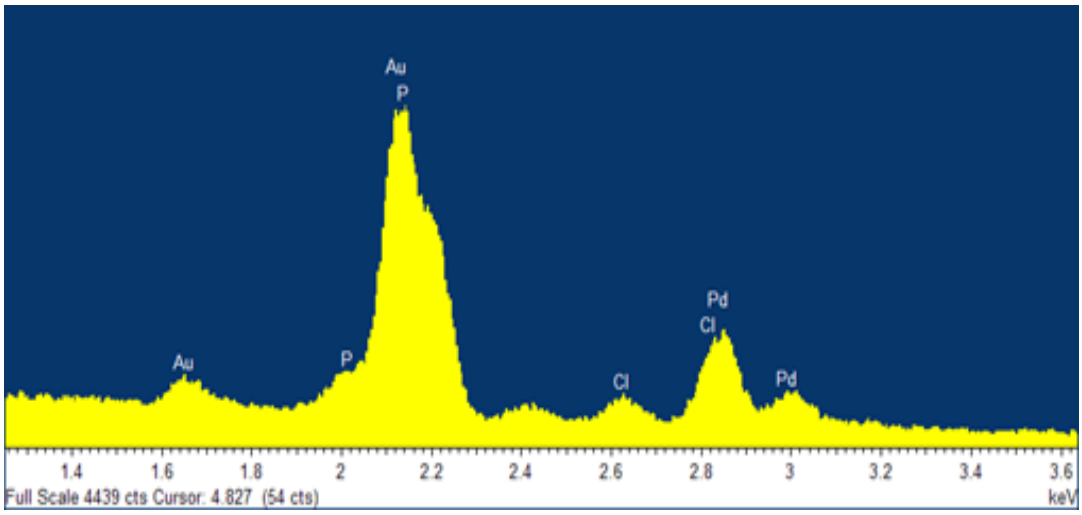

Figure 3.32. EDX spectrum of a PPyEtCN grown at 0.850 V using 0.020 M $LiClO_4$, 0.300 M $(NH_4)H_2PO_4$ with 0.075 M PyEtCN in a water/ethanol (7:3) solution.

To investigate the evolution of the doping mechanism in the nanowires films over time, the amount of elemental chlorine and phosphorous were analysed at polymerisation times of 5 and 30 min. Five sites on the electrode were examined to give an average value. This was important as elevated readings for one particular ion can predominate over the other at certain sites. This can be explained by CPs having islands of conjugated and doped areas in high and low concentration throughout the polymer, which was reported for simple bulk PPy.[23] In the more complicated nanowire system studied here it was possible that this process was also occurring. As shown in Figure 3.33, when the nanowires were analysed by EDX after 5 min polymerisation the atomic amount of chlorine and phosphorous were 0.56 and 0.31%, respectively. This corresponds to a ratio of approximately 1.8:1 Cl:P for the 5 min growth. Since the $H_2PO_4^-$ is in a large excess to the ClO_4 this result may be unusual. However, it can be explained by the possibility that during polymer growth that the neutral phosphoric acid was produced which would not partake in doping. This will be discussed in detail in Chapter 4.

At 30 min growth however, the atomic values for chlorine and phosphorous were 0.62 and 2.05% respectively. This signified a much greater content of phosphorous, at 1:3.3 Cl:P. This means that ClO_4^- favorably dopes the PPyEtCN nanowires in the early stages of growth since there was 15 times more $H_2PO_4^-$ in the electrolyte mixture, yet double the amount of ClO_4^- incorporated into the polymer. It was most likely that this small concentration (0.020 M) of ClO_4^- was eventually consumed to a

greater extent at the electrode surface (compared to the 0.300 M phosphate). This would leave a much greater amount of $H_2PO_4^-$ left in solution to dope the polymer or possibly become entrapped depending on the charged state it was in. This explains the higher phosphorous content in the EDX at the 30 min polymerisation. It was observed in both cases that there was always a higher content of oxygen present. This was to be expected as a combination of dopant, overoxidation sites and entrapped solvent leads to this high elemental percentage. Therefore, while ClO_4^- was the preferred dopant it was not the main contributor to overall doping level due to its lower concentration compared to the $H_2PO_4^-$ anion. It was also possible that during polymer growth that the neutral phosphoric acid would be trapped within the polymer matrix as it propagated. Again these hypotheses are discussed in greater detail in Chapter 4.

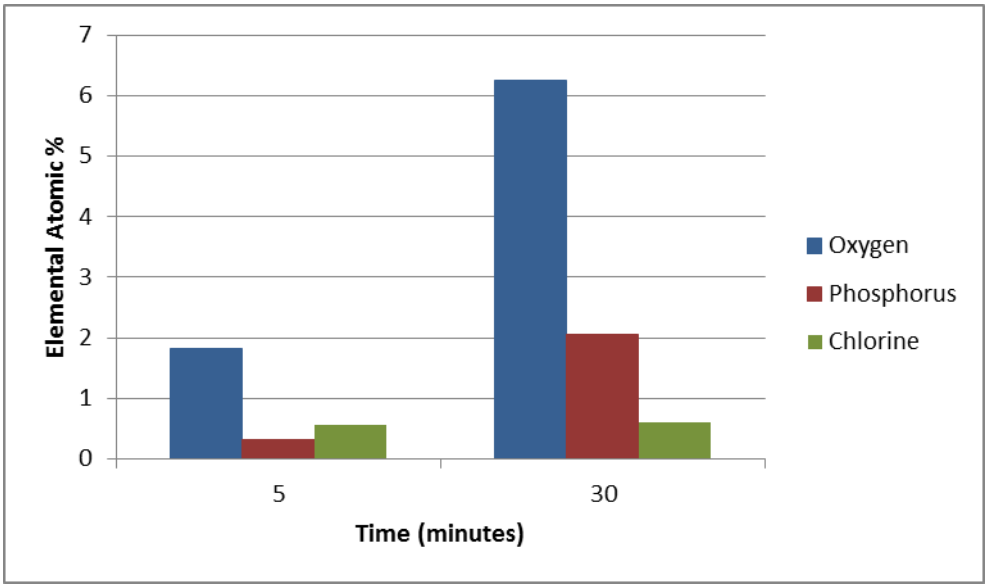

Figure 3.33. EDX spectrum recorded of a PPyEtCN nanowires after 5 and 30 min growth at 0.850 V using 0.020 M $LiClO_4$, 0.300 M $(NH_4)H_2PO_4$ with 0.075 M PyEtCN in water/ethanol (7:3) water solution.

3.3 Conclusion

A one step electrochemical deposition method for the formation of novel PPyEtCN nanowire films was developed. The processibility problems associated with the PyEtCN monomer were overcome by using a mixed solvent system comprised of water and ethanol in a 7:3 ratio. This allowed for the solubility of the monomer and doping salts to be maintained. The effect of the solvent mixture, substrate, polarisation time and type and concentration of the dopant salts were investigated to ascertain their effect on the nanowire morphology. By changing these parameters a high level of control was achieved over the resultant nanowire morphology, while employing a template free method. Electrochemical measurements revealed the nanowires were electroactive and showed an increased current response as the length of the nanowires increased.

The initial growth of the nanowires was observed to follow a 3-D instantaneous nucleation and growth model, leading to a uniform polymer film with a near homogeneous nanowire length. Due to this nucleation phase the nanowires were bound together, and to the substrate, by a base layer. TEM analysis confirmed the nanowires were solid tapered materials while Infra-red spectroscopy was used to identify that the cyano moiety remained intact once the nanowires were formed.

Raman spectroscopy characterised the repeating Py units in the polymer backbone and gave a complete picture of the chemical state of the formed nanowires. The data was consistent with the conjugation length in the PPyEtCN nanowires being relatively short with charge carriers predominantly comprised of polaron species. Dopant information was obtained from EDX measurements where it was observed that even though the ClO_4^- was the preferred dopant it was not observed in large quantities in the polymer due to the excess of $H_2PO_4^-$ in solution.

3.4 References

1. Johanson, U.; Marandi, M.; Tamm, T.; Tamm, J. *Electrochim. Acta* **2005,** *50*, 1523-1528.
2. Dziewoński, P. M.; Grzeszczuk, M. *J. Phys. Chem. B* **2010,** *114*, 7158-7171.
3. George, P. M.; Lyckman, A. W.; LaVan, D. A.; Hegde, A.; Leung, Y.; Avasare, R.; Testa, C.; Alexander, P. M.; Langer, R.; Sur, M. *Biomaterials* **2005,** *26*, 3511-3519.
4. Nie, G.; Zhang, Y.; Guo, Q.; Zhang, S. *Sens. Actuators, B* **2009,** *139*, 592-597.
5. Peng, H.; Soeller, C.; Vigar, N.; Kilmartin, P. A.; Cannell, M. B.; Bowmaker, G. A.; Cooney, R. P.; Travas-Sejdic, J. *Biosens. Bioelectron.* **2005,** *20*, 1821-1828.
6. Li, X.; Xia, J.; Zhang, S. *Analytica Chimica Acta* **2008,** *622*, 104-110.
7. Hafaid, I.; Chebil, S.; Korri-Youssoufi, H.; Bessueille, F. O.; Errachid, A.; Sassi, Z.; Ali, Z.; Abdelghani, A.; Jaffrezic-Renault, N. *Sens. Actuators, B* **2010,** *144*, 323-331.
8. Ouerghi, O.; Senillou, A.; Jaffrezic-Renault, N.; Martelet, C.; Ben Ouada, H.; Cosnier, S. *J. Electroanal. Chem.* **2001,** *501*, 62-69.
9. Um, H.-J.; Kim, M.; Lee, S.-H.; Min, J.; Kim, H.; Choi, Y.-W.; Kim, Y.-H. *Talanta* **2011,** *84*, 330-334.
10. Fabregat, G.; Córdova-Mateo, E.; Armelin, E.; Bertran, O.; Alemán, C. *J. Phys. Chem. C* **2011,** *115*, 14933-14941.
11. Zang, J.; Li, C. M.; Bao, S.-J.; Cui, X.; Bao, Q.; Sun, C. Q. *Macromolecules* **2008,** *41*, 7053-7057.
12. Catherine, D.-C. *Electrochem. Commun.* **2009,** *11*, 298-301.
13. Long, Y.-Z.; Li, M.-M.; Gu, C.; Wan, M.; Duvail, J.-L.; Liu, Z.; Fan, Z. *Prog. Polym. Sci.* **2011,** *36*, 1415-1442.
14. Roy, C. J.; Leprince, L.; De Boulard, A.; Landoulsi, J.; Callegari, V.; Jonas, A. M.; Demoustier-Champagne, S. *Electrochim. Acta* **2011,** *56*, 3641-3648.
15. Lin, M.; Cho, M.; Choe, W.-S.; Yoo, J.-B.; Lee, Y. *Biosens. Bioelectron.* **2010,** *26*, 940-945.
16. Percec, S.; Skidd, G.; Zheng, M. *J. Polym. Sci., Polym. Chem.* **2009,** *47*, 6014-6024.
17. Lallemand, F.; Auguste, D.; Amato, C.; Hevesi, L.; Delhalle, J.; Mekhalif, Z. *Electrochim. Acta* **2007,** *52*, 4334-4341.
18. Cambra, A.; Redondo, M. I.; González-Tejera, M. J. *Synth. Met.* **2004,** *142*, 93-100.
19. González-Tejera, M. J.; de la Blanca, E. S.; Carrillo, I.; Redondo, M. I.; Raso, M. A.; Tortajada, J.; García, M. V. *Synth. Met.* **2005,** *151*, 100-105.
20. Huang, J.; Wei, Z.; Chen, J. *Sens. Actuators, B* **2008,** *134*, 573-578.

21. Wang, J.; Wang, J.; Wang, Z.; Wang, S. *Synth. Met.* **2006,** *156*, 610-613.
22. Saunders, B. R.; Fleming, R. J.; Murray, K. S. *Chem. Mater.* **1995,** *7*, 1082-94.
23. Chandrasekhar, P. *Conducting Polymers, Fundamental and Applications*. Kluwer Academic Publishers: **1999**.
24. Huang, J.; Wang, K.; Wei, Z. *J. Mater. Chem.* **2010,** *20*, 1117-1121.
25. Ge, D.; Mu, J.; Huang, S.; Liang, P.; Gcilitshana, O. U.; Ji, S.; Linkov, V.; Shi, W. *Synth. Met.* **2011,** *161*, 166-172.
26. Shi, W.; Ge, D.; Wang, J.; Jiang, Z.; Ren, L.; Zhang, Q. *Macromol. Rapid Commun.* **2006,** *27*, 926-930.
27. Nakabayashi, K.; Amemiya, F.; Fuchigami, T.; Machida, K.; Takeda, S.; Tamamitsu, K.; Atobe, M. *Chem.Commun.* **2011,** *47*, 5765-5767.
28. Gao, Y.; Zhao, L.; Li, C.; Shi, G. *Polymer* **2006,** *47*, 4953-4958.
29. Kemp, N. T.; Cochrane, J. W.; Newbury, R. *Synth. Met.* **2009,** *159*, 435-444.
30. Liu, J.; Lin, Y.; Liang, L.; Voigt, J. A.; Huber, D. L.; Tian, Z. R.; Coker, E.; McKenzie, B.; McDermott, M. J. *Chem.–Eur. J.* **2003,** *9*, 604-611.
31. Lu, G.; Li, C.; Shi, G. *Polymer* **2006,** *47*, 1778-1784.
32. Xia, L.; Wei, Z.; Wan, M. *J. Colloid Interface Sci.* **2010,** *341*, 1-11.
33. Qu, L.; Shi, G.; Yuan, J.; Han, G.; Chen, F. E. *J. Electroanal. Chem.* **2004,** *561*, 149-156.
34. Milan Paunovic, M. S. *Fundamentals of Electrochemical Deposition*. Wiley: **2006**; p 52.
35. Monk, P. M. S., *Fundamentals of Electroanalytical Chemistry*. **2001**.
36. Lone, B. G.; Undre, P. B.; Patil, S. S.; Khirade, P. W.; Mehrotra, S. C. *J. Mol. Liq.* **2008,** *141*, 47-53.
37. Pusztai, L.; Soetens, J.-C.; Bopp, P. A. *Physica A: Statistical Mechanics and its Applications* **2003,** *323*, 42-50.
38. Roncali, J. *Chem. Rev.* **1992,** *92*, 711-738.
39. Zhang, J.; Zhao, X. S. *J. Phys. Chem. C* **2012,** *116*, 5420-5426.
40. Carquigny, S.; Segut, O.; Lakard, B.; Lallemand, F.; Fievet, P. *Synth. Met.* **2008,** *158*, 453-461.
41. Otero, T. F.; Rodríguez, J. *J. Electroanal. Chem.* **1994,** *379*, 513-516.
42. Shere, I. G.; Pawar, V. P.; Mehrotra, S. C. *J. Mol. Liq.* **2007,** *133*, 116-119.
43. Downard, A. J.; Pletcher, D. *J. Electroanal. Chem. Interfacial Electrochem.* **1986,** *206*, 139-145.
44. Zotti, G.; Schiavon, G.; Berlin, A.; Pagani, G. *Electrochim. Acta* **1989,** *34*, 881-884.
45. Li, Y.; Qian, R. *Electrochim. Acta* **2000,** *45*, 1727-1731.
46. Qian, R.; Qiu, J. *Polym. J.* **1987,** *19*, 157-172.

47. Liang, L.; Liu, J.; Windisch, J. C. F.; Exarhos, G. J.; Lin, Y. *Angew. Chem., Int. Ed.* **2002,** *41*, 3665-3668.

48. Huang, J.; Quan, B.; Liu, M.; Wei, Z.; Jiang, L. *Macromol. Rapid Commun.* **2008,** *29*, 1335-1340.

49. Ge, D.; Wang, J.; Wang, Z.; Wang, S. *Synth. Met.* **2002,** *132*, 93-95.

50. Li, J.; Lin, X. *Sens. Actuators, B* **2007,** *126*, 527-535.

51. Wang, J.; Mo, X.; Ge, D.; Tian, Y.; Wang, Z.; Wang, S. *Synth. Met* **2006,** *156*, 514-518.

52. Hu, M.; Zhai, Q.; Liu, Z. *J. Chem. Eng. Data* **2004,** *49*, 717-719.

53. Massafera, M. P.; CÃrdoba de Torresi, S. I. *J. Electroanal.Chem. 669*, 90-94.

54. McGuinness, N.; McCarthy, C.; Rooney, D. Unpublished work

55. Smela, E.; Gadegaard, N. *Adv. Mater.* **1999,** *11*, 953-957.

56. Zhou, M.; Heinze, J. *J. Phys. Chem. B* **1999,** *103*, 8443-8450.

57. Qian, R.; Li, Y.; Yan, B.; Zhang, H. *Synth. Met.* **1989,** *28*, 51-58.

58. Sabouraud, G.; Sadki, S.; Brodie, N. *Chem. Soc. Rev.* **2000,** *29*, 283-293.

59. Unsworth, J.; Innis, P. C.; Lunn, B. A.; Jin, Z.; Norton, G. P. *Synth. Met.* **1992,** *53*, 59-69.

60. Zhang, X.; Wang, J.; Wang, Z.; Wang, S.-C. *J. Macromol. Sci., Part B: Phys.* **2006,** *45*, 475-483.

61. Jérôme, C.; Labaye, D. E.; Jérôme, R. *Synthetic Metals* **2004,** *142*, 207-216.

62. Tian, Y.; Li, Z.; Xu, H.; Yang, F. *Separation and Purification Technology* **2008,** *63*, 334-340.

63. Aitout, R.; Makhloufi, L.; Saidani, B. *Thin Solid Films* **2006,** *515*, 1992-1997.

64. Le, W.-Z.; Liu, Y.-Q. *Sens. Actuators B* **2009,** *141*, 147-153.

65. Kiema, G. K.; Aktay, M.; McDermott, M. T. *J. Electroanal.Chem.* **2003,** *540*, 7-15.

66. Kozub, B. R.; Rees, N. V.; Compton, R. G. *Sens. Actuators B* **2010,** *143*, 539-546.

67. Kamau, G. N. *Analytica Chimica Acta* **1988,** *207*, 1-16.

68. Taylor, R. J.; Humffray, A. A. *J. Electroanal. Chem. Interfacial Electrochem.* **1973,** *42*, 347-354.

69. Engstrom, R. C. *Anal. Chem.* **1982,** *54*, 2310-2314.

70. Engstrom, R. C.; Strasser, V. A. *Anal.Chem.* **1984,** *56*, 136-141.

71. Qiao, J. X.; Luo, H. Q.; Li, N. B. *Colloids and Surfaces B: Biointerfaces* **2008,** *62*, 31-35.

72. Dauginet-De Pra, L.; Demoustier-Champagne, S. *Polymer* **2005,** *46*, 1583-1594.

73. Sarkar, D. K.; Zhou, X. J.; Tannous, A.; Louie, M.; Leung, K. T. *Solid State Commun.* **2003,** *125*, 365-368.

74. Naoi, K.; Oura, Y.; Maeda, M.; Nakamura, S. *J. Electrochem. Soc.* **1995,** *142*, 417-22.

75. Silk, T.; Hong, Q.; Tamm, J.; Compton, R. G. *Synth. Met.* **1998,** *93*, 59-64.

76. Siegfried, M. J.; Choi, K.-S. *Adv. Mater.* **2004,** *16*, 1743-1746.

77. Hwang, B. J.; Santhanam, R.; Lin, Y. L. *Electrochim. Acta* **2001,** *46*, 2843-2853.

78. Yan, Y.; Yu, Z.; Huang, Y. W.; Yuan, W. X.; Wei, Z. X. *Adv. Mater.* **2007,** *19*, 3353-3357.

79. Silk, T.; Hong, Q.; Tamm, J.; Compton, R. G. *Synth. Met.* **1998,** *93*, 65-71.

80. Bankura, A.; Carnevale, V.; Klein, M. L. *J. Chem. Phys.* **2013,** *138*, 014501/1-014501/10.

81. Jeon, S. S.; Park, J. K.; Yoon, C. S.; Im, S. S. *Langmuir* **2009,** *25*, 11420-11424.

82. Asavapiriyanont, S.; Chandler, G. K.; Gunawardena, G. A.; Pletcher, D. *J. Electroanal. Chem. Interfacial Electrochem.* **1984,** *177*, 229-44.

83. Hamnett, A.; Hillman, A. R. *J. Electrochem. Soc.* **1988,** *135*, 2517-24.

84. J.A.Harrison, H. R. T. *Electroanal. Chem*. Marcel Dekker: New York **1971**; Vol. 5.

85. Koehler, S.; Ueda, M.; Efimov, I.; Bund, A. *Electrochim. Acta* **2007,** *52*, 3040-3046.

86. Fabregat, G.; Alemán, C.; Casas, M. T.; Armelin, E. *J. Phys. Chem. B* **2012,** *116*, 5064-5070.

87. Li, C.; Bai, H.; Shi, G. *Chem. Soc.Rev.* **2009,** *38*, 2397-2409.

88. Aradilla, D.; Torras, J.; Alemán, C. *J. Phys. Chem. B* **2011,** *115*, 2882-2889.

89. Gupta, S. *J. Raman Spect.* **2008,** *39*, 1343-1355.

90. Aradilla, D.; Estrany, F.; Oliver, R.; Alemán, C. *Eur. Polym. J.* **2010,** *46*, 2222-2228.

91. Aradilla, D.; Estrany, F.; Armelin, E.; Oliver, R.; Iribarren, J. I.; Alemán, C. *Macromol. Chem. Phys.* **2010,** *211*, 1663-1672.

92. Yamauchi, T.; Kojima, K.; Tanaka, K.; Unuma, T.; Shimomura, M.; Miyauchi, S. *Polymer* **1996,** *37*, 1289-1291.

93. Joseph Goldstein, D. N., David Joy, Charles Lyman, Patrick Echlin, Eric Lifshin, Linda Sawyer, and Joseph Michael, *Scanning Electron Microscopy and X-Ray Microanalysis*. Springer: New York, **2007**.

94. Egerton, R. F., *Physical Principles of Electron Microscopy*. Springer: **2005**.

95. Liu, Y.-C.; Hwang, B.-J. *Synth. Met.* **2000,** *113*, 203-207.

96. Demoustier-Champagne, S.; Stavaux, P.-Y. *Chem.Mater.* **1999,** *11*, 829-834.

97. Chen, F. E.; Shi, G.; Fu, M.; Qu, L.; Hong, X. *Synth. Met.* **2003,** *132*, 125-132.

98. Teixeira-Dias, B.; Alemán, C.; Estrany, F.; Azambuja, D. S.; Armelin, E. *Electrochim. Acta* **2011,** *56*, 5836-5843.

99. Marti, M.; Fabregat, G.; Estrany, F.; Alemán, C.; Armelin, E. *J. Mater. Chem.* **2010,** *20*, 10652-10660.

100. Zhong, C. J.; Tian, Z. Q.; Tian, Z. W. *J. Phys. Chem.* **1990,** *94*, 2171-2175.

101. Han, Y.; Qing, X.; Ye, S.; Lu, Y. *Synth. Met.* **2010,** *160*, 1159-1166.

102. Zarbin, A. J. G.; De Paoli, M.-A.; Alves, O. L. *Synth. Met.* **1999,** *99*, 227-235.

103. He, J.; Chen, W.; Xu, N.; Li, L.; Li, X.; Xue, G. *Applied Surface Science* **2004,** *221*, 87-92.

104. Arjomandi, J.; Shah, A.-u.-H. A.; Bilal, S.; Van Hoang, H.; Holze, R. *Spectrochimica Acta Part A: Molecular and Biomolecular Spectroscopy* **2011,** *78*, 1-6.

105. Liu, Y.-C. *Langmuir* **2001,** *18*, 174-181.

106. Liu, Y.-C.; Hwang, B.-J.; Jian, W.-J.; Santhanam, R. *Thin Solid Films* **2000,** *374*, 85-91.

107. Rout, C. S.; Kumar, A.; Xiong, G.; Irudayaraj, J.; Fisher, T. S. *Appl. Phys. Lett.* **2010,** *97*, 133108.

108. Kelly, K. L.; Coronado, E.; Zhao, L. L.; Schatz, G. C. *J. Phys. Chem. B* **2002,** *107*, 668-677.

109. Nie, S.; Emory, S. R. *Science* **1997,** *275*, 1102-1106.

110. Ray Iii, K. G.; McCreery, R. L. *J. Electroanal. Chem.* **1999,** *469*, 150-158.

111. Kagan, M. R.; McCreery, R. L. *Anal. Chem.* **1994,** *66*, 4159-65.

Chapter 4

The Electrochemical Deposition of Poly[*N*-(2-cyanoethyl)pyrrole] Microtubes and Microcontainers from an Acoustically Formed Emulsion

4.1 Introduction

There has been extensive research focusing on methods to control the growth of conducting polymers, as many studies have illustrated that their physical properties are a consequence of their morphology.[1-2] Hollow nano/micro structured polymeric materials are a rapidly developing research topic due to the significant range of applications for which they are suited, including immobilisation, drug delivery, sensing, separation, encapsulation, catalysis and as nanoreactors.[2-7] Much recent attention has focused on the design and fabrication of polypyrrole (PPy) into hollow open-pore nano/microtubes[8-11] or hollow closed-pore nano/microspheres[12-13] as these structures have potential application in controlled drug delivery systems. Several authors have developed methods to construct hollow open tubular structures anchored to substrate materials, which allows greater control over their use.[6, 14-16] Furthermore, the permeability of conducting polymers can be altered as a function of applied potential or pH[17] and this property has been exploited to encapsulate and subsequently release guest species from within polypyrrole microstructures.[18]

Recently there have been reports on applying a one-step electrochemical template-free approach to preparing nanostructures of covalently functionalised poly(3,4-ethylenedioxythiophene) (PEDOT) [19] and PPy.[20] While the nano/micro morphologies of conducting polymers have been comprehensively studied, very little has been performed with their covalently functionalised counterparts. Electrodes modified with covalently functionalised conducting polymers have been utilised in sensor applications, whereby employing the appropriate moiety at the substituted position exhibits supramolecular interactions with other molecules and compounds. For example, poly(*N*-(2-cyanoethyl)pyrrole) (PPyEtCN) modified electrodes have been used to immobilise specific antibodies for the fabrication of biosensors[21] and in the electrochemical sensing of dopamine.[22] Alternatively, the functional group can be chemically modified in order to covalently attach a wide range of species to the polymer surface which include carbon nanotubes,[23] biomolecules[24] or fluorinated alkyl chains.[25]

There is a growing interest in preparing polypyrrole nano/microstructures employing facile template-free or soft-template electrochemical approaches.[26-28] The advantage of these methodologies is that the steps used to construct and subsequently dissolve

the hard template are not required. Furthermore, the morphology of the polymer formed can be controlled by simply altering the electrochemical conditions. Chapter 3 describes the development of an electrochemical template-free procedure to form a novel *N*-substituted polypyrrole (PPyEtCN) film with a nanowire morphology.[20] In this chapter we report the electrochemical deposition of microscale tubular structures of PPyEtCN, in which the tubes are anchored to an electrode surface. Mazur and co-workers recently developed an elegant interfacial chemical oxidation polymerisation method using an organic or aqueous solvent microdroplets to entrap either hydrophobic[29] or hydrophilic[13] compounds within polypyrrole microsvessels. Herein, we report the first application of this microdroplet method in an electrochemical polymerisation reaction, using adsorbed toluene droplets as soft templates.[30] Although we have chosen PPyEtCN for these studies, our system can be used to design similar structures for any monomer system in which an organic/aqueous based solvent system may be employed. This opens up a new avenue of polymer microstructuring for monomers which would typically have been disregarded due to their insolubility in aqueous electrolytes.

4.2 Results and Discussion

4.2.1 Poly(*N*-(2-cyanoethyl)pyrrole) (PPyEtCN) Microtube Formation

When forming the PPyEtCN nanowires (Chapter 3) it was observed that in certain experiments large circular shaped PPyEtCN microtubes were produced in a vertically aligned but random fashion across the electrode, Figure 4.1a and 4.1b. As shown in Figure 4.1b insets, the microtubes were produced with either a smooth or rippled exterior. The rippling effect was related to their size as it was only observed for the larger diameter tubes. This was a peculiar observation as ripple shaped polymer microtubes have only been reported for PPy using cyclic growth techniques.[14] Those authors used a CV technique to scan the applied potential between the oxidative and reductive potentials of Py, initialising and terminating growth successively. A clear correlation was observed between the number of cycles performed and the number of annular parts in the microstructures. In our system however, we employed a constant

oxidising growth potential which should not lead to the rippled morphology, since polymer growth was maintained continuously. The PPyEtCN microtubes were produced in either large condensed groups over the electrode or in an irregular dispersed pattern, Figure 4.1c and 4.1d respectively. Therefore it was not possible to control or predict their formation.

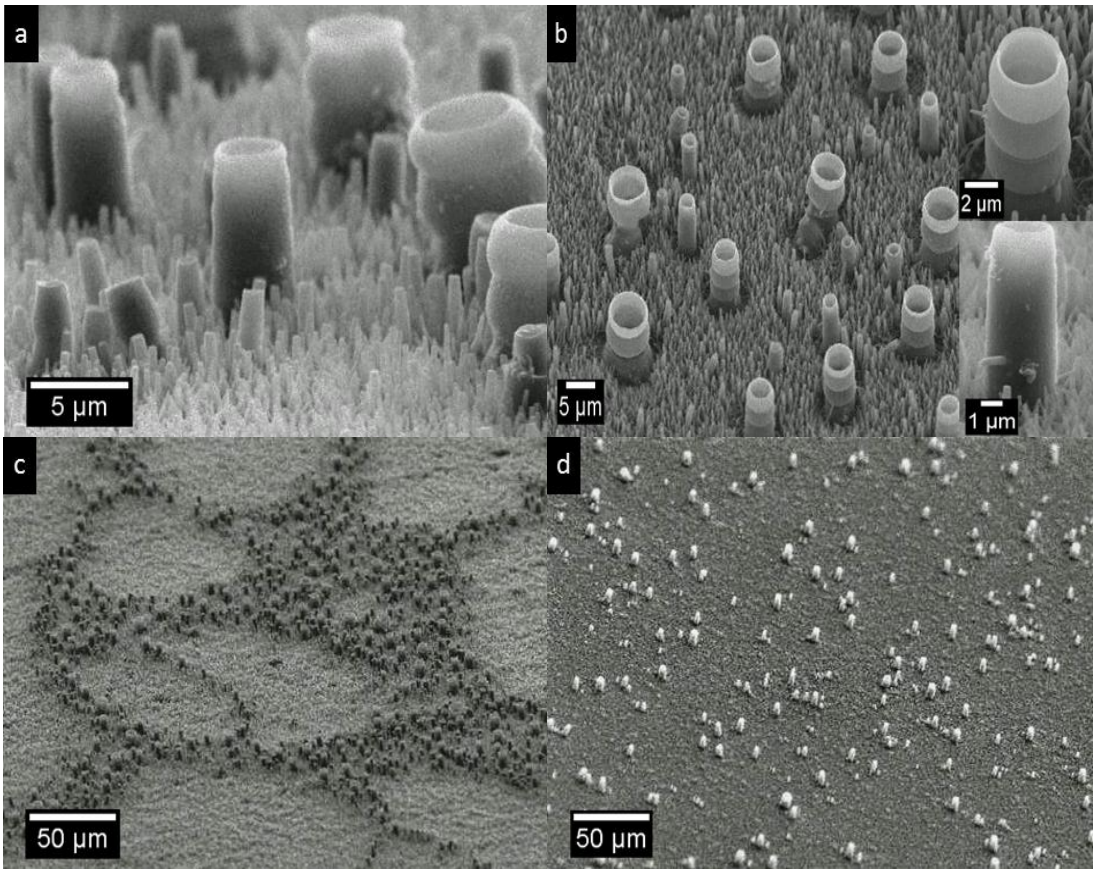

Figure 4.1. SEM micrographs of random microtube grown at 0.850 V (a) side profile (b) top down view (c) clustered morphology and (d) dispersed morphology. Polymerisation mixture contained $LiClO_4$ (0.020 M), $(NH_4)H_2PO_4$ (0.300 M) with PyEtCN (0.075 M) in 10 mL water/ethanol (7:3).

Comparing the growth profiles of the randomly formed microtube films and the nanowire films grown in Chapter 3 revealed no major difference in the magnitude of the current response over the entire growth, Figure 4.2 inset. This is to be expected since both polymer films were synthesised under the exact same experimental conditions. However, examination of very early stages of the growth (< 40 s), corresponding to the nucleation phase, revealed a sharp increase in the recorded current transient. This narrow 'pre-peak' was only present for the films possessing

microtubes, indicating that they were formed at the beginning of the nucleation phase. It was probable that insoluble monomer droplets had adsorbed on the electrode surface which would also contain the dopant $LiClO_4$, since it is soluble in organic media.[31] Having both monomer and dopant in close vicinity to the electrode would produce an increase in polymerisation rate at early times, leading to the increase in the current recorded. Although this observation does not derive much information about the mechanism of microtube growth, it does indicate they are formed at the beginning of nucleation under abnormal conditions.

This result was supported by EDX analyses of the interior cavity and exterior walls of the tubes. Confining the X-ray collection area to a narrow section (low electron kV and beam current) it was possible to analyse inside the tubes without generating X-rays from the tube walls.[32] As shown in Figure 4.2b, both the inside and outside of the tubes had signals for chlorine at 0.18, 2.62 and 2.82 kV which arose due to the perchlorate anion doping the polymer. It can be seen however, that the signal for chlorine from inside the microtube (spectrum 2) was stronger than for outside the microtube (spectrum 1), Figure 4.2b. This suggests that surface adsorbed monomer droplets, with a high concentration of ClO_4^-, are responsible for creating the microtubes. A similar observation was reported by Huang and co-workers as they successfully developed a PPy nano morphology employing undissolved monomer droplets.[33] Atobe and co-workers also reported stable nano and microdroplets of monomer when insoluble monomer/electrolytes were used.[31, 34-35] Based on these reports the monomer droplet hypothesis for the formation of the PPyEtCN microtubes had reasonable credibility.

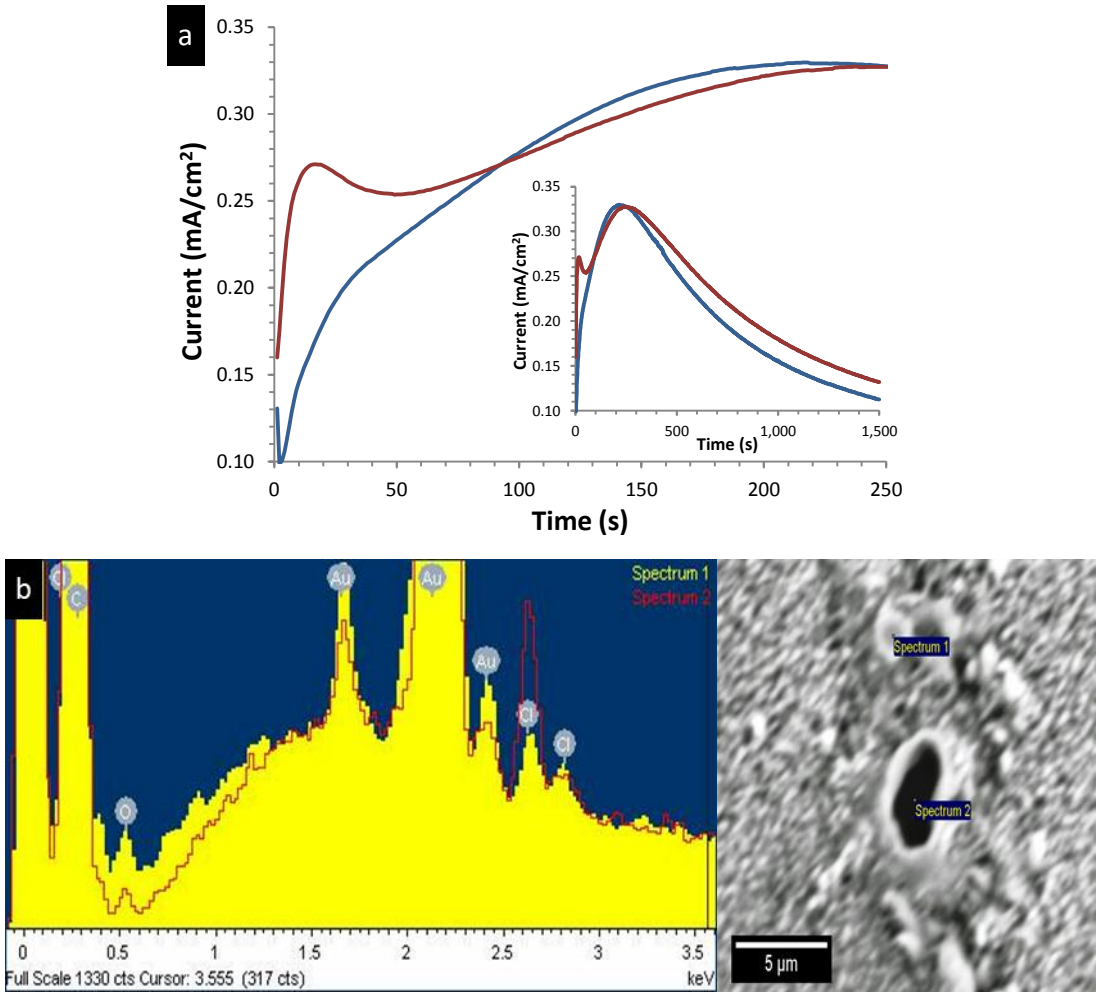

Figure 4.2. Polarisation profile of PPyEtCN polymers deposited at 0.850 V in $LiClO_4$ (0.020 M) $(NH_4)H_2PO_4$ (0.300 M) with PyEtCN (0.075 M) in 10 mL water/ethanol (7:3) with (red trace) and without (blue trace) microtubes (a). EDX data with corresponding SEM micrograph of area analysed (b).

To further substantiate this monomer droplet mechanism the polymerisation solutions which produced the microtube morphology were examined. Visual inspection of solutions which had been vigorously stirred displayed no signs of monomer droplets (Chapter 3, Section 3.2.1). At short stirring times however, the monomer would not fully solubilise and formed as small globules at the bottom of the vial. Furthermore, when the solutions were left uncovered for 48 hours the ethanol evaporated and monomer droplets rose to the surface, Figure 4.3a. A bulk sample of this solution was pipetted onto a glass slide and circular insoluble monomer droplets were observed on the glass surface, Figure 4.3b. These spherical insoluble monomer droplets were similar in size to the polymer microtube structures formed on the electrode surface.

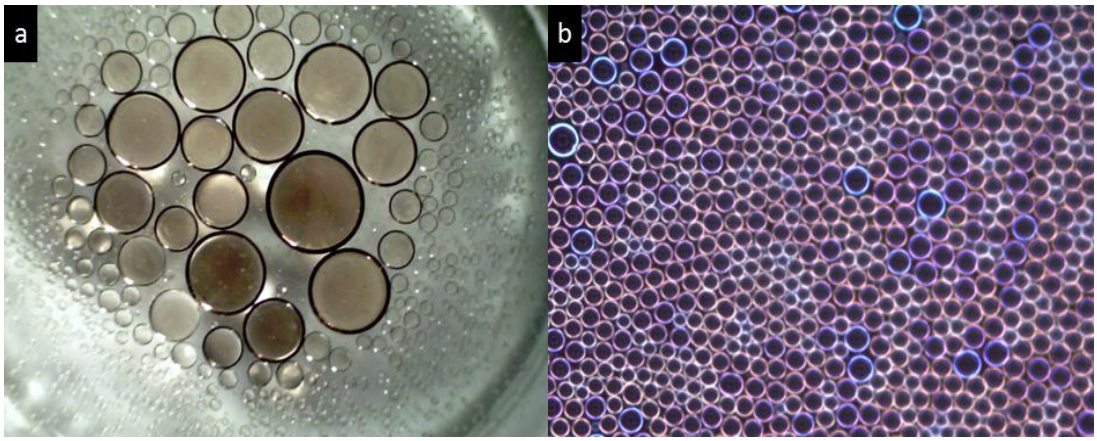

Figure 4.3. Microscope images of (a) low magnification of solution surface and (b) high magnification of glass slide after solution was pipette onto it. Solutions containing $LiClO_4$ (0.020 M), $(NH_4)H_2PO_4$ (0.300 M) with PyEtCN (0.075 M) in 10 mL water/ethanol (7:3). Resultant images after vials left uncovered for 48 hours.

Large micron sized PyEtCN droplets were capable of forming in solutions as PyEtCN has a low solubility in aqueous systems. It is known that oil droplets mixed in water simply by stirring have a large size distribution.[36] This could explain the large size distribution of the microtubes which was observed for all instances of their formation. Similar results were obtained by Atobe and co-workers for PEDOT emulsions where a direct relationship between droplet size and polymer grain size was observed.[34] This is consistent with the random nature of the microtube formation since it was possible that in some experiments the monomer did not become fully solubilised and polymerised into the microtube structures. Similar results have been reported by Shi and co-workers for the fabrication of polyaniline (PANi) microcups where insoluble aniline droplets, formed by sonication, had a template role during polymerisation.[37] In another report they used a very high concentration (1 mol/L) of Py monomer which facilitated the growth of PPy microcontainers.[38] Interestingly, they reported that the pH of the solution had a direct effect on the morphology obtained, as microcontainers were only formed in neutral solutions. Lower pH solutions led to enhanced monomer solubility and therefore no microcontainers were generated due to the reduction of undissolved monomer droplets. Therefore, monomer solubility has a direct effect on the formation of the microtubes using this monomer droplet mechanism.

Examination of the base of the microtubes revealed that the PPyEtCN microtubes were not fully hollow from base to tip. It was possible to knock the tubes over, Figure 4.4a, and leave them horizontal by employing a high pressure air flow (before Au/Pd coating). The SEM stage was then tilted to 20-45^{o} angles so that the base of the microtubes could be inspected. High magnification of the microtube base section revealed that both the base of the tube and the corresponding electrode area contained polymer material, Figure 4.4b. This would indicate that the microtube nucleation did not occur by polymerising around an area of inhibited growth; but rather since the monomer contained the ClO_4^- dopant, growth proceeded inside and around the droplet simultaneously. It was difficult to acertain how far the solid growth extended inside the tube by SEM analysis. Therefore, TEM analysis was performed to investigate the microtube interior composition.

The microtube films were removed from the surface by a surgical blade and placed on a TEM grid after sonication in ethanol. The resultant images recorded at 200 kV are shown in Figure 4.4c. In this image it can be seen that the top or mouth of the tube has a lighter contrast compared to the rest of the strucutre. This contrast difference extends half way down the tube where it merges with the darker contrast. Typically, for a hollow polymer materials an extreme contrast difference is regestered between the walls and center cavity using TEM.[39-40] This was not the case for the PPyEtCN microtubes however. Two possible reasons have been identified to explain this; either the electron beam was not powerful enough to penetrate through the microtubes near the base, or the hollow cavity in the center was very narrow and had a comparable density to the walls. In an attempt to ascertain the length of the hollow section, the microstructures were milled by foccussed ion beam (FIB) through the halfway point. However, even with low voltages and long milling times the FIB proccess degraded the microtubes until only a powder residue was observed, Figure 4.4d, signifying they could not withstand damage casued by the ion beam process. These experiments were inconclusive in determining the length of the hollow cativy within the tubes, therefore, semi-hollow character was concluded as the most probable morphology.

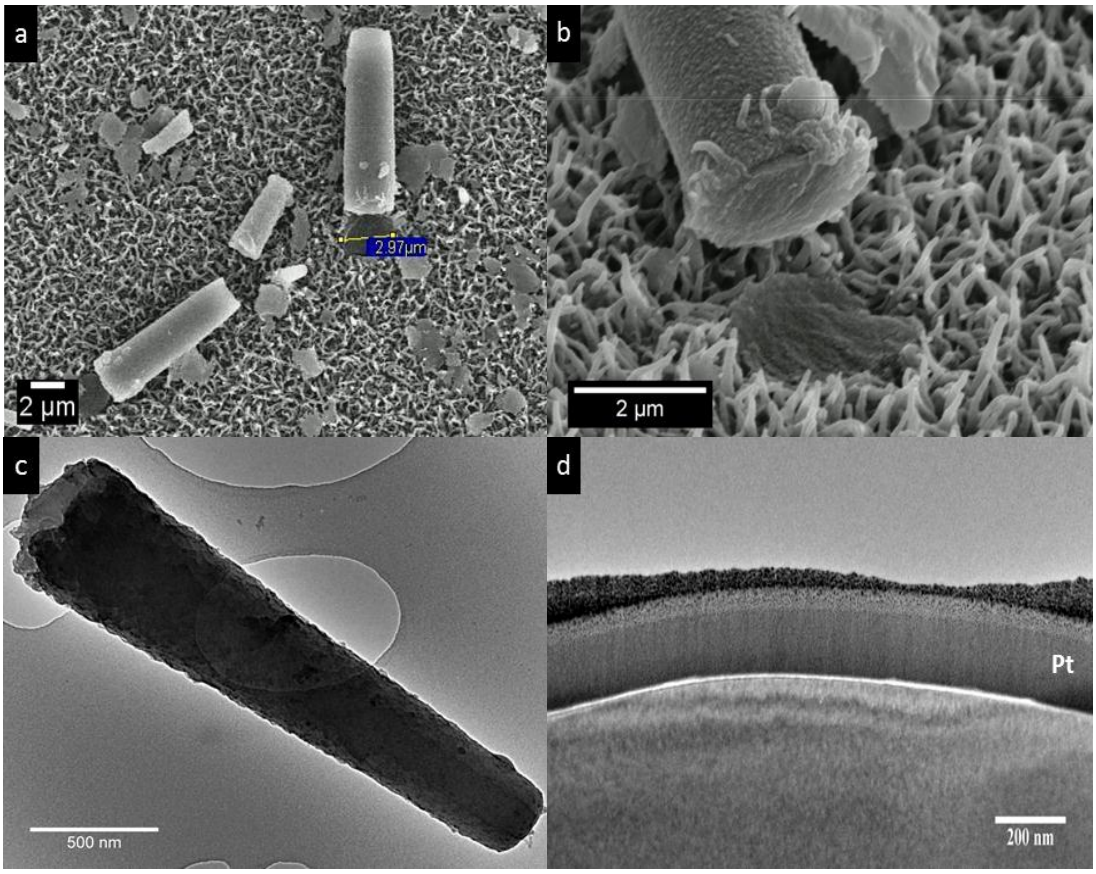

Figure 4.4. SEM micrographs of microtubes which have been knocked over (a) and magnification of the base area of an individual tube (b). TEM micrograph of a microtube (c). FIB cross section image of area where microtube was milled by ion beam (d). Polymerisation solution contained $LiClO_4$ (0.020 M), $(NH_4)H_2PO_4$ (0.300 M) with PyEtCN (0.075 M) in 10 mL water/ethanol (7:3).

Having come to a reasonable conclusion for the mechanism of the semi-hollow microtube growth, experiments were then performed to encourage a larger distribution of insoluble monomer droplets to produce a consistent microtube coverage. Increasing the monomer concentration significantly led to a greater proportion of monomer forming insoluble droplets. Indeed this was observed by visual inspection of higher concentration solutions. Further proof of their occurrence was evident from the corresponding polarisation curves at monomer concentrations of 0.075, 0.093 and 0.150 M, Figure 4.5a, 4.5b and 4.5c, respectively.

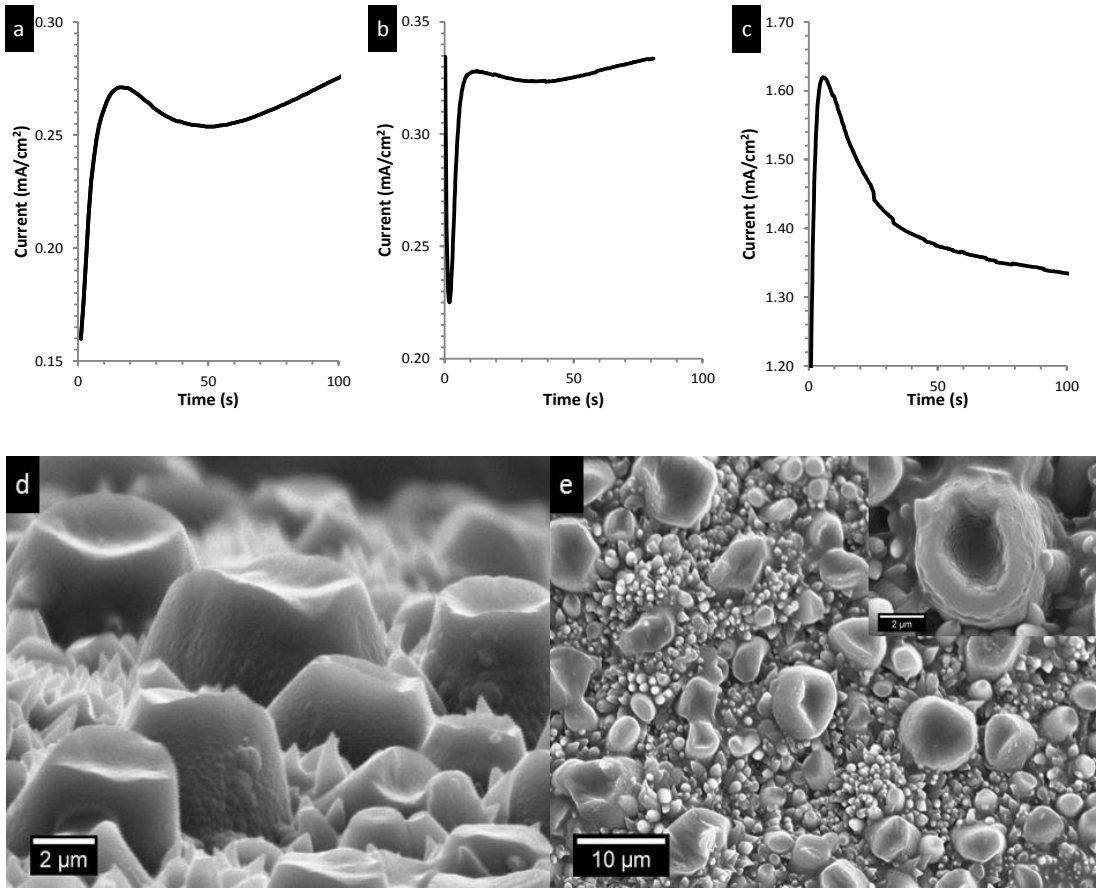

Figure 4.5. Polarisation profiles of PPyEtCN polymers deposited at 0.85 V with (a) 0.075 (b) 0.093 and (c) 0.150 M PyEtCN. Emulsion contained $LiClO_4$ (0.020 M) and $(NH_4)H_2PO_4$ (0.300 M) in 10 mL water/ethanol (7:3) after stirring. Corresponding SEM micrographs of 1.50 M experiment side angle (d) and top-down (e).

Increasing the concentration of monomer and allowing the electrode to sit for 15 min in the polymerisation solution resulted in a larger 'pre-peak' forming. As can be seen from Figure 4.5, the intensity of this I_p, increased with increasing concentration of PyEtCN. The recorded values were 0.27, 0.32 and 1.62 mA/cm^2 for concentrations of 0.075, 0.093 and 0.150 M, respectively. Furthermore, the I_p was evident at earlier times shifting from 16.05, 12.22 to 5.34 s for concentrations in Figure 4.5a, 4.5b and 4.5c respectively. This significant increase in current and earlier forming 'pre peak' at the 0.150 M experiment was indicative of a larger surface concentration of monomer.[37] An increase in microstructure surface coverage was observed, Figure 4.5d, and they formed in a reproducible manner. However, while the structures resembled the morphology in Figure 4.1, they were in fact solid with only small indentations at their apex, Figure 4.5e. Due to a high concentration of dopant

residing inside the monomer, fully hollow microtubes could not be fabricated by this method since polymerisation was favored inside the monomer droplet. Therefore this method was disregarded as a useful means for producing fully hollow PPyEtCN microtubes.

4.2.2 Forming an Emulsion using Toluene

Further extensive experimentation attempting to form hollow microtubes using methodologies such as: employing an oxidised monomer, acid surfactants, electrode surface oxidation/roughening and H_2 bubble generation were ineffective (data not shown). It was concluded that it was not possible to reproducibly control the semi-hollow microtubes from Section 4.2.1. However, in some experiments employing the $PPyEtN_3$ monomer, which was synthesised at NUIM, several SEM micrographs revealed hollow microtube morphologies were present. The NMR data from the purified monomer revealed that there was a toluene impurity remaining which correlated directly with the microtube occurrence. This raised the possibility of using this impurity for the generation of the hollow tubular structures. A new 'droplet mechanism' was followed which would replace the monomer with toluene as the template directing entity. Employing a droplet which would discourage polymerisation within its core would favor a hollow morphology. It has been well documented in the literature that toluene emulsions have been successfully employed to produce hollow polymeric microvessels in solution by chemical means.[29, 41-42] Therefore, in our polymerisation system, the monomer droplet template was substituted with a toluene droplet.

Adding toluene to the PPyEtCN polymerisation mixture, combined with vigorous stirring, led to an emulsion forming which was only slightly opaque. Mazur and co-workers observed that when using a toluene emulsion that toluene droplets adsorbed onto solid surfaces and could be used as a template for chemical polymerisation.[42] In our system, when the toluene droplets adsorbed at an electrode surface it was possible to use them as templates for electrochemical anodic polymerisation of PyEtCN into a range of microstructures. It was observed that inside the toluene droplet became a zone of zero growth, forcing the polymer to grow on the exterior of

the droplet instead. Again, similar to Figure 4.2 and Figure 4.5 shown previously, when the emulsion was present an increase in current was observed at very early polymerisation times, Figure 4.6. Since the monomer was soluble inside the toluene it was leading to faster growth by supplying monomer to the extremity of the droplet to partake in polymerisation. No growth was observed inside the toluene droplets which produced a hollow interior. A second increase in peak current was also recorded at around 200 s in the polarisation transients, similar to what was observed for the nanowire polymers in Chapter 3. Since nanowires were also present in the toluene emulsion polymerisations, it was safe to assume that this second peak current increase was associated with their formation.

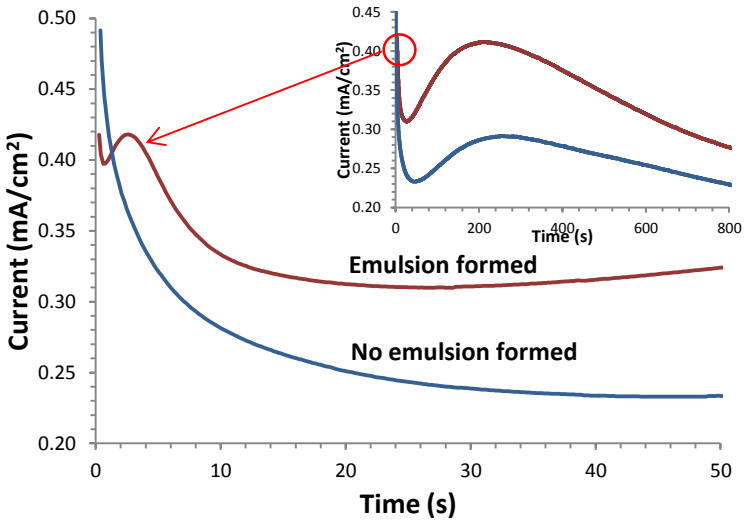

Figure 4.6. Polarisation profile of PPyEtCN polymers deposited at 0.850 V with (red trace) and without (blue trace) emulsion present. Emulsion contained PyEtCN (0.075M), $LiClO_4$ (0.020 M), $(NH_4)H_2PO_4$ (0.300 M) and toluene (40 µL) in 10 mL water/ethanol (7:3) produced by stirring.

It was observed that the emulsions produced by this stirring method had a low stability and usually dissipated within 10-15 min, returning to a clear solution. Polymerisation in an emulsion produced with the addition of 40 µL toluene led to different morphologies forming depending on whether the emulsion was present or had dissipated, Figure 4.7a, 4.7b and 4.7c. Shown here, when polymerisation was performed immediately after the emulsion was formed, hollow and open tube structures were produced, Figure 4.7a. If polymerisation was initiated as the emulsion was dissipating the structures did not retain as much hollow character,

Figure 4.7b and 4.7c. Once the emulsion has completely dissipated only nanowires were observed with no indication of any hollow or pillar like morphologies, Figure 4.7d.

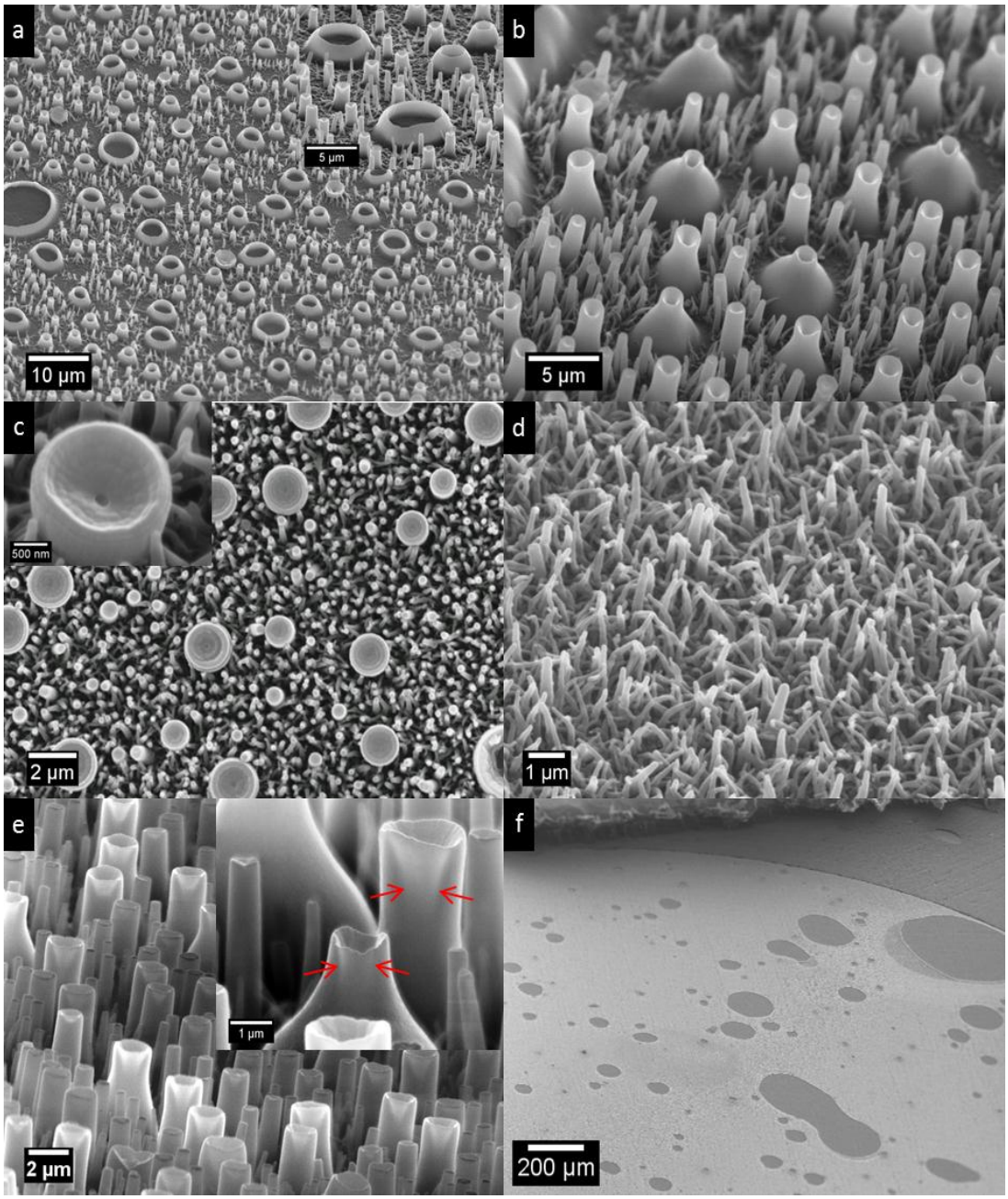

Figure 4.7. SEM micrographs of a PPyEtCN films grown after emulsion had been allowed to dissipate for (a) 0, (b) 5, (c) 10 min and (d) total dissipation. SEM analysis of structures at 30 kV grown at 5 min dissipation (e). Typical low magnification of void toluene gaps covering electrode (f). Emulsion mixture contained $LiClO_4$ (0.020 M), $(NH_4)H_2PO_4$ (0.300 M) with PyEtCN (0.075 M) with 40 µl toluene in 10 mL water/ethanol (7:3) produced by stirring.

These results indicate that the extent of microtube formation is directly related to the level of emulsion present in solution. It was unclear if all of the structures in Figure 4.7b were hollow or just indented at their tips. In an attempt to obtain more information about their internal density SEM micrographs were recorded at the maximum accelerating voltage (30 kV). At this speed the electrons would be capable of penetrating the thinner parts of the polymer walls. To offset the increase in energy being applied to the surface which significantly increased the occurrence of charging effects, the beam current was reduced to the lowest possible value (< 1 µA). The corresponding SEM micrographs are shown in Figure 4.7e. Here it can be seen that the larger tube openings have a lighter contrast at their center which is surrounded by a darker exterior. This would be consistent with a hollow center since the outside wall area would contain more polymer and therefore be denser. If the smaller pillars are inspected it can be seen that they have a constant contrast over their entire length, signifying a uniform density. It is therefore possible to speculate that the larger structures have mostly hollow interiors while the medium and smaller sized structures have a significantly dimpled apex with the possibility of semi-hollow character.

Using this weak agitation method (stirring) produced inherent drawbacks in this system. The reproducibility was low since the emulsions were unstable, this led to coalescence of toluene droplets and possibly to Ostwald ripening.[43-44] Although Ostwald ripening is not a dominant process in macro emulsions with large droplet sizes (> 1-2 µm).[43] Even still, these larger toluene agglomerations produced vast areas over the electrode which were void of polymer growth, Figure 4.7f. These defects were present for all polymerisation experiments performed with emulsions produced by stirring. This problem was overcome by employing sonication techniques to generate more stable emulsions and reduce the size of the toluene droplets. The results are discussed in the following sections.

4.2.3 Acoustically Formed Toluene Emulsions

When sufficient energy was applied to the toluene/ethanol/water system, through ultrasonication, it was possible to create a homogeneous dispersion of toluene micro-droplets within the continuous phase. This turbidity was maintained for several hours without the need for any surfactants or stabilisers. This was a key factor in utilising this system as a soft template method, as the absence of stabilising agents left the toluene micro-droplets available to adsorb to solid surfaces.[41] The electrochemical polymerisation mixture, $LiClO_4$ (0.020 M), $(NH_4)H_2PO_4$ (0.100 M), PyEtCN (0.056 M) and toluene (80 µL) in 10 mL water/ethanol (7:3), was emulsified using two methods (Scheme 4.1). The mixture was either shaken vigorously and then sonicated for 1 min using an ultrasonication probe (Scheme 4.1 Method (A)) or stirred vigorously for 5 min and then sonicated for 1 min using an ultrasonication bath (Scheme 4.1 Method (B)). In both cases the solution went from a transparent multiphasic system to an opaque emulsion. However, the emulsion formed using the ultrasonic probe was much more opaque and possessed a longer period of stability than that formed employing the ultrasonic bath. It has been reported that using an ultrasonic probe compared to an ultrasonic bath results in more stable emulsions consisting of smaller sized oil droplets.[45] In the absence of the toluene no emulsion was formed. Using these two sonication methods produced a range of different PPyEtCN morphologies. Both sonication procedures, along with the morphologies they produce, will be discussed as separate methodologies.

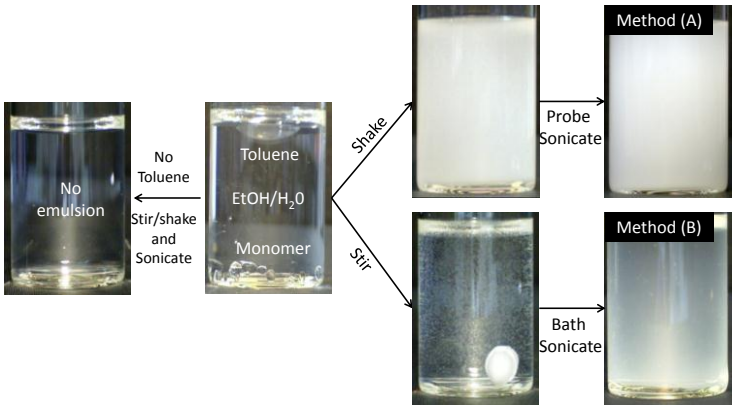

Scheme 4.1. Multiphasic starting solution of toluene, monomer and water/ethanol. Resultant emulsion mixtures from shaking and probe sonication, Method (A) and stirring and bath sonication, Method (B). Resulting solution of $EtOH/H_20$/PyEtCN in the absence of toluene is shown on the left.

4.2.4 Method A: Probe Sonicator

When PyEtCN was polymerised from an emulsion produced by Method (A) it was possible to reproducibly fabricate tubular hollow microstructures on the electrode surface. Using this method these structures were formed in both water and water/ethanol emulsions, Figure 4.8. In the absence of ethanol incomplete films were produced. The formation of microtubes occurred but there were large areas (20 – 50 µm in diameter) across the electrode surface which had total absence of polymer growth, Figure 4.8a. Moreover, as Figure 4.8b illustrates, the tubes formed in a highly irregular fashion with a large variation in the size distribution of their height and diameter.

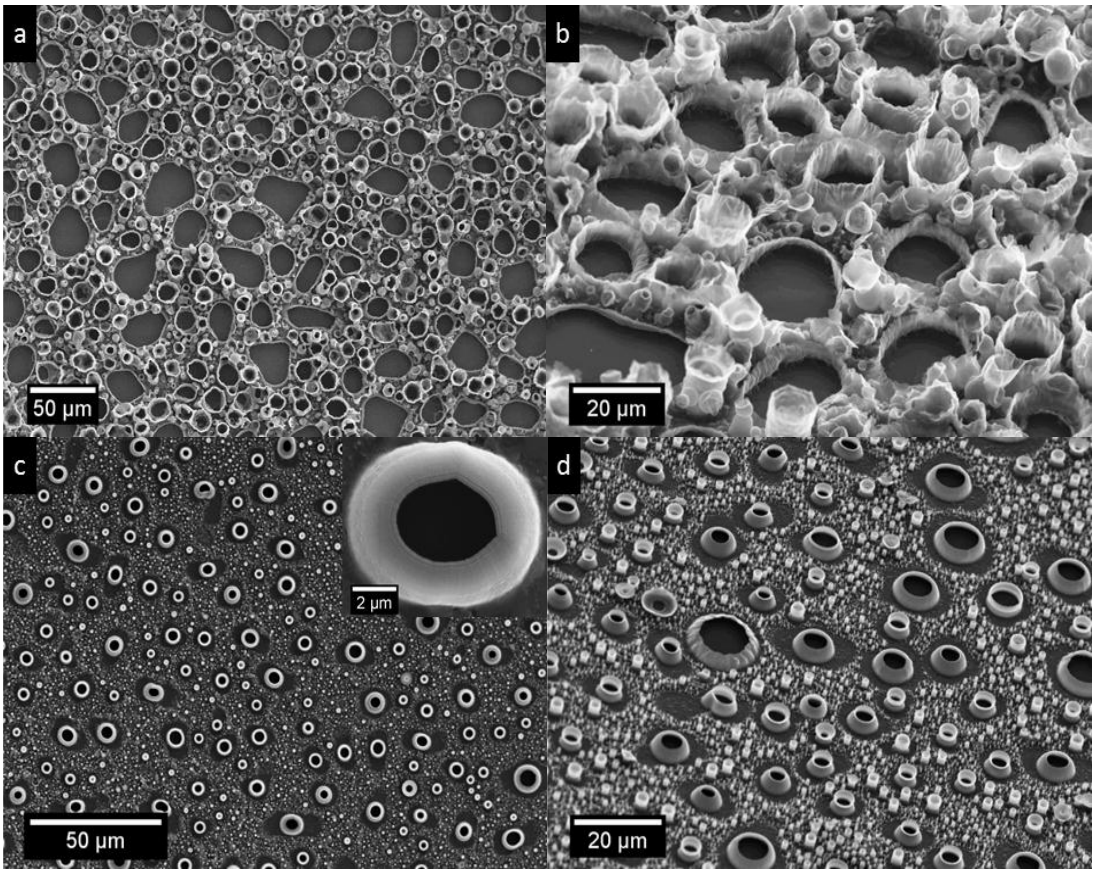

Figure 4.8. SEM micrographs of PPyEtCN microstructures deposited at 0.950 V from 10 mL (a), (b) water and (c), (d) water/ethanol (7:3) solutions. Emulsion mixture contained PyEtCN (0.056 M), $LiClO_4$ (0.020 M), $(NH_4)H_2PO_4$ (0.100 M) and toluene (80 µL) with 1 min sonication by probe.

Homogeneous films of microtubes were only formed when ethanol was added to the system as a co-solvent, as seen in Figure 4.8c and 4.8d. Here, the tubes possess a

smooth exterior and have an increased uniformity in their size distribution. They also had a relatively constant vertical height with most tubes approximately 3 µm in size. The density of tubes (≥ 0.5 µm) on the surface was approximately 3000 units/cm^2. As can be seen from Figure 4.8c (inset) these structures had an empty cavity in the center and were hollow through to the substrate surface. It was clear from these SEM micrographs that the addition of the ethanol has a strong influence on the growth of the tubes.

This difference in morphology can again be explained due to the effect ethanol has on the polymerisation rate, similar to Chapter 3, Section 3.2.1.1. As can be seen from Figure 4.9a, when the water and water/ethanol emulsion polymerisation transients were compared there was a significant difference in the growth rate. The polymerisation current for the water emulsion increased rapidly to reach a plateau after 1 min, at 2 mA/cm^2. Over the same time period the polymerisation currents for the water/ethanol were significantly lower and steadily decreased to 0.5 mA/cm^2. This increase in reaction rate can be explained by the difference in dielectric constants of the two mediums, the solubility of monomer and dopants and the change in solvation of these components, as discussed in Chapter 3 Section 3.2.1.1. It leads to microtubes forming in an unordered fashion in water due to the much more rapid growth rate. This difference in growth rate has an impact on the morphology as shown in Figure 4.9b and 4.9c. Clearly, the polymer formed from the ethanol solution contains similar sized structures with smooth exteriors and obvious vertical alignment. Other authors have highlighted the effect of the growth rate on polymer morphologies, with vertically aligned nanostructures typically following slower growth methodologies.[33, 46-47]

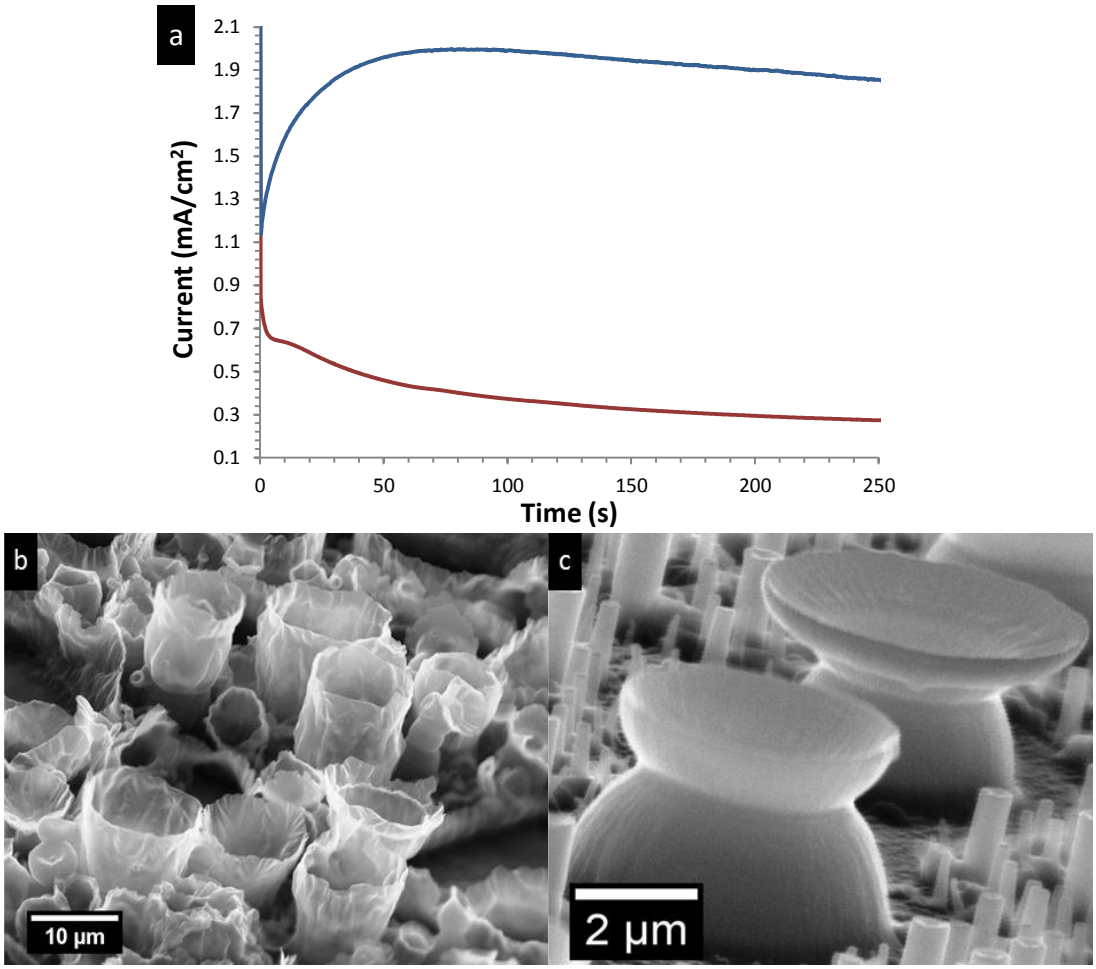

Figure 4.9. Polarisation profile of PPyEtCN polymers deposited at 0.95 V from 10 mL (blue trace) water and (red trace) water/ethanol (7:3) solutions (a) with corresponding opaque angle SEM for water (b) and water/ethanol (c). Emulsion mixture contained PyEtCN (0.056 M), $LiClO_4$ (0.020 M), $(NH_4)H_2PO_4$ (0.100 M) and toluene (80 µL) with 1 min sonication by probe.

4.2.4.1 Mechanism of Microtube Growth

The experiments contained in this section were performed to understand the mechanism behind the growth of the microtubes and identify the main factors affecting it. Particular attention was paid to the electrolyte solution and its effect on obtaining vertically aligned microtubes.

4.2.4.1.1 Toluene Droplet Soft-Template

A schematic illustrating the proposed mechanism of microtube formation is displayed in Scheme 4.2. Here, the toluene droplet can be seen adsorbed to the electrode surface, containing some monomer which is soluble in organic media (1). Once an oxidative potential is applied, dopant from the surrounding bulk solution diffuses towards the adsorbed droplet (2). Growth proceeds favorably at the edge of the droplet due to electric field effects (3).[33] In addition, at this interface both monomer and dopant are present in sufficient quantities to enable polymerisation to proceed. Finally, polymer growth mimics the shape of the original droplet leaving a hollow interior (4).

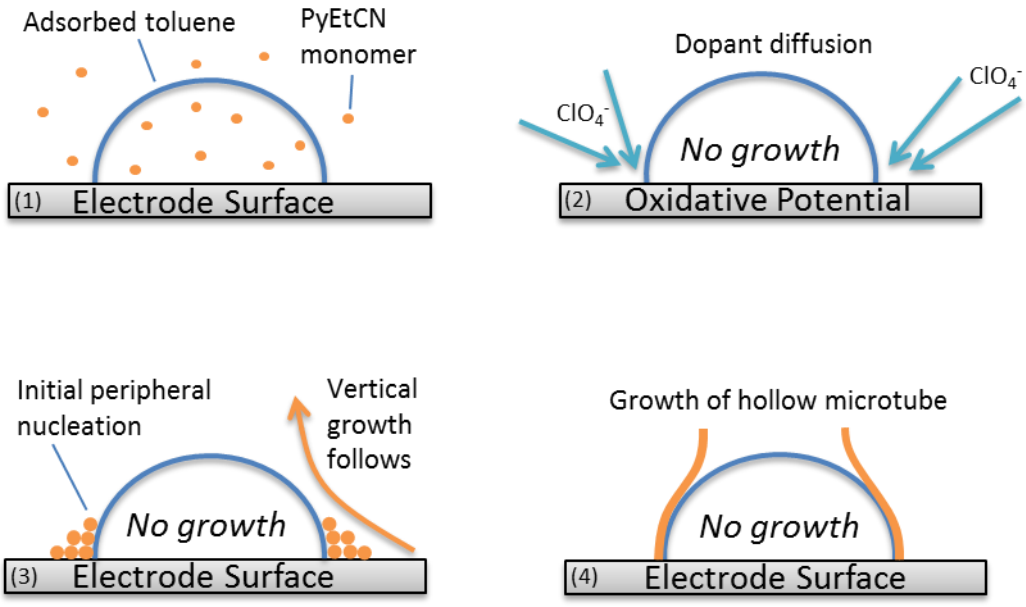

Scheme 4.2. Formation mechanism of PPyEtCN microtubes based on toluene droplet adsorption at the substrate followed by polymerisation around these droplets.

The diameters of the toluene emulsion droplets and polymer microtubes were compared to confirm that the addition of the toluene was responsible for the microtube morphology. An emulsion was formed and several drops were placed on a glass slide and allowed to adsorb for 5 min before imaging was performed using an optical microscope, Figure 4.10a. Similarly, an SEM micrograph was recorded of a polymer film formed from an identical emulsion mixture, Figure 4.10b. The diameters of the droplets and polymer microtubes were then measured and the distribution of their sizes is given in Figure 4.10a (inset) and 4.10b (inset), respectively. Given the significant difference in resolution between the microscopes used there is a still a good correlation between the droplet size and the microtube diameter.

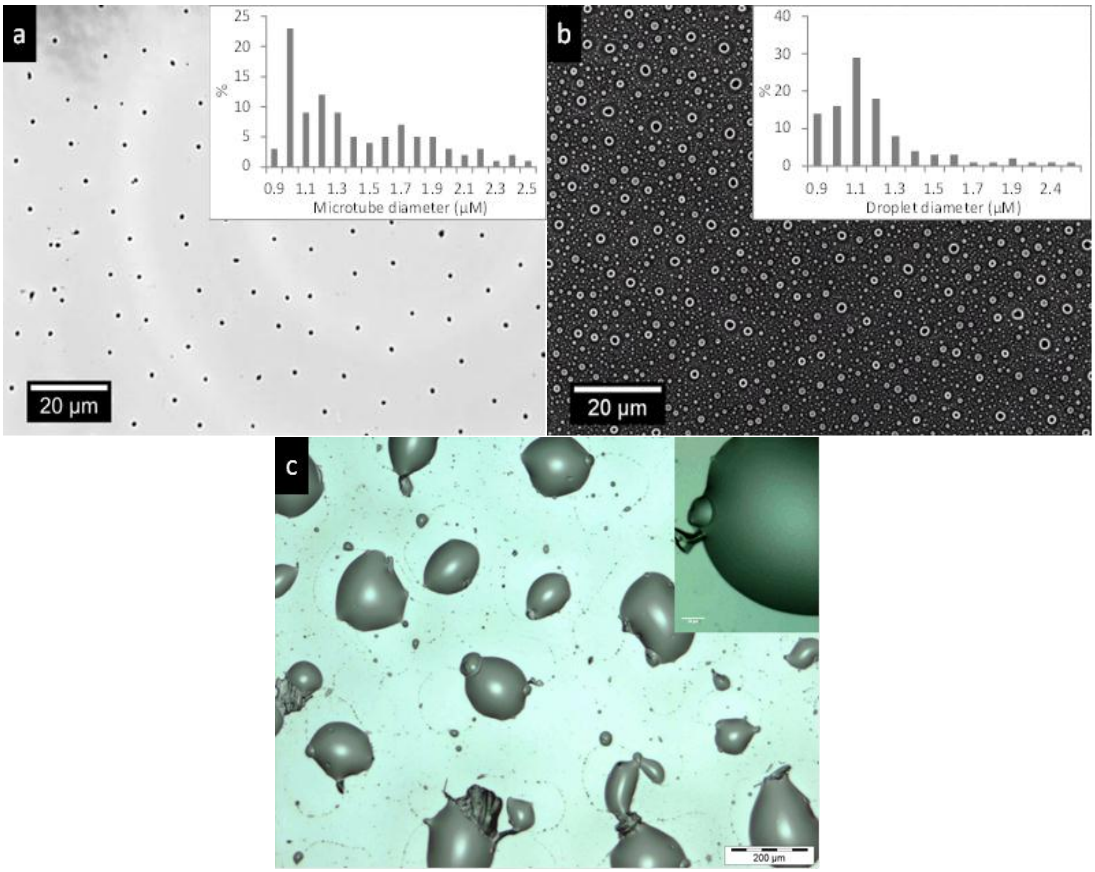

Figure 4.10. Optical microscope (a) and SEM images (b) of emulsion droplets and polymer microstructures respectively with inset of diameter and % of droplets/microtubes, produced with 1 min sonication by probe. Emulsion produced by shaking only and pipette onto glass slide and allowed to evaporate (c). Emulsion contained PyEtCN (0.056 M), $LiClO_4$ (0.020 M), $(NH_4)H_2PO_4$ (0.100 M) and toluene (80 µL) in 10 mL water/ethanol (7:3).

The average diameter of the adsorbed toluene droplet was 1.00 μm while the average diameter of the microtubes was 1.44 μm. Considering the typical thickness of the microtube walls is approximately 200 nm, these values are consistent with each other. However, the reflectance light microscope was incapable of high magnification of the small toluene micro droplets (1.00 μm). To overcome this limitation an emulsion was produced by vigorous shaking only, which led to larger droplets forming (100 μm). As can be seen from Figure 4.10c raised hemispherical toluene droplets were observed in large quantities. These results confirm that the toluene droplets do in fact act as the templates for the microtube formation by undergoing adsorption onto the substrate and acting as a soft template for the propagating PPyEtCN polymer.

4.2.4.1.2 Role of the Electrolyte Components

The electrolyte mixture ($LiClO_4$ (0.002 M)/$NH_4H_2PO_4$ (0.100 M)) was chosen as previous studies regarding nanowire formation have indicated that this type of system will promote the growth of polypyrrole nanowires in the direction perpendicular to the electrode surface.[20, 28, 48] However, to the best of our knowledge, this work is the first report utilising this type of electrolyte system to form hollow polypyrrole-based microstructures. It has been proposed that the role of the HPO_4^{2-} or $H_2PO_4^-$ anions during electrochemical deposition of polypyrrole nanowires is to control the vertical growth by acting as a scaffolding agent through H-bonding between the polypyrrole chains.[28] However, interestingly, Debiemme-Chouvy determined during the electrochemical deposition of polypyrrole nanowires from $NaClO_4$ (0.001 M)/Na_2HPO_4 (0.020 M) solutions that the ClO_4^- anion was preferentially incorporated into the polymer to balance the positive charges on the polymer chains.[48] She proposed that when amphoteric HPO_4^{2-} anions are in close proximity to the propagating polymer they become protonated by the H^+ cations which are expelled during polymer formation. This would produce phosphoric acid in its uncharged form (pK_a of H_3PO_4 is 2.6) and therefore does not partake in doping of the polymer backbone. To verify this, experiments were performed in a two-step method. A GC electrode was polymerised in a $LiClO_4$ (0.020 M) emulsion first and then transferred to a $(NH_4)H_2PO_4$ (0.100 M) emulsion for a second stage of

polymerisation. The first step was aimed at nucleating the polymer (growth for 30 s) while the second step was intended to assist growth in a vertical direction (growth for 5 min). Inspection of the electrode after this two-step polymerisation did not show any indication of microtube formation. This highlighted that the perchlorate was required throughout the polymerisation process as the dihydrogen phosphate was not efficiently doping the polymer. This is in conjunction to what was observed when growing the PPyEtCN nanowires in Chapter 3 Section 3.2.3.4.

The $H_2PO_4^-$ not efficiently supporting polymerisation was reflected in the polymerisation transients, in Figure 4.11a, curve 1. Here, the polymer growth profile in a $(NH_4)H_2PO_4$ (0.010 M) emulsion containing no $LiClO_4$ is shown; upon application of the oxidising potential the current density remained very small and dropped as a function of time. The SEM recorded at the end of the process showed no evidence for the formation of a polymer film. In contrast, when $LiClO_4$ (0.020 M) was added to the same polymerisation mixture the growth profile (Figure 4.11a, curve 2) showed a significantly larger current density indicating that an electrochemical deposition was taking place. The first part of the growth curve follows the increase in current density observed for electrolyte systems containing solely $LiClO_4$ (Figure 4.11a, curve 3). However, at *ca.* 20 s the curve reaches a maximum and the rate of polymerisation decreases down to a plateau at *ca.* 80 s which is typical of systems containing a hydrogen phosphate electrolyte.[48] The SEM micrographs recorded of this electrode after 300 s of growth shows the polymer microtubular structures (Figure 4.11c). Additionally, nucleation of the polymer occurs around each toluene droplet simultaneously as the sides of each tube are observed to be identical in height. When polymerisation was performed using only $LiClO_4$ (0.020 M) as the electrolyte, a much more rapid polymerisation was observed in the growth profile (Figure 4.11a, curve 3) resulting in bulk polymer forming around the adsorbed toluene droplets Figure 4.11b. This identifies that reaction conditions which lead to a fast rate of polymerisation are not favourable for producing vertical polymer growth perpendicular from the electrode surface.

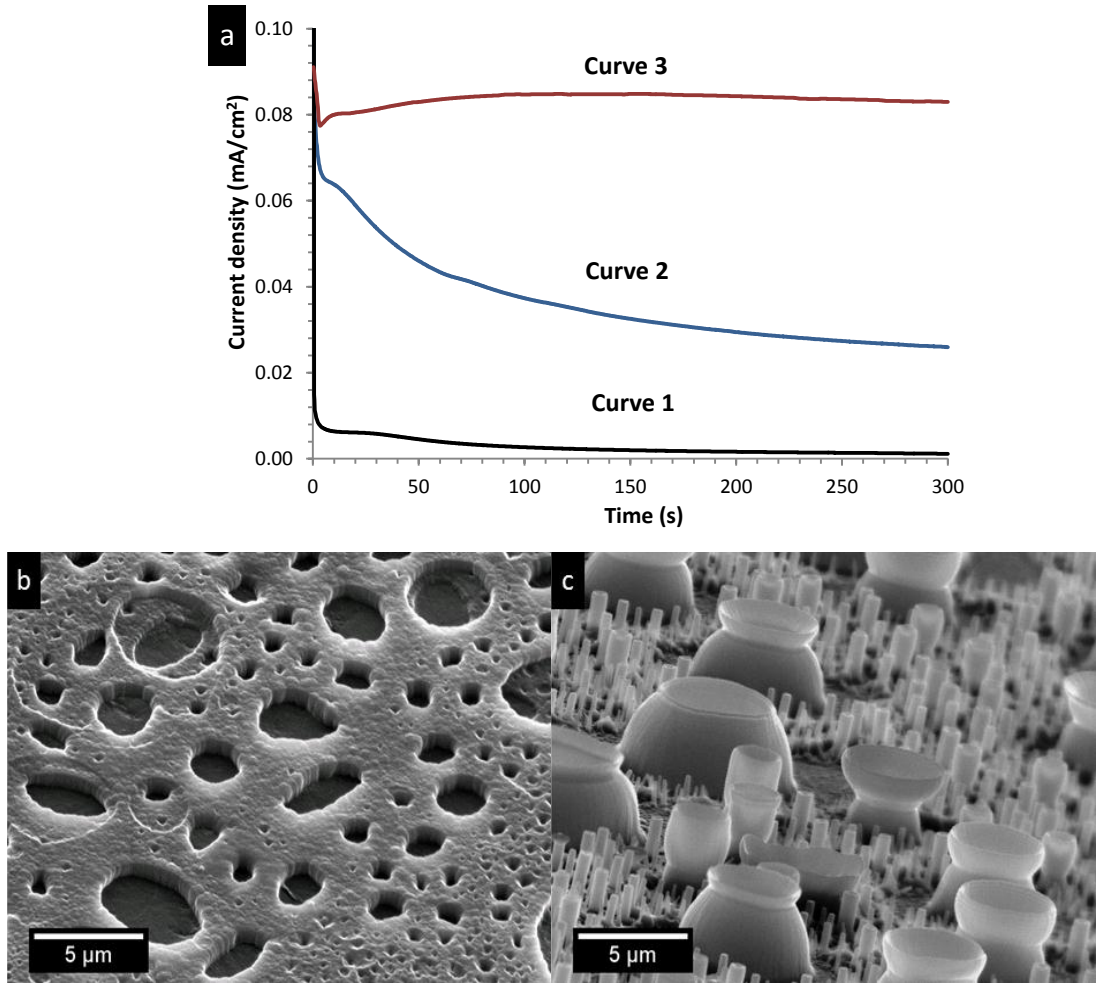

Figure 4.11. Polarisation profile of PPyEtCN polymers deposited from an emulsion mixture containing PyEtCN (0.056 M) and toluene (80 µL) in 10 mL water/ethanol (7:3) with 1 min sonication by probe (a). Electrolytes - curve 1) $(NH_4)H_2PO_4$ (0.100 M), curve 2) $LiClO_4$ (0.020 M) with $(NH_4)H_2PO_4$ (0.100 M) and curve 3) $LiClO_4$ (0.020 M). Oblique-angle view SEM micrograph of resulting polymers (b) and (c) from Figure 4.11a curve 3 and curve 2 respectively.

Using this mixed electrolyte system provided control over the rate of the polymerisation. A number of reports have shown that controlling the kinetics of polymerisation, during electrochemical deposition, is the key to growing conducting polymers in an ordered morphology.[33, 47, 49] In these studies the applied current density was reduced in a stepwise fashion to allow for initial fast nucleation followed by slow propagation yielding uniformly orientated conducting polymer nanowires/tubes. In the present system it was clear from the growth curve (Figure 4.11a, curve 2) that the initial stage of the polymerisation was also rapid. However, this initial fast growth rate was not maintained due to the presence of $H_2PO_4^-$. We propose that the role of the $H_2PO_4^-$ ion was to prevent an increase in H^+ ion

concentration close to the polymer surface as the polymer propagated. Studies have shown that the rate of polymerisation of polypyrrole is increased under acidic conditions.[50] Furthermore, highly protonated solutions lead to the formation of nonconjugated trimers which will be incorporated into the polymer, reducing overall conductivity.[51] This will be reduced within the system studied here leading to a more electroactive polymer.

These results, combined with results from Section 4.2.2 and 4.2.3, outline that for the hollow and vertically aligned microtubes to be produced a stable toluene emulsion is required with both ClO_4^- and $H_2PO_4^-$ doping ions present in solution. If the emulsion has dissipated or if either of the dopants were not present, the polymerisation produces a bulk-like morphology. The aim of the next sections was to investigate whether control over the microtube height and diameter could be obtained by employing different anodic growth potentials and polymerisation times, similar to the PPyEtCN nanowires of Chapter 3. This control is very important, particularly the size of the cavity opening and depth of the tubes, as these will affect the final applications the tubes can be employed in, e.g. encapsulation or drug delivery.

4.2.4.2 Effect of Applied Potential and Polymerisation Time on Morphology

In a typical polymerisation experiment using the ultrasonic probe to create the emulsion it was observed that microtubes were produced between the range of oxidation potentials studied (0.850 - 1.300 V). Regardless of applied potential, it was the adsorbed toluene droplets which influenced growth resulting in the tubular morphology. However, the applied potential determined the rate at which the tubes formed and this was found to influence the shape of the hollow tube structure, Figure 4.12. At a low potential (0.850 V Figure 4.12a) plate like structures were produced which had very little vertical growth. As the potential was increased from 0.900 to 1.000 V in 0.050 V increments (Figure 4.12b, 4.12c and 4.12d respectively) the final morphology resembled a more bowl-like structure as the polymer took the shape of the adsorbed toluene droplet to a greater extent. Furthermore, the polymer growth extended in a vertical direction and the tubes increased in height, this has also been observed for other PPy microtube systems.[14, 16] At higher oxidising potentials of 1.100 and 1.200 V (Figure 4.12e and 4.12f) the tubes had increased substantially in

height but were also observed to have an increase in diameter at their openings. Increasing the potential to 1.300 V formed the microtubes, but large cracks appeared throughout the film due to the excessive amount of polymer loading on the electrode.

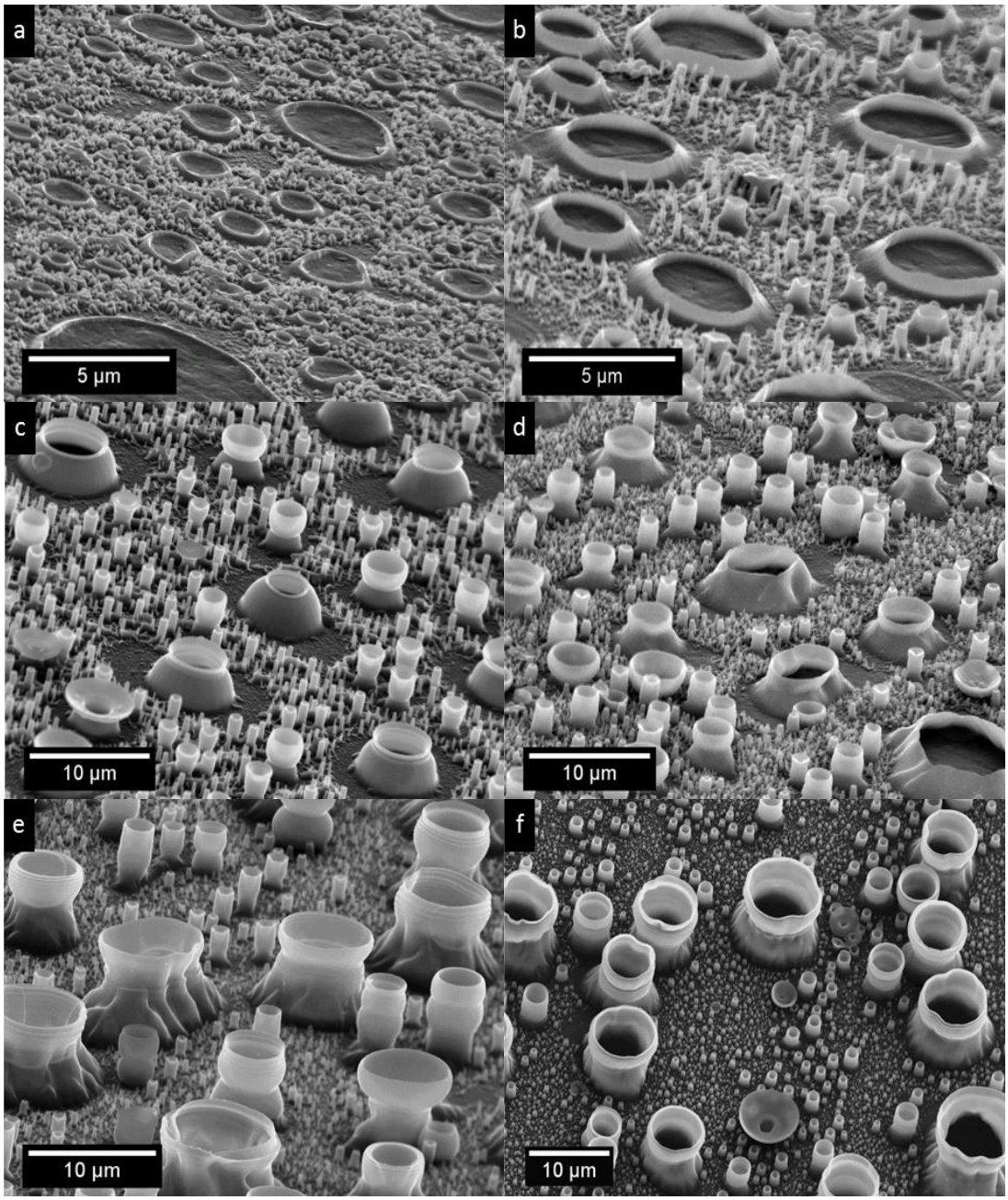

Figure 4.12. SEM micrographs of microstructures deposited at (a) 0.850, (b) 0.900, (c) 0.950, (d) 1.000, (e) 1.100 and (f) 1.200 V. Emulsion: PyEtCN (0.056 M), $LiClO_4$ (0.020 M), $(NH_4)H_2PO_4$ (0.100 M), toluene (80 µL) in 10 mL water/ethanol (7:3) with 1 min probe sonication.

These morphologies are very similar to what Qu and Shi *et al.* observed when they developed hollow microstructures of polypyrrole using poly(styrene sulfonic acid)

(PSS) and camphorsulfonic acid (CSA) respectively.[14-16, 52] They reported a high density of microtubes (2000 units/cm^2) with thin exterior skins (< 1 μm) which were smooth and compact. Their tubes, similar to ours, could be removed from the electrode while maintaining their tubular structure, signifying strong structural integrity. Their growth mechanism is based on the formation of O_2 bubbles at the working electrode which were stabilised by a surfactant. These bubbles then act as a template to direct growth similar to the way toluene performs in our system. Their procedure has the advantage of being able to form microtubes with a very narrow size distribution. It was also observed however, that their growth was limited to aqueous electrolytes since the generated O_2 bubbles could not be enwrapped by surfactant in organic media,[14] this would limit the use of nonpolar functionalised monomers studied here, i.e. PyEtCN.

Inspection of the recorded polarisation curves from the PPyEtCN microtube films shown in Figure 4.12 reveals some interesting trends. It can be seen in Figure 4.13 that at low potentials, such as 0.750 V, the current remains very low and shows no section with a rising transient. This was indicative of the absence of an electrochemical reaction occurring.[53] Furthermore, SEM analysis of the electrode after polymerisation did not display any signs of polymer growth. Increasing the potential to 0.850 V led to an initial small increase of current until ~ 15 s and this was maintained over the entire polarisation time. This suggested that some polymer was being deposited and was confirmed by inspection of the SEM in Figure 4.13a. Further increments of the applied potential from 0.900 to 1.000 V showed that the system responds as expected; as more energy was applied to the electrode the polymerisation increased correspondingly.[53] This was evident from the current responses which gradually became larger with increasing potential. However, if the 1.000 and 1.100 V transients are examined it can be seen that the currents show a significant drop from their starting values until 100 s. Furthermore, in the 1.100 V transient, a constant and significant drop in current was observed, eventually dropping below the values obtained for the 1.000 V experiment. This may be due to the fact that at these higher applied potentials the rate of polymerisation will be very rapid. Since a significant amount of polymer would have formed on the electrode during initial nucleation, further growth at these thicker layers may have been hindered. This will be compounded by PPyEtCN polymers possessing insulating

properties at these high potentials due to over-oxidation.[54] Another reason for these decreasing currents may arise due to the electrode consuming all the available monomer at the surface in a very short time forming a larger diffusion layer.[55] Fresh monomer must diffuse from the bulk solution and this is generally the slow step in electrochemical processes.[53]

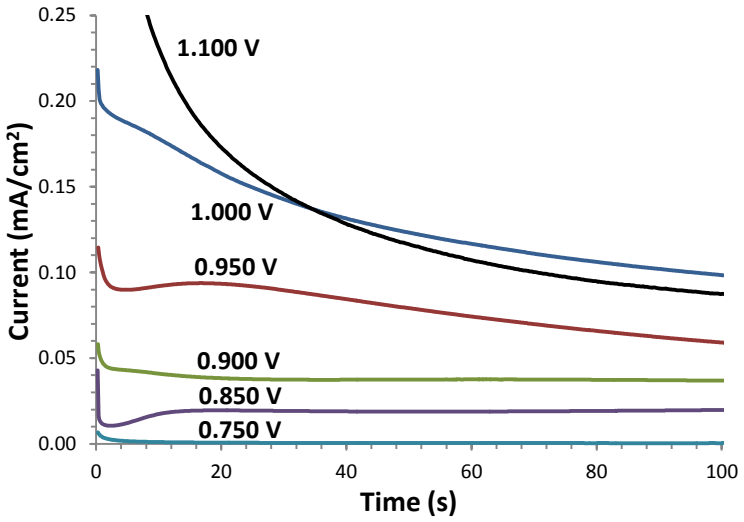

Figure 4.13. Polarisation profile of PPyEtCN polymers deposited at 0.750, 0.850, 0.900, 0.950, 1.000 and 1.100 V from an emulsion mixture containing PyEtCN (0.056 M), $LiClO_4$ (0.020 M), $(NH_4)H_2PO_4$ (0.100 M) in 10 mL water/ethanol (7:3) with 1 min sonication by probe.

Upon closer inspection of the SEM micrographs of the PPyEtCN microtubes it was seen that the areas surrounding the microtubes had very little polymerisation present, Figure 4.14a. In the toluene/water emulsion experiments carried out by Mazur and co-workers, using chemical oxidation, it was clear that most of the pyrrole monomer resided inside the toluene droplets as polymerisation only occurred at the surface of the droplets and not in the bulk solution.[29] Similarly, in the present system, the preferential formation of PPyEtCN at the toluene droplet interfaces indicates that when using the probe sonicator a substantial proportion of the PyEtCN monomer was contained within the toluene droplets. As the duration of sonication time was increased the average diameter of the tubes decreased. This observation is consistent with the known literature regarding droplet size as a function of sonication time[45] and it allows a means of controlling the size of the tubes. It was also observed using the probe sonicator that initial sonication produced a very opaque emulsion. However, if the sonication time surpassed 60 s the solution would begin to revert to clear. At 75 s

the solution would become completely transparent and not return to its original multiphasic state. This has been shown to be the formation of a nanoemulsion and signifies that this system could be employed to fabricate hollow nanotubes.[35]

Interestingly, for prolonged periods of growth (30 min) a second stage of microtube nucleation was observed, yielding smaller tubes developing within the larger tubes, Figure 4.14b and 4.14c. Growth of these smaller microtubes always evolved from the inner walls of the bigger microtubes and was never observed from the base center. This indicates that the toluene droplets adhere strongly to the substrate throughout the polymerisation process and prohibit polymer growth at these sites. It can also be concluded that the emulsion droplets formed by this method are very stable since fresh droplets are still available for polymerisation even over long periods of time. This second stage of nucleation of 'tubes inside tubes' was not observed for the lower potential of 0.850 V, Figure 4.14d; instead polymerisation continues at the walls of the microcontainers eventually leading to their collapse, Figure 4.14d inset. It can be concluded that a lower oxidising potential (0.850 V) was not capable of promoting new nucleation on the insulating PPyEtCN surface, however, once enough energy was applied (0.950 V) new polymerisation sites were favoured which produced a novel morphology. This morphology, due to its unique hierarchical structure, most likely possessed hydrophobic water interactions, a characteristic which would have been investigated if time had permitted.

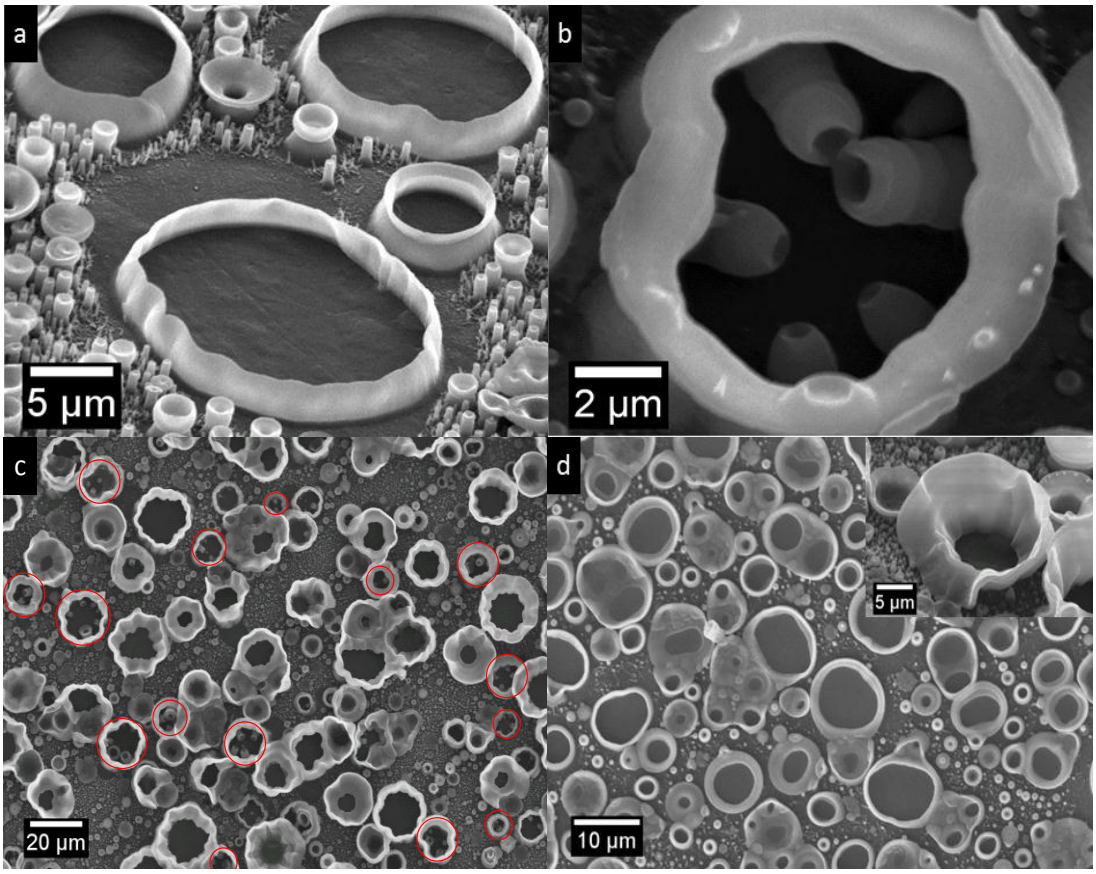

Figure 4.14. SEM micrograph of PPyEtCN microstructures deposited at 0.950 V for (a) 5 min and (b) high and (c) low magnification of polymerisation after 30 min. Microtubes produced at 0.85 V for 30 min (d). Emulsion mixture contained PyEtCN (0.056M), $LiClO_4$ (0.020 M), $(NH_4)H_2PO_4$ (0.100 M) and toluene (80 µL) in 10 mL water/ethanol (7:3) with 45 s sonication by probe.

While SEM is a useful tool for identifying the hollow character within the tubes using a top-down view, it does not have the resolution to distinguish smaller tube openings at high magnifications nor does it give structural density measurements over the whole microtube. Employing TEM can overcome these limitations since the electrons are fired at a much higher speeds it allows them to easily pass through thin materials. Excellent resolution is also achieved at much greater magnifications using these higher electron accelerating speeds, as the electrons have a smaller wavelength associated with them.

TEM micrographs recorded for individual smaller tubes (< 500 nm) show that the hollow cavity extends the entire length of the structure, Figure 4.15a. It also confirms that the tube morphology remains intact despite being removed from the surface and sonicated, indicating high structural stability.[16] High magnification TEM analysis of the outer walls showed that there was a dense packing of polymer surrounding the

hollow interior, Figure 4.15b. This high density in the tube walls most likely arises due to the combination of slow rate of polymer propagation (common in phosphate based electrolytes) combined with the preferential polymerisation at the droplet surface. The electron diffraction pattern, which shows a diffusive ring, Figure 4.15a inset, identified the microtubes as having an amorphous structure.[39]

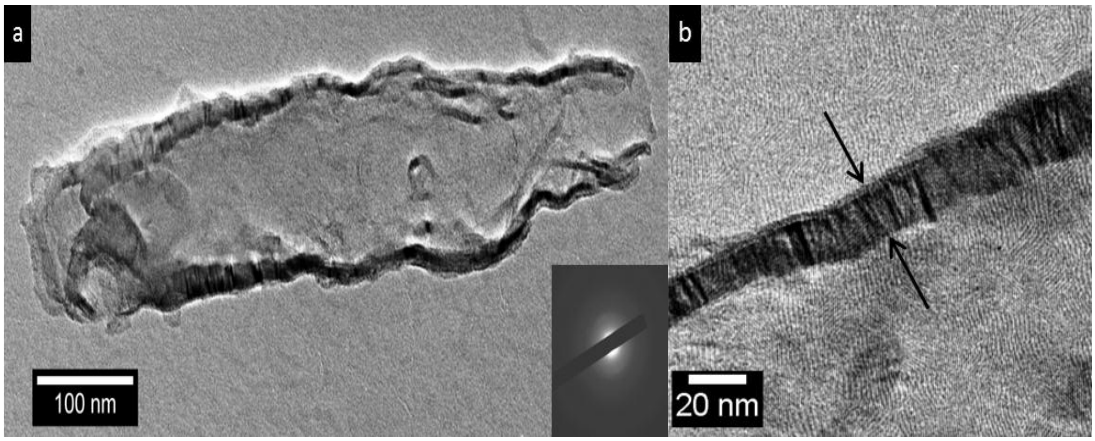

Figure 4.15. TEM micrograph of individual PPyEtCN tube (a) and magnification of exterior wall area of tube (b). Emulsion mixture contained PyEtCN (0.056 M), $LiClO_4$ (0.020 M), $(NH_4)H_2PO_4$ (0.100 M) and toluene (80 µL) in 10 mL water/ethanol (7:3) with 1 min sonication by probe.

Since surface morphology of the microtube polymers was fully characterised using SEM and TEM analysis and a reasonable ability to control the microtube height and morphology had been demonstrated; the next step was to investigate their surface wetting and electrochemical properties and relate these to the doping levels within the polymer. The benefit of synthesising nanomaterials is that quite commonly they have superior electrochemical and wetting properties compared to bulk materials.[56-57]

4.2.4.3 Microtube Surface Wettability

The surface wettability is a very important characteristic for solid state materials as it will strongly influence possible practical applications. Wettability is most commonly described with reference to the leaf surfaces of hydrophobic plants. In particular the water repellant properties of the lotus leaf have attracted much attention.[58] The surfaces of these leaves have been observed by SEM to be covered in micro and nano structured 'bumps' in a hierarchical fashion,[59-60] which leads to an increase in the surface roughness and to an increased hydrophobicity.[61] Surface wettability is measured by placing a water droplet on a surface and measuring the external angle between the surface and droplet. Contact angles above 90^{o} signify hydrophobicity and below 90^{o} indicate hydrophilicity.

Static water contact angle measurements were carried out on PPyEtCN films for both the bulk and microtubule morphologies and resulted in average values of 19^{o} and 38^{o} respectively, indicating that both films had superhydrophilic properties. This has previously been shown for *N*-substituted polypyrrole films containing a polar functional group.[62] Inspection of Figure 4.16a shows the bulk PPyEtCN films allow the water droplet to spread over the film, signifying hydrophilicity. The microtube film also maintained this hydrophilic property, but did not allow the droplet to spread as significantly, Figure 4.16b. It can be seen from Table 4.1 that the bulk polymers were generally more hydrophilic than their microtube counterparts by 20^{o} and as the growth potential was increased both films displayed a slight increase in hydrophilic character. It is known that contact angle results are very sensitive to polymer preparation methods and can be effected by the type of dopant incorporated[63] and oxidation state of the polymer.[64-65] Switching between wettabilities has also been observed by applying different electrical potentials which controls the movement of ions in and out of the film.[66]

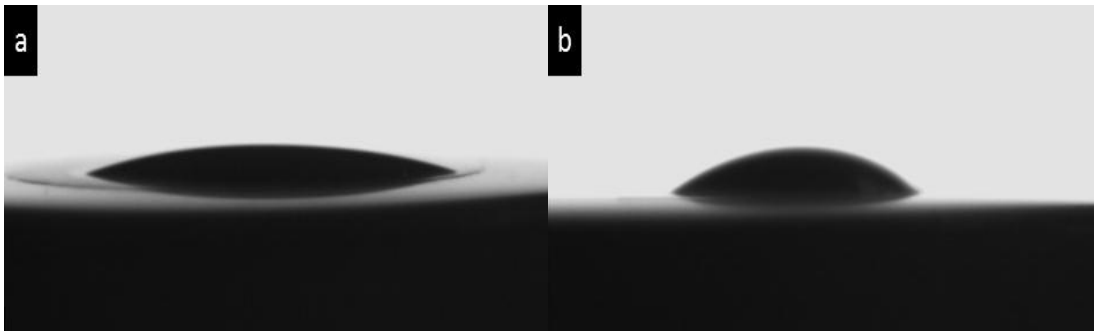

Figure 4.16. Contact angle image of water droplet (1µl) exposed to (a) bulk PPyEtCN and (b) a microtube film of PPyEtCN. Experimental conditions outlined in Table 4.

Table 4.1. The water contact angles at different growth potentials for both bulk and microtube films. Emulsion mixture contained PyEtCN (0.056 M), $LiClO_4$ (0.020 M), $(NH_4)H_2PO_4$ (0.100 M) in 10 mL water/ethanol (7:3) with 1 min sonication by probe. For PPyEtCN microtubes toluene (80 µL) was added to the polymerisation mixture to form the emulsion.

Growth Potential	Contact Angle	
Voltage (V)	Bulk (°)	Microtubes (°)
0.850	21.5	42.9
0.900	17.3	37.0
0.950	17.2	36.3

The influence of the microtubes on the contact angle of the polymer films can be explained by several reasons. It could be that the microtubes have a higher surface roughness i.e. hierarchical in nature,[57, 64] they are in a more oxidised state[65] or their large dimensions produce air pockets.[67-68] It is most likely that the latter reason predominantly governs the increase in hydrophobicity since it is clear that the microtubes do not possess an increased roughness on the nanoscale, Figure 4.11c. Furthermore, they have been polymerised at the same potential and concentration of dopants as the bulk polymer so are likely to be in the same oxidation state. Zhu and co-workers identified an increase in contact angle for polymer nanopillars as their diameter decreased.[67] This decrease in pillar diameter allowed for a greater fraction of air between each structure. This higher proportion of air was responsible for the enhancement of the contact angle. Furthermore, in their in-depth paper on contact

angle mechanisms, Lui and Choi reported that if the water droplet is larger than the size of the microstructure that it will bridge the tips of the microstructure and entrap air beneath.[68] As we have shown previously the microtubes clearly have an empty cavity which could be filled with air leading to an increase in hydrophobic character.

These contact angle measurements prove that these hollow microtubes are capable of increasing the hydrophobicity of a surface. This is an interesting characteristic as common hydrophobic materials are employed in self-cleaning applications. Since this toluene emulsion procedure is not limited to the PPyEtCN monomer studied here, it should be possible to introduce a monomer with a long chain substituent and develop microtubes which would create superhydrophilic materials.

4.2.4.4 Electrochemical Characterisation

Cyclic voltammograms (CVs) were recorded of both microtubule and bulk (grown in the absence of toluene) PPyEtCN films, Figure 4.17. As can be observed from the CVs, the PPyEtCN microstructures (red line) have an increased electrochemical response compared to a bulk polymer (blue line). A weak reduction peak was observed for the bulk film indicating that dopant expulsion was more difficult. If the expulsion was a slower process it would happen over a larger potential window leading to a broader peak.[69] This may occur due to the slow rate of growth of this film leading to an increased compactness. The microtubes however, show typical redox properties with anodic and cathodic I_p corresponding to the oxidation and reduction of the polymer backbone.[69] The I_p are larger for the microtube polymer due to the greater ease at which the bulk electrolyte solution can dope and de-dope the polymer. This is due to the increased amount of electrolyte which can interact with the polymer due to the greater surface area supplied by the tubular morphology.[70] It is also observed that the oxidation of the polymer, shown at approximately 0.690 and 0.570 V respectively, for bulk and tube morphologies, was shifted to lower overpotentials for the microtube polymer. This signifies that the charge transport is easier when the microtubes are present and would arise due to their higher porosity compared to the bulk polymer.[71]

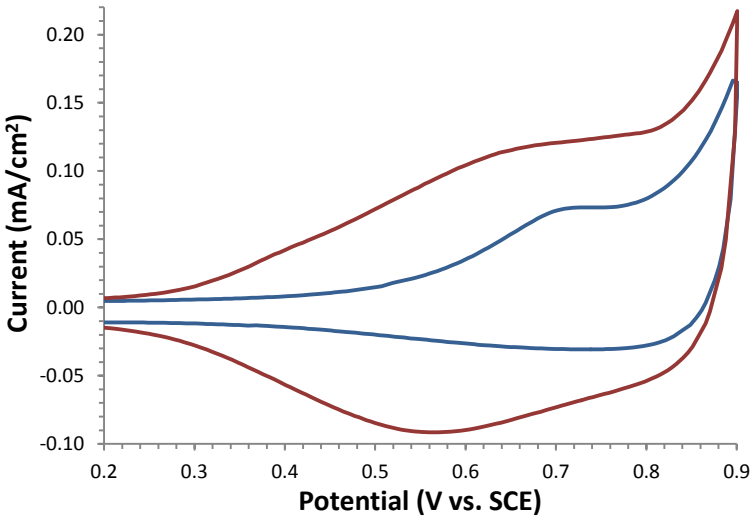

Figure 4.17. Cyclic voltammograms performed at 50mV/s in 0.100 M $LiClO_4$ between 0.000 and 0.850 V for PPyEtCN microtubes (red line) and bulk PPyEtCN (blue line). Emulsion mixture contained PyEtCN (0.056 M), $LiClO_4$ (0.020 M), $(NH_4)H_2PO_4$ (0.100 M) in 10 mL water/ethanol (7:3) with 1 min sonication by probe. In the case of the PPyEtCN microtubes toluene (80 μL) was added.

An increase in both the anodic and cathodic currents and a shift in potentials to more favorable values may indicate better electrical properties of the microtube films. A similar increase in electrochemical activity was observed for PPy nanowires and was attributed to a higher specific surface area present for the nanowires compared to the bulk polymer.[72] These characteristics of controllable surface wettability and increased electrochemical response are desirable attributes for a polymer material. Since both of these properties are dopant dependent, it was prudent to investigate the doping mechanism for the microtubes and ascertain if they deviate from the PPyEtCN nanowires discussed in Chapter 3.

4.2.4.5 Investigation of Dopant Ratio's by EDX Analysis

In Chapter 3 the EDX spectra for the PPyEtCN nanowires were recorded at different time intervals. This revealed that $H_2PO_4^-$ was incorporated into the polymer to a greater extent at longer polymerisation times. Herein, we repeat this study for the microtube polymers. Furthermore, we extend this EDX analysis to investigate microtube polymers as a function of applied potential, since this has the greatest effect on the microtube morphology. EDX measurements are very sensitive to

surface morphology and structure. Since X-rays are the lightest of the radiation types they can be adsorbed and deflected even by thin materials. Therefore it was important to be confident that the results obtained were real and not outliers of sites with high or low concentrations of certain elements. This would give misleading readings and not represent the whole electrode surface. As an example, taking EDX measurements at five sites on a microtube polymer it was observed (for e.g. carbon) that the min/max range was sufficiently narrow (95.07 and 96.24% atomic), while the standard deviation was 0.44% atomic. It can therefore be concluded that the mean value, taken over 5 sites of interest, is a sensible indicator of the elemental composition of the entire electrode.

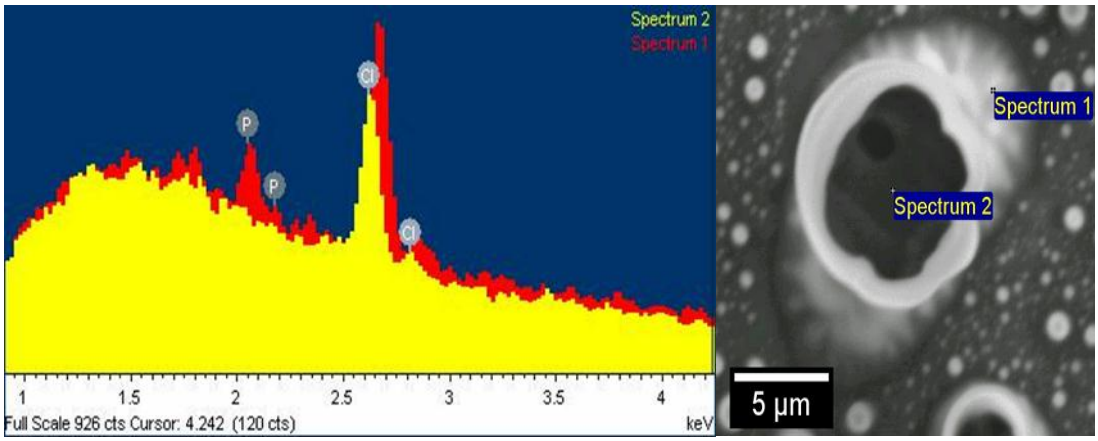

Figure 4.18. EDX spectrum and corresponding site of acquisition of PPyEtCN polymer deposited from an emulsion mixture contained PyEtCN (0.056 M), $LiClO_4$ (0.020 M), $(NH_4)H_2PO_4$ (0.100 M) and toluene (80 µL) in 10 mL water/ethanol (7:3) with 1 min sonication by probe.

A typical EDX spectrum of PPyEtCN microtubes is given in Figure 4.18. Here it can be observed that chlorine signals at 0.18, 2.62 and 2.82, phosphorus at 2.09 and 2.20 are present as a consequence of doping polymer backbone. Interestingly, when EDX measurements were obtained from inside the cavity and on the exterior walls (similar to Section 4.2.1, Figure 4.2) it was observed that only chlorine was present in the center cavity, Figure 4.18, Spectrum 2, while both chlorine and phosphorus are present in the exterior walls, Figure 4.18, spectrum 1. This result was validated by taking measurements over several microtubes and is consistent with some $LiClO_4$ being soluble in toluene.[31] However, it is obvious that the bulk electrolyte which consisted of H_2PO_4 was not present within the cavity. As there was relatively small concentration of LiClO4 in the electrolyte there would be a high resistance within the

toluene droplets due to the lack of electrolyte. This would prohibit any electrochemistry taking place inside the droplet. Since the phosphate was only detected in places where polymer was deposited, this further confirms that the tubes synthesised by the toluene emulsion method have little to no polymer deposited at their base and are hollow.

EDX spectra of PPyEtCN microtubes grown at 0.95 V for various time intervals (60, 120 and 300 s) indicate that both perchlorate and phosphate anions were present in the polymer matrix. Inspection of the quantitative data for the 120 and 300 s polymers shows approximately a 1:1 ratio of phosphorus to chlorine despite the 5:1 ratio of phosphorus to chlorine in the electrolyte mixture (as $H_2PO_4^-$ and ClO_4^- anions), Table 4.2. This would indicate that the perchlorate anion was the preferred dopant over the phosphate anion, as also seen in Chapter 3 for the PPyEtCN nanowires.

Table 4.2. EDX quantitative data for PPyEtCN microtubes grown for 60, 120 and 300 s. Emulsion mixture contained PyEtCN (0.056 M), $LiClO_4$ (0.020 M), $(NH_4)H_2PO_4$ (0.100 M) and toluene (80 µL) in 10 mL water/ethanol (7:3) with 1 min sonication by probe.

	Results in atomic composition (%)			
Growth Time (s)	Carbon	Oxygen	Phosphorus	Chlorine
60	99.02	0.87	0.06	0.04
120	98.44	1.28	0.13	0.14
300	95.80	3.94	0.11	0.10

However, when the 60 s data was examined it was observed that the phosphate (on average) was present by 30% more at this time. As explained previously (Section 4.2.4.1.2), the pH at the electrode increases due to the release of protons during polymerisation; this protonates the dihydrogen phosphate dopant producing the neutral phosphoric acid which will not partake in doping.[73] However, when the oxidising potential is applied the majority dihydrogen phosphate will be in the charged form, only transforming to H_3PO_4 when the change in pH is induced by polymerisation. Therefore, there is sufficient $H_2PO_4^-$ anion concentration to partake

in doping at these early times. This is reflected in the EDX data in, Table 4.2, where a higher amount of phosphorus was recorded compared to the chlorine, at earlier times.

The result of chlorine/phosphorus being present in equal amounts is not what has been observed in the literature for similar systems. As discussed previously (Section 4.2.4.1.2) Debiemmie-Chouvy[48] found using Py that the amount of chlorine compared to phosphorus present after polymerisation of nanowires was 10 and 90% respectively. This would suggest that the pH during the propagation of pyrrole is much lower than the PyEtCN system. Since Py has a lower oxidising potential compared to PPyEtCN it will oxidise faster at the same potentials.[22, 74] Therefore, Py propagation will produce more H^+ being released into solution. Likewise PPyEtCN propagates slower and therefore a higher pH will be observed at the double layer leading to more $H_2PO_4^-$ anions doping the polymer as they are less likely to become protonated. Therefore, if the polymerisation rate of PPyEtCN was increased, through increases in the oxidising potential, the pH at the electrode should decrease and protonate more $H_2PO_4^-$ ions. This would lead to a greater proportion of the neutral phosphoric acid being formed which is incapable of doping. Indeed this was observed at potentials of 1.100 and 1.200 V for the PPyEtCN microtubes, Table 4.3.

Table 4.3. EDX quantitative data of PPyEtCN polymers deposited at 0.950, 1.100 and 1.200 V. Emulsion mixture contained PyEtCN (0.056 M), $LiClO_4$ (0.020 M), $(NH_4)H_2PO_4$ (0.100 M) and toluene (80 µL) in 10 mL water/ethanol (7:3) with 1 min sonication by probe.

	Results in atomic composition (%)			
Growth Potential (V)	Carbon	Oxygen	Phosphorus	Chlorine
0.950	95.80	3.94	0.11	0.10
1.100	97.72	1.50	0.15	0.63
1.200	95.93	2.03	0.13	1.91

As shown in Table 4.3, at oxidising potentials of 0.950, 1.100 and 1.200 V the amount of chlorine registered by EDX was 0.10, 0.63 and 1.91 (% atomic) respectively. These results indicate that for the polymerisation at 1.200 V, approximately 93.4% of the dopant was perchlorate and only 6.37% was phosphate. It can therefore be concluded that by increasing the oxidising potential and therefore the growth rate, the pH close to the electrode decreased resulting in the polymer being predominantly doped by perchlorate anions as the neutral phosphoric acid was generated at a higher rate.

To conclude, the microtubes formed by the probe sonication method are hollow and can be controlled by the growth potential. A hybrid morphology of 'tubes inside tubes' was produced at longer polymerisation times. PPyEtCN surfaces display typical superhydrophilic properties, which increases to a more hydrophobic character with the presence of the microtubes. Electrochemical characterisation shows the microtubes are more electrochemically active than their bulk counterpart, while EDX data shows the doping ratios are similar to those observed for the PPyEtCN nanowires. The perchlorate anion was incorporated to a greater degree when the oxidising potential was increased due to a decrease in the local pH producing more phosphoric acid which was incapable of doping. The next section will focus on the morphology obtained using the bath sonicator method while employing the same polymerisation electrolyte.

4.2.5 Method B: Bath Sonicator

When the polymerisation of PyEtCN was carried out from an emulsion formed using a bath sonicator, inspection of the resulting film, Figure 4.19, revealed interesting morphological differences compared to the films observed using the emulsion formed Method (A) (Section 4.2.4, Figure 4.8).

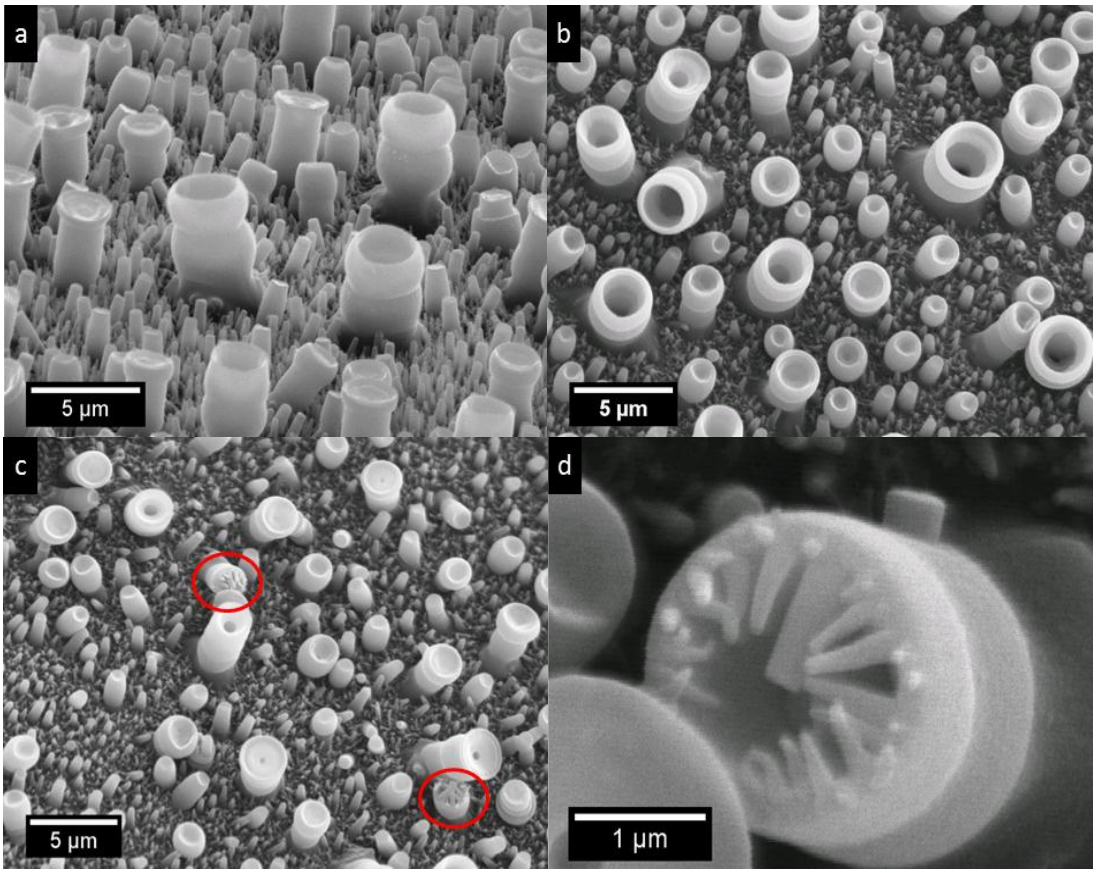

Figure 4.19. SEM micrographs of PPyEtCN polymers grown at 0.950 V for 10 min (a) side view and (b) top-down view. (c) low magnification and (d) high magnification of second stage of nucleation. Emulsion mixture contained PyEtCN (0.056 M), $LiClO_4$ (0.020 M), $(NH_4)H_2PO_4$ (0.100 M) and toluene (60 µL) in 10 mL water/ethanol (7:3) with 1 min sonication by bath.

SEM micrographs recorded after 5 min polymerisation, at an applied potential of 0.950 V, revealed that open-ended circular microtubes were formed. As is clear from Figure 4.19b, hollow open ended tubes are only observed for the larger diameter structures. A large proportion of the polymer growth was comprised of medium sized diameter nanowires (~ 500 nm) and there is a much more varied height distribution between the tubes compared to polymers formed Method (A). Their surface coverage was more random in nature with only a proportion of tubes being aligned vertically

from the electrode. Interestingly, some of the tips of the microtubes had a second stage of growth at longer polymerisations as seen previously for the 'tubes inside tubes' in Section 4.2.4.2, Figure 4.14. However, in this case the growth of smaller nanowires initiated at the rim of the original microtube and protruded in towards the center, Figure 4.19c and 19d. As Figure 4.19c shows these were observed for the minority of tubes and only in certain sections of the film. It is also apparent that this type of second nucleation which has been observed in some form for both sonication (bath and probe, at 0.950 V) was not present for the emulsions produced by stirring. This further highlights the increased stability given to the toluene emulsion from sonication techniques. These experiments also highlight that the sonication method has a large impact on the extent of hollow character obtained by the microtubes.

4.2.5.1 Effect of the Concentration of Toluene

A study was performed to ascertain the effect of the toluene concentration on the microtube morphology. For consistency all the polymers were grown at 0.900 V. The concentrations of toluene used were 20, 60, 80 and 120 µl. As can be seen from Figure 4.20a, when 20µl of toluene was used in the polymerisation mixture only short stumpy nanowires were produced. While for the higher concentration of toluene, 120 µl completely open ended tubes were evident, Figure 4.20d.

Employing intermediate concentrations of toluene (60 and 80 µl) produced a similar trend with more toluene leading to larger microtubes with bigger openings. When measurements were taken of the inner diameters of the tube openings (excluding the diameter of the wall) a trend was evident. At 20, 60, 80 and 120 µl toluene the average openings for the resultant microtubes were 0 nm, 496 nm, 1.866 µm and 3.886 µm respectively. In the films produced with 120 µl toluene the areas in-between the larger hollow tubes showed structures which were larger in size than typically present at all other concentrations of toluene. These circular structures all have dimpled or concave tips which is not seen for the lower concentrations, Figure 4.20d. Clearly the higher concentration of toluene has an effect on the morphology of the entire polymer leading to an increase in hollow character for all sized structures. Therefore, it is evident that, like polymerisation potential, the concentration of

toluene added to the polymerisation mixture can be an effective means of controlling the size of the resultant microtubes. However, the bath sonication method is not as effective at producing the hollow character within the microstructures compared to the probe sonication (Method (A)).

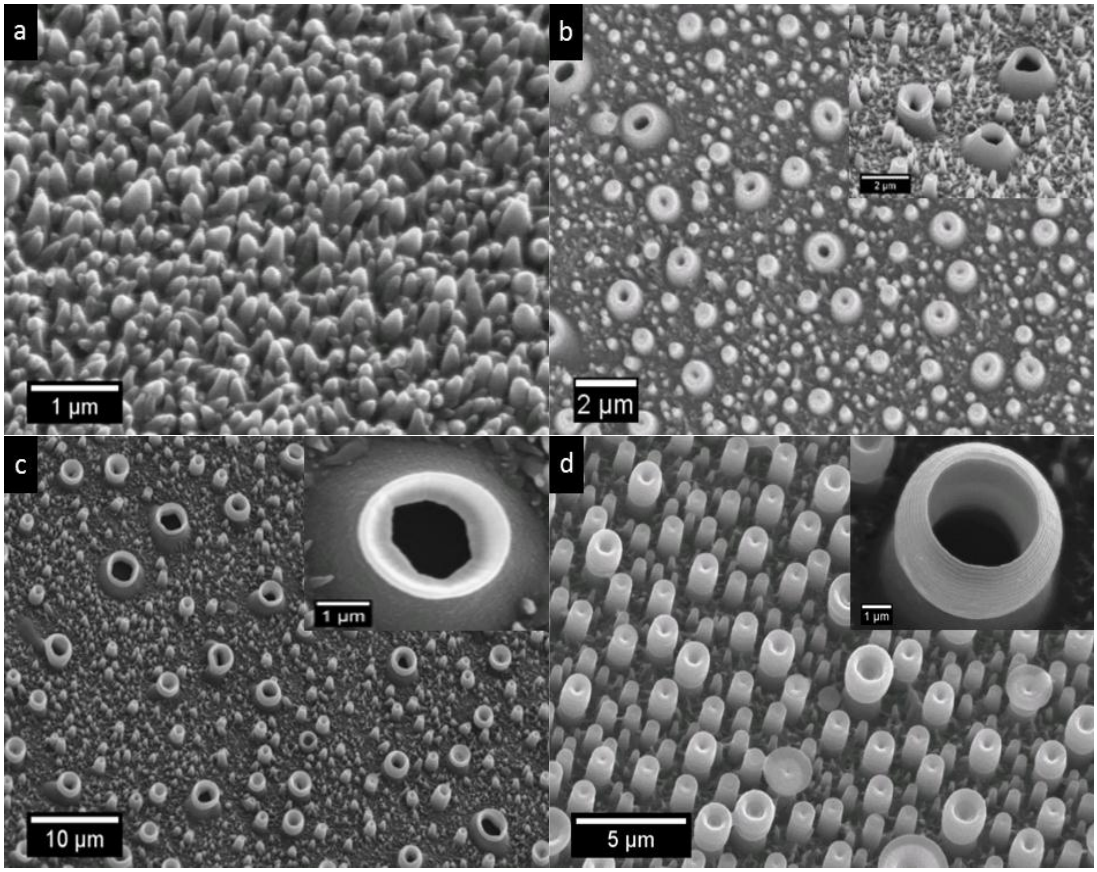

Figure 4.20. SEM micrographs of PPyEtCN polymers grown using (a) 20, (b) 60, (c) 80 and (d) 120 µl of toluene. Emulsion mixture contained PyEtCN (0.056 M), $LiClO_4$ (0.020 M), $(NH_4)H_2PO_4$ (0.100 M) in 10 mL water/ethanol (7:3) with 1 min sonication by bath.

4.2.5.2 Effect of Substrate Composition and Orientation

The composition of the substrate material and its orientation were investigated to ascertain whether the microtubes only formed at certain materials. This is important as in some electrochemical/spectroscopic processes only specific substrates can be employed (i.e. indium-tin-oxide (ITO) in UV-Vis). Different materials including Au, Pt and ITO were used as alternate substrates. It was observed that these substrates were capable of growing the microtubes with similar morphologies as shown previously, with Pt shown as an example in Figure 4.21a. While these results indicate

that the substrate had little effect on the resultant morphology, this was not the case if the substrate was excessively rough or fractal. Here, Figure 4.21b, it can be seen that the microtubes are not present in the same consistent manner as seen for smooth electrodes. Random micro and nanowires are present at the scratch sites. This is consistent with the toluene adsorption being the principal effect determining the successful growth of a uniform microtube film, as adsorption was hindered at the roughened substrates. Therefore, it is apparent that the microtubes will polymerise on most conducting substrates regardless of composition as long as the toluene is capable of adsorption. This is consistent with what was discussed in Section 4.2.4.2 where the toluene was observed to undergo a strong adsorption to the substrate as further growth was not observed at the microtube base center over long polymerisation times.

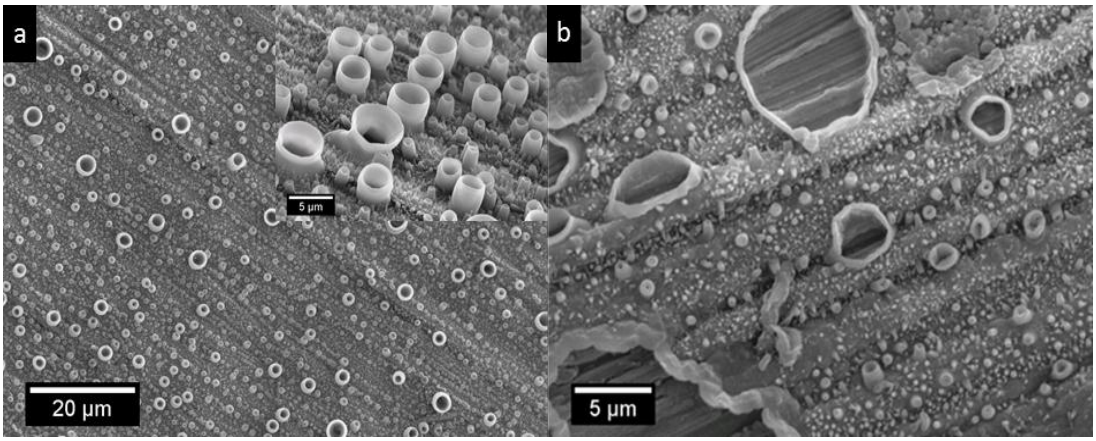

Figure 4.21. SEM micrographs of PPyEtCN polymers grown at (a) polished Pt and unpolished Pt electrodes (b) for 20 min using 0.056 M monomer, 80 µl toluene, with PyEtCN (0.056 M), $LiClO_4$ (0.020 M), $(NH_4)H_2PO_4$ (0.100 M) with 1 min sonication at 0.900 V.

Further investigation of this strong adsorption process was done by employing different orientated electrodes. The electrodes were perpendicularly orientated (with reference to the solution surface) and allowed to sit in the emulsion solution for 5 min to allow the toluene droplets to adsorb, as shown below in Figure 4.22. The microtubes were produced at the electrode similar to what has been shown for the electrodes orientated parallel to the solution surface, Figure 4.23a. The ability to form PPyEtCN microstructures was observed at both metal and carbon electrodes regardless of the electrode orientation. This further highlights the toluene adsorption as the critical process in producing microtubes. Furthermore, the density of the

microtubes formed in the experiments using perpendicularly aligned electrodes was uniform over the electrode, Figure 4.23b. This suggests that buoyant forces are not a predominant effect during microtube growth.

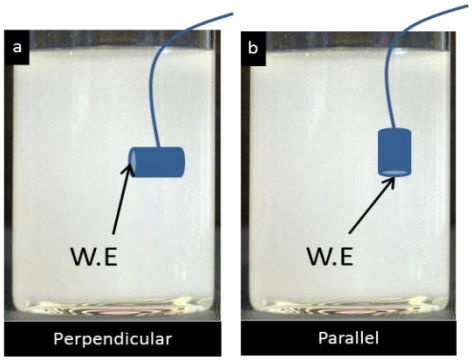

Figure 4.22. Diagram of polymerisation solution with different orientations of the working electrode with reference to the solution surface (a) perpendicular and (b) parallel.

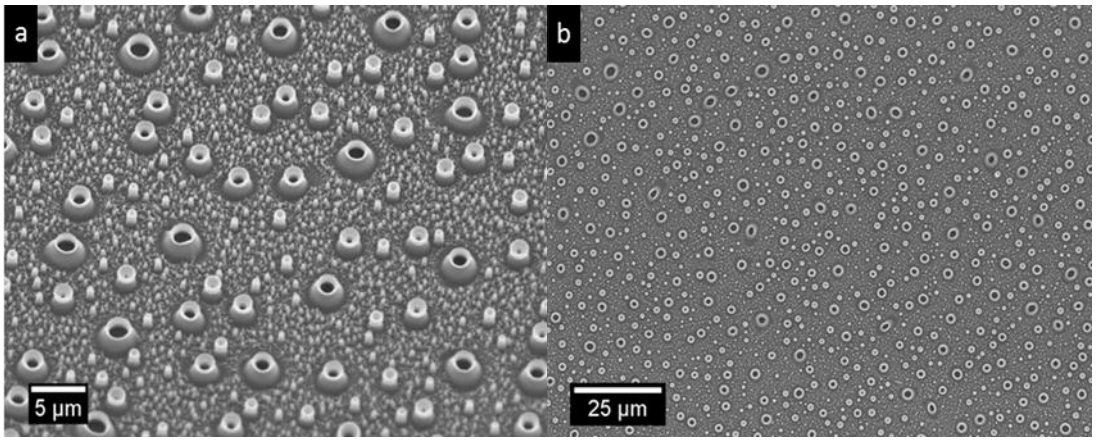

Figure 4.23. SEM micrographs of microtubes grown at an electrode aligned perpendicular to solution surface (a) high magnification with tilting and (b) low magnification.

Sections 4.2.5.1 and 4.2.5.2 highlight that the emulsion mixture used to form the microtubes was very versatile. Extra additions of toluene had a direct effect on the microtube size. This, in conjunction with the applied potential and sonication time, shows that this emulsion procedure was easily altered to control the microtubes diameter. Furthermore, from the studies on substrate materials, it is apparent that the microtube morphology was only dependant on the ability of the toluene to adsorb. Interestingly, combining the bath sonicator with a low growth potential produced a closed container morphology. This is discussed within the next section.

4.2.5.3 Synthesising Closed Microcontainers

Similar to the microtubes formed by Method (A), the effect of the applied potential and polymerisation time were also investigated for the polymer formations produced by Method (B) emulsions. It can be seen from an SEM micrographs recorded after 5 min at an applied potential of 0.850 V, that the microstructures originally formed in an open tube morphology, Figure 4.24a. However, as polymerisation continued (30 min) the opening of the tubes grew towards the center and tapered completely closed, Figure 4.24b. This was also seen by Martin and co-workers for their work on the template growth of PPy polymer tubes.[75] Similar to our system, they observed that when extended polymerisation times were employed the PPy tubes closed over to form fibrils. For the PPyEtCN microtubes, TEM analysis was performed to ascertain if they maintained a hollow cavity once closed. When the smaller and thinner walled microcontainers were sampled, which the electron beam could penetrate, it was obvious that a cavity remained near the base of the tube Figure 4.24c, which was covered by a more dense material above it. In some cases a clear droplet-like shape was apparent at the base, which had a uniform density within and a perfectly smooth circumference, Figure 4.24c inset. As we have discussed previously, Section 4.2.4.2, as the toluene is strongly adsorbed to the electrode surface, at the low polymerisation potentials the polymer proceeds to close over the toluene droplet. This was not observed for the higher growth potentials shown in Section 4.5.2. This makes these materials a potential candidate for entrapping hydrophobic compounds within a conducting polymer microcontainer with the advantage of being anchored to an electrode surface.

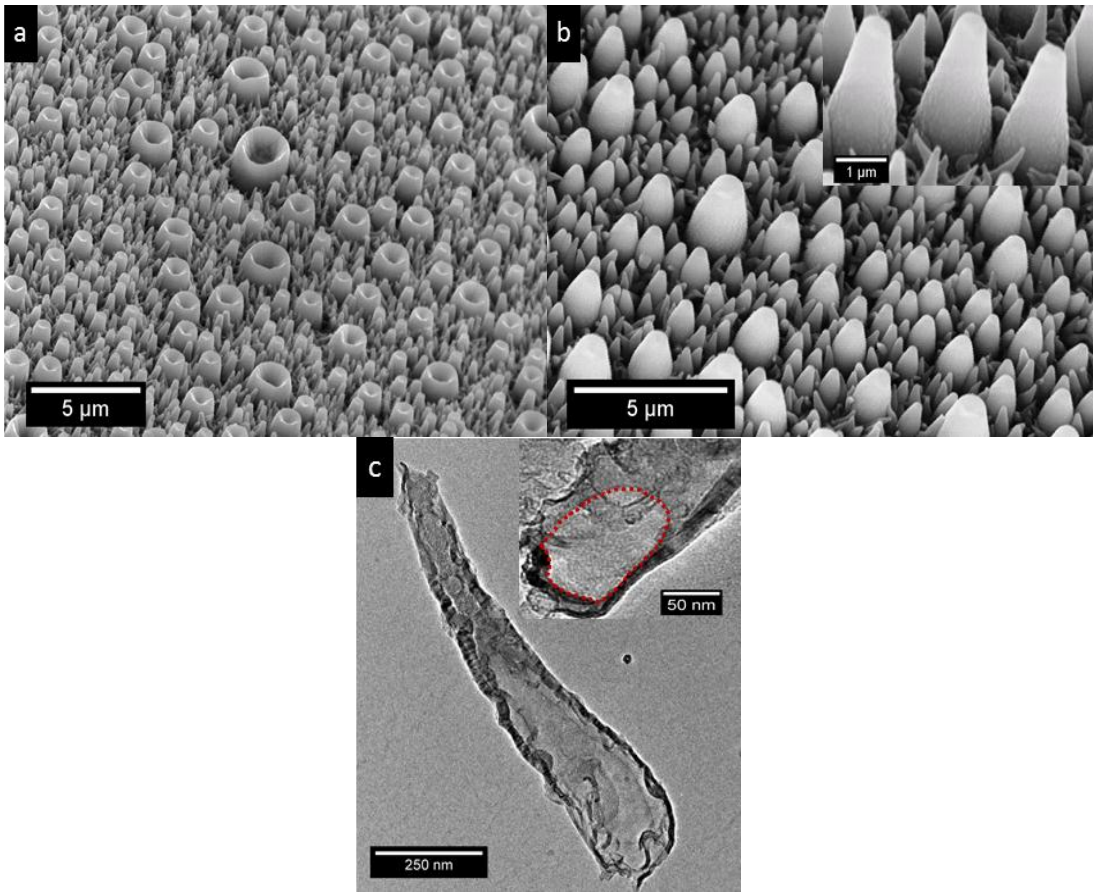

Figure 4.24. SEM micrographs of PPyEtCN polymers grown at 0.850 V for (a) 5 and (b) 30 min. Corresponding TEM micrograph (c) of individual tube from (b), inset magnification of base area of tube with hollow cavity highlighted inset. Emulsion mixture contained PyEtCN (0.075 M), $LiClO_4$ (0.020 M), $(NH_4)H_2PO_4$ (0.100 M) and toluene (60 µL) in 10 mL water/ethanol (7:3) with 1 min sonication by bath.

The closed-tip morphology was also observed at lower concentrations of monomer (0.280 M) under the same experimental conditions including the low applied potential of 0.850 V. Similar to what was previously seen at short polymerisation times (300 s) the tubes originally formed in an open morphology and demonstrated good coverage over the electrode surface, Figure 4.25a. When the experiment was repeated using a longer growth time (900 s) the morphology proceeded to form a cap or closing over the original 'doughnut' structure, Figure 4.25b. As seen from Figure 4.25b inset 1, the original circular 'doughnut' structure at the base of the polymer can still be identified signifying that long and short periods of growth followed the same nucleation pattern. Interestingly, at some points of the electrode (near the edge) where growth rates may have varied an intermediate structure was present, Figure 4.25b inset 2. Here it could be seen that the hollow opening was still present through

the center. This confirms that the original hollow microstructures are being closed over rather than being filled in. This is consistent with the TEM micrographs in Figure 4.24c for the higher monomer concentration polymers which also displayed a hollow center at the base.

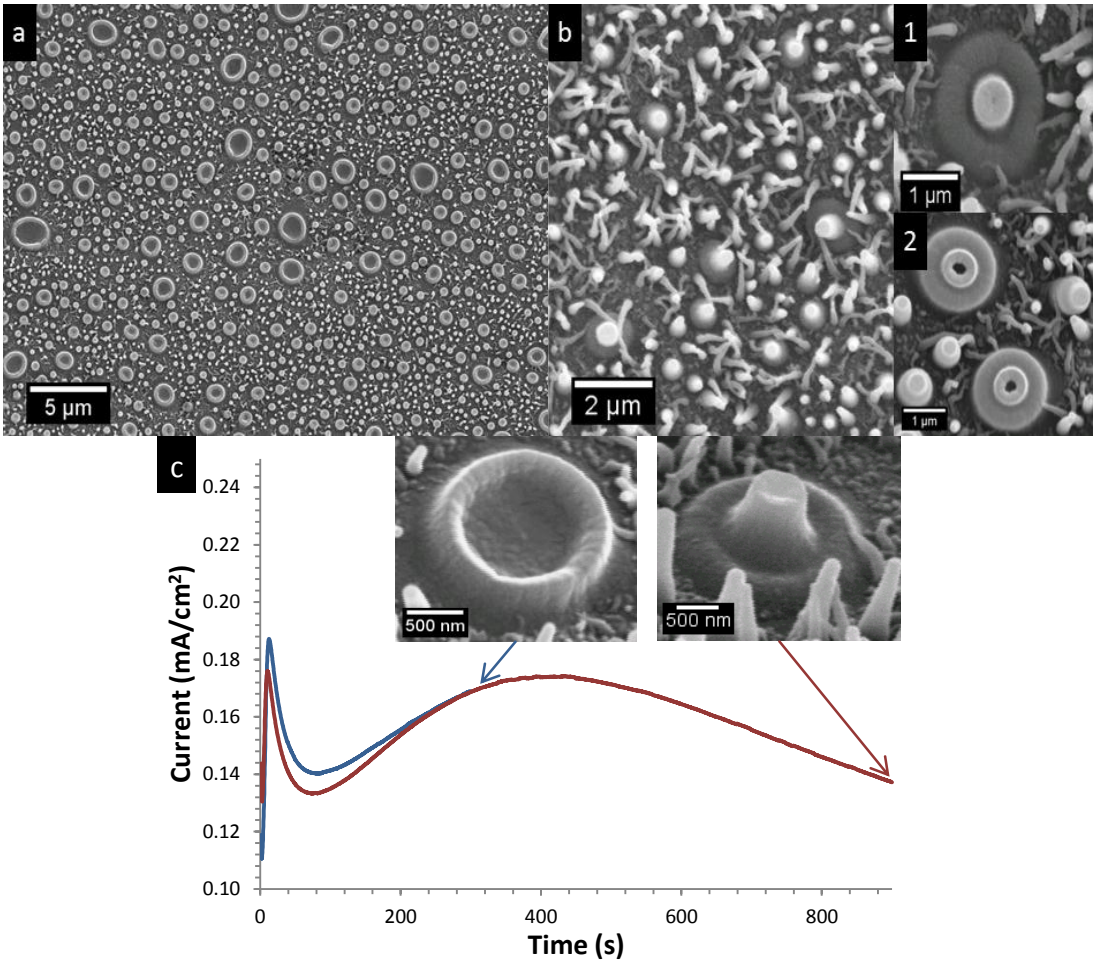

Figure 4.25. SEM micrographs of PPyEtCN polymers grown for (a) 5 and (b) 15 min at 0.850 V. Inset (b1) high magnification of individual closed microstructure and (b2) intermediate microstructure with open pore. Polarisation profile showing termination of growth with corresponding morphology (c). Emulsion mixture contained PyEtCN (0.028 M), $LiClO_4$ (0.020 M), $(NH_4)H_2PO_4$ (0.100 M) and toluene (80 µL) in 10 mL water/ethanol (7:3) with 1 min sonication by bath.

Comparing the growth profiles for the short and long experiments shows that this experimental setup was very reproducible (using different solutions and electrodes). Both current transients overlap and have their I_p at the same magnitude and time, Figure 4.25c. It also highlights the ease at which these separate microstructure morphologies can be controlled by simply limiting the time of polymerisation. This is a useful characteristic for producing hollow, semi-hollow and fully closed

analogues of the same polymer. It could also be possible to produce an open morphology, allow a molecule to diffuse into the opening, and then repeat the polymerisation step to close the 'mouth' and trap a compound within. This has been observed for other polymer systems.[6] The same authors performed a continuous polymerisation with a fluorescent label in solution and found it present in water samples after removing the polymer from the surface, indicating the fluorescent molecule was entrapped during polymerisation. While these techniques were not attempted for this work, the results presented and discussed here suggest it would be possible to re-create them for the PPyEtCN microtube system.

4.2.6 Using Other Monomers to Produce Microtubes

To investigate the versatility of the methodology developed to grow PPyEtCN microstructures and test if it could be used successfully on other monomers, a study was carried out using Py and 3,4-ethylenedioythiophene (EDOT). These monomers have differing water solubility's corresponding to 2.7×10^{-2}, 2.6×10^{-1} and 7.8×10^{-3} mol/L for PyEtCN, Py and EDOT respectively. Electropolymerisation from the toluene emulsions formed upon probe sonication of both Py and EDOT resulted in the formation of hollow polymer microstructures on the electrode surface, Figure 4.26. There are some noticeable differences in the morphologies of the resultant polymers; however this can be expected due to the different characteristic properties of each monomer, specifically their water solubilities and ease of oxidation. Interestingly, for the PPy microstructures the concentration of dihydrogen phosphate had to be increased (0.300 M) due to faster growth of Py at these potentials. At standard conditions of dihydrogen phosphate (0.100 M) only bulk PPy was deposited with no vertical microstructures. This again highlights that the rate of polymerisation is key to fabrication of the microtubes.

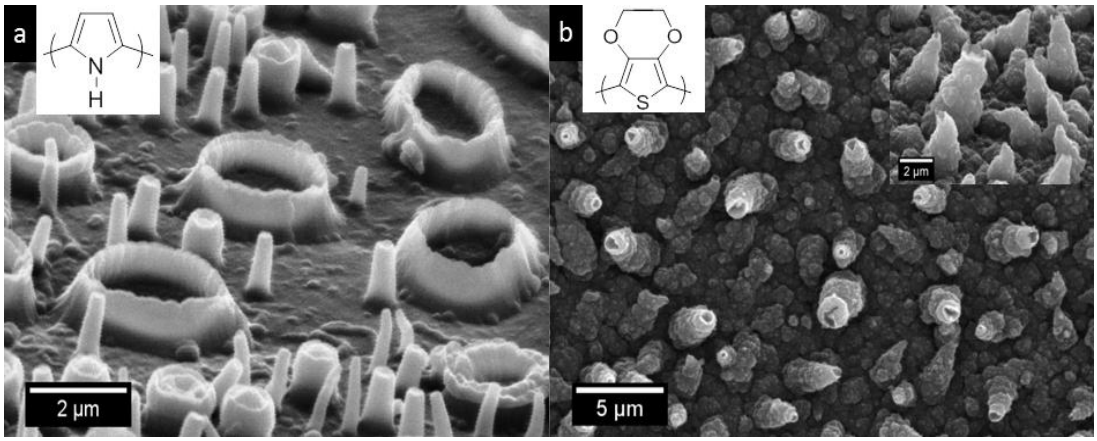

Figure 4.26. SEM micrograph of microstructures deposited at 0.850 and 1.050 V using (a) Py and (b) EDOT. Emulsion mixture contained corresponding monomer (38 µL), $LiClO_4$ (0.200 M) and toluene (80 µL) in 10 mL water/ethanol (7:3) with 45 s sonication by probe. The Py solution contained $(NH_4)H_2PO_4$ (0.300 M) and the EDOT had $(NH_4)H_2PO_4$ (0.100 M).

To confirm that the microtubes were composed of the different monomer units an FTIR spectrum was recorded for the PPyEtCN, PPy and PEDOT microtube films in KBr. Shown in Figure 4.27a, the characteristic ν(C≡N) stretch for the cyano moiety was present at 2251 cm^{-1} for the PPyEtCN microtubes. This band was not evident in the PPy spectrum as the cyano functionality was not present, Figure 4.27b, but the band at 1542 cm^{-1} was present which is the characteristic ν(N-H) stretching mode of PPy in the polymer backbone structure.[76] In both cases the stretching modes of PPy are shown in the region of 1600 – 1000 cm^{-1}.[77] In Figure 4.27c the spectrum for the PEDOT microtubes can be observed. C-S bond vibrations can be identified in the region of 830 to 686 cm^{-1}. This proves that this surfactant-free electrochemical procedure, which couples acoustic emulsification with a toluene template approach, can be used to form microstructures of a range of conducting polymers regardless of the differing water solubilities of their monomer analogues. In addition, it was observed during the studies on PyEtCN that when the polymerisation mixture was exposed to longer acoustic excitation times that the emulsion changed from being opaque to transparent. Separation back to the original multiphasic system was not observed over several days. This indicates the formation of a nanoemulsion and therefore with this system it should be possible to grow hollow nanotubes of PPyEtCN and other monomers.

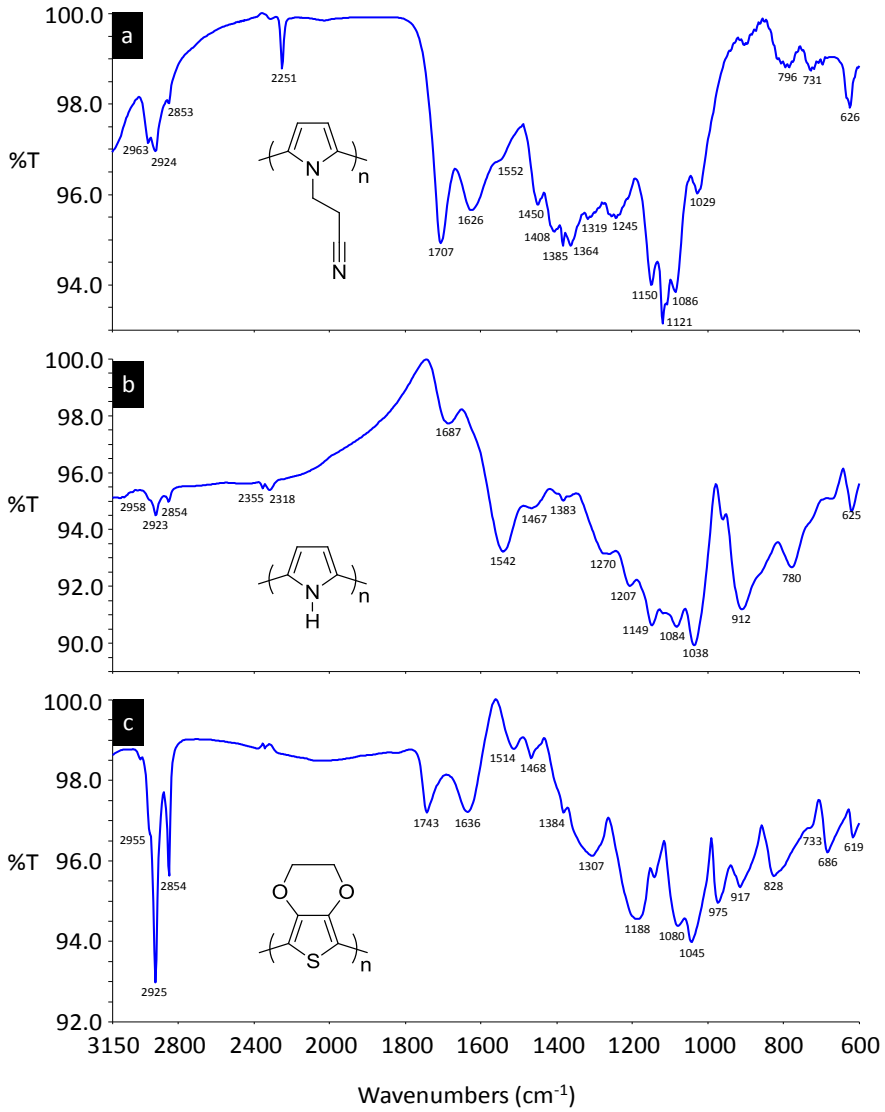

Figure 4.27. FTIR spectrum recorded in KBr of (a) PPyEtCN, (b) PPy and (c) PEDOT microtubes grown at 0.950 V using concentrations from Figure 4.26.

4.3 Conclusions

Investigation of the microtube formation in the PPyEtCN system revealed that they developed by a 'droplet guided' mechanism. This occurred with the PPyEtCN monomer since it has a low solubility in aqueous media. This monomer droplet mechanism proved too difficult to reproduce and was not capable of growing fully hollow tubes. Switching the droplet template from a monomer droplet to a toluene droplet had a significant effect on the resultant morphology.

Employing sonication to disperse toluene droplets in a homogenous distribution it was possible to use them to guide the polymerisation of the PPyEtCN polymer. This soft template approach, which has previously been used in a chemical oxidation methodology, has been successfully adapted to an electrochemical polymerisation procedure. This methodology allowed for novel PPyEtCN hollow microtubes and closed microcontainers to be synthesised attached to an electrode surface.

The method of sonication, applied potential and electrolyte mixture have been shown to have a significant effect on the morphology of the final structures. The polymerisation growth profiles indicate that the role of the mixed electrolyte system ($LiClO_4$ and $(NH_4)H_2PO_4$) was to allow fast nucleation followed by slow polymer propagation, leading to the formation of vertically aligned structures. The microtube films displayed an increased electrochemical response compared to the bulk film and possessed superhydrophilic properties. Toluene microdroplets have been entrapped within the microcontainers and so this methodology has the potential to dissolve species close to the electrode surface. Furthermore, the procedure described within has been proven to also form microstructures for both pyrrole and 3,4-ethylenedioythiophene. Therefore, is should be applicable for growing a range of microstructures for other functionalised and unfunctionalised conducting polymers. While these PPyEtCN microtubes were not suitable for nitrate testing due their low electrical conductivity, using the PPy microtubes should allow the possibility of developing a reliable nitrate sensor with good sensitivity.

4.4 References

1. Long, Y.-Z.; Li, M.-M.; Gu, C.; Wan, M.; Duvail, J.-L.; Liu, Z.; Fan, Z. *Prog. Polym. Sci.* **2011,** *36*, 1415-1442.
2. Uemura, T.; Kadowaki, Y.; Yanai, N.; Kitagawa, S. *Chem. Mater.* **2009,** *21*, 4096-4098.
3. Wang, Y.; Angelatos, A. S.; Caruso, F. *Chem. Mater.* **2007,** *20*, 848-858.
4. Fickert, J.; Makowski, M.; Kappl, M.; Landfester, K.; Crespy, D. *Macromolecules* **2012,** *45*, 6324-6332.
5. Li, G.; Li, Y.; Li, Y.; Peng, H.; Chen, K. *Macromolecules* **2011,** *44*, 9319-9323.
6. Bajpai, V.; He, P.; Dai, L. *Adv. Funct. Mater.* **2004,** *14*, 145-151.
7. Zhou, C.; Han, J.; Guo, R. *Macromolecules* **2009,** *42*, 1252-1257.
8. Gao, W.; Sattayasamitsathit, S.; Uygun, A.; Pei, A.; Ponedal, A.; Wang, J. *Nanoscale* **2012,** *4*, 2447-2453.
9. Surdo, S.; Strambini, L. M.; Malitesta, C.; Mazzotta, E.; Barillaro, G. *Electrochem. Commun.* **2012,** *14*, 1-4.
10. Cui, Y.; Wen, Z.; Liang, X.; Lu, Y.; Jin, J.; Wu, M.; Wu, X. *Energy & Environmental Science* **2012,** *5*, 7893-7897.
11. Roy, C. J.; Chorine, N.; De Geest, B. G.; De Smedt, S.; Jonas, A. M.; Demoustier-Champagne, S. *Chem. Mater.* **2012,** *24*, 1562-1567.
12. Mangeney, C.; Bousalem, S.; Connan, C.; Vaulay, M.-J.; Bernard, S.; Chehimi, M. M. *Langmuir* **2006,** *22*, 10163-10169.
13. Kijewska, K.; Blanchard, G. J.; Szlachetko , J.; Stolarski, J.; Kisiel, A.; Michalska, A.; Maksymiuk, K.; Pisarek, M.; Majewski, P.; Krysiński, P.; Mazur, M. *Chem. –Eur. J.* **2012,** *18*, 310-320.
14. Qu, L.; Shi, G.; Yuan, J.; Han, G.; Chen, F. E. *J. Electroanal. Chem.* **2004,** *561*, 149-156.
15. Qu, L.; Shi, G.; Chen, F. E.; Zhang, J. *Macromolecules* **2003,** *36*, 1063-1067.
16. Qu, L.; Shi, G. *J. Polym. Sci., Polym. Chem.* **2004,** *42*, 3170-3177.
17. Skotheim, T. A. R. T. R. *Handbook of Conducting Polymers*. CRC Press: Boca Raton, **2007**.
18. Parakhonskiy, B.; Andreeva, D.; Möhwald, H.; Shchukin, D. G. *Langmuir* **2009,** *25*, 4780-4786.
19. Luo, S.-C.; Sekine, J.; Zhu, B.; Zhao, H.; Nakao, A.; Yu, H.-h. *ACS Nano* **2012,** *6*, 3018-3026.
20. McCarthy, C. P.; McGuinness, N. B.; Alcock-Earley, B. E.; Breslin, C. B.; Rooney, A. D. *Electrochem. Commun.* **2012,** *20*, 79-82.
21. Um, H.-J.; Kim, M.; Lee, S.-H.; Min, J.; Kim, H.; Choi, Y.-W.; Kim, Y.-H. *Talanta* **2011,** *84*, 330-334.

22. Fabregat, G.; Córdova-Mateo, E.; Armelin, E.; Bertran, O.; Alemán, C. *J. Phys. Chem. C* **2011,** *115*, 14933-14941.

23. Sravendra, R.; Niranjan, K.; Jae Whan, C.; Young Ho, K. *Nanotechnology* **2008,** *19*, 495707.

24. Kwon, O. S.; Park, S. J.; Jang, J. *Biomaterials* **2010,** *31*, 4740-4747.

25. Shida, N.; Ishiguro, Y.; Atobe, M.; Fuchigami, T.; Inagi, S. *ACS Macro Letters* **2012,** *1*, 656-659.

26. Wang, J.; Xu, Y.; Yan, F.; Zhu, J.; Wang, J. *J. Power Sources* **2011,** *196*, 2373-2379.

27. Al-Mashat, L.; Debiemme-Chouvy, C.; Borensztajn, S.; Wlodarski, W. *J. Phys. Chem. C* **2012,** *116*, 13388-13394.

28. Zang, J.; Li, C. M.; Bao, S.-J.; Cui, X.; Bao, Q.; Sun, C. Q. *Macromolecules* **2008,** *41*, 7053-7057.

29. Kępińska, D.; Blanchard, G. J.; Krysiński, P.; Stolarski, J.; Kijewska, K.; Mazur, M. *Langmuir* **2011,** *27*, 12720-12729.

30. McCarthy, C. P.; McGuinness, N. B.; Carolan, P. B.; Fox, C. M.; Alcock-Earley, B. E.; Breslin, C. B.; Rooney, A. D. *Macromolecules* **2013,** *46*, 1008-1016.

31. Asami, R.; Atobe, M.; Fuchigami, T. *J. Am. Chem. Soc.* **2005,** *127*, 13160-13161.

32. Instruments, O., *INCAEnergy Applications Training Course*. Oxford: Oxford, **2009**.

33. Huang, J.; Quan, B.; Liu, M.; Wei, Z.; Jiang, L. *Macromol. Rapid Commun.* **2008,** *29*, 1335-1340.

34. Asami, R.; Fuchigami, T.; Atobe, M. *Langmuir* **2006,** *22*, 10258-10263.

35. Nakabayashi, K.; Amemiya, F.; Fuchigami, T.; Machida, K.; Takeda, S.; Tamamitsu, K.; Atobe, M. *Chem. Commun.* **2011,** *47*, 5765-5767.

36. Nagy, E.; Hadik, P. *Ind. Eng. Chem. Res.* **2003,** *42*, 5363-5372.

37. Gao, Y.; Zhao, L.; Li, C.; Shi, G. *Polymer* **2006,** *47*, 4953-4958.

38. Gao, Y.; Zhao, L.; Bai, H.; Chen, Q.; Shi, G. *J. Electroanal. Chem.* **2006,** *597*, 13-18.

39. Jang, J.; Yoon, H. *Langmuir* **2005,** *21*, 11484-11489.

40. Chen, Y. F.; Liu, J.; Yao, H. J.; Mo, D.; Duan, J. L.; Hou, M. D.; Sun, Y. M.; Zhang, L.; Maaz, K. *Physica B: Condensed Matter 405*, 2461-2465.

41. Mazur, M. *Langmuir* **2008,** *24*, 10414-10420.

42. Kubacka, D.; Krysiński, P.; Blanchard, G. J.; Stolarski, J.; Mazur, M. *J. Phys. Chem. B* **2010,** *114*, 14890-14896.

43. Taylor, P. *Colloids and Surfaces A: Physicochemical and Engineering Aspects* **1995,** *99*, 175-185.

44. Kabalnov, A. S.; Pertzov, A. V.; Shchukin, E. D. *J. Colloid and Interface Science* **1987,** *118*, 590-597.

45. Lad, V. N.; Murthy, Z. V. P. *Ind. Eng. Chem. Res.* **2012,** *51*, 4222-4229.

46. Jiang, H.; Zhang, A.; Sun, Y.; Ru, X.; Ge, D.; Shi, W. *Electrochim. Acta* **2012,** *70*, 278-285.

47. Liang, L.; Liu, J.; Windisch, J. C. F.; Exarhos, G. J.; Lin, Y. *Angew. Chem. Int., Ed.* **2002,** *41*, 3665-3668.

48. Catherine, D.-C. *Electrochem. Commun.* **2009,** *11*, 298-301.

49. Li, M.; Wei, Z.; Jiang, L. *J. Mater. Chem.* **2008,** *18*, 2276-2280.

50. Zhou, M.; Heinze, J. *J. Phys. Chem. B* **1999,** *103*, 8443-8450.

51. Sabouraud, G.; Sadki, S.; Brodie, N. *Chem. Soc. Rev.* **2000,** *29*, 283-293.

52. Yuan, J.; Qu, L.; Zhang, D.; Shi, G. *Chem. Commun.* **2004,** *0*, 994-995.

53. Monk, P. M. S. *Fundamentals of Electroanalytical Chemistry*. **2001**.

54. Li, Y.; Qian, R. *Electrochimica Acta* **2000,** *45*, 1727-1731.

55. Fisher, A. C. *Electrode Dynamics*. Oxford Universtiy Press: Oxford, **1996**.

56. Cho, S. I.; Lee, S. B. *Acc. Chem. Res.* **2008,** *41*, 699-707.

57. Ge, D.; Huang, S.; Qi, R.; Mu, J.; Shen, Y.; Shi, W. *ChemPhysChem* **2009,** *10*, 1916-1921.

58. Barthlott, W.; Neinhuis, C. *Planta* **1997,** *202*, 1-8.

59. Sun, T.; Feng, L.; Gao, X.; Jiang, L. *Acc. Chem. Res.* **2005,** *38*, 644-652.

60. Feng, L.; Li, S.; Li, Y.; Li, H.; Zhang, L.; Zhai, J.; Song, Y.; Liu, B.; Jiang, L.; Zhu, D. *Adv. Mater.* **2002,** *14*, 1857-1860.

61. Yong Chae, J.; Bharat, B. *Nanotechnology* **2006,** *17*, 4970.

62. Weiss, Z.; Mandler, D.; Shustak, G.; Domb, A. J. *J. Polym. Sci., Polym. Chem.* **2004,** *42*, 1658-1667.

63. Stewart, E. M.; Liu, X.; Clark, G. M.; Kapsa, R. M. I.; Wallace, G. G. *Acta Biomaterialia* **2012,** *8*, 194-200.

64. Teh, K. S.; Takahashi, Y.; Yao, Z.; Lu, Y.-W. *Sens. Actuators* **2009,** *155*, 113-119.

65. Wang, X.; Berggren, M.; Inganäs, O. *Langmuir* **2008,** *24*, 5942-5948.

66. Chang, J. H.; Hunter, I. W. *Macromol. Rapid Commun.* **2011,** *32*, 718-723.

67. Guo, C.; Feng, L.; Zhai, J.; Wang, G.; Song, Y.; Jiang, L.; Zhu, D. *ChemPhysChem* **2004,** *5*, 750-753.

68. Liu, Y.; Choi, C.-H. *Colloid Polym. Sci.* **2013,** *291*, 437-445.

69. P, C., *Conducting Polymers, Fundamental and Applications*. Kluwer Academic Publishers: **1999**.

70. Xu, P.; Han, X. J.; Wang, C.; Zhang, B.; Wang, H. L. *Synth. Met.* **2009,** *159*, 430-434.

71. Van Dyke, L. S.; Martin, C. R. *Langmuir* **1990,** *6*, 1118-1123.

72. Ge, D.; Mu, J.; Huang, S.; Liang, P.; Gcilitshana, O. U.; Ji, S.; Linkov, V.; Shi, W. *Synth. Met.* **2011,** *161*, 166-172.

73. Koehler, S.; Ueda, M.; Efimov, I.; Bund, A. *Electrochimica Acta* **2007,** *52*, 3040-3046.

74. Aradilla, D.; Estrany, F.; Armelin, E.; Oliver, R.; Iribarren, J. I.; Alemán, C. *Macromol. Chem. Phys.* **2010,** *211*, 1663-1672.

75. Martin, C. R. *Acc.Chem. Res.* **1995,** *28*, 61-68.

76. Lee, J.-W.; Serna, F.; Nickels, J.; Schmidt, C. E. *Biomacromolecules* **2006,** *7*, 1692-1695.

77. Liu, Y.-C.; Hwang, B.-J.; Jian, W.-J.; Santhanam, R. *Thin Solid Films* **2000,** *374*, 85-91.

Chapter 5

The Electrodeposition of Copper Micro/Nano Structures at Polypyrrole and Poly[*N*-(2-cyanoethyl)pyrrole] Polymers for the Electrochemical Detection of Nitrate

5.1 Introduction

There has been extensive research in recent years in developing means to gain control over the morphology when synthesising metallic materials.[1-4] Using electrochemistry to control their formation allows for a range of applications to become available. Several researchers have highlighted the versatility of this technique. [5-7] In Chapter 3 and Chapter 4, the electrochemical deposition of poly(*N*-(2-cyanoethyl)pyrrole (PPyEtCN) nanowires and microtubes were investigated. In this chapter we build on these electrodeposition methods and include the electrodeposition of copper. Employing the beneficial properties of the polymer nanowires will allow a greater range of possible applications to become available. Polymer nanocomposites [8] and nanowire/metal hybrids[9] have already been applied in nanodevices such as sensors.

Synthesising a nanowire/copper composite and obtaining control over the morphology with a facile and reproducible method, has obvious advantages. Investigating this process at both polypyrrole (PPy) and PPyEtCN as bulk and nanostructured films will reveal information about the mechanism of the copper electrodeposition. Since copper materials have been proven as effective sensors for the nitrate reduction reaction in aqueous systems,[10] the nanocomposites developed here will be tested for their ability to electrochemically reduce the nitrate ion.

5.2 Results and Discussion

5.2.1 Electrochemical Deposition of Copper at Bulk Polypyrrole

Using polymers such as PPy as supports for electrochemical deposition of metals has a range of beneficial properties. The PPy material is capable of encouraging the oxygen reduction reaction (ORR)[11] which leads to the successful deposition of copper oxide (Cu_2O and CuO) species.[12-13] There is a strong interest in Cu_2O materials for use in solar cells; recent progress has focused on the increase in efficiency obtained by Cu_2O nanostructuring.[14-15] The morphology and surface area of the electrodes can have a direct impact on the efficiency and stability of photo-electrochemical cells.[16] Therefore, using PPy substrates as a means of controlling the electrodeposition of copper nanomaterials can produce materials capable of photochemical applications.

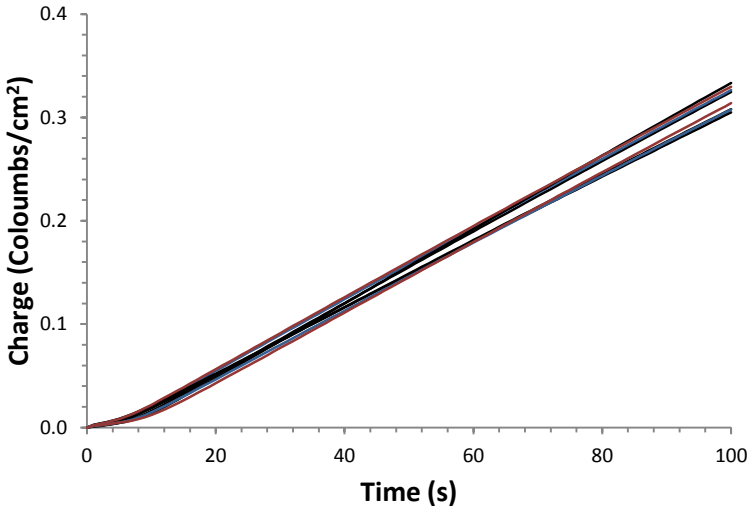

Figure 5.1. Growth profiles of eight PPy polymers grown at 0.700 V for 100 s with 0.100 M monomer at a GC electrode.

A homogeneous and reproducible coverage of the substrate by PPy was desirable as it has been observed that different polymer thicknesses can lead to changes in nucleation rates during electrochemical deposition. This is due to differences in conductivity and electric field strength between thick and thin polymer layers.[17-18] By employing 0.100 M of pyrrole (Py) at a constant potential of 0.700 V for 100 s it was

possible to obtain a reasonably reproducible PPy surface between each experiment. As shown in Figure 5.1, the polymerisation rate was almost linear over the entire period of growth, with a lower rate evident before 10 s due to the polymer nucleating on the electrode surface. When the growth transients for eight PPy films were compared, their final accumulated charge was reasonably consistent. The average charge recorded was 0.318 C/cm^2 with a standard deviation of 0.029 C/cm^2 (n=8). Polymer growth profiles which deviated significantly from these values were not used. This ensured that any differences observed in the morphology or nucleation density of the copper structures was due to the changes in the experimental deposition parameters employed.

5.2.1.1 Effect of Copper Concentration on Deposition Morphology

When depositing copper materials onto metal or conducting polymer (CP) substrates it has been reported that the concentration of the Cu salt in the electrolyte solution has a strong influence on the resultant copper deposits. Zhou *et al.* [17] observed an increase in number density of deposits when the copper concentration was increased from 0.001 to 0.010 M. However, increasing from a copper concentration of 0.010 to 0.050 M produced a dramatic increase in the size of the deposits and resulted in a significant decrease in their number density. This was also observed here during the electrochemical deposition of copper onto the bulk PPy substrates. Using two different concentrations of copper (0.005 and 0.050 M $CuSO_4$ in 0.050 M Na_2SO_4) and applying a constant reduction potential (-0.135 V) a change in the number density of deposits was observed. As shown in Figure 5.2, there was a marked decrease in the number density of nucleation sites using 0.050 M of $CuSO_4$. At this concentration, the deposits transform into discrete isolated particles, Figure 5.2b, compared to the almost complete substrate coverage seen for 0.005 M $CuSO_4$, Figure 5.2a. In fact, areas of PPy free from copper deposits were only observed in the circumference of larger grown deposits as shown in Figure 5.2a. The size of the deposits increased from approximately 20 to 400 nm with the 10 fold increase in copper concentration.

There was also another larger sized copper particle observed for the film deposited from 0.050 M $CuSO_4$ solution, which was on average ~2.7 µm in diameter. This second microstructure produced a diffusion limited peak in the deposition profile which was not observed for the deposition using the 0.005 M $CuSO_4$ concentration. As can be seen in Figure 5.2c, a reductive I_{pmax} is present at 24 s and decreases thereafter to a constant current density of approximately -2.5 mA/cm^2. A negative current response is indicative of metal reduction (electrodeposition) and the magnitude of the reductive current signifies the electrodeposition rate. Analysis of the 0.005 M $CuSO_4$ experiment shows that the negative current remained very low and did not exceed -0.5 mA/cm^2 once the double layer charging had completed (~10 s). This indicated that the rate of electrodeposition using 0.005 M of $CuSO_4$ was particularly slow; this was confirmed by the SEM analysis.

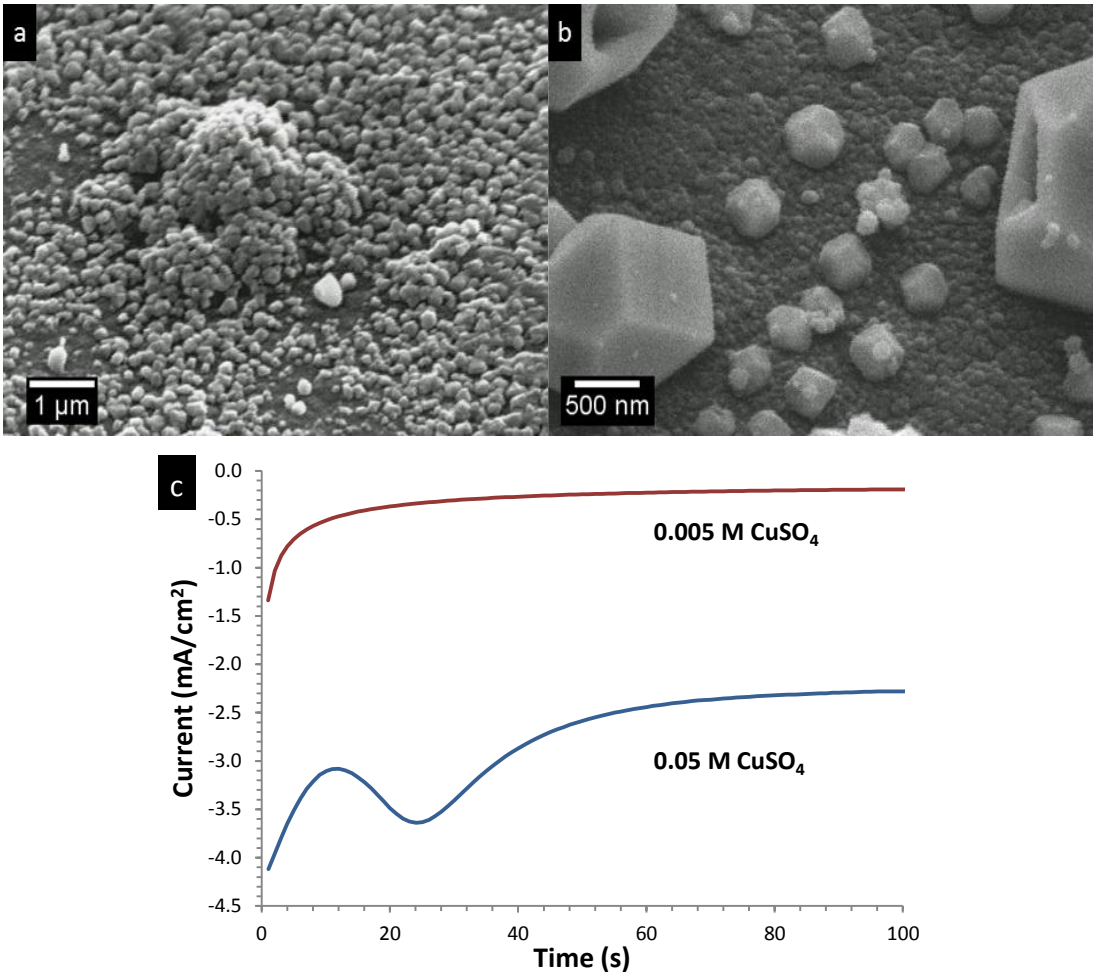

Figure 5.2. SEM micrographs of PPy films grown at 0.700 V for 100 s with 0.100 M monomer electrodeposited with copper at -0.135 V at (a) 0.005 M and (b) 0.050 M $CuSO_4$ in 0.050 M Na_2SO_4 for 6 min with (c) corresponding electrodeposition profile.

SEM analysis was used to investigate the diffusion limited peak generated during the copper electrodeposition to ascertain if it was due to the nucleation processes of either the small or large copper structures. It was possible that the nucleation phases occurred either simultaneously or consecutively at times before or after this peak maximum, described as instantaneous or progressive nucleation.[19]

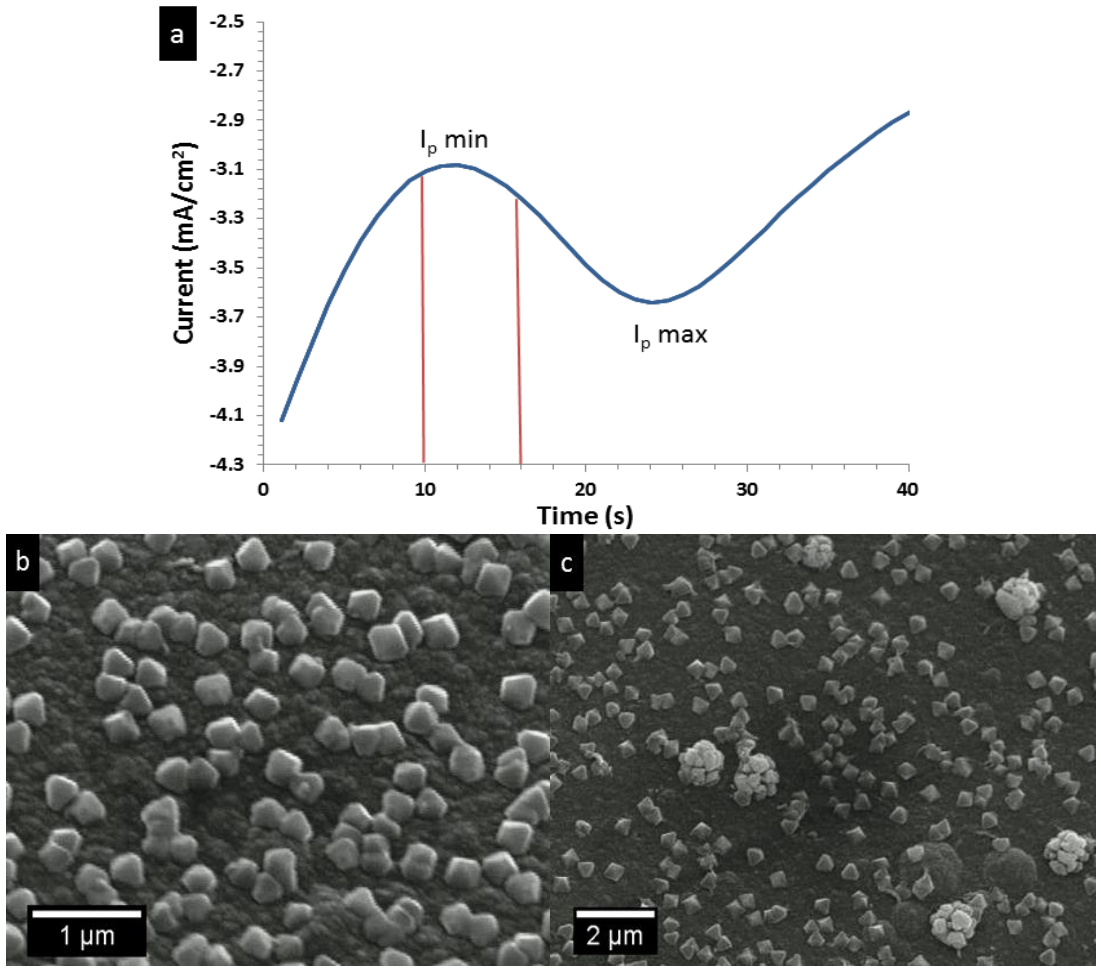

Figure 5.3. Electrodeposition profile PPy films grown at 0.700 V for 100 s with 0.100 M monomer electrodeposited in 0.050 M $CuSO_4$ in 0.050 M Na_2SO_4 at -0.135 V (a). SEM micrograph at (b) 10 and (c) 16 s.

Deposition experiments were terminated at 11 and 16 s which correspond to times before the current minimum (I_{pmin}) and on the rising transient towards the current maximum (I_{pmax}), respectively. This is highlighted in Figure 5.3a where the experimental termination points can be observed along with the I_{pmin} and I_{pmax} points. When the polymer films were examined under SEM it was seen that in the 11 s deposition the main structure consisted of a small cube morphology, Figure 5.3b.

However, in the 16 s experiment there were areas on the electrode which had larger clusters of copper deposits in conjunction with the smaller cube morphology, Figure 5.3c. The deposits had different crystal sizes as they grew for different periods of time. This was indicative of a progressive nucleation process forming new sites of copper deposition during the growth phase. The progressive growth may be encouraged due to the deposition overpotential being relatively low. If the potential were much larger it would allow all the deposits to nucleate instantaneously. This is due to larger a reductive potential making more sites on the electrode more favourable for deposition compared to a lower potential.

This observation indicated that the larger structures developed at times leading up to the I_{pmax} and their development was associated with current at the peak maximum. This diffusion limited peak was formed because as the nucleation sites grow they consume the available copper within the electrode vicinity, causing the diffusion fields to overlap.[20] For growth to continue, fresh copper must diffuse from the bulk electrolyte, but the diffusion of these ions (Cu^{2+}) is much slower than their electrochemical reduction and therefore the current gradually drops. This means that the reduction reaction cannot continue at the same rate as there is insufficient material. This is a commonly seen process in electrochemical systems where electron transfer is the fast reaction step.[21]

To confirm these results two diagnostic relationships developed by Scharifker and Hills were employed to analyse the current response for the deposition process,[22] Equations 2.4 and 2.5, given in Chapter 2. The data obtained from the experimental current density-time transients were normalized by current density maximum (j_{max}, t_{max}) and a comparison was made to dimensionless theoretical models. In the present system for an electrochemical deposition using -0.135 V, the j_{max} was -3.6 mA/cm^2 and t_{max} was 24.07 s. The instantaneous and progressive 3D models obtained from these data can be observed in Figure 5.4. It can be seen that the experimental data overlaps with the progressive 3D model before the t/t_{max} value. Points after this are more closely related to the progressive 3D plot rather than the instantaneous 3D plot. Therefore, it can be concluded that the SEM data and modelling equations are both in agreement with a progressive copper nucleation process. This is in contradiction with what Sakar *et al.*[18, 23] reported when they electrodeposited copper nanocrystals onto PPy substrates. They observed excellent

agreement with the instantaneous models. However, this was most likely due to their large negative potential of -0.900 V which would shift the nucleation process away from progressive nucleation.

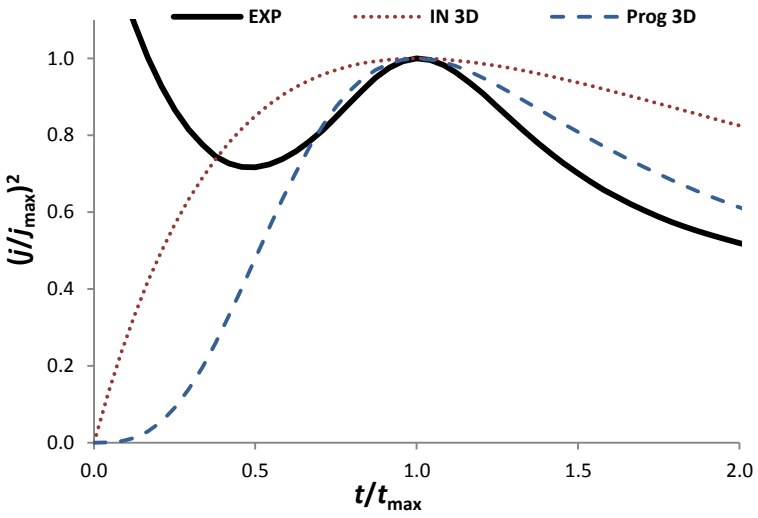

Figure 5.4. Dimensionless plot of the current response of electrodeposited copper at a PPy substrate at -0.135 V with the theoretical dimensionless plots for instantaneous and progressive nucleation 3D (IN 3D and Prog 3D respectively). Equations provided in Chapter 2.

5.2.1.2 Effect of the Reduction Potential

Using PPy as the substrate material and keeping all the parameters as described previously, 0.050 M $CuSO_4$ in 0.050 M Na_2SO_4, the effect of the reductive current was investigated. As shown in Figure 5.5, when the reductive current was changed to -0.105, -0.135 and -0.165 V it resulted in an increase in the negative current being recorded and shifted the I_{pmax} from 30 to 24 s. This signified that a larger electrodeposition reaction was taking place and consuming more of the copper at earlier times. It was also indicitive of a greater amount of nuclei at the surface due to the more negative potentials applied.[20] For deposition carried out at -0.165 V, as a diffusion limited peak is not observed, it was probable that this negative potential reduced the available copper at the electrode surface at a much faster rate. The copper ions in solution were not capable of accumulating at the surface as they were instantly reduced and converted to other species.

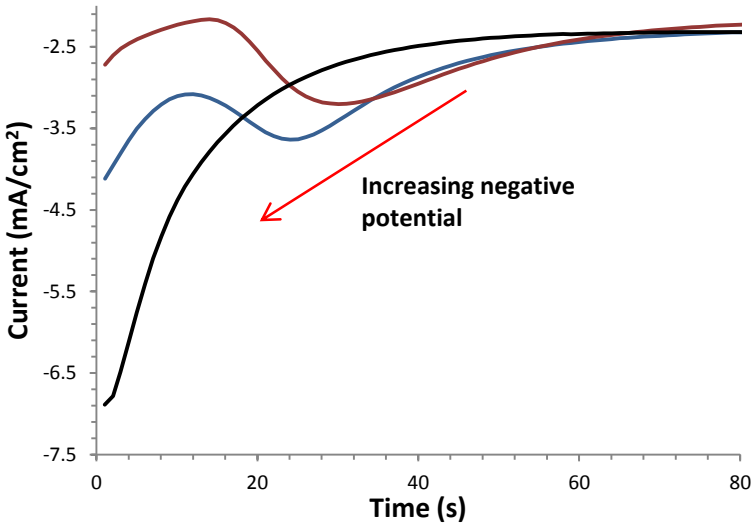

Figure 5.5. Current vs. time profiles for the electrodeposition of copper particles from a 0.050 M $CuSO_4$/0.050 M Na_2SO_4 solution at -0.105, -0.135 and -0.165 V.

Inspection of the SEM micrographs of the resultant PPy surface after the deposition process confirmed this increase in the reaction rate. Applying increasing negative potentials from -0.105 V (Figure 5.6a) to -0.135 V (Figure 5.6b) and -0.165 V (Figure 5.6c) revealed that all three potentials produced the two sized nucleations. The structures formed from subsequent nucleations were significantly larger in perpendicular height from the electrode surface at the more negative potentials. Comparing Figure 5.6a1, b1 and c1 for the density of nucelations, it was observed that the nucleation of the smaller cubes increases steadily with increasing negative potentials. As seen for the -0.165 V experiment (Figure 5.6c1) a much greater number of the smaller deposits were present almost completely covering the PPy substrate. The increase in negative potential created more nucleation sites for copper deposition, as more areas on the electrode exceed the minimum energy needed for crystal growth.[22] This has also been observed by other researchers where increasing the negative potential for electrodeposition of copper produces a much higher number of nucleation sites.[5, 23]

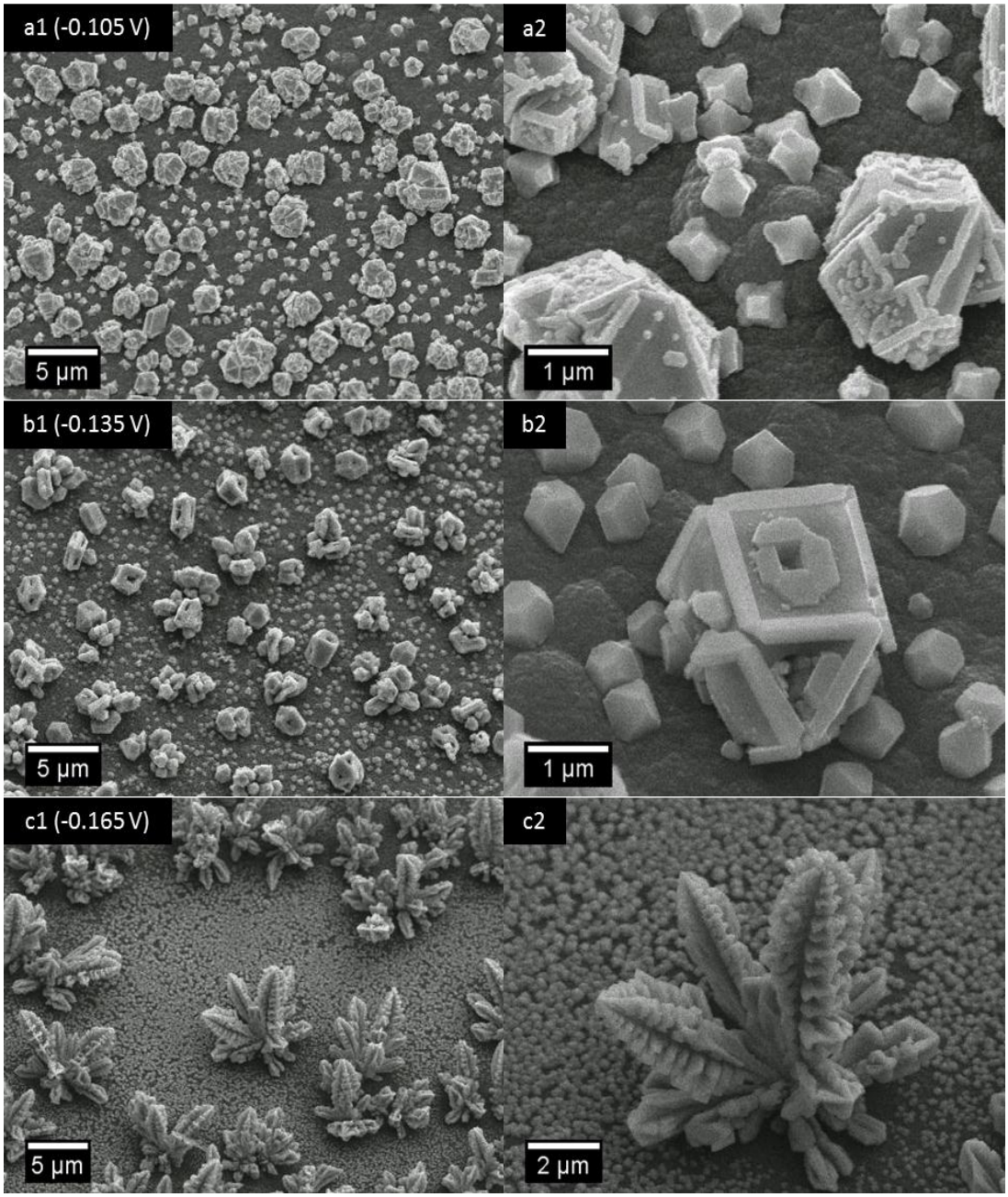

Figure 5.6. SEM micrographs of PPy films grown at 0.700 V for 100 s with 0.100 M monomer electrodeposited in 0.050 M $CuSO_4$ in 0.050 M Na_2SO_4 at -0.105 V (a), (b) -0.135 V and (c) -0.165 V.

The orientation (faces) of Cu_2O crystals have also been observed to be potential dependant.[24] Inspection of the shape of the smaller deposits formed using progresively more negative potentials shows that they change from truncated pyramids (Figure 5.6a2) to a cube type structure (Figure 5.6b2 and c2). Furthermore, an increase in faceting of the deposits was also seen for the larger deposits, changing from amorphous type crystals (-0.105 V) to deposits with ordered and flat sections

(-0.135 V) to large scale ordered branch type structures (-0.165 V). Similar to what has been observed for the growth of PPyEtCN nanowires and microtubes, Chapter 3 and Chapter 4 respectively, it is apparent that the growth rate for copper electrodeposition has a significant effect on the resultant morphology obtained. The formation of these copper dendrites shown Figure 5.6c2, at a PPy surface, have not been reported in the literature. Furthermore, Cu_2O dendrites have been shown to produce a photocurrent enhancement compared to bulk deposits.[25] Therefore, producing and controlling this morphology will be examined in the next section.

5.2.1.3 Formation of Copper Dendrites

It was clear from the previous studies that increasing the electrodeposition potential led to the formation of the branch type dendrites. Increasing the electrodeposition time has been shown to produce larger crystal growth and change the final crystal structure.[23] Therefore, to encourage the deposition of the branched structure, a constant deposition potential of -0.200 V was chosen and maintained for various electrodeposition times. The morphology produced at this potential was investigated at electrodeposition times of 30, 90, 180, 360, 420, 480 and 600 s, with the copper concentration as previously outlined, 0.050 M $CuSO_4$ in 0.050 M Na_2SO_4. As shown in Figure 5.7a, the charge consumed at the electrode increases from -0.123, -0.336, -1.240, -1.449, -1.937, and -2.435 mC/cm^2 for the deposition times ranging from 30 to 600 s, respectively. As shown in Figure 5.7b these values increase linearly with deposition time with an R^2 value of 0.981.

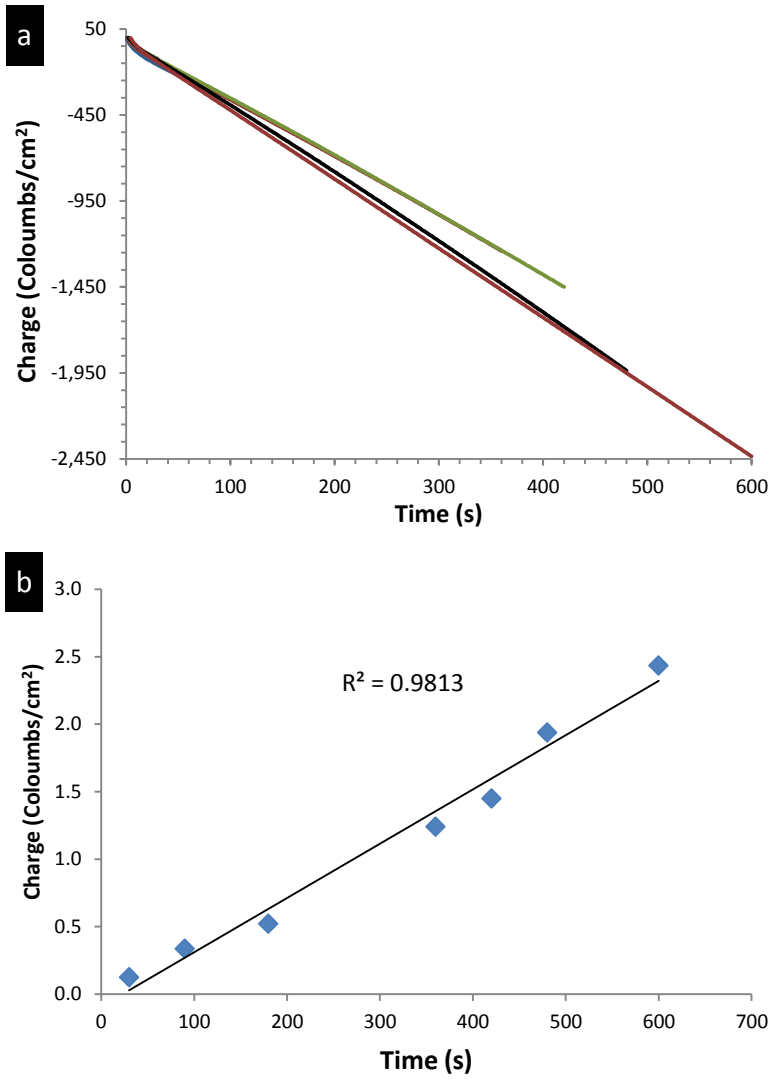

Figure 5.7. (a) Current vs. time profiles for the electrodeposition of copper particles from a 0.050 M $CuSO_4$/0.050 M Na_2SO_4 solution at -0.200 V for 30, 90, 180, 360, 420, 480 and 600 s and (b) total charge consumed plotted vs. electrodeposition time.

SEM micrographs of the resulting polymers are displayed in Figure 5.8. Similar to what was observed for the -0.165 V experiment shown in Figure 5.6c, the -0.200 V potential produced a branch like morphology homogeneously over the PPy substrate. Interestingly, it was possible to monitor the evolution of this morphology from nucleation to growth as the longer deposition times were employed. As shown in Figure 5.8a (30 s), the main morphology was the typical cube shape discussed previously. However, the stems for the larger structures were dispersed uniformly around these cubes as short small clusters. These stems continued to grow in size up to 360 s with limited branching occurring perpendicular to the main stem, as shown in Figure 5.8c. At 420 s the branching from the main stem had increased significantly

and these branched sites had further growth along their main axis in the form of short limbs, Figure 4.8d. At 480 and 600 s the branched morphology continued to extend until the entire electrode was covered, Figure 5.8e and 5.8f.

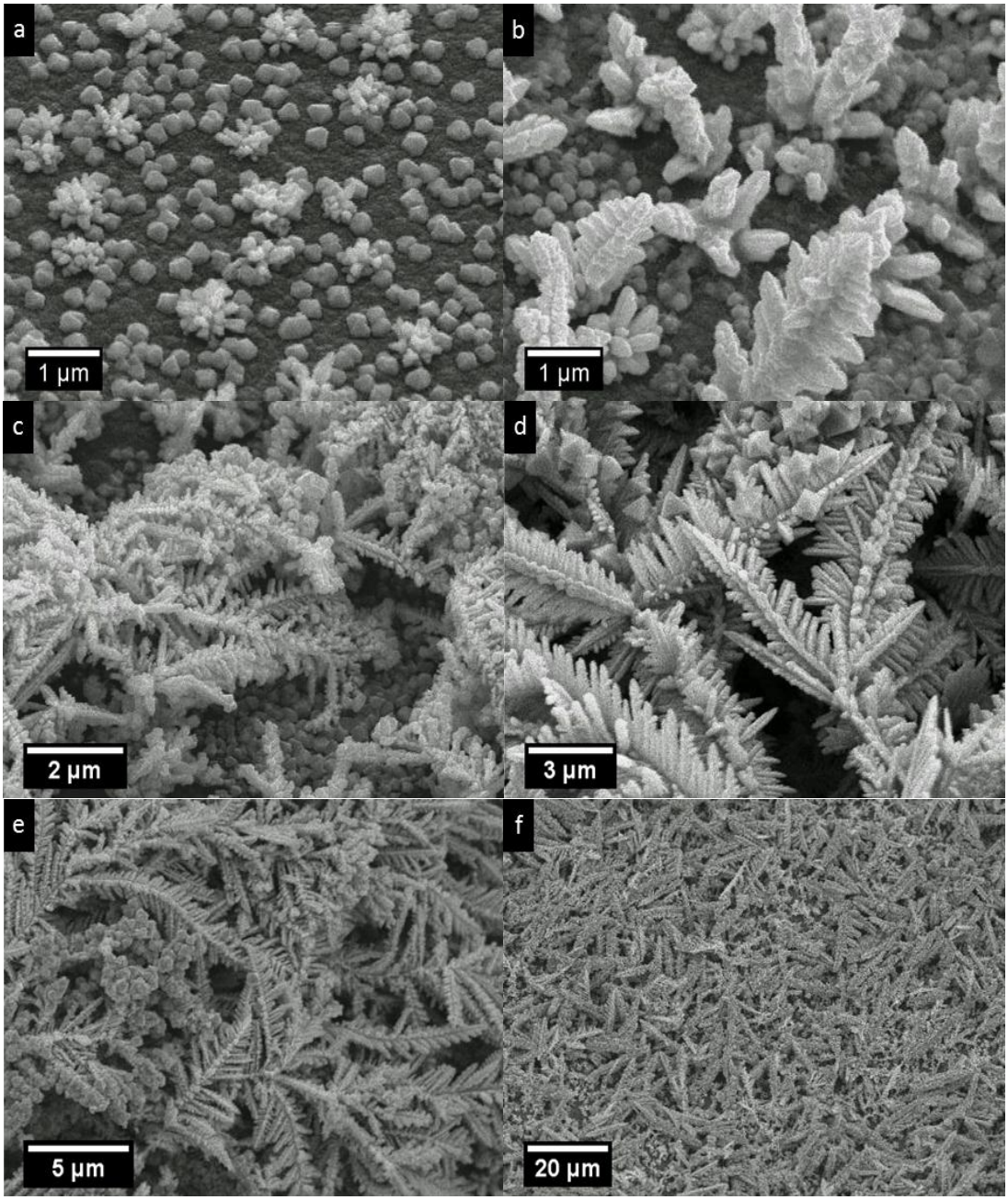

Figure 5.8. SEM micrographs of copper particles electrodeposited onto a bulk PPy film using -0.200 V for (a) 30, (b) 90, (c) 360, (d) 420 (e) 480 and (f) 600 s from a 0.050 M $CuSO_4$ solution in 0.050 M Na_2SO_4.

When tilted SEM analysis was performed on the branched microstructures it was observed that the stems were perpendicularly aligned from the surface when deposited for 420 s, Figure 5.9a. Further growth after this time however, led to the stems collapsing under their own weight as shown in Figure 5.9b. The stems then lay parallel to the substrate and were possibly not connected to the substrate depending on where the stems cracked or detached. Orientating the stems perpendicular to the substrate produces a high surface area while maintaining good physical and electrical continuity between the branched structure and the electrode.[26] Since multiple branch points develop from a single nucleation point, efficient charge transport to the electrode is maintained while benefiting from the increase in surface area provided by the dendritic extensions.[2] This highlights that the growth time should be limited to approximately 400 s as beyond this time the branch structures lose the beneficial properties which they possess.

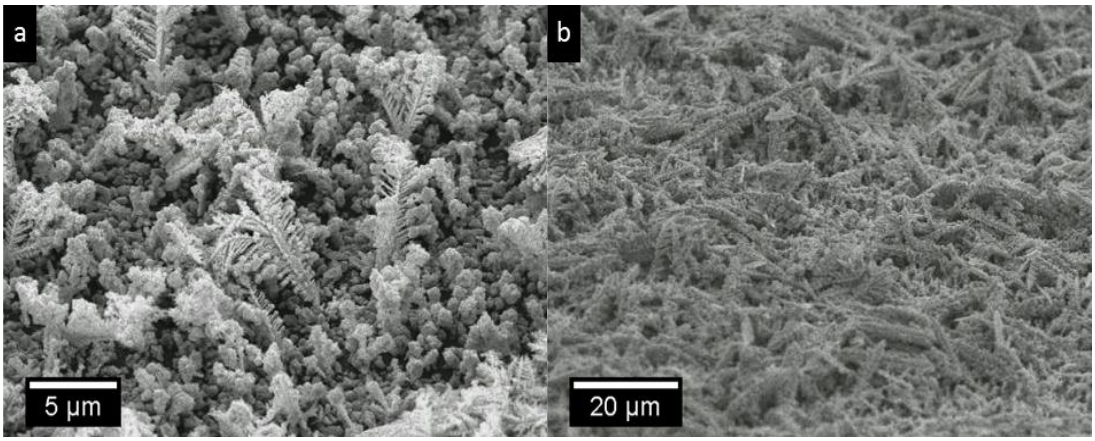

Figure 5.9. Tilted SEM micrographs of copper particles electrodeposited onto a bulk PPy film using -0.200 V for (a) 420, (b) 600 s from a 0.050 M $CuSO_4$ solution in 0.050 M Na_2SO_4.

Choi and Siegfried[27] hypothesised the reason for branched growth of Cu_2O deposits. They observed the branched structures only at fast growth rates (high negative potentials) forcing the crystal structures to adopt non-polyhedral shapes. This is summarised in Scheme 5.1.[28] The branched growth is favoured as the crystal growth becomes limited by mass transport of the Cu^{2+} ions.[16] Since the apex of the growing crystal protrudes further into the solution, where there is a higher copper concentration, growth can resume at these sites.[29] This produces copper deposits which extend upwards from the electrode surface as they search for fresh material to

consume. Furthermore, the evolution of the branches is pH dependant since at a high pH Cu^{2+} ions have limited solubility. Therefore, they will crystallise at the surface even if this results in deposit shapes which are not thermodynamically favourable.[29] At a low pH however, the solubility of Cu^{2+} increases and therefore deposition will occur in ordered thermodynamically favourable crystal habits. A medium pH, as used in this study (pH 4.7) and by Choi and Siegfried (pH 4.9), combined with the -0.200 V overpotential promotes branching and faceted growth.[25]

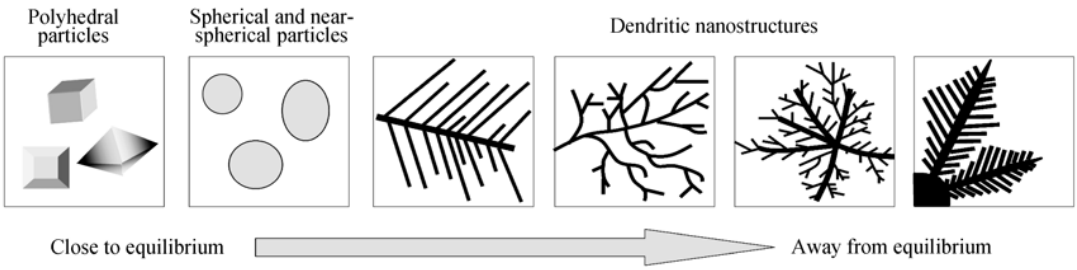

Scheme 5.1. Evolution of crystal structure based on the driving force required for crystallisation. 'Away from equilibrium' signifies a larger negative electrodeposition potential. Reproduced from reference.[28]

The process of stem nucleation and growth is depicted in Scheme 5.2. Here the stem growth can be observed as a function of increasing electrodeposition time (1)-(6). As discussed previously, the initial nucleation was always composed of cube shaped structures nucleated in a homogenous distribution over the PPy substrate (1). The nucleation points for the stems occur on top of these formed cubes (2). Increasing the electrodeposition time causes the stems to grow in height perpendicular to the electrode surface (3). Further growth leads to branching of the stems (4) and to the production of short limbs in the nano dimension along the branches. This forms a hierarchical structure, Figure 5.10(4). Closer inspection reveals that nanoparticles have nucleated along the stem backbone and to a lesser degree on the branches (5) and Figure 5.10(5). Finally at the longest deposition time (600 s) growth of octahedral shaped structures formed at points along the ends of branches or on the stems (6) and Figure 5.10(6), similar to the initial cube formation on the PPy substrate. The crystal habit however, was not specific to one shape and conformed to a range of cubic and pyramidal shapes.

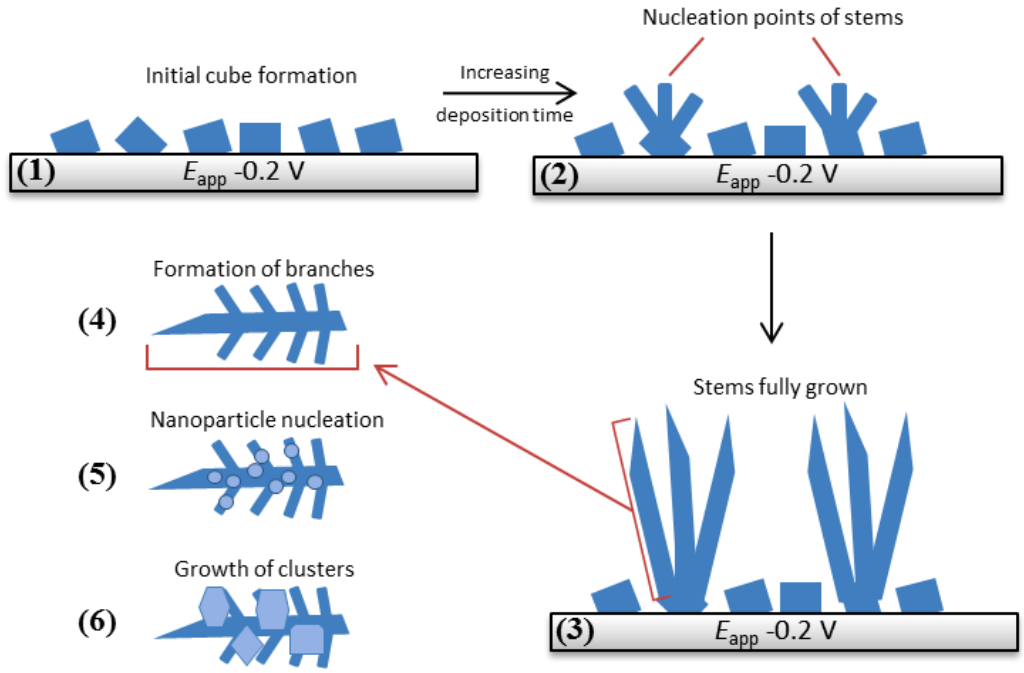

Scheme 5.2. Diagram depicting growth of the stem and hierarchical copper structures.

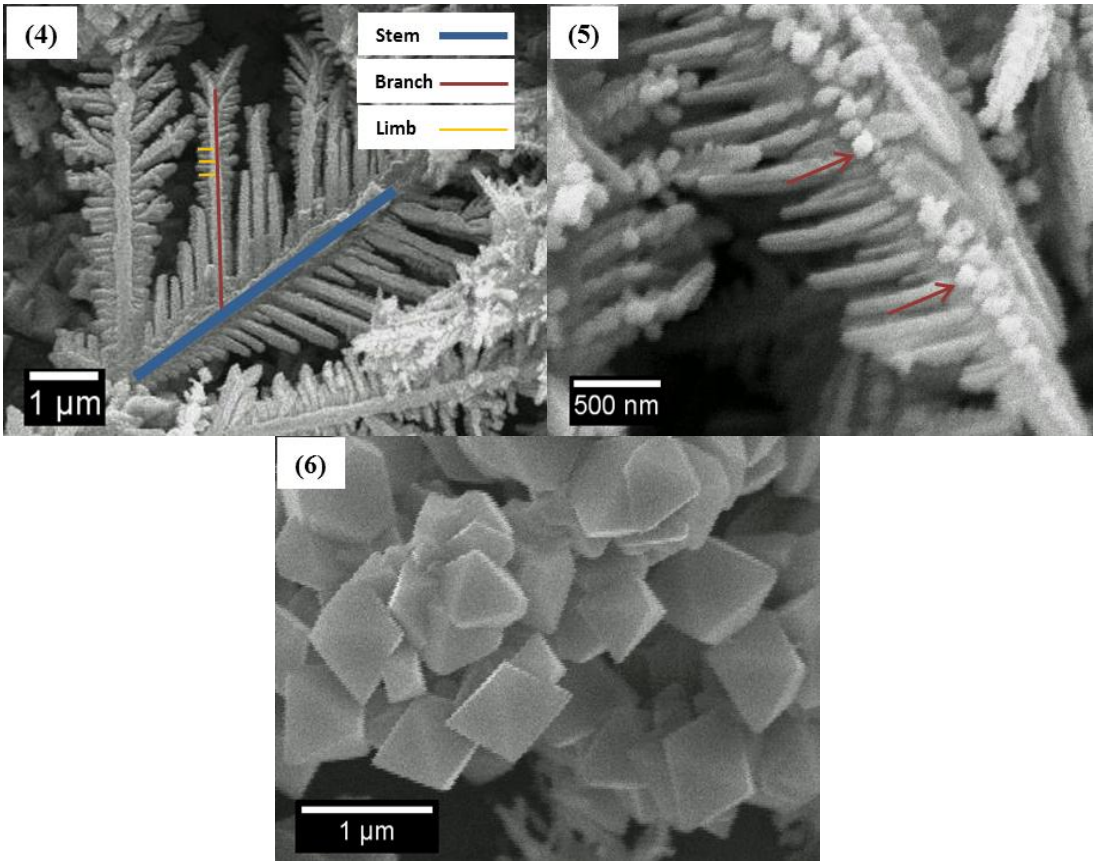

Figure 5.10. SEM micrographs highlighting morphological changes in crystal structures as depicted in Scheme 5.2, (4) branching, (5) nanoparticles formation and (6) cubooctahedral growth. Electrodeposition performed on a bulk PPy film using -0.200 V for (4) 420 (5) 480 and (6) 600 s from a 0.050 M $CuSO_4$ in 0.050 M Na_2SO_4.

Similar to the results displayed when altering the applied potential, the surface morphology of copper deposits has been shown to change by employing different copper salts and additives.[30-31] Changing the copper salt to $CuCl_2$ or adding sodium dodecyl sulfate (SDS) to the electrolyte medium has a dramatic effect on the resultant structures formed. This is due to the chloride and dodecyl sulfate ions adsorbing on certain orientations of copper and allowing other facets to grow.[27] Interestingly, the $CuCl_2$ deposition solution produced flat sheets of copper electrodeposits, Figure 5.11a and 5.11b. While the SDS solution led to similar type microstructures forming as shown previously, since DS^- and SO_4^{2-} have been shown to produce similar types copper deposits as they adsorb to the same facets,[5] Figure 5.11c and 5.11d.

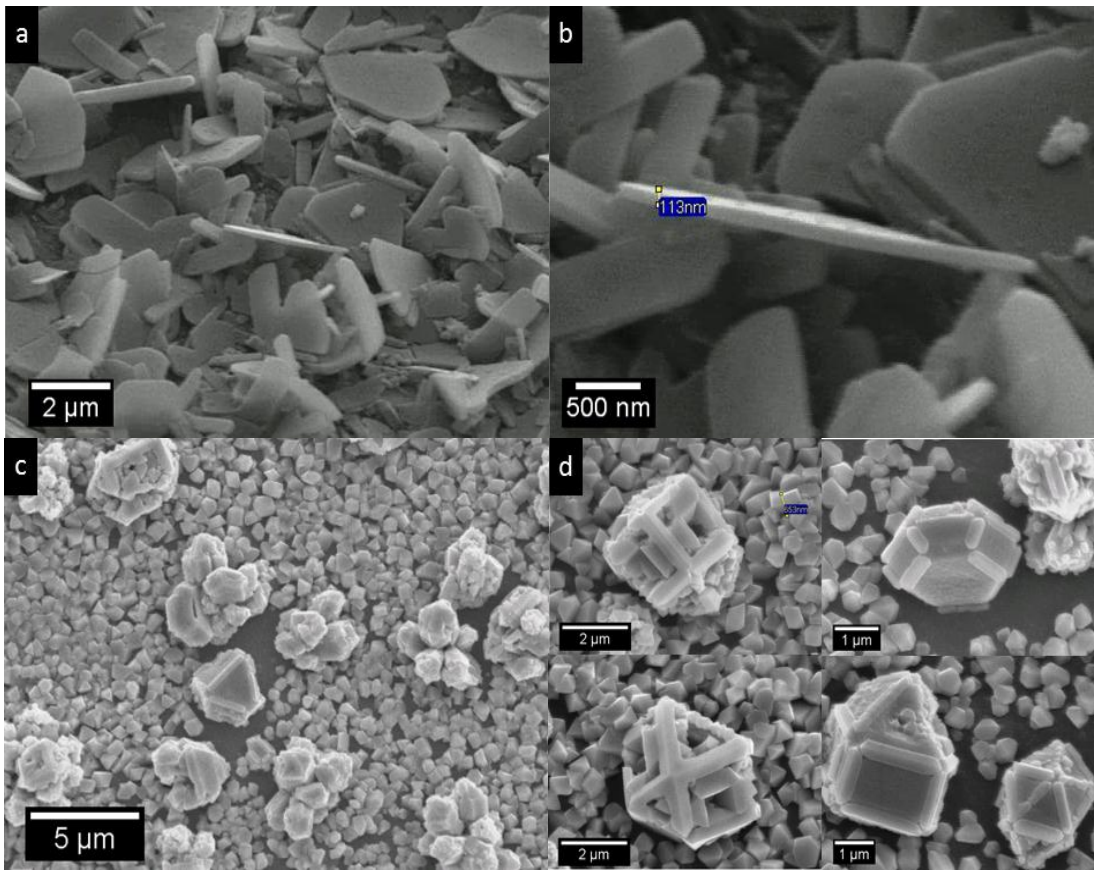

Figure 5.11. SEM micrographs of copper particles electrodeposited onto a bulk PPy film using -0.135 V for 6 min in solutions of (a), (b) 0.050 M $CuCl_2$ in 0.050 M NaCl and (c),(d) 0.050 M $CuSO_4$ in 0.100 M Na_2SO_4 with the addition of 5% wt SDS.

These experiments highlight that the electodeposition potential has a significant effect on the resultant morphopogy and density of nucleation sites. In particular a large deposition overpotential was required to produce the copper branch structures. In addition, an increase in the electrodeposition time increases the surface area of the copper deposits by producing hierarchial structures. This methodology of combining the correct copper salt concentration with an appropriate deposition potential and growth time can be useful for fabricating materials with specific types and sizes of copper deposits. Displaying this level of control over copper deposition employing a PPy substrate, through deposition time and potential, has not been reported in the literature to date.

5.2.1.4 Estimation of Copper Crystal Oxidation State

Identification of the copper oxidation state is a very important aspect when dealing with copper deposition since the various oxidation states yield different properties and practical applications. Cu_2O is the most interesting of these oxidation states due to its band gap of 1.9 - 2.2 eV which is desirable for solar energy conversion.[16, 25] Different researchers fabricating designer copper materials have strived to unequivocally determine the resultant materials oxidation state. One of the more prominent research groups for depositing copper materials on CPs, Tsakova and co-workers,[6, 32-36] have highlighted the difficulty with assigning oxidation states for electrodeposited copper by XPS analysis.[37] It is also known that XPS analysis only penetrates the uppermost 10 nm layers of a sample due to the excitation source consisting of X-rays. Therefore, it is difficult to ascertain if the material is pure Cu_2O or elemental Cu with a small layer of surface Cu_2O obtained from exposing the sample to air. While EDX is not capable of determining oxidation states it is a sufficient tool for identifying the quantity of oxygen within a material. Since it was possible to obtain EDX measurements at NUIM, the sample exposure time to air could be limited. This has been highlighted as an issue for obtaining the correct oxygen content with samples exposed to air.[38]

For these reasons, the oxidation state of the copper deposits discussed in this chapter were identified through the crystal shape, interfacial processes, EDX data and

comparative analysis of the current literature relating to copper electrodeposition that primarily focus on PPy substrate materials.

5.2.1.4.1 Crystal Habit Shape

Analysing the deposited coppper crystal morphology to identify the oxidation state can be achieved since certain oxidation states only conform to specific crystal habits. These ordered crystal facets are produced as the shapes are driven to achieve a minimum surface energy.[16] In general, the fastest crystal growth will occur perpendicular to the face with the highest surface energy, Scheme 5.3.[5] This results in the elimination of the highest energy surfaces with lower energy surfaces increasing in size. This has been observed to occur for Cu_2O materials electrochemically deposited on conducting substrates.[27, 31]

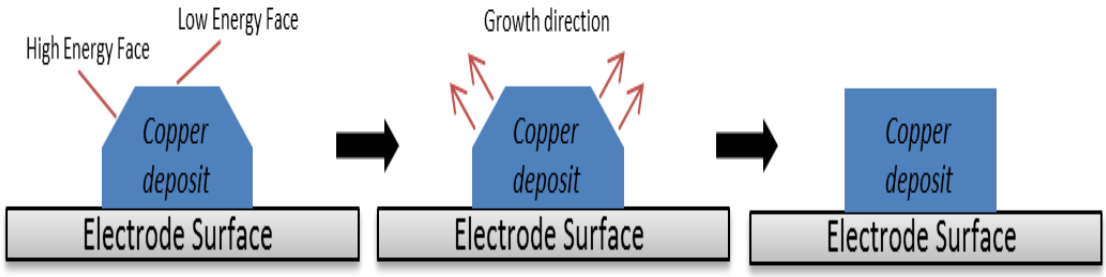

Scheme 5.3. Crystal habit growth occur along high energy facets (reproduced from reference [5]).

As can be seen from Scheme 5.4,[39] different cubooctahedron shapes are apparent depending on the growth rates achieved along the ⟨100⟩ and ⟨111⟩ directions. Siegfried and Choi demonstrated, using a pH similar to that used here, pH 4.1-4.9, that a range of Cu_2O structures could be deposited at gold electrodes.[5, 27] These structures shown in Scheme 5.4 are common crystal shapes for copper oxide materials.[5, 27, 40]

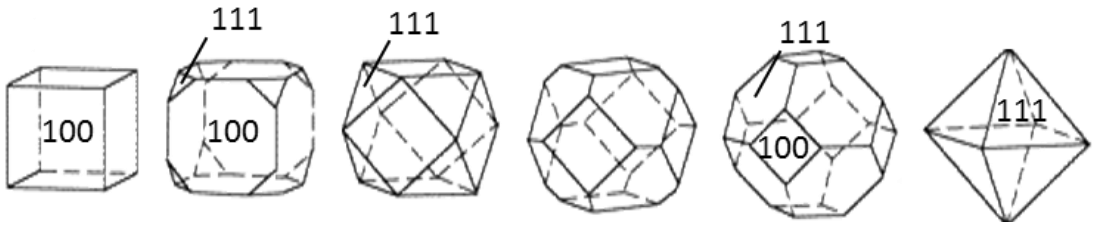

Scheme 5.4. Orientations of different crystal surfaces.

Comparision of the literature Cu_2O crystal habits with the structures produced in this study (pH 4.8) are outlined in Figure 5.12. It was observed that the smaller copper deposits conform to some of the crystal habits reported for Cu_2O. As more negative potentials were applied the crystals transformed from high energy ochaedral shapes with predominantly (111) facets to low energy cubic structres with more (100) orientations. This is due to the growth rate increasing dramatically with an increase in negative potential causing the high energy faces (111) to grow at a faster rate leaving only low energy orientations remaining (100), as highlighted in Scheme 5.3. Identification of the exposed crystal face is an important aspect since differenct faces produce different photoelectrochemical properties.[16]

In Figure 5.12a-d the potential was changed from -0.105, -0.135, -0.165 and -0.200 V. From these high magnification SEM micrograpahs it was observed that the structures formed at -0.105 V resemble triangle-based pyramids (Figure 5.12a) changing to truncated octahedrons (-0.135 and -0.165 V, Figure 5.12b and 5.12c, respectively) with increasing negative potential. Finally, at the most negative potential, -0.200 V, the deposits resemble cube structures, Figure 5.12d. Therefore, in the system studied here, it was apparent that the smaller sized deposits were composed of Cu_2O as they conform to common Cu_2O crystal habits reported in the literature. Previous work with our research group further stengthens this hypothesis.[13] Unfortunately, the larger sized deposits have not been reported in the literature to the best of our knowledge, therefore the same approach cannot be applied to predict their oxidation state.

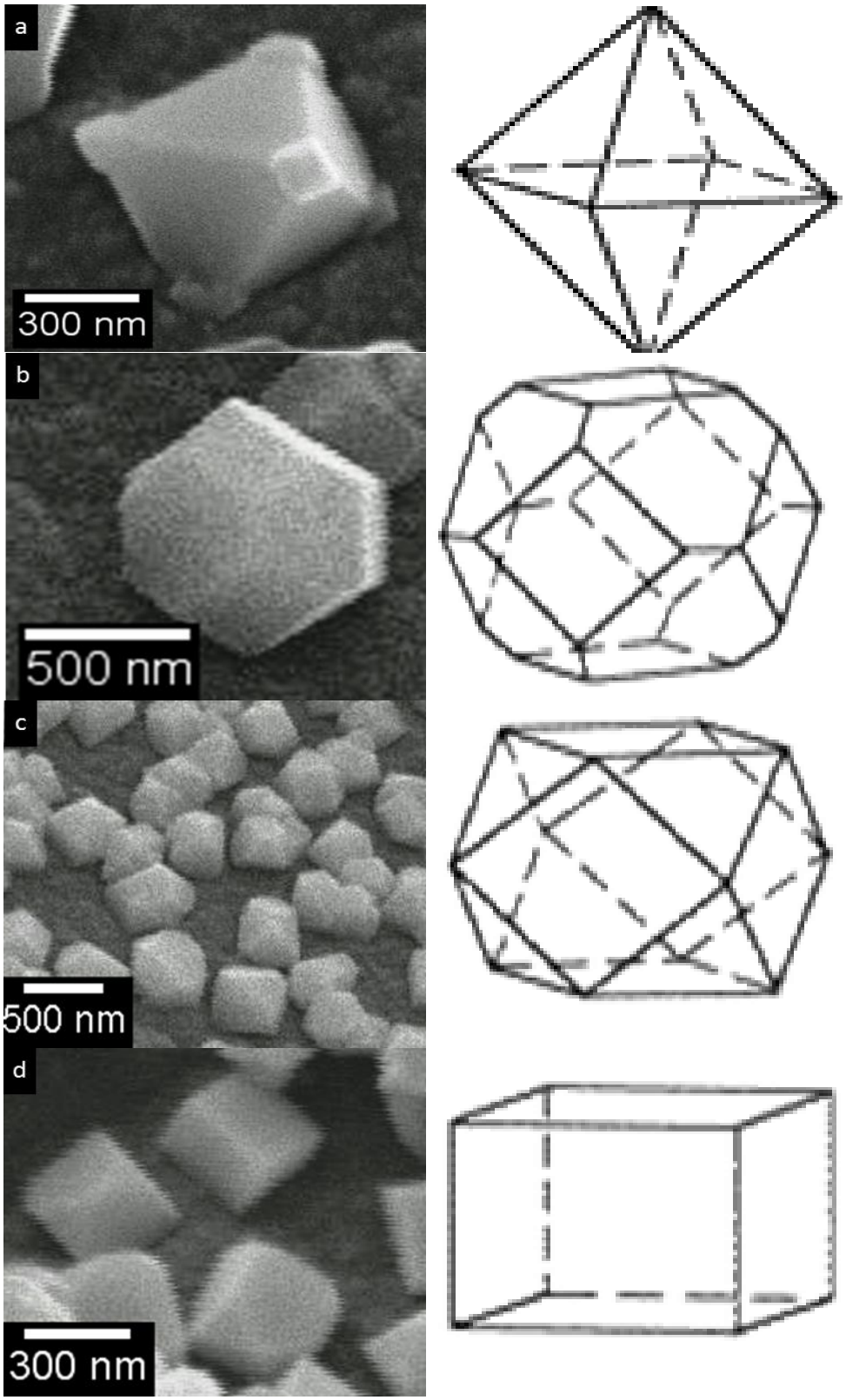

Figure 5.12. SEM micrographs of PPy films grown at 0.700 V for 100 s with 0.100 M monomer electrodeposited in 0.050 M $CuSO_4$ in 0.050 M Na_2SO_4 at (a)-0.105 V, (b) -0.135 V and (c) -0.165 V and (d) -0.0200 V.

It was observed that the structures deposited at the PPy surface were pH dependent. If a lower pH of 2.0 was employed, by additions of HCl, the previously formed deposits were not observed, Figure 5.13a. The structures formed under these HCl conditions resembled a honeycomb construct and the appearance of the standard Cu_2O crystal shapes did not occur, Figure 5.13b. It is known that in more basic pH the deposited copper is more likely to be in the oxide form due the greater availablility of OH^- ions in solution. Therfore, after observing this significant morphology change, it was possible the solutions used in this study were basic enough (pH 4.9) to encourge the formation of Cu_2O; while a pH of 2.0 led to an increase in Cu(0) depositions.

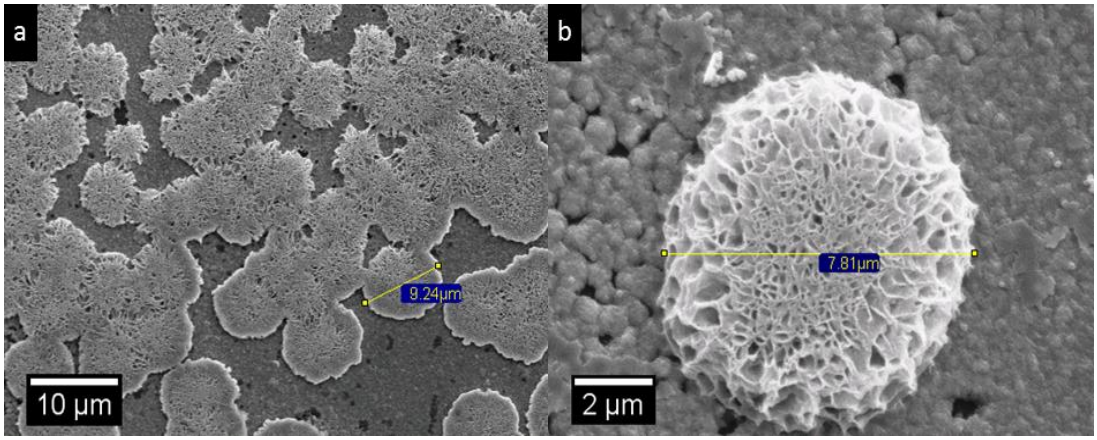

Figure 5.13. SEM micrographs of copper particles electrodeposited onto a bulk PPy film using -0.135 V for 6 min from a 0.050 M $CuSO_4$ solution in 0.050 M Na_2SO_4 brought to a pH of 2 using HCL.

5.2.1.4.2 Oxygen Reduction Reaction

Previous researchers within our research group have established the important role PPy plays in catalytically increasing the oxygen reduction reaction (ORR).[12-13, 41] This was confirmed by Andreoli *et al.* [12] by comparing a PPy covered substrate against a bare electrode in linear sweep experiments performed in oxygen saturated solutions. It was observed that the currents recorded were much greater for the PPy covered substrate highlighting its enhancement of the ORR. The process was described as oxygen molecules adsorbing at the PPy surface and being electrochemically reduced at negative potentials. This produced high levels of OH^- at

the electrode surface. These OH^- ions then partake in the deposition process with the Cu salts producing $Cu(OH)_2$ or CuO and cause a local rise of pH close to the electrode surface. Other researchers have also highlighted the benefit of O_2 in the formation CuO deposits.[42]

Applying this understanding to our system, since our electrode potentials are at more negative values than the study conducted Andreoli *et al.*, it is possible that the ORR reaction was further enhanced during the -0.135, -0.165 and -0.200 V deposition experiments. This would suggest that a greater amount of OH^- ions would be generated in our system. However, the pH of the bulk solutions was 4.8 and the actual increase in pH at the electrode surface was unknown. Since the Pourbaix diagram predicts copper metal formation at -0.100 V at a pH below 6.0 it is not clear whether the conditions studied here are favourable for copper metal or copper oxide deposition. Furthermore, since our solutions are not purged with oxygen the ORR may not have the same effect as the Andreoli studies have proven.

To investigate the effect of oxygen within our system a series of experiments were performed to remove the dissolved oxygen from the electrodeposition solution. Purging the solutions for 20 min with N_2 significantly reduced the overall oxygen content, however complete removal cannot be assumed. Comparing the currents recorded for the deoxygenated and standard solutions shows the former solution does not contain the diffusion limited peak common for the standard solutions, Figure 5.14a. Comparison of the SEM micrographs for these two solutions shows a significant variation in morphology. The most striking observation was that the smaller cuboocatahedron deposits are not present in the deoxygenated deposition, Figure 5.14b. However, the larger sized structures had deposited, although in a different morphology compared to the standard solution deposition, Figure 5.14c. Since the deoxygenated solution has a lower content of oxygen available to partake in the ORR it may suggest that the larger deposited structures are composed of Cu(0). Comparatively, since the standard solution contains similar sized structures but with a varying morphology they may be a hybrid form of Cu(0), Cu(I) and Cu(II). Therefore, this direct comparison only leads to the conclusion that the larger structures are not easily recognised as one specific oxidation state, but are possibly a hybrid form of Cu and Cu(I) and/or Cu(II).

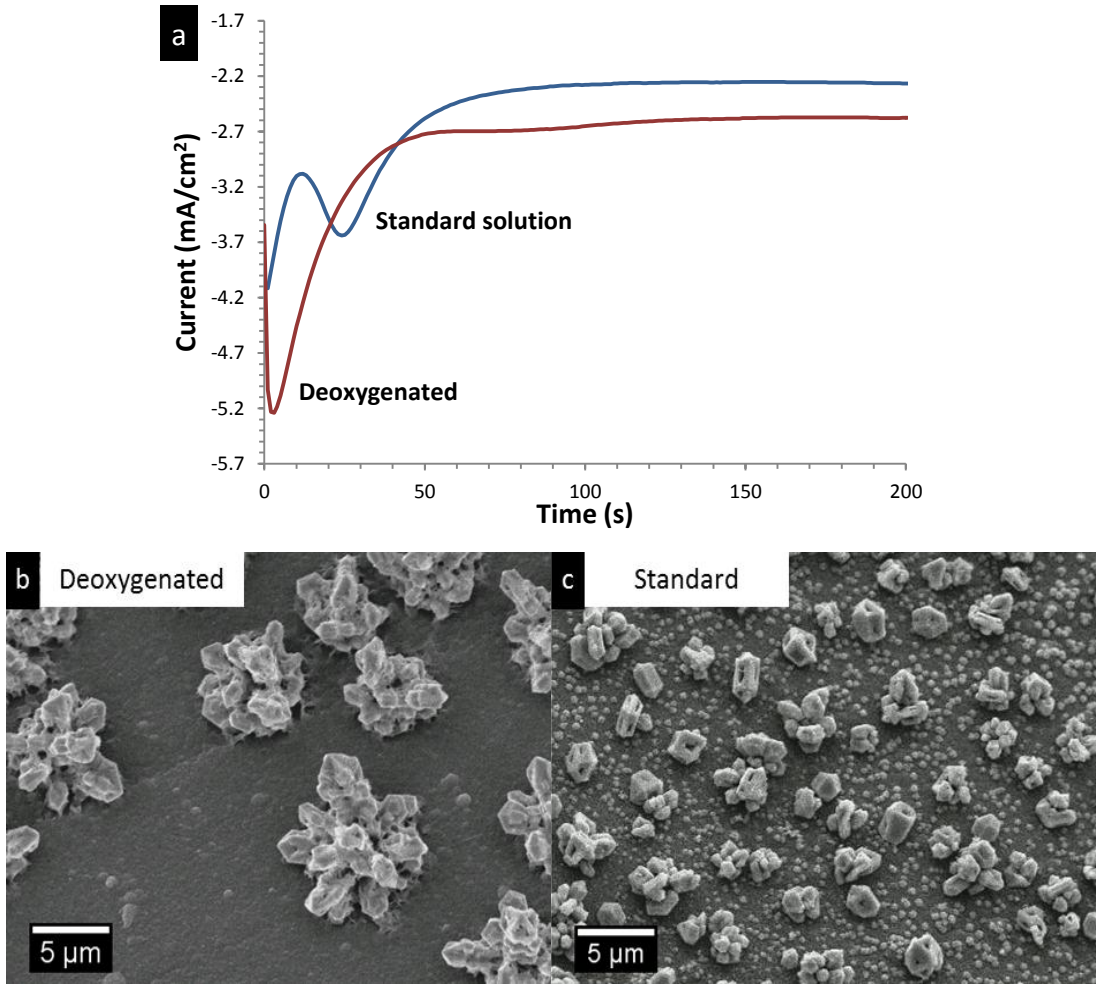

Figure 5.14. Electrodeposition profile of PPy films grown at 0.700 V for 100 s with 0.100 M monomer electrodeposited in 0.050 M $CuSO_4$ in 0.050 M Na_2SO_4 at -0.135 V for 6 min in a standard solution and deoxygenated solution (a), SEM micrograph of deoxygenated (b) and standard (c) solutions.

EDX analysis of the structures produced from the deoxygenated solution reveals that no oxygen or copper was present at the PPy substrate, Figure 5.15a. When the electron beam was focused on the copper structures; signals for both copper and oxygen were registered. This oxygen may be present due to a thin oxide layer on the surface. However, as stated previously, since care was taken when handling the electrodes to prevent their exposure to air, it is possible that this oxygen signal originated from within the structure as some form of CuO. This result shows that even the structures deposited in the deoxygenated solutions are possibly some form of hybrid oxide/metal crystal. Analysis of the experiments performed in this section has led to a mixed conclusion to the valance state of the deposited copper. Therefore, to assist in predicting the valance state of the deposited materials, electrochemical

copper deposition procedures from the literature were analysed and compared to the conditions used in the system.

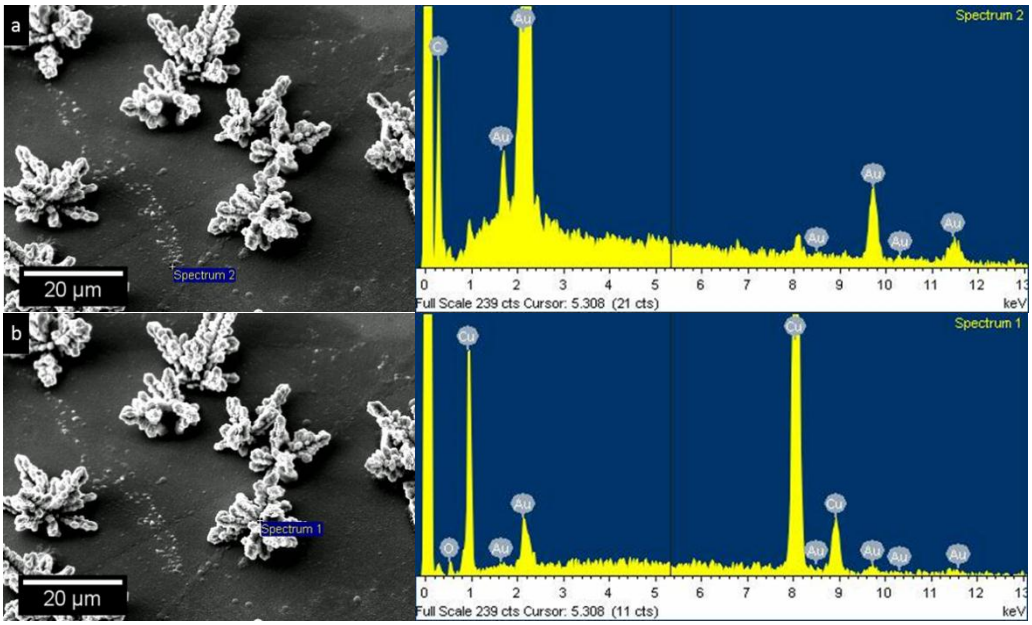

Figure 5.15. SEM micrographs and corresponding EDX spectrum of PPy polymers grown at 0.700 V for 100 s electrodeposited in a deoxygenated 0.050 M $CuSO_4$ in 0.050 M Na_2SO_4 solution at -0.135 V for 6 min. Points of interest (a) PPy film substrate and (b) copper microstructure.

Tanaka *et al.* [43] have observed, at an amorphous carbon electrode using $CuSO_4$ (pH 2), that Cu metal was only deposited at potentials lower than -0.600 V. Furthermore, they suggest that SO_4^{2-} anions suppress the formation of Cu metal at the electrode surface. They also observed Cu_2O deposition in a deoxygenated solution at similarly low pH identifying H_2O as sufficient for promoting Cu_2O deposition. Compton and co-workers observed copper Cu(II) reduction to Cu(0) only by reduction of their solution pH to a value of 3.0.[10] The substrate used was a much more conducting boron doped diamond. Likewise Zheng *et al.* [44] produced Cu(0) films at ITO electrodes at a pH of 1.2, but Cu_2O at pH values of between 3.0 and 5.0. This would suggest that the pH (4.8) used in this system would not support the deposition of Cu(0) materials.

At PPy coated electrodes it has been observed by Cioffi *et al.* [36] using a pH of 5.0 and a pulsed potential (-0.350 V) that CuO species were deposited at PPy films under these conditions, confirmed by XPS. Similar work by Sakar *et al.* [23] shows that CuO was deposited on PPy films at negative potentials of -0.900 V vs Ag/AgCl. Finally, it

has been reported from ESR experiments that Cu(I) species tend to associate at electron rich atoms such as sulfur or nitrogen.[6] Other reports highlight that Cu(I) forms a stable complex with PPy compared to Cu(0) and can improve the conductivity of PPy by interacting with the nitrogen lone pair.[45-47] Since this copper form would then be more stabilised over the elemental form it will be harder to reduce.[48] Therefore, at the negative potentials employed for this system (~ -0.200 V) it was possible to solely deposit only Cu_2O materials.

From the experiments outlined in this section we are able to conclude that the oxygen within the deposition solution has a profound effect on the number and morphology of the copper deposits. However, strictly assigning the structures formed in these deoxygenated solutions as Cu(0) may not be correct since our mildly acidic pH, relatively low potential (~ -0.135 V) combined with the enhanced ORR at PPy surface suggests that the standard conditions described herein should produce Cu_2O deposits. This was reiterated by similar studies performed in the literature. Further studies will use XRD to qualitatively determine the nature of the copper species.

5.2.1.5 Electrodeposition of Copper onto Poly(*N*-(2-cyanoethyl)pyrrole) Polymers

The PPyEtCN polymers discussed in Chapter 3 were a novel morphology of CP, therefore the electrochemical deposition of Cu on their surface was attempted to identify their ability to be effective supports for copper deposition. These materials could then also be tested for their ability to be used as a nitrate sensing material. Studying the electrochemical deposition process at bulk PPyEtCN materials has also not been reported in the literature. This may be due to the fact that these polymers are not as intrinsically conducting as the polymers formed using the typical un-substituted Py and so are not suitable candidates.[49] The lower electrical conductivity observed for the PPyEtCN nanowires studied in Chapter 3 was explained due to steric clashing from the substituted group and an over oxidation process at the carbon β position. This produced a low π-π overlap between the Py rings. However, in spite of this, having the C≡N moiety at the nitrogen position of the Py may have permitted

a new interaction between the polymer and the electrodeposited copper. This possibility was to be investigated.

Using the condition described previously for the electrochemical deposition of $CuSO_4$ at PPy, Section 5.2.1.1, the PPyEtCN bulk polymers were initially used as the substrate material followed by the nanowire/microtube polymers. The low electrical conductivity was evident in the electrochemical deposition experiments as the current recorded for the electrodeposition of Cu at potentials of -0.135 and -0.200 V, Figure 5.16a, was low, signifying a slow deposition rate. These were the same potentials which produced a complete coverage of large copper microdeposits on PPy films. While the current recorded did increase for experiments at -0.200 V it was not a large increase. This was due to the more insulating PPyEtCN films requiring more energy to transfer electrons through the polymer layers which resulted in a low reduction of Cu^{2+} across the electrode. Furthermore, when EDX and SEM analysis were obtained neither displayed any indication of the presence of copper deposits. Only when extremely negative potentials were applied, lower than -1.000 V, was a deposition process observed.

The currents recorded for experiments employing -1.100 and -1.200 V are displayed in Figure 5.16b. Here it can be seen that the currents recorded at both overpotentials were significantly larger than that of the -0.200 V experiments. Comparing the total charge passed at 180 s for each experiment shows that at -0.200 and -1.200 V the charges passed were 6.8 $x10^{-5}$ and 3.5 $x10^{-2}$ mC/cm^2 respectively. It is evident that overcoming the resistance of the PPyEtCN films was only achieved at the negative potentials of -1.200 V. This was apparent from the large negative current recorded at this overpotential.

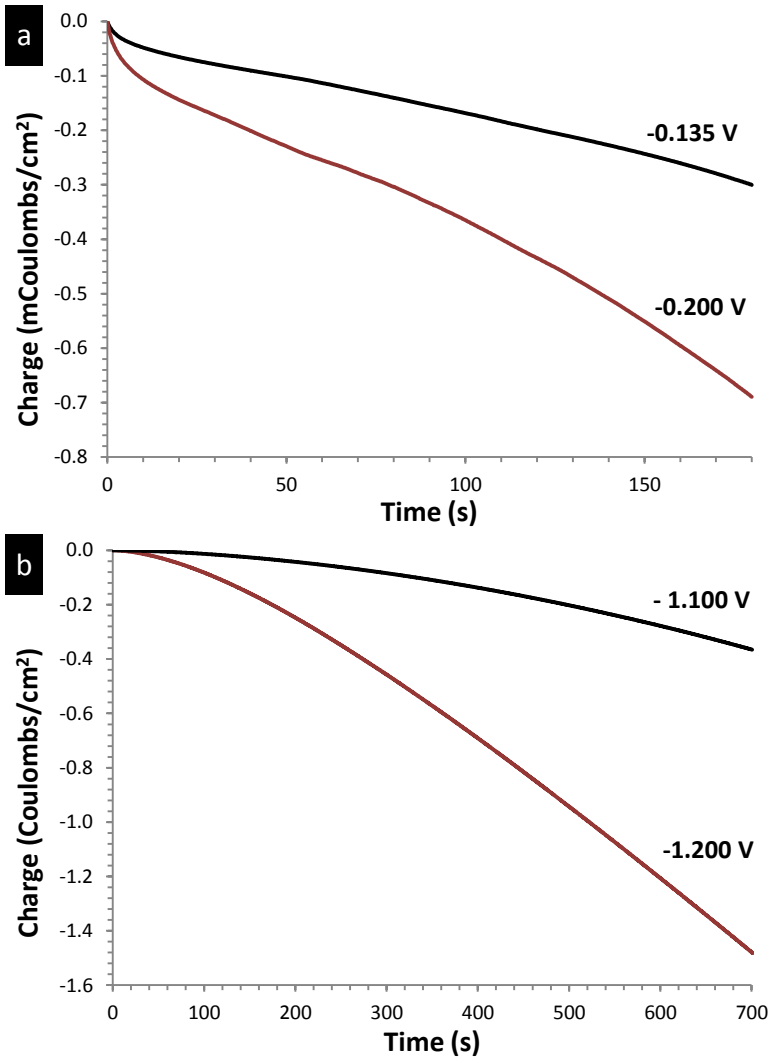

Figure 5.16. Electrodeposition onto PPyEtCN films from a 0.050 M $CuCl_2$ in 0.100 M Na_2SO_4 solution at (a) -0.135 and -0.200 V and (b) -1.100 and -1.200 V.

Inspection of the SEM micrographs obtained from the electrodeposition at -1.100 V displays some interesting nucleation of copper microstructures. At a low magnification a large ring of copper was observed around the outside of the electrode, Figure 5.17a. These structures had grown significantly in size and extended their length over electrode without creating new nucleation sites, Figure 5.17b. Closer inspection of the original nucleation sites reveals that the copper was in fact nucleating down the side of the electrode which was possibly not covered by insulating PPyEtCN, Figure 5.17c. The high energy barrier associated with depositing on the PPyEtCN film forced the copper to nucleate at these exposed areas of bare electrode. Once deposition sites had formed, fresh copper deposition continued at these copper deposits rather than forming new nucleation sites on the

insulating PPyEtCN surface. This produced the extremely large microstructures observed in Figure 5.17a.

Inspection of the centre of the electrode which was covered in a uniform film of PPyEtCN, it was seen that a relatively small amount of copper was deposited. Small ~300 nm copper cubes were seen to form in a dispersed pattern, Figure 5.17d. This was an interesting result since this deposition was performed with a chloride copper salt in a sulphate electrolyte. In Section 5.2.1.3, it was shown that a chloride salt in a chloride electrolyte produced a sheet type morphology. However, this morphology was not present in the mixed Cl^-/SO_4^{2-} solution discussed here. Therefore the, SO_4^{2-} anion has a greater impact on the final morphology of the deposits, even in a mixed electrolyte.

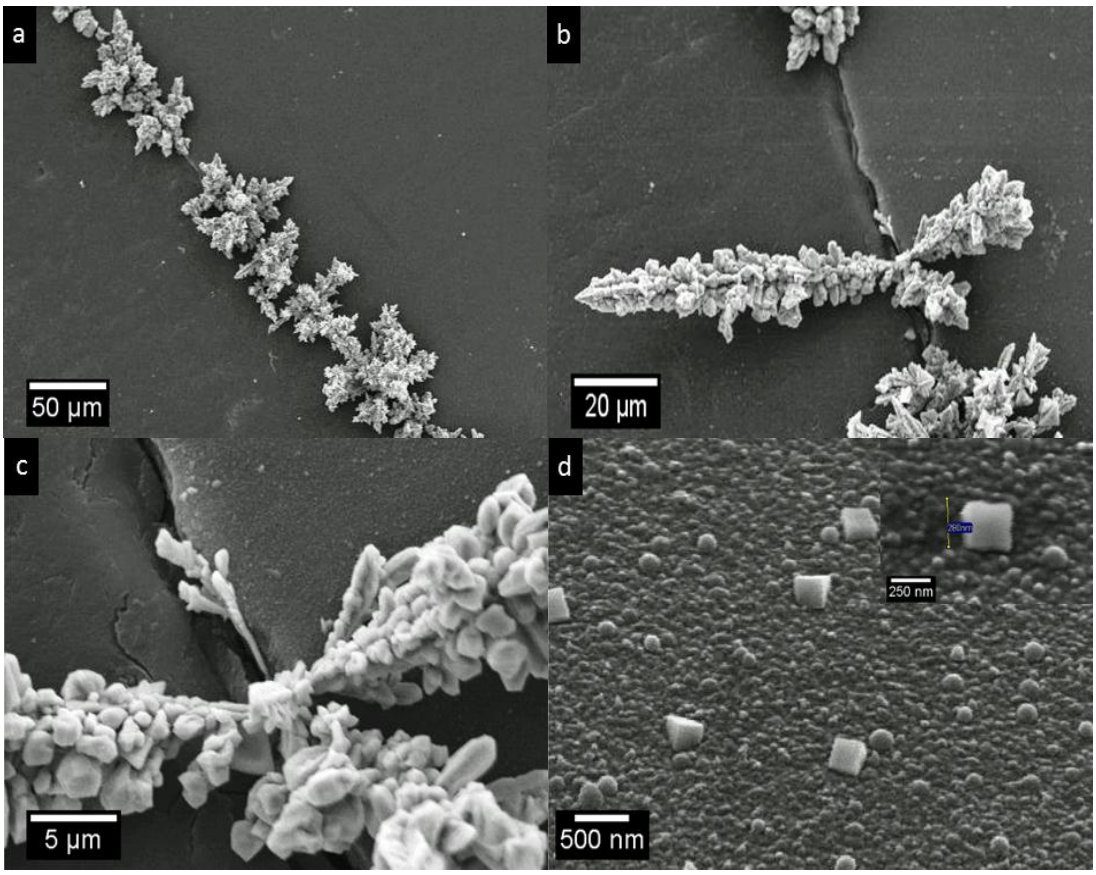

Figure 5.17. SEM micrographs of electrodeposited copper on PPyEtCN films from a 0.050 M $CuCl_2$ in 0.100 M Na_2SO_4 solution at -1.100 V for 700 s (a)-(c) various magnifications of edge of electrode and (d) centre of electrode.

It was clear that an applied potential of -1.100 V was not sufficiently negative to lower the deposition barrier to form micro deposits on the PPyEtCN polymer surface.

Increasing the potential to -1.200 V led to a larger increase in the current recorded, Figure 5.16b. Inspection of the centre of the electrode by SEM revealed large deposits of copper covering the entire electrode, Figure 5.18a. Similar to the -1.100 V experiments these deposits, once formed on the electrode, grew as very large microstructures. These copper structures grew to a large vertical height perpendicular from the electrode as fresh copper growth only occurred from nucleation sites of already deposited copper. Figure 5.18b. The deposits were very random in nature with a range of structures forming including cube, triangle, branch and sheet type morphologies. Some examples are highlighted in Figure 5.18c to 5.18f. These materials were verified as copper by EDX analysis.

It was observed that the deposits were nucleating in a progressive manner as there was a dramatic difference in the deposit size across the electrode surface. The same types of structures could also be seen at different growth stages on the same electrode. An example is shown in Figure 5.19a, the short branch like morphology were present while at another section of the electrode the same structure could be seen in a much larger size, Figure 5.19b. A more extended growth can be seen in Figure 5.18e.

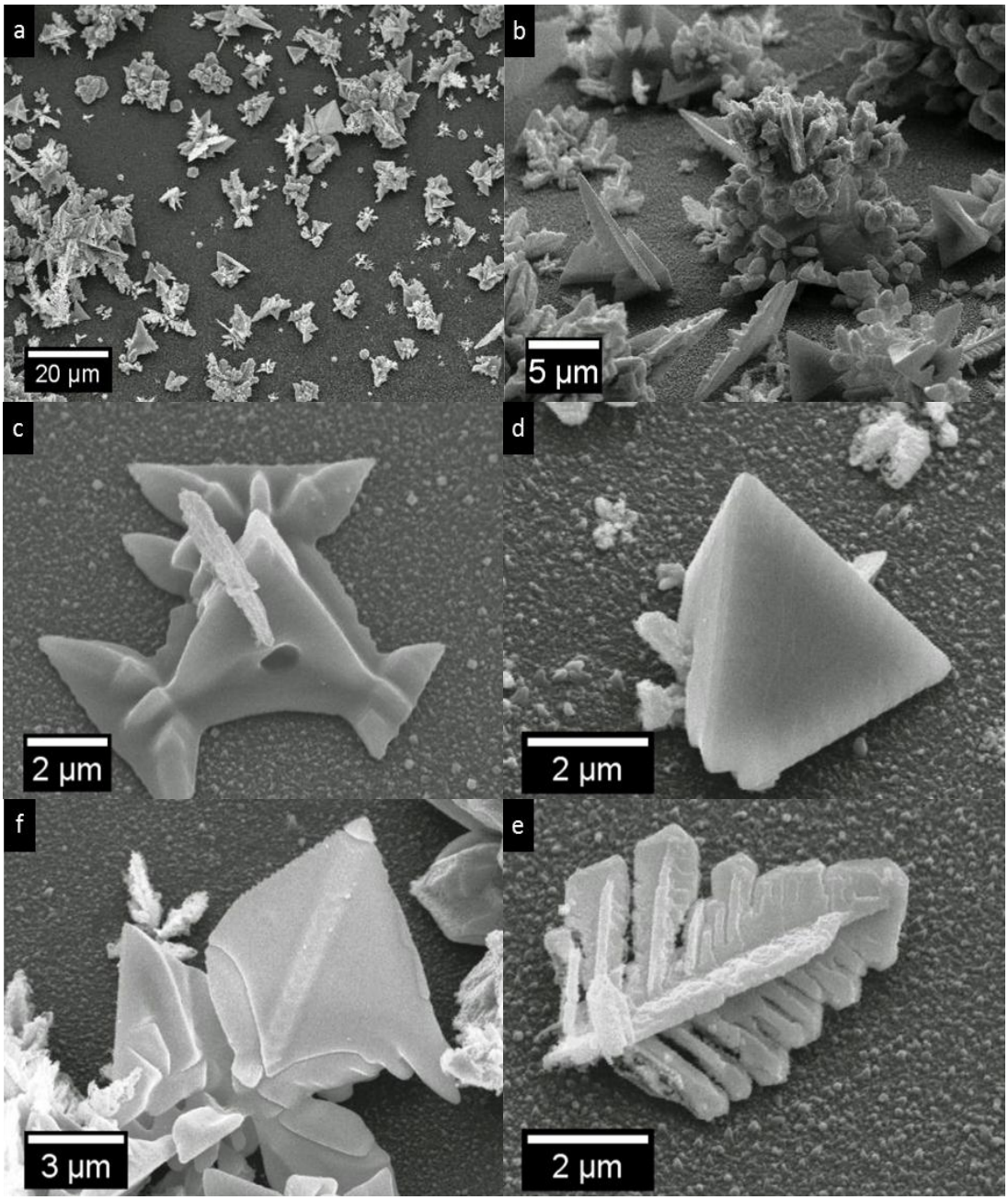

Figure 5.18. SEM micrographs of electrodeposited copper on PPyEtCN polymers from a 0.050 M $CuCl_2$ in 0.100 M Na_2SO_4 solution at -1.200 V for 700 s (a) top view, (b) tilted view and (c)-(f) prominent copper micro morphologies formed.

These three separate stages of growth occurred on the same electrode and are indicative of a progressive nucleation process. This may have occurred as the first nucleation sites grew excessively large they were incapable of further deposition. The growth rate was maintained at these initial copper deposits as it was possible new nucleation sites were not easily formed due to the resistive nature of the PPyEtCN. As the copper deposits developed into µm sized structures, electron

transfer to the electrode may have become a slower process. The PPyEtCN substrate would then more energetically favourable for copper deposition to restart at its surface. This would lead to new nucleation sites forming intermittently throughout the experiment. This is the opposite to what was observed for the electrodeposition of PPyEtCN nanowires which nucleated instantaneously on the conducting GC substrate (Chapter 3), leading to wires of a homogenous size. Although copper deposition on the PPyEtCN polymer nanowires was observed to be a very slow process which required a much greater driving force (applied potential) compared to PPy, the films still responded similarly in terms of electrodeposition rates. An increase in current was observed when an increase in copper concentration was employed and when a cyclic program was used the polymers displayed the typical reductive peaks associated with copper electrodeposition (not shown).

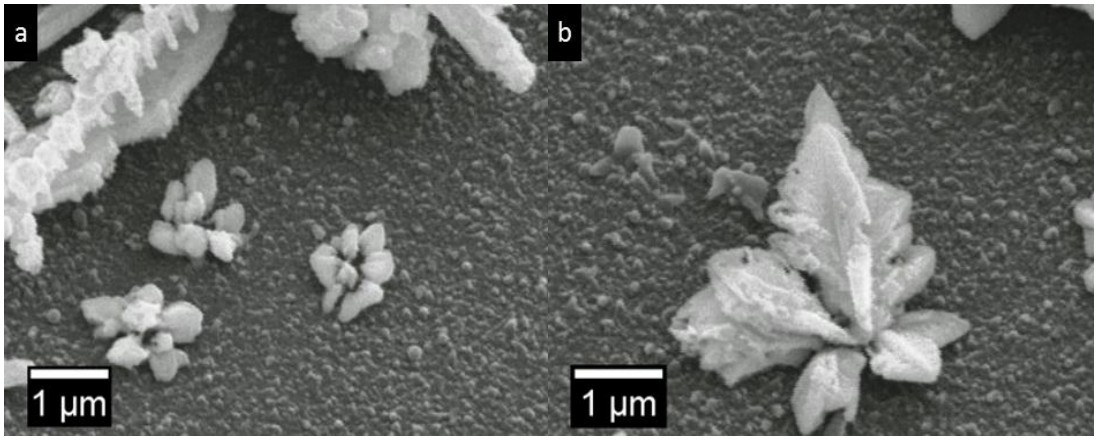

Figure 5.19. SEM micrographs of electrodeposited copper on PPyEtCN films from a solution of 0.050 M $CuCl_2$ in 0.100 M Na_2SO_4 at -1.200 V for 700 s, showing progressive formation of leaf structures (a) early stage and (b) developed growth.

In a preliminary experiment using the PPyEtCN nanowires/microtube films (formed from monomer droplet methodology, Chapter 3 Section 4.2.1) it was possible to electrodeposit large structures of hierarchical copper using H_2SO_4 as a supporting electrolyte. The deposition was not uniform however and only occurred towards the outer areas of the PPyEtCN films. It can be seen from Figure 5.20a that the copper structures deposited on both the nanowires and the semi hollow microtubes. The copper was observed wrapped around the outside of the microtubes and grew outwards from them, Figure 5.20b. In other cases the copper was observed in several

sections along walls of the tubes, Figure 5.20c. Unexpectedly, it was seen that even thick and potentially insulating microtubes which were several microns from the electrode surface had copper deposits at their extremities, as shown in Figure 5.20d.

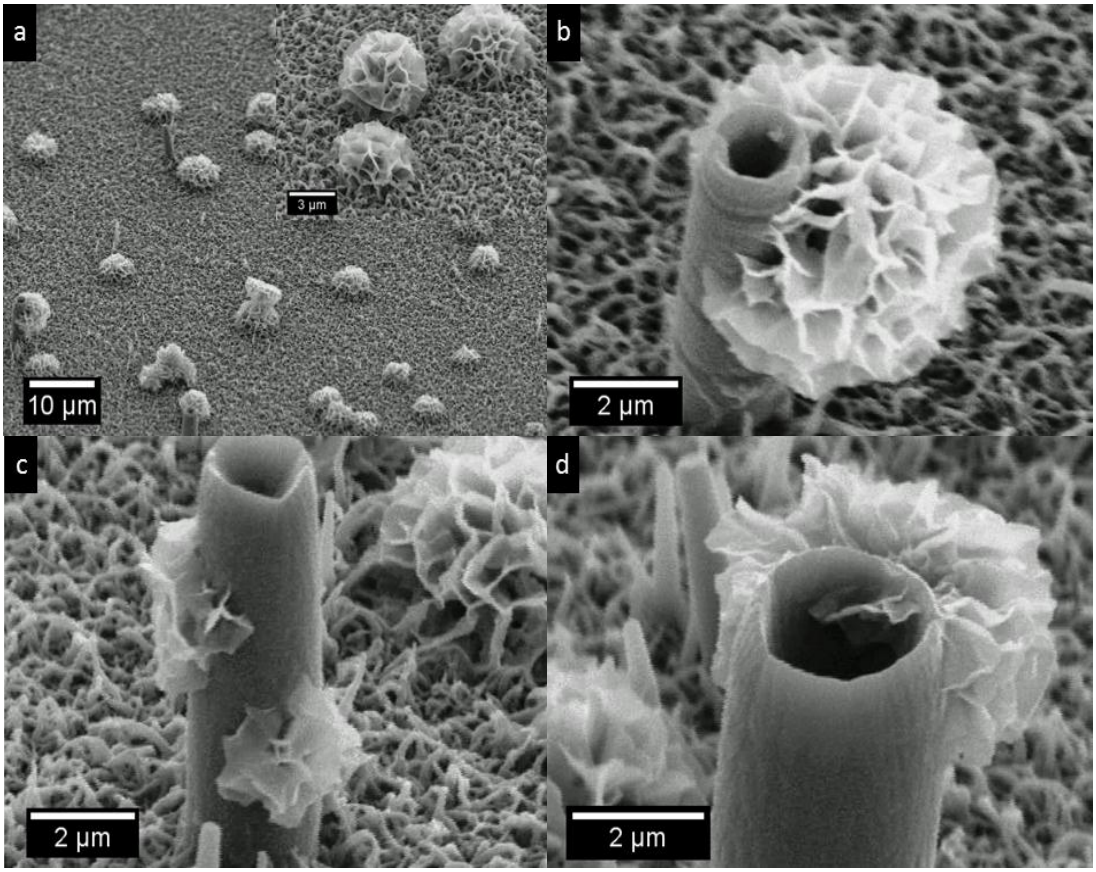

Figure 5.20. SEM micrographs of electrodeposited copper on PPyEtCN nanowires and microtubes from a solution of 0.050 M $CuCl_2$ in 0.050 M H_2SO_4 at -1.200 V for 700 s. Distribution of copper particles on nanowires (a) and different nucleation points of copper structures on the microtubes (b)-(d).

These experiments highlight that while it was possible to electrodeposit copper materials onto PPyEtCN polymers the process was very slow due to the low electrical conductivity of the polymer. Therefore, as a substrate material, PPyEtCN was not an efficient material for electrodeposition of metallic structures due to its insulating properties compared to typically employed CPs. However, during the course of these studies a second application for these insulating materials was identified.

Employing the emulsion procedure described in Chapter 4 to produce the hollow PPyEtCN morphology, it may be possible to use these polymers as templates for Cu electrodeposition. As shown in this section, PPyEtCN is only capable of reducing copper at potentials more negative than -1.000 V, however since the microtubes have an exposed GC base area, the copper would nucleate at these points at an extremely fast rate. Ideally the copper would grow to fill the hollow microstructure. Once the polymer 'shell' is removed it would leave free standing Cu microstructures. These structures could then be employed for the sensing of nitrate as their unique microstructure would provide them with the benefit of a larger surface area. This combined with the fact that they are anchored to an electrode surface may provide a cheap and reliable method of producing a sensor which is stable and robust. This is a novel and interesting alternative to templating which typically consists of purchasing costly aluminium template grids. Furthermore, as discussed in Chapter 4, the PPyEtCN microtube diameter can easily be controlled by altering the sonication time or toluene addition. This produces a versatile and cheap polymer template system for the production of electrodeposited metal microstructures. Experiments are currently being performed to investigate the feasibility of this idea.

5.2.2 Copper Deposition on Polypyrrole Nanowires

As discussed in Section 5.2.1.5, the PPyEtCN nanowire films were not capable of facile electrodeposition of copper. To overcome the insulating nature of the PPyEtCN and still maintain the attractive properties of a nanowire polymer, experiments were performed using PPy nanowires as an alternate polymer substrate. This would utilise the larger surface area of the nanowires combined with the ability to easily electrodeposit copper at PPy substrates.

5.2.2.1 Nanowire Reproducibility

PPy nanowires have been reported in the literature by various researchers using different methods. Dongtao Ge and co-workers used a carbonate based system which provided precise control over the resultant wires, by pH and applied potential alterations.[50-51] The copper electrodeposition procedures outlined Section 5.2.1 for bulk PPy highlighted PPy as an excellent material for copper deposition. Employing PPy nanowires as a substrate for electrodeposition of copper takes advantage of the increased surface area of the wires. This provides enhanced electrochemical properties which will benefit the composite material due to the increased interaction with the electrolyte leading to a faster electrochemical response.[52] This stems from a shorter diffusion length of counter ions from the bulk solution to the surface of the nanomaterial.[53]

This carbonate system was used in conjunction with 0.100 M $LiClO_4$ and 0.100 M Py monomer. It was observed that the concentration of the carbonate in the polymerisation solution had a marked effect on the nanowire polymerisation rate and electrode coverage. The carbonate solution was comprised of Na_2CO_3 and $NaHCO_3$. The ratio of these salts in the electrolyte mixture affected the solution pH. Additions of 0.100 M Na_2CO_3 to 0.100 M $LiClO_4$ resulted in a pH of 10.5. At this pH the growth of the polymer was very slow and resulted in patchy and uneven polymer deposits, as shown in Figure 5.21a and 5.21b. In an attempt to reduce the electrolyte pH, the concentration of $NaHCO_3$ in the electrolyte was varied to 0.100, 0.200 and 0.300 M. This led to the decrease in the pH from 10.5 to 9.8, 9.5 and 9.3

respectively. The lower pH was more suitable for growing the PPy nanowires and significantly reduced the irregular growth issues described.

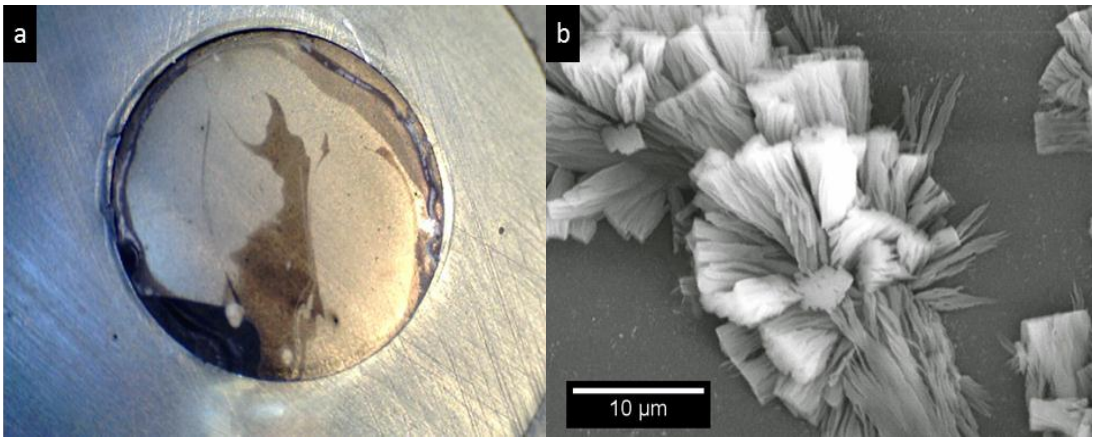

Figure 5.21 Low magnification microscope image of the entire electrode surface (a) and high magnification SEM micrograph of irregularly formed nanowire structures (b) when using 0.100 M Na_2CO_3, 0.100 M $LiClO_4$ with 0.100 M Py monomer at a pH of 10.5.

However, this high concentration of salts (0.100 M Na_2CO_3, 0.300 M $NaHCO_3$ and 0.100 M $LiClO_4$) was detrimental to the surface of the counter electrode. It is known that a current is passed through the counter electrode during a redox reaction which is of an opposite nature to the current flowing at the working electrode. If the surface area of the counter electrode is smaller than that of the working electrode it can impede the reaction taking place at the working electrode.[54] Therefore, it is common in electrochemical systems to employ high surface area counter electrodes such as coiled wires or a fine mesh. After several experiments polymerising the nanowires while reusing the same counter electrode, it was observed that the current response during polymerisation would decrease.

Inspection of the counter electrode using SEM and EDX revealed that the surface was contaminated with a range of salt deposits, Figure 5.22a. The EDX analysis revealed they were composed of a range of salts contained in the various electrolytes, Figure 5.22b. Further inspection using EDX mapping shows that the signal for the Pt counter electrode was not apparent on the sites of the salts, Figure 5.23. It also shows the composition of the various salts by colour, or by coverage as shown inset for carbon and oxygen. These salts would reduce the electrochemical reaction taking place at the working electrode and limit the nanowire growth rate. To overcome this

problem a fine platinum mesh was incorporated into the counter electrode and cleaned after every experiment by heating over a naked flame. Furthermore, it became apparent that the carbonate anions had to be removed from the PPy nanowires after they had been electrodeposited.[55] Employing an acidic solution and cycling between the set potentials of 0.100 to -0.400 V would reduce their occurrence within the polymers and condition the nanowires for the copper deposition procedure, which also cycled from 0.100 to -0.400 V, Section 5.2.2.3.

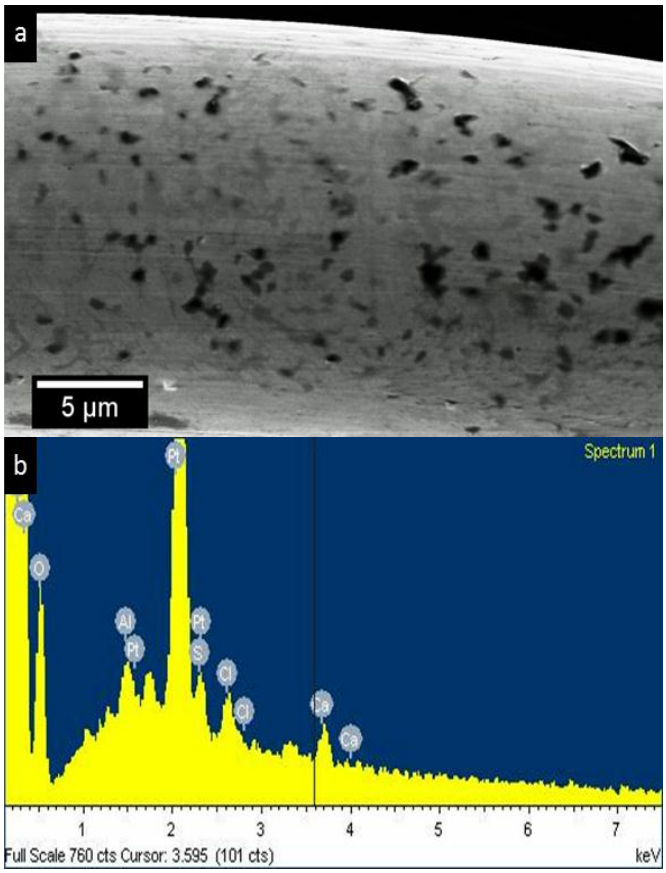

Figure 5.22. SEM micrograph of contaminated Pt counter electrode displaying salt depositions (a) and EDX spectra of salt contaminations (b).

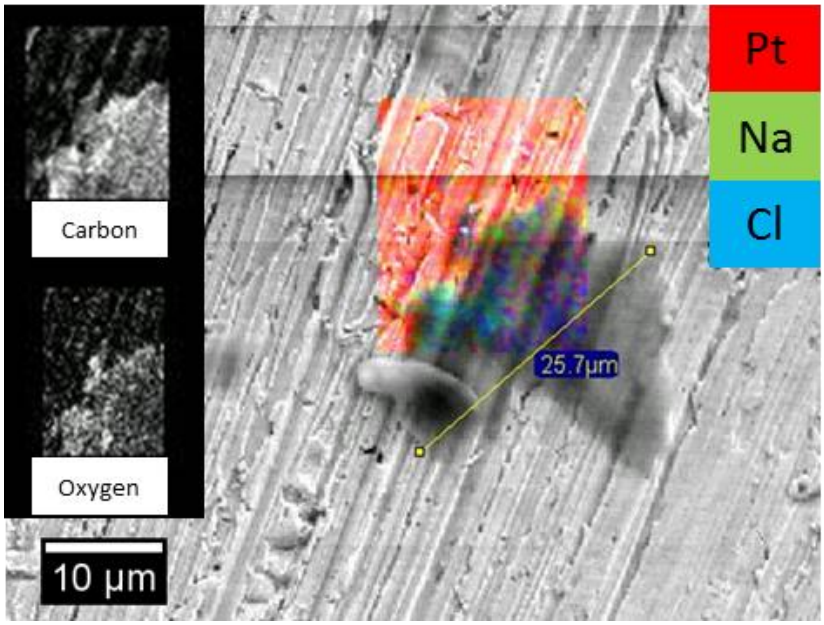

Figure 5.23. SEM micrograph of contaminated Pt counter electrode displaying salt deposition with overlapping EDX map of various elements. Elements with corresponding colours: red-Pt, green-Na and blue-Cl. Overlapping colours produce new colours dark green and purple. Carbon and oxygen contents shown as individual greyscale maps inset, while area correspond to carbon or oxygen while the dark area is the underlying Pt electrode.

5.2.2.2 Polypyrrole Nanowire Electrochemical Response

Similar to the experiments using bulk PPy, Section 5.2.1, there was a necessity to reproducibly fabricate the nanowire polymers. As described previously thinner and thicker areas of PPy on the electrode surface leads to different nucleation rates for copper particles.[18] To measure the reproducibility of the nanowire polymers a $[Fe(CN)_6]^{3-}$ probe was used to investigate their electrochemical activity. The current response and location of the E_p of the Fe^{2+}/Fe^{3+} couple would reveal the level of activity of the nanowire electrode. A higher current response would signify an increased surface area at the electrode and a shift in the redox potentials would be indicative of a difference in electrical conductivity, as the reaction had become thermodynamically more difficult.[21]

Comparison of a bare GC electrode to a PPy nanowire modified electrode shows that the peak and background currents were larger for the modified electrode, Figure 5.24. This broader background was due to the larger capacitance and higher

electrochemical response associated with the nanowires.[56-57] Capacitive effects may originate from the higher surface area of the nanowires being able to store more charge. This in turn would require a larger double layer forming in solution to counter balance this charge.[19] This increase in capacitance is commonly seen for CP nanowire materials.[58] The nanowire modified surface provides a larger surface area which allows more of the electrochemical reaction to take place compared to the geometric surface area.

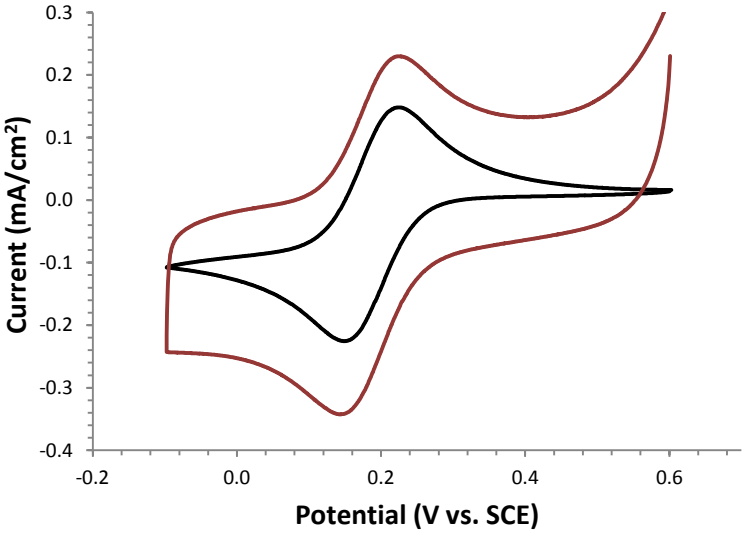

Figure 5.24. Cyclic voltammetry of PPy nanowires grown in 0.100 M Na_2CO_3/0.300 M $NaHCO_3$ (red trace) with 0.100 M Py (a) vs. bare GC electrode (black trace) in 5 mM $[Fe(CN)_6]^{3-}$ with 0.100 M KCl.

Controlling the charge passed at the electrode during the growth process was an accurate means of controlling the length and thickness of the nanowires. Comparing the current recorded using the $[Fe(CN)_6]^{3-}$ probe for several nanowire growth charges identified which polymer thickness produced the greatest surface area. It was observed that the capacitance value increased as the thickness (or charge passed) for the PPy nanowire films increased from 0.2 to 0.3 C, Figure 5.25a and 5.25b. This was due to the thinner polymer (0.2 C) having shorter nanowires and a smaller surface area. Further increasing the thickness to 0.4 C produced a drop in the capacitance value as shown in Figure 5.25b. This was due to longer wires produced at this thickness misaligning to a greater extent and hindering diffusion of ions to inner parts of the nanowire film.[53, 58] Further increments of charge passed to 0.5 and 0.6 C produced similar drops in capacitance and even shifted the I_p of the redox

couple to higher and lower overpotentials for the oxidation and reduction of the Fe ion respectively. Therefore the large growth charges corresponding to 0.5 and 0.6 C were not employed.

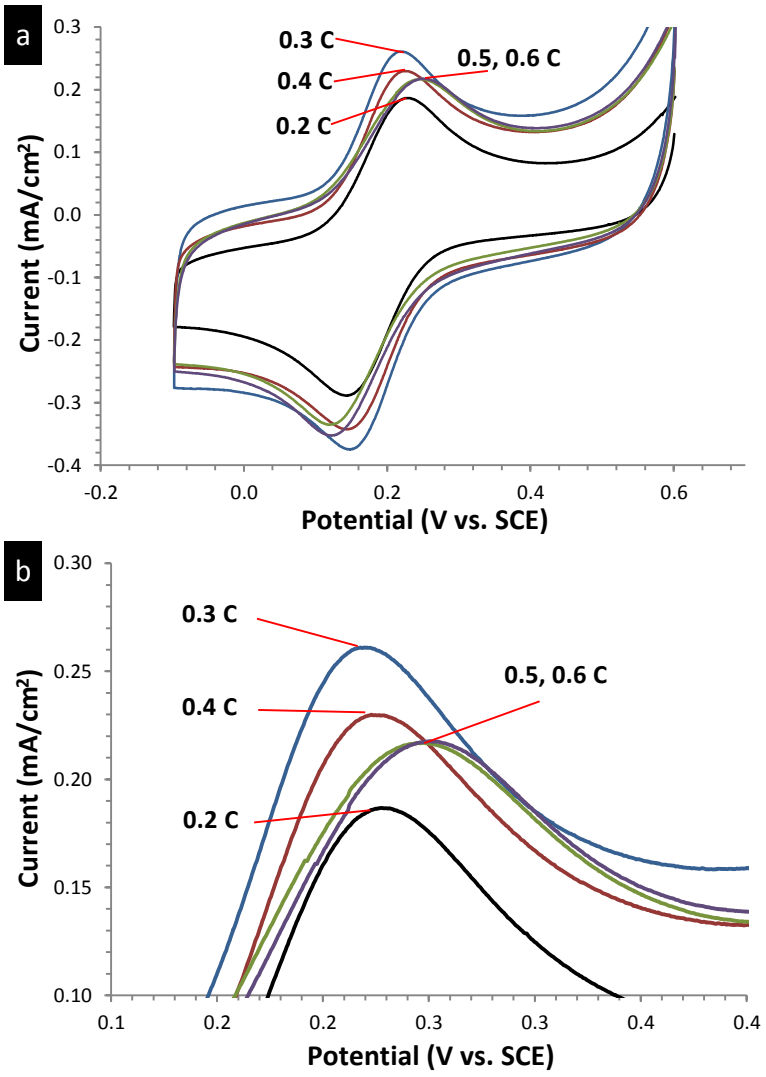

Figure 5.25. Cyclic voltammetry of PPy nanowires grown in 0.100 M Na_2CO_3/0.300 M $NaHCO_3$ in 5 mM $[Fe(CN)_6]^{3-}$ with 0.100 M KCl. Nanowire response with increasing total charge passed during growth (a), magnification region with of [Fe(CN)6] couple (b).

Another important factor when producing the PPy nanowires was the magnitude of the applied potential. Increasing the potential during PPy nanowire growth has been shown to form nanowires with increased length and disorder.[57] For the applied potentials studied here (0.700, 0.750 and 0.800 V) it was observed that increasing the growth potential slightly decreased the reversibility of the redox reaction while producing similar capacitive values, Figure 5.26. The higher potentials showed a

shift in the E_p separation for the redox chemistry of the Fe^{2+}/Fe^{3+} couple; similar to what was observed for the nanowires grown to larger thicknesses. Inspection of the nanowires grown at 0.700 V and 0.750 V shows very little differences between their morphology, Figure 5.26b and 5.26c. However, the 0.800 V polymers had some large agglomerations or wires present in some sections of the surface, Figure 5.26d. These large agglomerations may have blocked areas on the electrode or increased the thickness of the polymer layers making them more resistive.

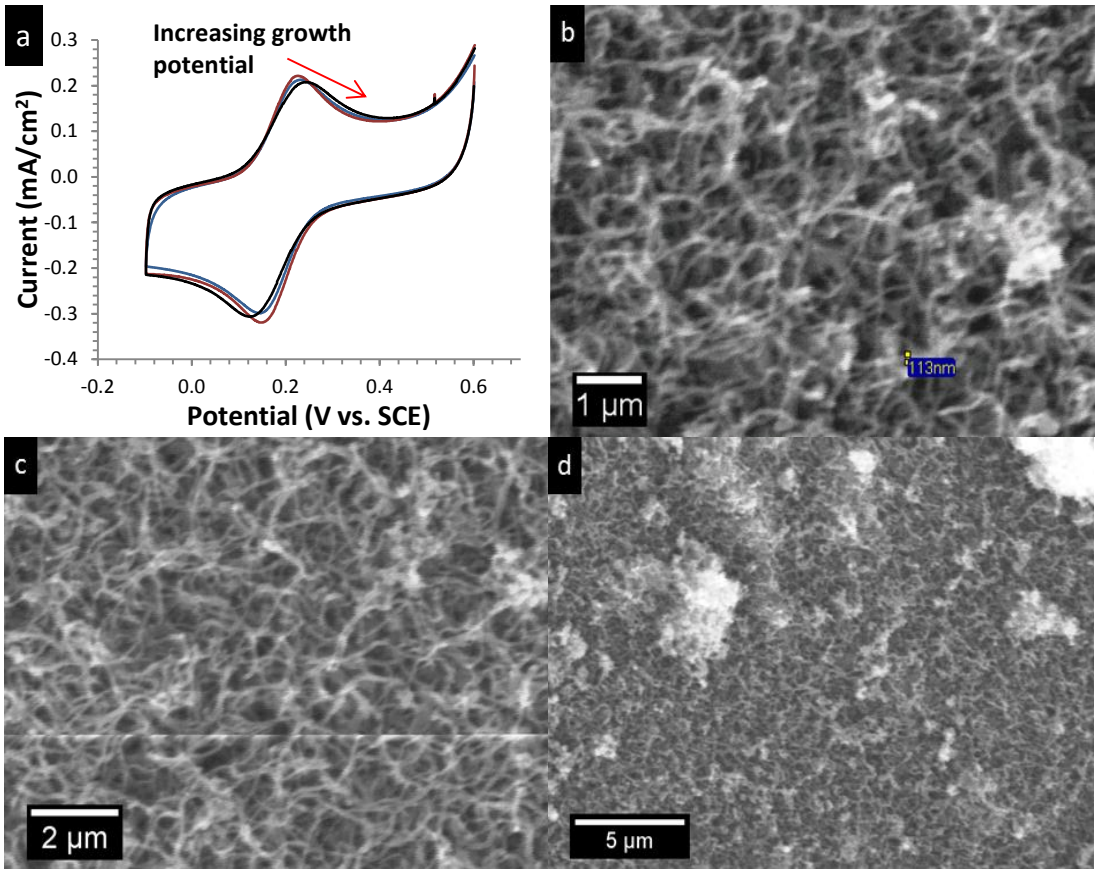

Figure 5.26. Cyclic voltammetry of PPy nanowires grown in 0.100 M Na_2CO_3/0.300 M $NaHCO_3$ with 0.100 M Py (a) comparing growth potentials of 0.700, 0.750 and 0.800 V. corresponding SEM micrographs of nanowire polymers grown at (b) 0.700 V, (c) 0.750 V and (d) 0.800 V.

The large agglomerations which formed during nanowire growth were associated with the applied potential. It was also observed that the diameter of the nanowires were potential dependant, Figure 5.27a. As the applied potential was increased from 0.700 V to 0.800 V, the average diameter of the nanowires increased from ~124 to ~160 nm. However, as more anodic potentials were employed the relative amount of

large agglomerations that formed increased in size, Figure 5.27b. These agglomerated areas may have given rise to the reduced electrochemical response observed in the CVs of the nanowires produced with higher anodic potentials, Figure 5.26a. At 0.800 V a proportion of these large agglomerations reached over 200 μm in size which was a significant proportion of the electrode surface. Therefore, the optimal growth potential was deemed as between 0.700 and 0.750 V.

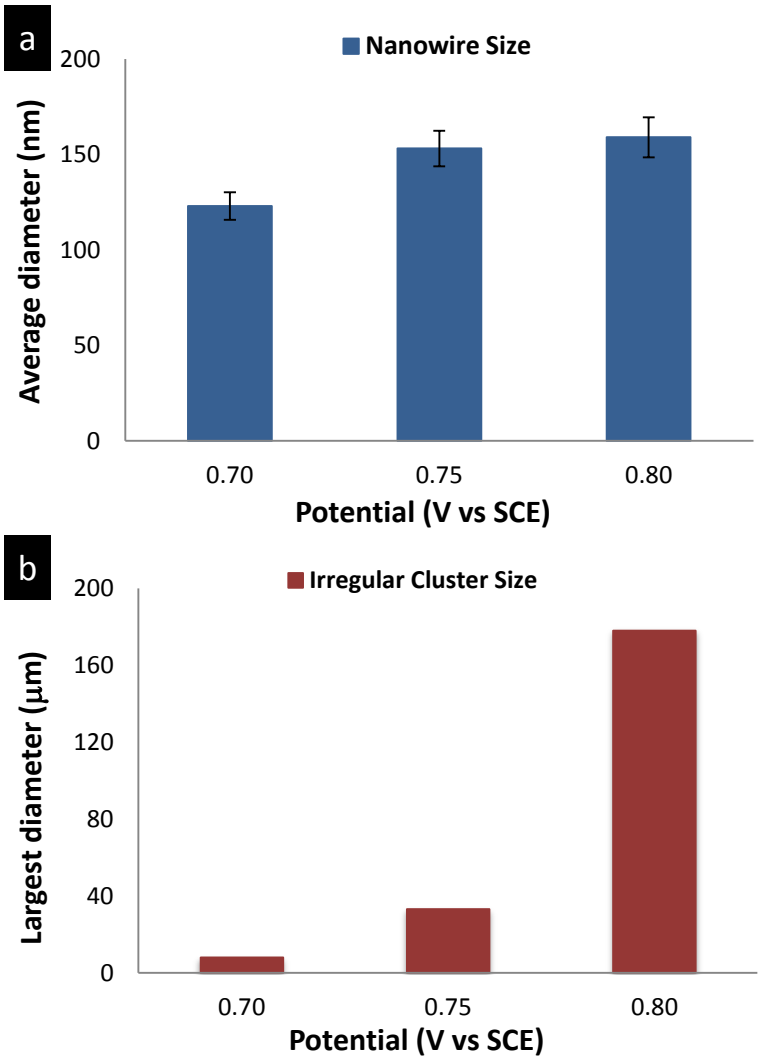

Figure 5.27. Average diameter of the nanowires (nm) (a) and average diameter of the largest irregular clusters (μm) (b) as a function of potential and observed by SEM.

These experiments firstly highlight the beneficial properties of the nanowire films compared to a bare electrode and secondly that it was possible to control their electrochemical activity by changing the growth potential and thickness. Finally it proves that the nanowire system can be reproduced effectively despite the complex

growth mechanism associated with their formation compared to a typical bulk polymer.[59]

5.2.2.3 Copper Deposition Using Cyclic Voltammetry

As previously discussed in Section 5.2.1, the electrodeposition of copper onto bulk PPy polymers was achieved using constant reductive electrodeposition. In an attempt to gain further control over the deposition process a cyclic reductive and oxidative routine (CV) was applied to the PPy nanowires while immersed in a copper salt. As shown in Figure 5.28, as the polymer was cycled between two set potentials the copper was electrodeposited at reductive potentials and then re-oxidised at anodic potentials.[60] It was observed that once the copper became oxidised it would dissolve back into solution at a very fast rate when the switching potential was more positive than 0.100 V. Similarly applying reductive potentials below -0.400 V caused an excessive amount of copper to deposit on the electrode. Therefore, the results for the cyclic window of 0.100 and -0.400 V will only be discussed here.

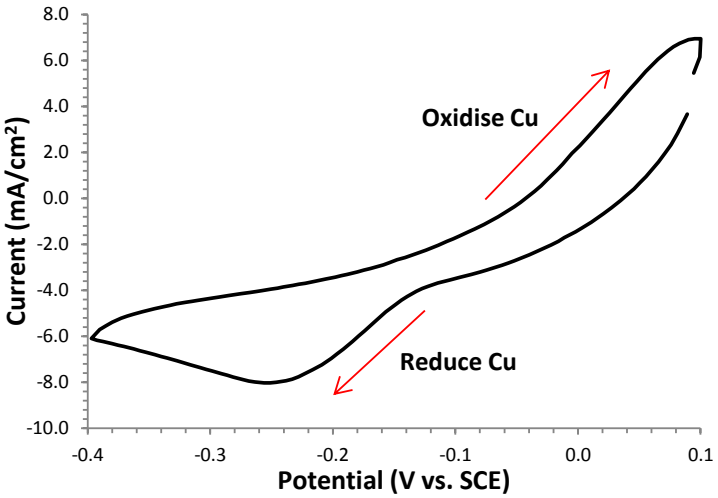

Figure 5.28. Typical CV of a copper species being oxidised and reduced at a PPy electrode.

It has been shown that CV deposition is capable of identifying the morphology of the copper deposits since each copper species has different redox potentials.[61] Applying an oxidative potential will affect the final oxidation state of the electrodeposited copper by removing the elemental copper preferentially over the valence copper.[47]

The main consideration is ensuring the reductive potential window is extended further than the oxidative segment; otherwise the oxidative process may remove all the deposited copper. The magnitude of the recorded currents signifies the amount of deposition or dissolution taking place at the electrode surface. Varying the extent of time spent reducing and oxidising the copper, through appropriate scan rates, allows another level of control over the deposit morphology which was not possible in the constant potential experiments. The copper electrochemistry follows the equations:

Oxidation reactions:[61]

$Cu + OH^- - e^- \rightarrow CuOH$

$2CuOH \rightarrow Cu_2O + H_2O$

$CuOH + OH^- - e^- \rightarrow CuO + H_2O$

Reduction reactions:

$CuO + H_2O - e^- \rightarrow CuOH + OH^-$

$CuOH - e^- \rightarrow Cu + OH^-$

$Cu_2O + H_2O - 2e \rightarrow 2Cu + 2OH$

The CV deposition method was similar to how some authors perform a pulsed routine between oxidative and reductive potentials for metal deposition.[36, 62] However, a study on the effects of cyclic deposition parameters of copper deposition on PPy nanowire films has not been reported in the literature to date. Therefore, the procedure studied herein is a novel means of fabricating copper electrodeposits of controlled size and shape at a PPy nanowire electrode.

5.2.2.4 Copper Electrodeposition at Different Scan Rates

Altering the scan rate within the potential window for the electrodeposition had a dramatic effect on the overall morphology of the copper deposits. Analysis of the slowest scan rate of 50 mV/s shows that the initial currents are low. However, as

consecutive cycles are performed the currents recorded at approximately -0.100 and -0.300 V steadily increase over 10 cycles, Figure 5.29a. Lee *et al* [63] associated this with the new copper deposits interacting with copper rather than a PPy surface. This scan rate produced triangular shaped copper deposits covering the electrode, Figure 5.29b, and each large triangular deposit was composed of smaller pyramidal shaped structures, Figure 5.29c. The composition of the deposit was confirmed by EDX analysis. As can be seen from Figure 5.30, peaks arising from copper, oxygen and chlorine are present. While the electrolyte was composed of SO_4^{2-} ions, which can direct the deposit morphology, it is most likely that the structures are composed of $CuCl_2$ due to the large chlorine and non-existent sulphur peaks. The copper electrodeposition can be observed by eye as the black PPy nanowires turn a dark brown colour due to the deposited copper, Figure 5.30.

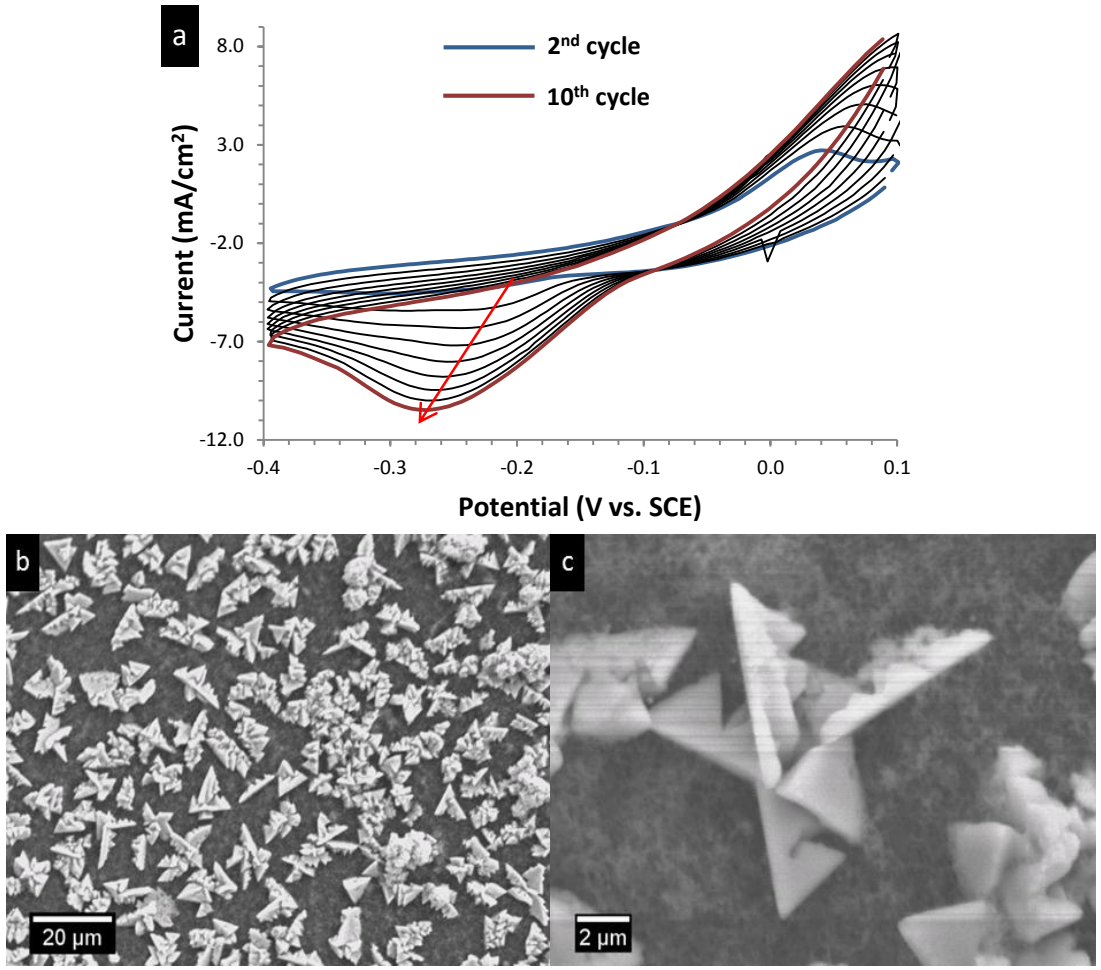

Figure 5.29. CVs of a copper electrodeposition at PPy nanowires in a solution of 0.050 M $CuCl_2$ in 0.050 M H_2SO_4 in a potential window of 0.100 to -0.400 V at 50mV/s for 10 cycles (a), SEM micrographs of resultant morphology (b) and (c).

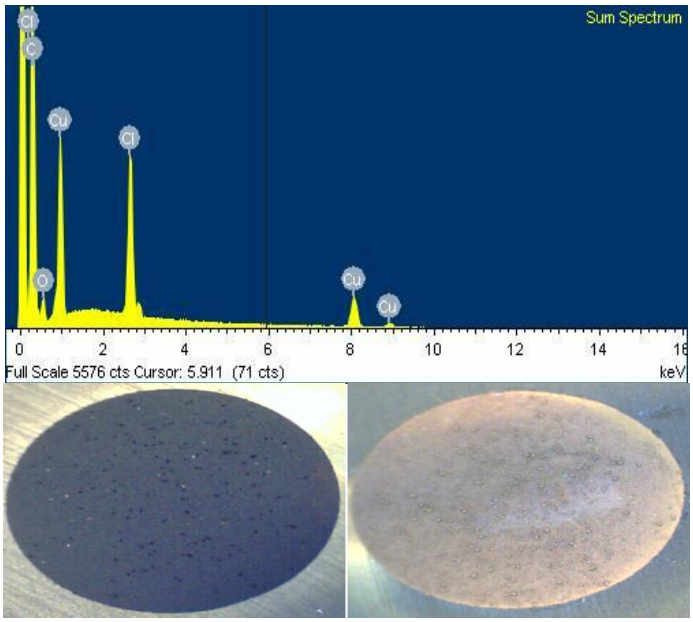

Figure 5.30. EDX of a copper deposit formed by cyclic voltammetry at 50 mV/s between 0.100 and -0.400 V. Low magnification microscope images are of the nanowire polymer before and after deposition.

When the number of cycles used for deposition was increased to 40 there was a significant change in the currents recorded. As shown in Figure 5.31a, the currents recorded for the 40th cycle (-25 mA/cm^2) were over double the values recorded at the 10th cycle (-11 mA/cm^2). This occurred due to the slow scanning speed permitting the nanowires to spend long periods at reductive potentials leading to large amounts of copper deposition, increasing the surface area of the electrode. Further copper growth is then initiated on this larger surface area allowing a greater deposition rate to be achieved. This explains the regular and incremental increase in the reductive currents recorded. However, for this reason, the electrode becomes almost completely covered in copper material, Figure 5.31b. Interestingly, from cycle 20-30 the currents discontinued shifting to higher overpotentials as seen for the first 10 cycles, Figure 5.29a. Even more significant the final cycles from number 30 to 40 started slightly shifting to lower overpotentials, Figure 5.31a. This would be indicative of the deposition procedure becoming thermodynamically easier. Examination of the resultant polymer films shows electrodeposited copper was comprised of various crystal shapes and amorphous structures, Figure 5.31c. It can also be shown in the inset of Figure 5.31c that the nanowires were still present on the

electrode after the deposition process and the microparticles were imbedded within them.

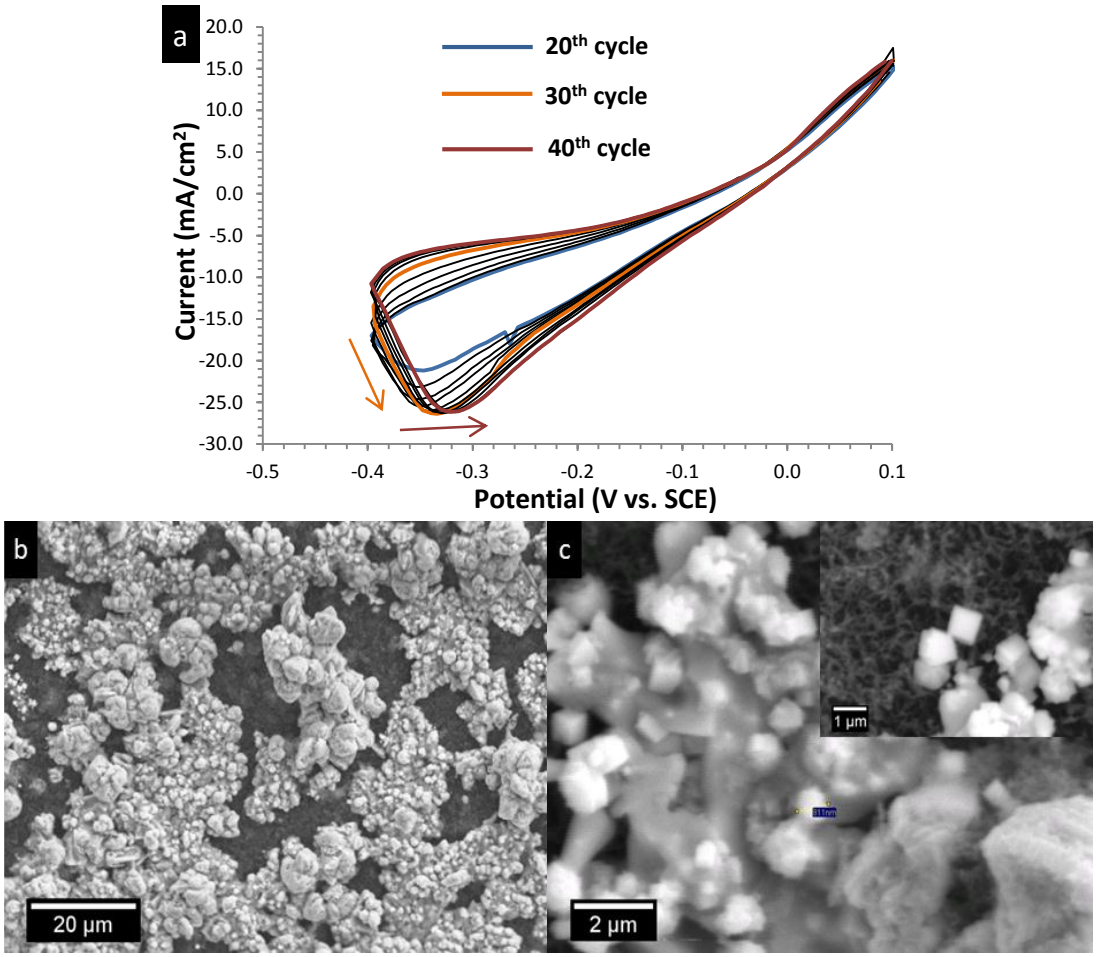

Figure 5.31. Cyclic voltammograms of a copper electrodeposition at PPy nanowires in a solution of 0.050 M $CuCl_2$ in 0.050 M H_2SO_4 in a potential window of 0.100 to -0.400 V at 50mV/s for 40 cycles (a), corresponding SEM micrographs of resultant morphology (b) and (c).

A similar trend was observed for the higher scan rate of 200 mV/s where the triangle shaped crystals formed as more discrete particles. There was less bulk deposition compared to the 50 mV/s deposition experiment, Figure 5.32a and 5.32b. Similar to the trend observed for the 50 mV/s experiment, increasing the number of cycles from 10 to 40 at 200 mV/s, produced larger copper deposits which lost the clear triangle crystal habit, Figure 5.32c and 5.32d.

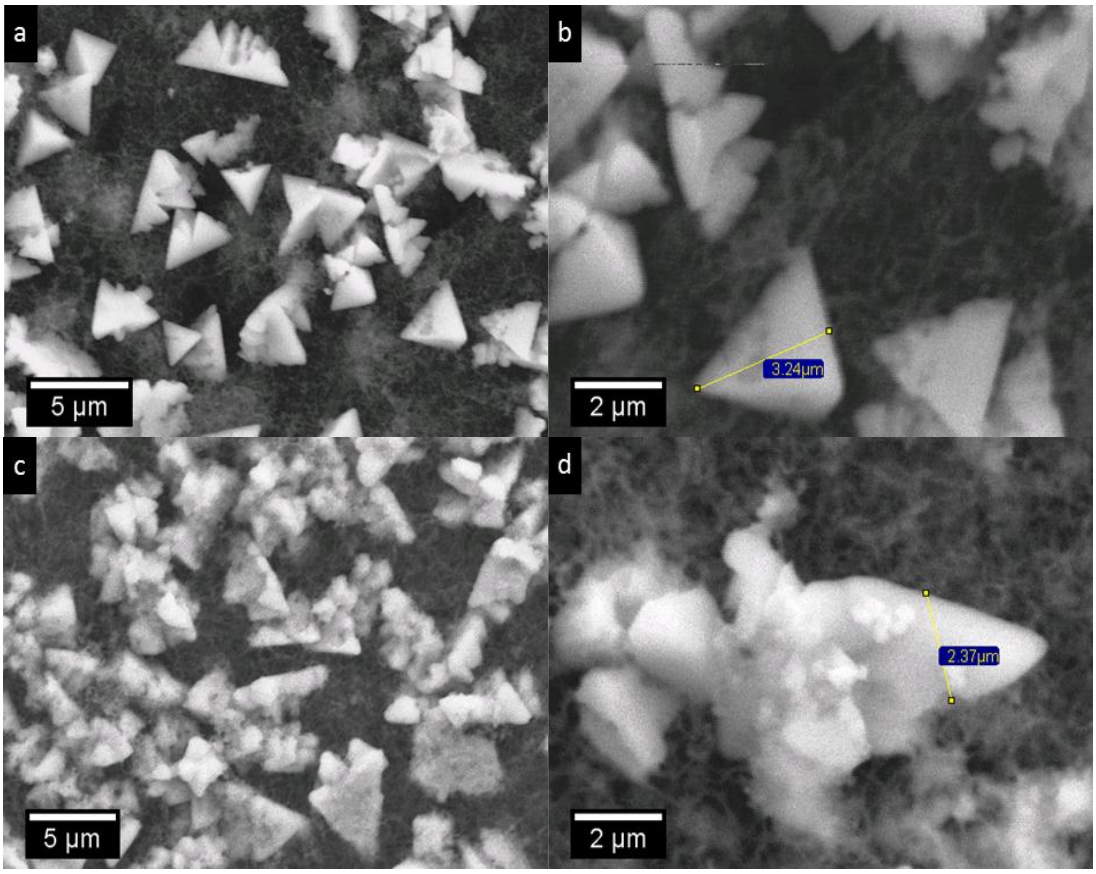

Figure 5.32. SEM micrographs of copper electrodeposition at PPy nanowires in a solution of 0.05 M $CuCl_2$ in 0.05 M H_2SO_4 in a potential window of 0.100 to -0.400 V at 200mV/s for (a), (b) 10 cycles and (c), (d) 40 cycles.

Increasing the scan rate further led to a change in the crystal structure from triangular towards spike, sheet and particle morphologies, Figure 5.33. At 300 mV/s using 40 cycles the predominant copper morphology was a thin sheet type deposit. There was no bulk deposits observed at this scan speed due to the very short time spent at the reductive potentials. Similarly, when the scan rate was increased to 400 and 500 mV/s with 40 cycles, only a spike shape structure was present, Figure 5.33b and 5.33c. Careful inspection of Figure 5.33c shows copper nanoparticles have nucleated in the background. The currents recorded for these scan rates were larger than those recorded for 50 mV/s depositions. However, this was due to the charging current was not being able to decay at these speeds, which is a typical electrochemical process.[21, 64] Therefore these currents were not directly related to the copper electrodeposition process. At the higher scanning speeds of 400 and 500 mV/s, the currents did not increase with successive cycles, as highlighted by the red arrows in Figure 5.33b and 5.33c. The current decrease was due to the speed at which the scan was switched

between the two set potentials acting more like a pulsed programme rather than cyclic. At these high speeds very little copper would be able to accumulate near the electrode surface since the potential would switch to oxidative potentials before a large influx of copper penetrated the diffusion layer. Also since only small discrete particles were deposited there was less copper material available at which it is thermodynamically easier for copper to nucleate and deposit. The fast nature of the scanning speed meant the potentiostat recorded a much lower amount of data points as the potential was cycled. This gave rise to a very square or straight appearance to the voltammograms. To overcome this limitation a higher rate of data point acquisition should be set within the experimental set-up in Corrware (possibly 20 points per second).

Generally, it can be concluded that the PPy nanowires were capable of supporting the electrodeposition of copper species. Using a cyclic deposition routine and varying the scan rate from 50 to 500 mV/s caused the copper deposits to decrease in size. It also altered the morphology from polycrystalline cubes and triangles to sheet and spike structures. The number of repetitive scans performed was also capable of increasing the amount and size of copper deposits. Combining a high deposition scanning speed along with a low number of cycles resulted in small discrete particles being deposited at the PPy nanowires. Therefore, based on these observations the cyclic electrochemical deposition is a useful tool in controlling the final shape and size of copper deposits at PPy nanowires. A range of these polymer copper composites were tested for their ability to electrochemically reduce the nitrate ion, as will be discussed in the next section.

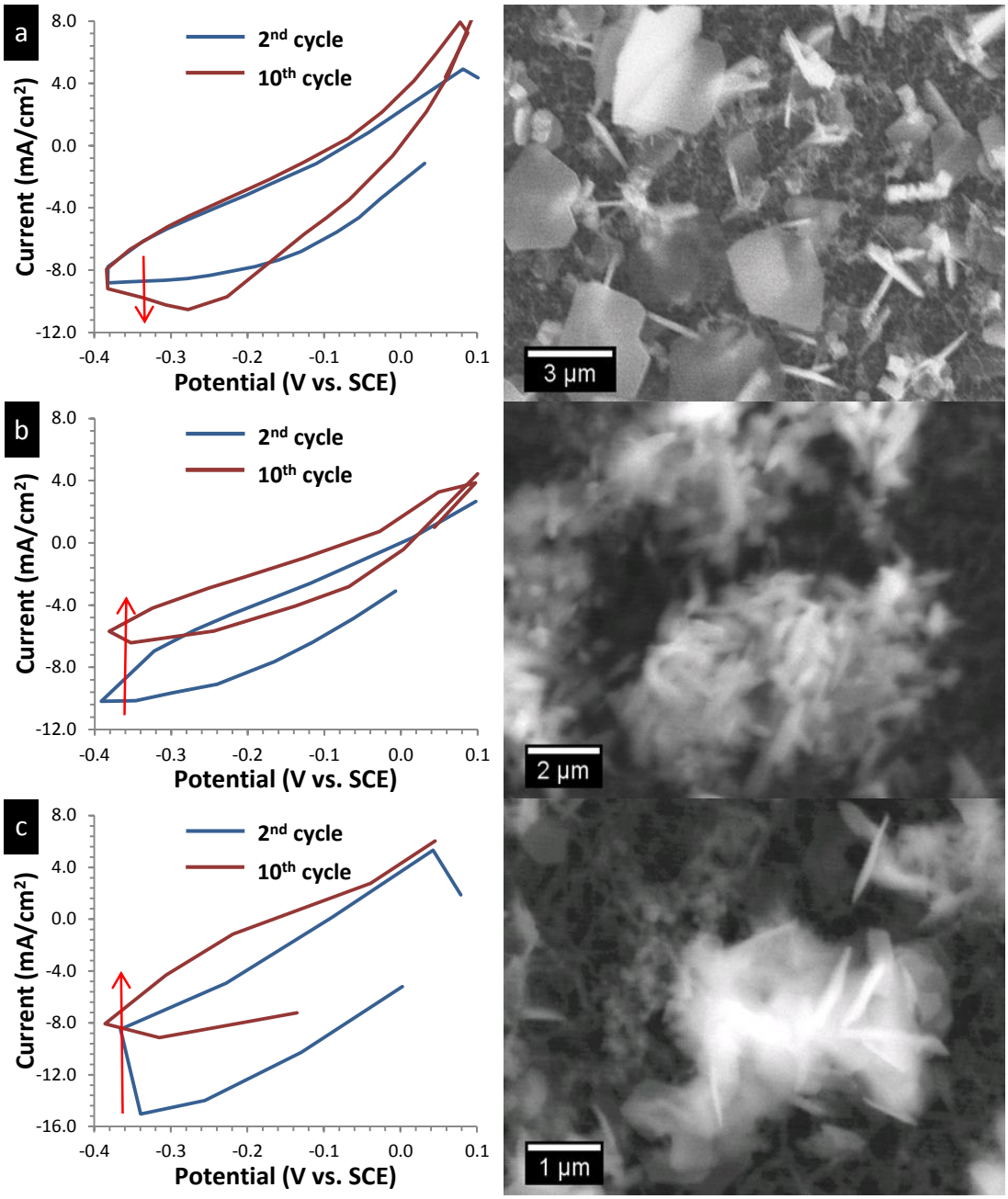

Figure 5.33. Cyclic voltammograms of a copper electrodeposition at PPy nanowires in a solution of 0.050 M $CuCl_2$ in 0.050 M H_2SO_4 in a potential window of 0.100 to -0.400 V at scan rates of (a) 300, (b) 400 and (c) 500 mV/s for 40 cycles with corresponding SEM micrograph adjacent.

5.2.3 Nitrate Sensing

It is well known that copper has a catalytic response for the electrochemical reduction of nitrate.[10, 65-68] Therefore the nanowire/copper composites produced in the previous sections were tested for their ability to electrochemically reduce nitrate. Firstly, the best parameters for studying the nitrate electroreduction were explored. A glassy carbon/copper electrode was used to optimise the best scanning window and loading of copper which favoured nitrate reduction. This removed problems associated with the irreproducibility of the nanowires which was discussed previously. Once the most optimised conditions were identified they were applied to the PPy nanowire/copper composite.

5.2.3.1 Glassy Carbon/Copper Nanocomposite

5.2.3.1.1 Nitrate Adsorption

Several authors have reported that the electrochemical reduction of nitrate is preceded by an adsorption step.[69-72] Nitrate has been shown to undergo a reversible adsorption process, particularly on copper surfaces.[67] To study this process for the copper nanomaterials employed in this work, a copper film was first deposited on a bare glassy carbon (GC) electrode using 100 mV/s for 10 cycles between 0.100 to -0.400 V in 0.050 M $CuCl_2$ (in 0.050 M H_2SO_4). This electrode was denoted as GC/Cu. As discussed in Section 5.2.2.4, a uniform copper layer with mixed nano and micro deposits was obtained under these conditions. This composite electrode showed almost ideal reproducibility between electrodes for the nitrate reduction reaction. Using cyclic voltammetry, the least sensitive method of detection, produced a detection limit of 8.0×10^{-4} M (data not shown). However, the nitrate electroreduction reaction at copper surfaces has been shown to be enhanced when cyclic voltammetry is employed. The sensitivity has been shown to increase as copper dissolution/redeposition produces a fresh copper layer which promotes the electroreduction of nitrate.[73] While the electrodeposition method described in this chapter is a novel method for controlling the copper deposition morphology, the electrodeposition of copper at a GC electrode as a nitrate sensor has been developed

in the literature previously.[65, 68] Therefore, the experiments outlined herein were designed to study the nitrate electroreduction reaction rather than the development of the GC/Cu electrode as a novel material. Employing the GC/Cu electrode and immersing it in 0.005 M $NaNO_3$ produced several reductive and oxidative signals, Figure 5.34. The signals more positive than -0.700 V are associated with the redox activity of the electrodeposited copper.[69] The signals more negative than -0.700 V are due to the irreversible reduction of the nitrate ion to nitrite and other products.[70] The processes associated with each are labelled and are summarised in Table 5.1.

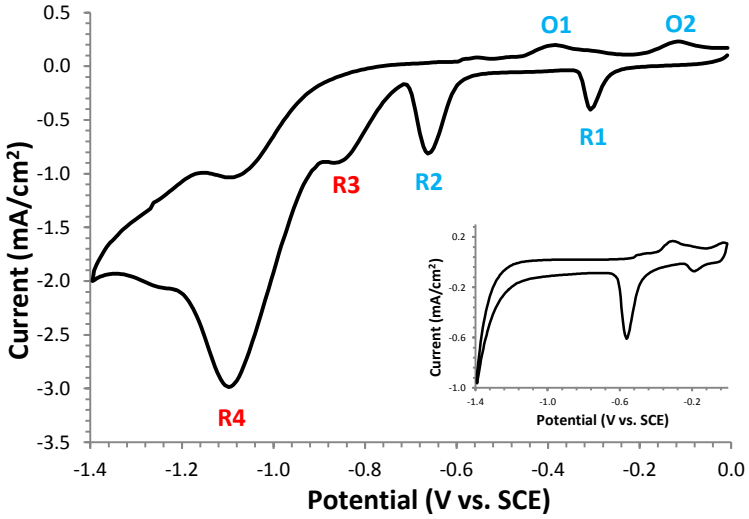

Figure 5.34. A GC/Cu electrode immersed in a 0.005 M $NaNO_3$ solution cycled between 0.000 and -1.400 V at 50 mV/s. Blue labels are associated with copper species and red labels are associated with the nitrate reduction. Cycles performed in 0.100 M Na_2SO_4 without 0.005 M $NaNO_3$ shown inset.

Table 5.1. The electrochemistry at a GC/Cu electrode in 0.005 M NaNO3. Peak labels taken from Figure 5.34.

Peak Label	Potential (V)	Process
R1	-0.300	$Cu(II) \rightarrow Cu(I)$
R2	-0.660	$Cu(I) \rightarrow Cu(0)$
R3	-0.840	$NO_3^- \rightarrow NO_2^-$
R4	-1.090	$NO_2^- \rightarrow NH_2OH/NH_3$
O1	-0.390	$Cu(0) \rightarrow Cu(I)$
O2	-0.110	$Cu(I) \rightarrow Cu(II)$

Varying the switching potentials from -0.400 to -0.300 and to -0.200 V at the GC/Cu composite electrode during the electroreduction of 0.005 M $NaNO_3$, showed that the reductive peaks for the copper species became more pronounced, Figure 5.35a. Bringing the anodic switching potential to 0.000 V produced the strongest copper signals without reducing the amount of copper on the surface through oxidation/dissolution. It also improved the signal for the nitrate reduction at peaks R3 and R4 from Figure 5.34.

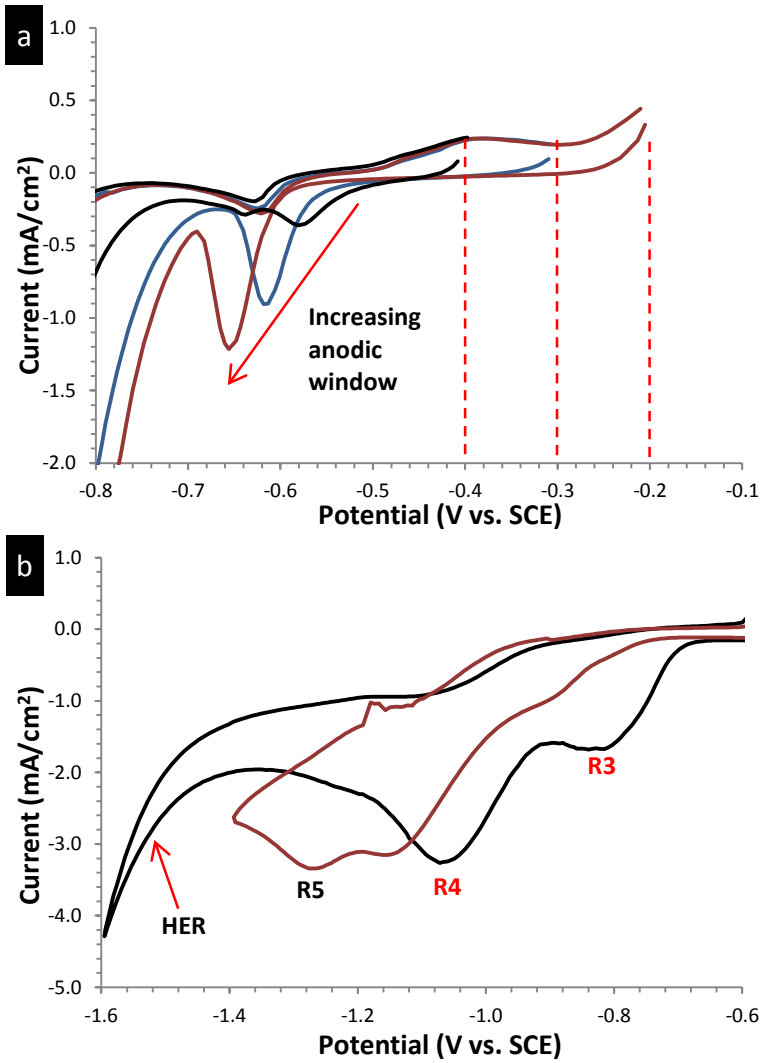

Figure 5.35. Cu deposited at a bare GC electrode using 10 cycles at 100 mV/s in 0.05 M $CuCl_2$ in 0.05 M H_2SO_4 then cycled in 0.005 M $NaNO_3$ at 50 mV/s between the potentials (a) -1.500 V and -0.400, -0.300 -0.200 V and (b) Anodic window maintained at 0.000 V while cathodic potential switched to -1.600 and -1.400 V.

Casella *et al.*[69] proposed that there was a preliminary nitrate adsorption process in the potential region 0.000 V. Employing a potential switching at 0.000 V would encourage this nitrate adsorption process and therefore lead to greater current response for the multistep nitrate reduction (R3 and R4). Interestingly, the R5 peak would disappear when the cathodic switching potential was brought into areas which produced the hydrogen evolution reaction (HER) (-1.600 V). As can be seen from Figure 5.35b, the peak R5 has been replaced by the increasing current associated with the HER. Hydrogen adsorption competes with the adsorption of nitrate and hence reduces the electrocatalytic activity of the Cu deposits due to surface poisoning.[70] For these reasons the vertex potentials in the nitrate reduction experiments were maintained at 0.000 to -1.400 V to avoid hydrogen adsorption and dissolution of the electrodeposited copper. These potentials would also encourage the nitrate adsorption onto the copper nanomaterials and promote electroreduction.

5.3.2.1.2 Copper Loading

The effect of increasing the copper loading on the GC/Cu composite electrode was measured using the optimised window described in the previous section (0.000 to -1.400 V). Increasing the amount of cycles in the copper deposition solution from 5 to 320 increased the current response for the peaks at R1, R2, O1 and O2, Figure 5.34. As shown in Figure 5.36a, the main copper peaks of R1 and R2 increase in current density as the copper deposition was increased from 5 to 320 cycles. This was expected as increasing the number of cycles led to a greater amount of copper on the electrode surface (SEM micrographs not shown). This increase in copper loading produced a greater response for the electrochemical reduction of nitrate. As shown in Figure 5.36b, the peak currents increase for the main nitrate peak and also shift towards lower overpotentials. The potential shifts from -1.100 to -1.010 V when the number of cycles in the copper solution increases from 5 to 320.

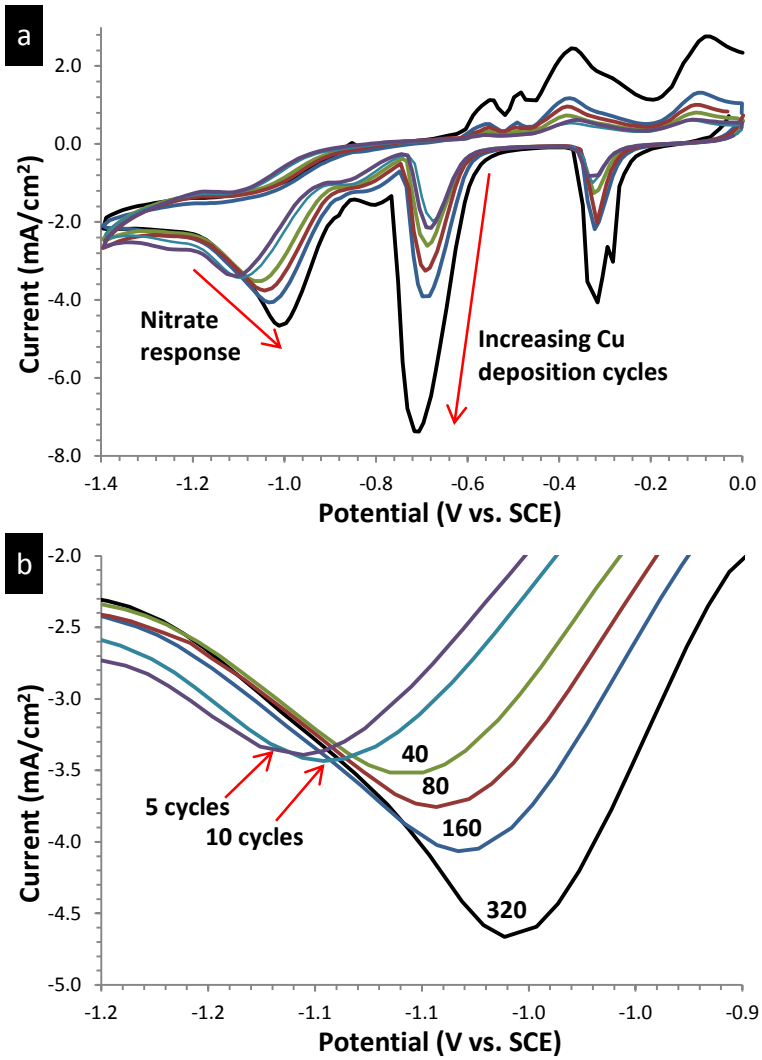

Figure 5.36. Cu deposited at a bare GC electrode using 5 to 320 cycles at 100 mV/s in 0.050 M $CuCl_2$ in 0.050 M H_2SO_4 then cycled in 0.005 M $NaNO_3$ at 100 mV/s between the potentials -1.400 and 0.000 V (a) and magnification of nitrate response area (b).

The relationship between increasing copper deposition and nitrate signal is displayed in Figure 5.37. Here, it can be seen that as the copper signal increases the nitrate response does not increase in a proportional manner. This may be due to the electrode being saturated in copper deposits forming a bulk-like layer, which does not increase the surface area of the active copper. However, with a greater copper loading there is a possibility of the copper leaching or detaching from the surface. Therefore, to avoid such issues, which would reduce the sensor lifetime significantly, the larger loadings were avoided for use in the electroreduction reaction. As shown in Figure 5.37, 160 cycles was observed to be the point where the maximum nitrate electroreduction was achieved before producing a large excess of copper on the

surface. Therefore, this value was used to deposit copper onto the PPy nanowire layers.

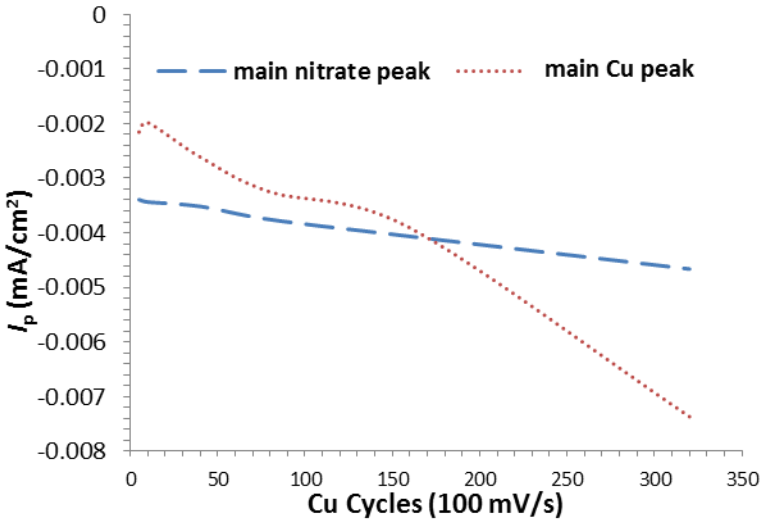

Figure 5.37. Current response from the main Cu peak R2 (Figure 5.35) with the main nitrate peak current R4 (Figure 5.35) as a function of increasing copper deposition cycles. Cu deposited at a bare GC electrode using 5 to 320 cycles at 100 mV/s in 0.050 M $CuCl_2$ in 0.050 M H_2SO_4 then cycled in 0.005 M $NaNO_3$ at 100 mV/ s between the potentials -1.400 and 0.000 V.

5.2.3.2 Polypyrrole Nanowires/Copper Nanocomposite.

The optimised conditions for nitrate electroreduction employed with the GC/Cu nanocomposite were applied to the PPy nanowire/Cu nanocomposite, denoted PPy-NW/Cu. As discussed in Section 5.2.2.4, the speed at which the copper deposition was performed had a direct influence on the resultant copper morphology. It was also observed that increasing the amount of copper deposition cycles produces a greater loading of copper at the electrode, which favourably increases the nitrate reduction reaction, Section 5.3.1.2. In an attempt to obtain the maximum amount of copper at the nanowire morphology, a large amount of cycles (160) were performed at an intermediate scan rate (300 mV/s). As can be seen from Figure 5.38a, the nitrate signal produced at this PPy-NW/Cu electrode was poor. The background cycle (black trace) and nitrate reduction (red trace) did not display the same reduction peaks as shown in Figure 5.34. Furthermore, the current response was significantly lower. This would suggest that nitrate electroreduction was not catalysed at this PPy-

NW/Cu electrode. Examination of the SEM micrograph, Figure 5.38a, reveals that the entire electrode had been covered in a bulk copper deposit. This excessively large copper loading combined with the semi-conducting nanowires would significantly reduce the electron transfer across the PPy-NW/Cu surface. Furthermore, the high surface area property of the nanowires was not being exploited since they were covered in a dense copper coating. It was apparent that even with the optimal 160 cycles that the slow sweep rate was still encouraging the formation of a bulk copper layer.

To reduce the amount of copper deposited at the PPy nanowires, the scan rate for the copper deposition was increased to 600 mV/s, while maintaining 160 cycles. This produced an increase in response for the nitrate reduction, as shown in Figure 5.38b, where an I_p was observed at ~-1.070 V with a magnitude of -0.38 mA/cm^2. The capacitive behaviour of the nanowires was also observed at ~-0.500 V signifying that a proportion of the nanowires were exposed to the electrolyte. The copper redox chemistry from Figure 5.34 (R1 and R2) was also present. Examination of the SEM micrograph confirmed these observations as the nanowire morphology was identified with large copper triangles deposited on the surface. Clearly these deposits were in the micro range and were similar to the copper morphology seen previously for slower scan rates using less cycles, Figure 5.32. The benefit of using faster scan rates with a greater number of cycles was that less bulk deposition was produced. However, the copper reductive peaks and the nitrate reduction were only marginally larger than the background signal.

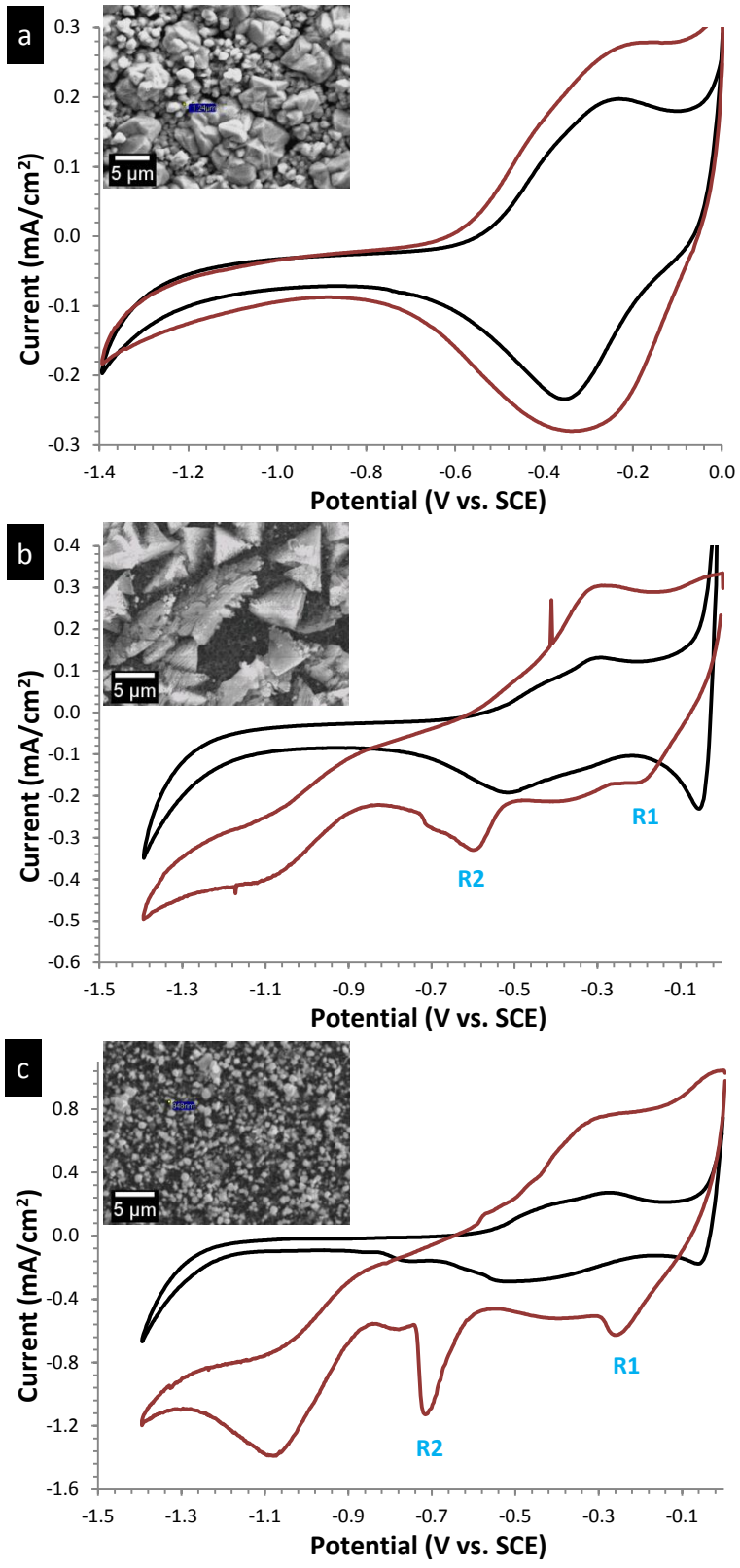

Figure 5.38. Cu deposited at PPy/Cu electrode for 160 cycles at (a) 300, (b) 600 and (c) 900 mV/s in 0.050 M $CuCl_2$ in 0.050 M H_2SO_4 then cycled in 0.005 M $NaNO_3$ at 20 mV/s between 0.000 - 1.400 V. Black trace is background cycle in 0.100 M Na_2SO_4 free of $NaNO_3$.

Employing a scan rate of 900 mV/s and maintaining 160 cycles produced the greatest response from the PPy-NW/Cu electrode, Figure 5.38c. Firstly the copper redox chemistry peaks (R1 and R2) were significantly more pronounced, this was indicative of a greater exposed surface area of copper deposits. Secondly, the capacitive region of the nanowire polymer at ~-0.500 V reached 0.80 mA/cm^2 compared to 0.40 mA/cm^2 for the 600 mV/s deposition experiments. Most significantly, a large nitrate reduction peak was generated at -1.080 V with a magnitude of -1.39 mA/cm^2. This compares to -0.38 mA/cm^2 for the PPy-NW/Cu electrode produced at 600 mV/s. Inspection of the SEM micrograph reveals the copper deposits were present with an average diameter of ~500 nm dispersed in a homogeneous distribution. No bulk deposition was present and the nanowires were clearly exposed through the embedded copper. These results outline that the PPy-NW/Cu nanocomposite was more effective when the deposited copper was in the nano dimensions. This allowed for a greater catalytic ability from the nanoparticles which were combined with the increased surface area of the exposed polymer nanowires.

The reproducibility of this system using an n = 3 produced a standard deviation of 5.08 $x10^{-5}$ mA/cm^{-2} with a percentage error of 1.59%. However, the GC/Cu electrode was more sensitive than the PPy-NW/Cu electrode as it recorded larger currents for the electroreduction of 0.005 M nitrate under the same conditions. In Figure 5.39, it can be seen that the GC/Cu electrode has a current magnitude of -2.3 mA/cm^2, almost double the -1.39 mA/cm^2 for the PPy-NW/Cu nanocomposite. Therefore, the PPy-NW/Cu electrode was not as effective at reducing the nitrate ion compared to the GC/Cu electrode. After several attempts to increase the sensitivity by altering the copper loading it was apparent that the PPy nanowires were impeding the reduction reaction in some way. It was possible that the nanowires were more insulating than the GC/Cu substrate but if this was indeed the case the nitrate peak would shift to larger overpotentials, while a slight shift was observed it was not significant. The PPy-NW electrode, despite the large surface area compared to the bare GC, performed as if it had a lower amount of effective copper present. This was a contradictory observation since SEM analysis shows nanoparticles of copper embedded on the PPy nanowires, suggesting a high surface area.

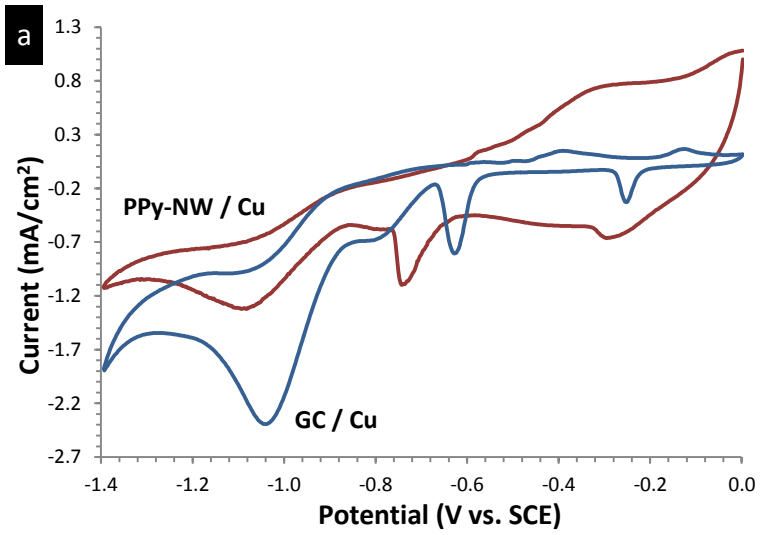

Figure 5.39. Cu deposited at electrodes for 160 cycles at 900 mV/s in 0.050 M $CuCl_2$ in 0.050 M H_2SO_4 at a GC/Cu electrode and a PPy-NW/Cu electrode, then cycled in 0.005 M $NaNO_3$ at 20 mV/s between 0.000 -1.400 V.

In conjunction with Section 5.2.3.1.1, it was concluded that the carbonate salts, which typically must be removed from nanowires after synthesis, were not completely removed by the acidic cycling procedure outline in Section 5.2.2.1 and were impeding the adsorption of nitrate. It has been reported by other authors that to remove the CO_3^{2-} they soak the polymers in an acid for 24 hours.[55, 74] It was also obvious that the acid treatment employed herein was not sufficient to remove all the reaming CO_3^{2-} from the polymer. When the acidic cycles were not performed there was an obvious reaction between the PPy-NW polymer and copper solution, possibly forming a copper carbonate. This was observed by eye as a yellow colour change at the electrode surface, Figure 5.40. This would suggest that the cycling in acid pre-treatment did not fully remove all of the carbonate remaining within the nanowires. Therefore, a much more rigorous acid pre-treatment step should be employed when utilising the carbonate grown nanowires with a copper electrodeposition procedure. This was attempted for some of the nanowires electrodes. They were left to sit in 0.100 M perchloric acid for times between 6 and 24 hours. This process was observed to be detrimental to the epoxy resin which surrounded the substrate and Teflon outer layer. Eventually large gaps would appear between these two surfaces which meant the electrode had to be re applied with fresh epoxy. In some cases the Teflon outer coating would melt away completely which made the electrodes un-useable. In general these acid treatments caused reproducibility problems as the

electrode surface was changing as the epoxy degraded. Furthermore, the copper wiring which connected to the potentiostat was in danger of detaching after repeated exposure to the acid solution. For these reasons the harsh acid treatments were not continued.

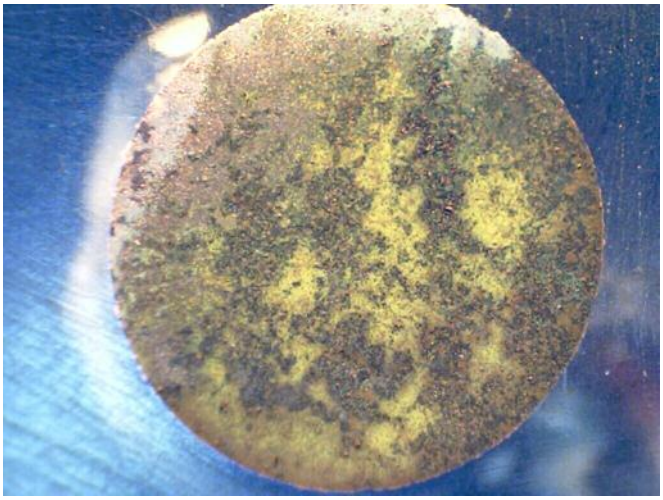

Figure 5.40. Optical microscope of a PPy-NW electrode immersed in a $CuSO_4$ solution without firstly removing the CO_3^{2-} ions from the nanowire polymer.

It was concluded that the sensitivity of the PPy-NW/Cu electrode was not as high as the GC/Cu electrode due to the carbonate interference. However, despite this, the electrode did have an increased stability over a larger number of cycles compared to the GC/Cu electrode. As shown in Figure 5.41 the PPy-NW/Cu electrode response for the reduction of nitrate decreases from -1.57 to -1.28 mA/cm^2 over 15 cycles, a difference of 0.28 mA/cm^2. At the GC/Cu electrode however, the nitrate response degraded from -3.39 to -2.28 mA/cm^2 which was a difference of 1.11 mA/cm^2 over 15 cycles. This was possibly due to the GC/Cu electrode slowly dissolving the active copper from the electrode as it was cycled to oxidative potentials. This process would be reduced in the PPy system since PPy and Cu can form a charge transfer process which would stabilise the Cu within the polymer matrix.[46] This would suggest that the PPy nanowire composite would be suited to repetitive testing without as much degradation of the copper catalyst as compared to a GC electrode.

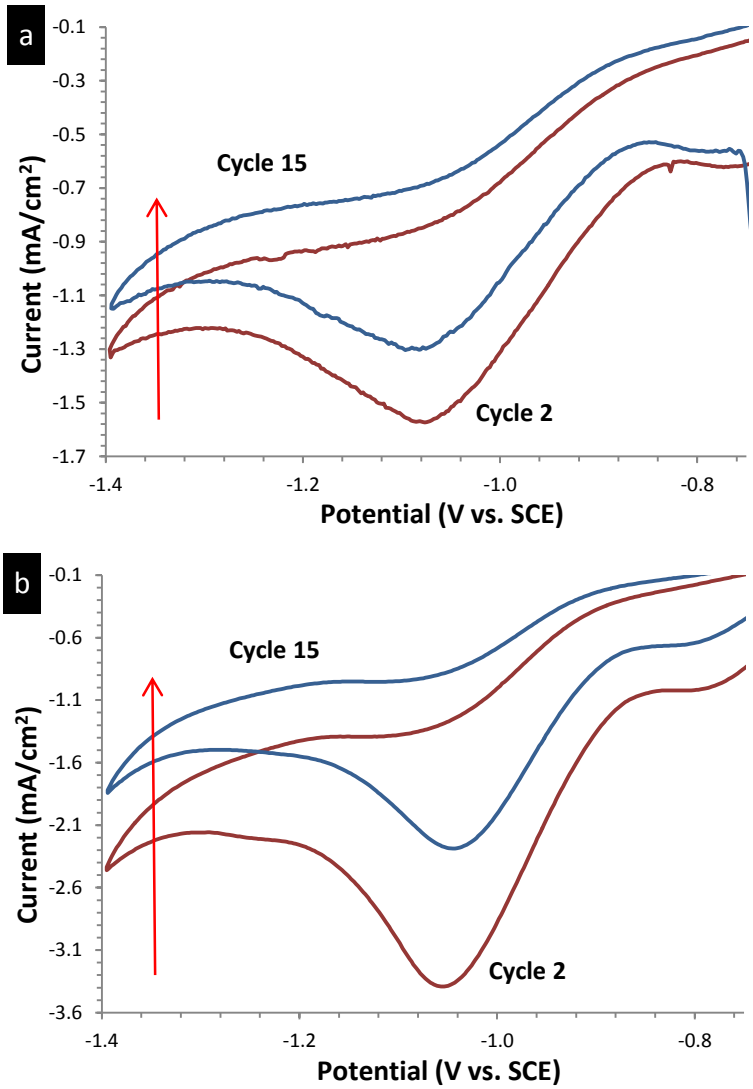

Figure 5.41. Cu deposited for 160 cycles at 900 mV/s in 0.050 M $CuCl_2$ in 0.050 M H_2SO_4 at (a) PPy-NW/Cu and (b) GC/Cu electrode. Comparison of 15 cycles in 0.005 M $NaNO_3$ at 20 mV/s.

In conclusion, the nitrate reduction reaction has been confirmed to respond as an adsorption/reduction reaction at sites on the electrodeposited copper surfaces synthesised in this work. Although the nanowires were capable of facilitating a large loading of copper, they inadvertently reduced their effectiveness towards the nitrate reaction from residual CO_3^{2-} remaining within the polymer matrix. This led to a reduction in their sensitivity compared to a GC/Cu electrode. However, the PPy was shown to increase the stability of the electrodeposited copper over the GC/Cu electrode, highlighting the possibility of using these electrodes in long term sensing applications. This may benefit incorporating these electrodes into remote sensing apparatus where the sensor lifetime is required to be as long as possible.

5.3 Conclusion

Electrochemically polymerised bulk PPy films were proven to be a reproducible substrate for the nucleation and growth of copper crystals. Using potentiostatic methods to electrodeposit copper at these PPy films produced a range of cubooctahedron shaped crystals. When these crystals were compared with relevant reports from the literature they were assigned as Cu_2O while the copper branched structures were speculated to be a mixed copper/copper oxide species. Using SEM and modelling equations their nucleation mechanism was deemed to be progressive. The magnitude of the reduction potential was observed to have a significant impact on the copper crystal morphology, with dendrite and branched shapes produced when a high concentration of copper was combined with a large reductive overpotential. Extending the copper deposition procedure to the PPyEtCN polymers studied in Chapter 3, revealed their insulating properties required a substantial increase in the reduction overpotential to make the surface thermodynamically favourable for copper deposition. For this reason the PPyEtCN polymers were not an effective material for encouraging copper electrodeposition.

The formation of PPy nanowires with a reproducible surface was investigated using an electrochemical probe. These nanowires were used to develop a cyclic deposition technique to fabricate a range of different copper deposits including, triangle, spike, sheet and particle. Cycle number and scan rate were seen to have a dramatic effect on the resultant copper morphology and loading. Increases in cycle number led to bulk deposition while increases in scan rate produced smaller and more discrete particles. These nanocomposites were tested as a surface for the electroreduction of the nitrate ion, which was shown to begin with an adsorption step. The resultant nanowire/copper hybrid had a lower sensitivity compared to a glassy carbon/copper composite. However, the PPy nanowires were shown to have a stabilising interaction with the copper through a charge transfer complex which resulted in a better stability of the sensor over time.

5.4 References

1. Huang, L.; Lee, E.-S.; Kim, K.-B. *Colloids Surf., A* **2005,** *262*, 125-131.
2. Srinivasan, R.; Gopalan, P. *Surf. Sci.* **1995,** *338*, 31-40.
3. Peng, Z.; Yang, H. *Nano Today* **2009,** *4*, 143-164.
4. Gutierrez-Wing, C.; Velazquez-Salazar, J. J.; Jose-Yacaman, M. *Methods Mol. Biol.* **2012,** *906*, 3-19.
5. Siegfried, M. J.; Choi, K.-S. *Adv. Mater.* **2004,** *16*, 1743-1746.
6. Ilieva, M.; Tsakova, V. *Synth. Met.* **2004,** *141*, 287-292.
7. Wang, T.; Hu, J.-S.; Yang, W.; Zhang, H.-M. *Electrochem. Commun.* **2008,** *10*, 814-817.
8. Rajesh; Ahuja, T.; Kumar, D. *Sens. Actuators, B* **2009,** *B136*, 275-286.
9. Li, J.; Lin, X. *Biosens. Bioelectron.* **2007,** *22*, 2898-2905.
10. Ward-Jones, S.; Banks, C. E.; Simm, A. O.; Jiang, L.; Compton, R. G. *Electroanalysis* **2005,** *17*, 1806-1815.
11. Balis, N.; Dracopoulos, V.; Antoniadou, M.; Lianos, P. *Electrochim. Acta* **2012,** *70*, 338-343.
12. Andreoli, E.; Rooney, D. A.; Redington, W.; Gunning, R.; Breslin, C. B. *J. Phys. Chem. C* **2011,** *115*, 8725-8734.
13. Andreoli, E.; Annibaldi, V.; Rooney, D. A.; Breslin, C. B. *J. Phys. Chem. C* **2011,** *115*, 20076-20083.
14. Mao, Y.; He, J.; Sun, X.; Li, W.; Lu, X.; Gan, J.; Liu, Z.; Gong, L.; Chen, J.; Liu, P.; Tong, Y. *Electrochim. Acta* **2012,** *62*, 1-7.
15. Mandke, M. V.; Pathan, H. M. *J.Electroanal. Chem.* **2012,** *686*, 19-24.
16. Choi, K.-S. *J. Phys. Chem. Lett.* **2010,** *1*, 2244-2250.
17. Zhou, X. J.; Harmer, A. J.; Heinig, N. F.; Leung, K. T. *Langmuir* **2004,** *20*, 5109-5113.
18. Sarkar, D. K.; Zhou, X. J.; Tannous, A.; Louie, M.; Leung, K. T. *Solid State Commun.* **2003,** *125*, 365-368.
19. Milan Paunovic, M. S. *Fundamentals of Electrochemical Deposition*. Wiley: 2006; p 52.
20. Ortega, J. M. *Thin Solid Films* **2000,** *360*, 159-165.
21. Fisher, A. C. *Electrode Dynamics*. Oxford Universtiy Press: Oxford, **1996**.
22. Scharifker, B.; Hills, G. *Electrochim. Acta* **1983,** *28*, 879-889.
23. Sarkar, D. K.; Zhou, X. J.; Tannous, A.; Leung, K. T. *J. Phys. Chem. B* **2003,** *107*, 2879-2881.
24. Zhou, Y.; Switzer, J. A. *Scripta Materialia* **1998,** *38*, 1731-1738.
25. McShane, C. M.; Choi, K.-S. *J. Am. Chem. Soc.* **2009,** *131*, 2561-2569.

26. López, C. M.; Choi, K.-S. *Langmuir* **2006,** *22*, 10625-10629.
27. Siegfried, M. J.; Choi, K.-S. *Angew. Chem., Int. Ed.* **2005,** *44*, 3218-3223.
28. Tang, S. C.; Meng, X. K. *Sci. China, Ser. E: Technol. Sci.* **2009,** *52*, 2709-2714.
29. Siegfried, M. J.; Choi, K.-S. *Angew. Chem. Int., Ed.* **2008,** *47*, 368-372.
30. Abdel, R. H. H.; Moustafa, A. H. E.; Abdel, M. S. M. K. *Int. J. Electrochem. Sci.* **2012,** *7*, 6959-6975.
31. Siegfried, M. J.; Choi, K.-S. *J. Am. Chem. Soc.* **2006,** *128*, 10356-10357.
32. Tsakova, V.,*J. Solid State Electrochem.* **2008,** *12*, 1421-1434.
33. Ilieva, M.; Tsakova, V.; Erfurth, W. *Electrochim. Acta* **2006,** *52*, 816-824.
34. Ilieva, M.; Tsakova, V. *Synth. Met.* **2004,** *141*, 281-285.
35. Tsakova, V.; Borissov, D.; Ivanov, S. *Electrochem. Commun.* **2001,** *3*, 312-316.
36. Cioffi, N.; Torsi, L.; Losito, I.; Di, F. C.; De, B. I.; Chiavarone, L.; Scamarcio, G.; Tsakova, V.; Sabbatini, L.; Zambonin, P. G. *J. Mater. Chem.* **2001,** *11*, 1434-1440.
37. Tsakova, V.; Borissov, D.; Ranguelov, B.; Stromberg, C.; Schultze, J. W. *Electrochim. Acta* **2001,** *46*, 4213-4222.
38. Otero, T. F.; Costa, S. O.; Ariza, M. J.; Marquez, M. *J. Mater. Chem.* **2005,** *15*, 1662-1667.
39. Wang, Z. L. *J. Phys. Chem. B* **2000,** *104*, 1153-1175.
40. Zhou, Y.; Switzer, J. A. *Scr. Mater.* **1998,** *38*, 1731-1738.
41. Andreoli, E.; Annibaldi, V.; Rooney, D. A.; Liao, K.-S.; Alley, N. J.; Curran, S. A.; Breslin, C. B. *Electroanalysis* **2011,** *23*, 2164-2173.
42. Brown, K. E. R.; Choi, K.-S. *Chem. Commun.* **2006**, 3311-3313.
43. Lu, D.-l.; Tanaka, K.-i. *J. Electrochem. Soc.* **1996,** *143*, 2105-2109.
44. Zheng, J. Y.; Jadhav, A. P.; Song, G.; Kim, C. W.; Kang, Y. S. *Thin Solid Films* **2012,** *524*, 50-56.
45. Liu, Y. C.; Hwang, B. J. *J. Electroanal. Chem.* **2001,** *501*, 100-106.
46. Liu, Y.-C.; Yang, K.-H.; Ger, M.-D. *Synth. Met.* **2002,** *126*, 337-345.
47. Liu, Y. C.; Hwang, B. J. *Thin Solid Films* **1999,** *339*, 233-239.
48. Liu, Y.-C.; Hwang, B. J. *Thin Solid Films* **2000,** *360*, 1-9.
49. Aradilla, D.; Estrany, F.; Armelin, E.; Oliver, R.; Iribarren, J. I.; Alemán, C. *Macromol. Chem. Phys.* **2010,** *211*, 1663-1672.
50. Ge, D.; Wang, J.; Wang, Z.; Wang, S. *Synth. Met.* **2002,** *132*, 93-95.
51. Wang, J.; Mo, X.; Ge, D.; Tian, Y.; Wang, Z.; Wang, S. *Synth. Met.* **2006,** *156*, 514-518.
52. Cho, S. I.; Lee, S. B. *Acc. Chem. Res.* **2008,** *41*, 699-707.

53. Huang, J.; Wang, K.; Wei, Z. *J. Mater. Chem.* **2010,** *20*, 1117-1121.
54. Monk, P. M. S. *Fundamentals of Electroanalytical Chemistry*. **2001**.
55. Tian, Y.; Wang, J.; Wang, Z.; Wang, S. *Sens. Actuators, B* **2005,** *B104*, 23-28.
56. Ge, D.; Mu, J.; Huang, S.; Liang, P.; Gcilitshana, O. U.; Ji, S.; Linkov, V.; Shi, W. *Synth. Met.* **2011,** *161*, 166-172.
57. Ge, D.; Huang, S.; Qi, R.; Mu, J.; Shen, Y.; Shi, W. *ChemPhysChem* **2009,** *10*, 1916-1921.
58. Gupta, V.; Miura, N. *Materials Letters* **2006,** *60*, 1466-1469.
59. Zang, J.; Li, C. M.; Bao, S.-J.; Cui, X.; Bao, Q.; Sun, C. Q. *Macromolecules* **2008,** *41*, 7053-7057.
60. Tian, Y.; Li, Z.; Xu, H.; Yang, F. *Separation and Purification Technology* **2008,** *63*, 334-340.
61. Le, W.-Z.; Liu, Y.-Q. *Sens. Actuators, B* **2009,** *141*, 147-153.
62. Nikolic, N. D.; Brankovic, G.; Maksimovic, V. M. *J. Solid State Electrochem.* **2012,** *16*, 321-328.
63. Lee, J. Y.; Tan, T. C. *J. Electrochem. Soc.* **1990,** *137*, 1402-8.
64. Chandrasekhar, P. *Conducting Polymers, Fundamental and Applications*. Kluwer Academic Publishers: **1999**.
65. Solak, A. O.; Gulser, P.; Gokmese, E.; Gokmese, F. *Mikrochim. Acta* **2000,** *134*, 77-82.
66. Yang, S.; Liu, X.; Zeng, X.; Xia, B.; Gu, J.; Luo, S.; Mai, N.; Wei, W. *Sens. Actuators, B* **2010,** *B145*, 762-768.
67. Badea, G. E. *Electrochim. Acta* **2009,** *54*, 996-1001.
68. Davis, J.; Moorcroft, M. J.; Wilkins, S. J.; Compton, R. G.; Cardosi, M. F. *Analyst* **2000,** *125*, 737-742.
69. Casella, I. G.; Gatta, M. *J. Electroanal. Chem.* **2004,** *568*, 183-188.
70. Reyter, D.; Belanger, D.; Roue, L. *Electrochim. Acta* **2008,** *53*, 5977-5984.
71. de, V. A. C. A.; van, S. R. A.; van, V. J. A. R. *J. Mol. Catal. A: Chem.* **2000,** *154*, 203-215.
72. Reyter, D.; Chamoulaud, G.; Belanger, D.; Roue, L. *J. Electroanal. Chem.* **2006,** *596*, 13-24.
73. Paixao, T. R. L. C.; Cardoso, J. L.; Bertotti, M. *Talanta* **2007,** *71*, 186-191.
74. Tian, Y.; Wang, J.; Wang, Z.; Wang, S. *Synth. Met.* **2004,** *143*, 309-313.

Chapter 6

Conclusions

6.1 Conclusions

The main aim of the research was to develop new technologies which could be used in devices such as sensors, capacitors, photochemical cells, storage devises or any other green technologies. In particular we focussed on the use of polymer materials to create an electrochemical sensor for the detection of the nitrate ion in aqueous systems. Nitrate contamination is a significant problem in countries with a large agricultural land usage, including Ireland. Therefore, the accurate and up-to-date monitoring of this pollutant is of utmost importance. This thesis focussed on the use of polypyrrole (PPy) and poly[N-2-(cyanoethyl)pyrrole] (PPyEtCN) polymers as they have successfully been applied in sensor applications.[1-2] To increase the sensitivity of these materials we aimed to develop them into a nanowire morphology; during this process we also developed a new methodology to fabricate hollow microtubes. As copper is known for its catalytic ability to electro-reduce nitrate we were eager to incorporate copper, again as a nanostructure, within these polymer nano/micro materials.

In Chapter 3 the investigation of the *N*-substituted PPyEtCN monomer was undertaken as it had shown promising application in sensor technology. This was mainly due to its ability to hydrogen bond and dipole-dipole interact with other molecules. This monomer is typically polymerised in organic media such as acetonitrile. However, to grow nanowires, an aqueous solvent must be employed as the morphology directing salts have a limited solubility in organic media. This leads to solubility problems with the PyEtCN monomer as it has a low solubility in water. These solubility problems were overcome by using a mixed solvent system comprised of water and ethanol in a 7:3 ratio. This allowed for a minimum solubility of the monomer and morphology directing salts to be maintained in sufficient concentrations to allow polymerisation.

The effect of the solvent mixture, substrate, polarisation time, type and concentration of the dopant salts were investigated to ascertain their effect on the nanowire morphology. By changing these parameters a high level of control was achieved over the resultant nanowire morphology, while maintaining a template free approach. The polarisation time controlled the length and diameter of the wires; increments from 5 to 60 min extended their length from nm to μm, while the diameter increased from

100 to 150 nm. Electrochemical measurements revealed the nanowires were electroactive and showed an increased current response as their length increased. However, for the polymer redox chemistry, a much broader reduction peak was observed compared to the oxidation peak, which may suggest a slow switching of the polymer between redox states and the possibility of hindered dopant expulsion.

$LiClO_4$ and $(NH_4)H_2PO_4$ were chosen as the electrolyte salts during polymerisation as they had excellent solubility in the mixed solvent system. Their optimal concentrations were 0.002 M and 0.300 M respectively and values which varied from these either produced microwires or irregular polymer deposits. It was also observed that by changing the ratio of these salts in comparison to the monomer, other polymer structures were produced which resembled the wire morphology. The initial growth of the nanowires was observed to follow a 3-D instantaneous nucleation and growth model, producing a uniform polymer film with a near homogeneous nanowire length. Due to this nucleation process the nanowires were bound together, and to the substrate, by a base layer of bulk polymer. TEM analysis (at 200 kV) confirmed that the nanowires were solid tapered materials while Infra-red spectroscopy was used to identify that the cyano moiety remained intact once the nanowires were formed. This was evident by a band at 2250 cm^{-1} in the FTIR spectrum of the polymer nanowires. The disappearance of the bands at ~3100 and 732 cm^{-1}, corresponding to the C-H_α and C-H_β stretching modes, suggested that the polymer was formed by both α-α and α-β linkages. This, combined with a band at 1708 cm^{-1}, corresponding to a ν(C=O) stretching mode, suggested that these polymers had a low π-π orbital overlap between adjacent monomers and possessed carbonyl groups which disrupted conjugation. This resulted in the PPyEtCN nanowires possessing a low electrical conductivity. This is consistent with reports relating to PPyEtCN polymers in the literature.[3-4]

Raman spectroscopy was used to characterise the repeating Py units in the polymer backbone and gave a complete picture of the chemical state of the formed nanowires. The data was consistent with the conjugation length in the PPyEtCN nanowires being relatively short with charge carriers predominantly comprised of polaron species. A band at 1707 cm^{-1} was also present which was indicative of a ν(C=O) mode, which is consistent with the FTIR data. The Raman spectra recorded at 660 nm did not supply

sufficient intensity for the polaron and bipolaron bands at 1075 and 974 cm^{-1} to overcome the background signal. In an attempt to resonantly enhance these bands, other laser excitations were employed. Wavelengths of 473 and 785 nm were tested for their resonance enhancement of these particular bands. It was observed that the 785 nm excitation was deemed the most effective for probing the oxidised species within the PPyEtCN polymers.

Dopant information was obtained from EDX measurements where peaks for chlorine (2.6 and 2.8 keV) and phosphorus (2.0 and 2.2 keV) were observed. This suggested that both ClO_4^- and $H_2PO_4^-$ ions were acting as counterion dopants within the polymer matrix. ClO_4^- ions were ascertained to be the preferred dopant as they were detected in large quantities in the polymer even though the electrolyte contained an excess of $H_2PO_4^-$ ions (15 times more). However, over longer polymerisation times, the quantity of phosphorus detected by EDX increased. This was most likely due to the consumption of the smaller quantity of ClO_4^- ions available in the electrolyte over a short time. It was also possible that the large phosphorus signal was generated by $H_2PO_4^-$ ions being trapped inside the polymer as it propagated, not necessarily acting as dopant.

It was hoped that these polymers could be utilised in application as a nitrate sensor. However, as was discussed in Chapter 5, the resistive nature of these nanowire films made the electrodeposition of copper onto their surfaces quite difficult. Overpotentials of -1.000 V had to be applied to overcome the insulating polymer layers. Discrete particles could not be obtained in a controllable fashion covering the electrode. Therefore, based on these results, the nitrate sensing abilities of these PPyEtCN nanowires were not pursued.

During the electrodeposition of the PPyEtCN nanowires a second morphology developed in certain experiments. The structures were composed of randomly formed microtubes. We investigated their occurrence in Chapter 4 and aimed to develop control over their electrodeposition. These new materials possessed unique properties for application in entrapment and drug delivery systems due to their exposed hollow centre.[5] Using the solubility of the monomer to control the occurrence of the microtubes revealed that they developed by a ‘droplet guided’ mechanism. They formed because large insoluble monomer droplets were present in the polymerisation

electrolyte, as identified by microscopy analysis. When these droplets adsorbed to the electrode surface, polymerisation occurred around and within their circumference. Their growth was associated with an increased current response at very early times in the polarisation plots. The current response was indicative of a fast reaction rate during the microtube formation. The microtubes were investigated by EDX analysis which identified chlorine within their cavity. This confirmed that $LiClO_4$ was soluble inside the monomer droplets. The combination of a high concentration of monomer and dopant at the electrode surface explained the initial fast growth rate, and confirmed the monomer droplet hypothesis. Although a strong understanding of the monomer droplet mechanism was developed, it proved too difficult to reproduce accurately between successive experiments. Furthermore, after extensive TEM and FIB analysis it was uncertain whether this methodology was capable of growing fully hollow tubes.

To overcome this issue, the monomer droplet was replaced with an insoluble droplet which would not promote polymerisation at its core. Sonication was employed to disperse toluene as insoluble droplets homogenously throughout the solution, forming an emulsion. This had a significant effect on the resultant morphology and fully hollow PPyEtCN microtubes were deposited at the electrode surface. This soft template approach, which was previously been used in a chemical oxidation methodology,[6] was successfully adapted to an electrochemical polymerisation procedure. The openings of the tubes were controlled by using two sonication methods (probe and bath) to form the emulsion solution. As the monomer was soluble within the entire solution, the level of sonication altered the amount of monomer partitioned between the continuous phase and toluene droplets. More monomer in the continuous phase promoted the tube ends to close over. This allowed for novel PPyEtCN hollow microtubes and closed microcontainers to be synthesised attached to an electrode surface.

Control over microtube diameter was achieved by simply altering the emulsion sonication time or the amount of toluene added to form the emulsion. The applied potential and electrolyte mixture were also shown to have a significant effect on the polymer morphologies. The polymerisation growth profiles indicate that the role of the mixed electrolyte system ($LiClO_4$ and $(NH_4)H_2PO_4$) was to allow fast initial nucleation followed by slow polymer propagation, leading to the formation of

vertically aligned structures. Without the addition of the $(NH_4)H_2PO_4$ the polymer grew very rapidly and formed a bulk-like layer without any vertical character. The role of the $H_2PO_4^-$ ion was to 'mop up' the protons which were released from PPy during polymerisation. Removing these protons raised the local pH at the electrode surface which favoured a slower polymer growth rate. Using EDX, the amount of $ClO4^-$ and $H_2PO_4^-$ within the polymer was analysed as a function of applied polymerisation potential. It was observed that the polymerisation potential was responsible for increasing the local pH at the electrode because, as the polymerisation rate increased, more H+ ions were released. Subsequently, more of the $H_2PO_4^-$ ions were converted to the uncharged H_3PO_4 species and did not partake in doping the polymer backbone. This was registered in the EDX spectra as the chlorine signal was much stronger for polymers grown at higher potentials. Since the $H_2PO_4^-$ ions were not available, the $ClO4^-$ was the only species available to act as a counter ion for the polymer.

Electrochemical characterisation indicated that the PPyEtCN microtube morphology had an increased electrochemical response compared to its bulk counterpart. They also increased the hydrophilicity of the polymer by trapping air within the tubes. TEM analysis of individual closed-pore microtubes identified a hollow interior at the base within which the toluene droplet was encapsulated. This cavity may be used to entrap other compounds making these materials useful in a range of applications. The methodology was also applied to form microstructures of poly(3,4-ethylenedioxythiophene) and PPy. Therefore, is should be applicable for growing a range of microstructures for other functionalised and unfunctionalised conducting polymers. As the PPyEtCN microtubes were subject to the same low conductivity limitations as the PPyEtCN nanowires, their nitrate sensing abilities were not explored. However, using them in another manner may allow for new materials to be developed to construct a cheap and reliable copper electrochemical sensor.

Employing the PPyEtCN hollow microtubes, it may be possible to use these polymers as templates for copper electrodeposition. As discussed in chapter 5, PPyEtCN is only capable of reducing copper at potentials more negative than -1.000 V. However, if a potential such as -0.200 V was employed, the copper would nucleate within the cavity of the microtubes due to the exposed electrode at their base. Ideally the copper would grow to fill the hollow microstructure, as the

deposition potential would not be sufficient to initiate copper deposition on the insulating PPyEtCN surface. Once the polymer 'shell' is removed it would leave free standing copper microstructures. These structures could then be employed for the sensing of nitrate as their unique microstructure would provide them with the benefit of a larger surface area. This combined with the fact that they are anchored to an electrode surface may provide a cheap and reliable method of producing a sensor which is stable and robust. This is a novel and interesting alternative to templating which typically consists of purchasing costly aluminium template grids. Furthermore, as discussed in Chapter 4, the PPyEtCN microtube diameter can easily be controlled by altering the sonication time or toluene addition. This would produce a versatile and cheap polymer template system for the production of electrodeposited metal microstructures. Experiments are currently being performed to investigate the feasibility of this idea.

In Chapter 5 the electrodeposition of copper onto PPy polymers was presented. This would overcome the resistive nature associated with PPyEtCN as the cyano substituent was not present to cause steric problems within the polymer. This allowed a greater planarity of adjacent monomer units and therefore a greater conductivity. Electrochemically polymerised bulk PPy films were proven to be a reproducible substrate for the nucleation and growth of copper crystals. Using potentiostatic methods to electrodeposit the copper produced a range of crystal shapes. Two types of structures nucleated at the PPy substrates, smaller cubooctahedron type deposits and larger more irregular deposits. These shapes were formed at potentials between -0.105 to -0.200 V. Using SEM in conjunction with modelling equations identified their nucleation mechanism as progressive in nature. As the deposition potential was brought to more reductive values the shapes of the cubooctahedron crystals changed from triangle-based pyramids to truncated octahedrons. These crystals shapes were compared with relevant reports from the literature and were assigned as Cu_2O. This was also reiterated by an understanding of the oxygen reduction reaction which is present PPy materials;[7] this would further encourage the formation of copper oxide species.

The larger deposition morphologies increased in diameter and height as the negative over-potential increased and shifted from cube to dendrite and to branched morphologies. These structures formed due to the larger negative potential

consuming all the available copper near the electrode. As deposition continued the copper deposits were forced to extend into the electrolyte to reach fresh copper. Due to a lack of quantitative surface analysis these branched structures were speculated to be a mixed copper/copper oxide species. During the course of writing this thesis, a selection of these materials was sent for XRD analysis to speciate the different copper structures. From these potentiostatic experiments a strong understanding of the copper electrodeposition mechanism at PPy surfaces was developed. This was then used to electrodeposit copper at PPy nanowires using a cyclic routine.

The formation of PPy nanowires with a reproducible surface was investigated using an electrochemical probe. It was observed that a high concentration of carbonate was detrimental to nanowire growth and contaminated the counter electrode surface. Using an acid treatment overcame these issues and a reproducible nanowire deposition was achieved. The PPy nanowire electrode was shown to have a greater electrochemical response compared to a bare electrode due to the higher surface area which it possessed. These nanowires were then used to develop a cyclic deposition technique to fabricate a range of different copper deposits including, triangle, spike, sheet and particle. Cycle number and scan rate were seen to have a dramatic effect on the resultant copper morphology and loading. Increases in cycle number from 5 to 320 led to bulk deposition while increases in scan rate from 50 to 900 mV/s produced smaller and more discrete particles.

These nanocomposites were tested as a surface for the electroreduction of the nitrate ion, which was shown to begin with an adsorption step. The ideal scanning window was between 0.000 and -1.400 V as nitrate adsorbs around 0.000 V. The window vertex was limited to -1.400 V as this removed interference from the hydrogen evolution reaction which competes with nitrate adsorption. The addition of a greater copper loading was seen to generate a greater response for the nitrate electroreduction. However, over-loading the electrode was possible at deposition cycles greater than 160, at 100 mV/s. The PPy nanowire/copper composite was observed to generate a larger current for nitrate electroreduction when smaller copper particles were deposited. However, the optimised nanowire/copper hybrid had a lower sensitivity compared to a glassy carbon/copper composite. This was due to residual carbonate remaining within the polymer matrix which formed a complex with the copper ions and interfered with the nitrate reaction. In spite of this, the PPy

nanowires were shown to have a stabilising interaction with the copper through a charge transfer complex, which resulted in a better stability of the sensor over time.

This chapter highlighted the catalytic ability of copper for increasing the electroreduction of the nitrate ion in aqueous solutions. The nanowires were seen as reproducible substrates for copper electrodeposition. While the sensitivity of the nanowire/copper hybrid was not as sufficient as hoped, the formation of a stable PPy/copper charge transfer complex allowed for a slower degradation of the nitrate reduction signal. This would suggest these electrodes would be applicable in long term sensing systems, where longevity rather than lowest sensitivity is necessary. If required, overcoming the drawbacks associated with the reduced sensitivity may be achieved by employing nanowires which are synthesised without the use of buffer solutions, possibly using a biomolecule approach.[8]

6.2 References

1. Fabregat, G.; Córdova-Mateo, E.; Armelin, E.; Bertran, O.; Alemán, C. *J. Phys. Chem. C* **2011,** *115*, 14933-14941.
2. Ramanaviaius, A.; Ramanaviaiena, A.; Malinauskas, A. *Electrochim. Acta* **2006,** *51*, 6025-6037.
3. Aradilla, D.; Estrany, F.; Armelin, E.; Oliver, R.; Iribarren, J. I.; Alemán, C. *Macromol. Chem. Phys.* **2010,** *211*, 1663-1672.
4. Fabregat, G.; Alemán, C.; Casas, M. T.; Armelin, E. *J. Phys. Chem. B* **2012,** *116*, 5064-5070.
5. Mazur, M. *Langmuir* **2008,** *24*, 10414-10420.
6. Kubacka, D.; Krysiński, P.; Blanchard, G. J.; Stolarski, J.; Mazur, M. *J. Phys. Chem. B* **2010,** *114*, 14890-14896.
7. Andreoli, E.; Rooney, D. A.; Redington, W.; Gunning, R.; Breslin, C. B. *J. Phys. Chem. C* **2011,** *115*, 8725-8734.
8. Shi, W.; Liang, P.; Ge, D.; Wang, J.; Zhang, Q. *Chem. Commun.* **2007**, 2414-2416.

Electrochemistry Communications 20 (2012) 79–82

Contents lists available at SciVerse ScienceDirect

Electrochemistry Communications

journal homepage: www.elsevier.com/locate/elecom

Facile template-free electrochemical preparation of poly[*N*-(2-cyanoethyl)pyrrole] nanowires

Conor P. McCarthy *, Niall B. McGuinness, Bernadette E. Alcock-Earley, Carmel B. Breslin, A. Denise Rooney

Department of Chemistry, National University of Ireland Maynooth, Maynooth, Co. Kildare, Ireland

ARTICLE INFO

Article history:
Received 11 February 2012
Received in revised form 21 March 2012
Accepted 28 March 2012
Available online 5 April 2012

Keywords:
Nanowires
Electrochemical deposition
Template free
Poly[*N*-(2-cyanoethyl)pyrrole]

ABSTRACT

In this paper the first synthesis of poly[*N*-(2-cyanoethyl)pyrrole] (PPyEtCN) in a nanowire morphology is reported. The method employed is a facile, one step electrochemical growth, which does not require the use of any templates or surfactants. Using optimised conditions the nanowires nucleate to give a homogeneous film across the electrode surface, with lengths of approximately 2 μm and diameters of approximately 150 nm. Structural information on the nanowires was obtained using vibrational spectroscopy. Evidence is presented to support an instantaneous 3-D nucleation and growth mechanism for the nanowires.

1. Introduction

Polypyrrole (PPy) is one of the most extensively studied conducting polymers due to its facile preparation and its attractive range of properties, including redox activity [1], ion exchange capabilities [2] and biocompatibility [3]. However, there is currently much interest in using functionalised monomers to generate conducting polymers as novel materials, in particular, as biosensors [4–7]. When the functional group on the substituted pyrrole contains a terminal cyano group, supramolecular interactions between that group and other molecules are possible. Indeed, PPyEtCN modified electrodes have been used to immobilise specific antibodies for the fabrication of biosensors [8,9] and in the electrochemical sensing of dopamine [10].

In recent years a number of authors have reported template-free electrochemical methods for the formation of polypyrrole nanowires [11,12]. These nanowires possess a higher surface area and shorter diffusion lengths than the analogous bulk materials providing the wires with more attractive properties [13]. Although *N*-substituted polypyrrole has been employed for sensor applications, there are few studies on the preparation of these polymers in the nanowire morphology. Moreover, these studies have utilised either a template approach or coated already grown polypyrrole nanowires with the functionalised polypyrrole [14,15]. Here, we present results for the synthesis of novel PPyEtCN nanowires, and to the best of our knowledge this is the first report of a one-step preparation of *N*-substituted polypyrrole nanowires using a facile template-free electrochemical approach.

2. Experimental

All chemicals were purchased from Sigma-Aldrich and were of analytical grade. *N*-(2-cyanoethyl)pyrrole was distilled under vacuum and stored under nitrogen at −40 °C. Electrochemical experiments were performed at room temperature using a standard three electrode cell. Potentials were referenced against a saturated calomel electrode (SCE) and a platinum wire was used as a counter electrode. The working electrode was a glassy carbon rod (4 mm diameter) embedded into a Teflon holder using an epoxy resin. Before each experiment the exposed surface was polished with successively finer grades of diamond paste (Buehler), sonicated in ethanol after each polishing step, and then finally sonicated in water. In a typical experiment the monomer (75 mM) was dissolved in EtOH (3 ml) while both $LiClO_4$ (20 mM) and $(NH_4)H_2PO_4$ (0.3 M) were dissolved in H_2O (7 ml). The two solutions were mixed, stirred for 10 min and finally a potential of 0.85 V vs. SCE was applied. SEM was performed using a Hitachi S-3200-N with a tungsten filament or a Hitachi S-4000 with a cold cathode field emission electron source (FE-SEM) and a JEOL 2000 FX, operating at 200 kV, was used for all TEM analyses. Raman measurements were performed with a LabRAM high resolution Raman spectrometer using a 660 nm solid state diode laser (100 mW). FTIR spectra were obtained using a Perkin Elmer 2000 FTIR spectrometer.

3. Results and Discussion

3.1. Electrochemical Growth of PPyEtCN Nanowires

Due to the different solubilities of the reagents used, the nanowires were electropolymerised from a 70:30 H_2O/EtOH mixture. In accordance

* Corresponding author. Tel.: +353 17086856.
E-mail address: conor.p.mccarthy@nuim.ie (C.P. McCarthy).

1388-2481/$ – see front matter © 2012 Elsevier B.V. All rights reserved.
doi:10.1016/j.elecom.2012.03.047

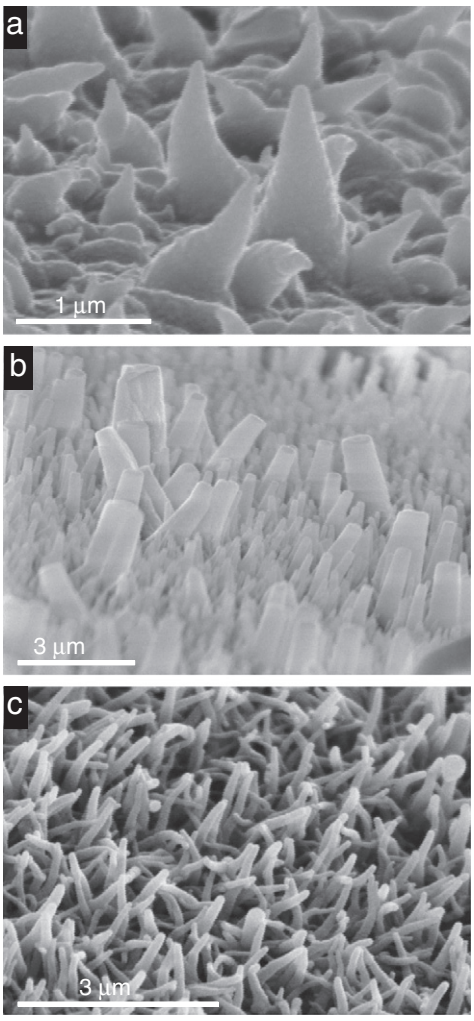

Fig. 1. SEM micrographs of PPyEtCN nanowires grown for 60 min at different molar ratios of monomer : $(NH_4)H_2PO_4$: $LiClO_4$ (a) 1:3:0.3 (b) 1:7:0.5 and (c) 1:4:0.3.

with previous studies nanowire formation was highly dependent on the growth conditions [16]. Their growth was only observed between the potential range of 0.8 to 1.0 V and the monomer to dopant ratio was critical (Fig. 1(a), (b) and (c)). Polymerisation using a low dopant concentration resulted in microwires which were significantly tapered towards the tip (Fig. 1(a)). Whereas, at higher dopant concentrations, vertical wires formed, but they possessed a wide distribution of sizes (Fig. 2(b)). Optimisation of these growth conditions led to a homogeneous and adherent nanowire film forming over the substrate (Fig. 1(c)).

FE-SEM micrographs recorded at various time intervals show that both the diameter and length of the wires were easily controlled by varying the electropolymerisation period. Only nodules are evident after 1 min of growth (Fig. 2(a)), after 5 min nanowire formation is clearly evident (Fig. 2(b)) and long slightly tapered wires are obvious after 60 min (Fig. 2(c)). Fig. 2(d) shows the relationship between electropolymerisation time and wire diameter and length.

3.2. Nucleation of the PPyEtCN Nanowires

Studies have shown that the preliminary stages of electrodeposition of conducting polymers occurs via diffusion controlled growth from nucleation sites [17,18]. A typical current-time transient recorded during the electropolymerisation period is shown in Fig. 3(a). Dimensionless $(I/I_{max})^2$ vs. (t/t_{max}) and (I/I_{max}) vs. (t/t_{max}) plots were produced from these data and compared to the theoretical 2-D and 3-D progressive and instantaneous models [19]. The resulting plots are shown in Fig. 3(b) and (c), and it is clear that for the early stages of growth the experimental data are consistent with the 3-D instantaneous phase of growth. Upon repeated experimentation we found that uniform nanowire films were only formed when the early stages of polymer growth followed the 3-D instantaneous growth model. This indicates that, even though a base layer of bulk polymer is formed before nanowire formation is observed, whether the polymer growth can result in the nanowire morphology is determined at the point of nucleation.

3.3. Structural Characterisation of PPyEtCN Film

A cross section of the PPyEtCN film is shown in Fig. 4(a), where it is clear that the wires are attached together at the base by a layer of bulk

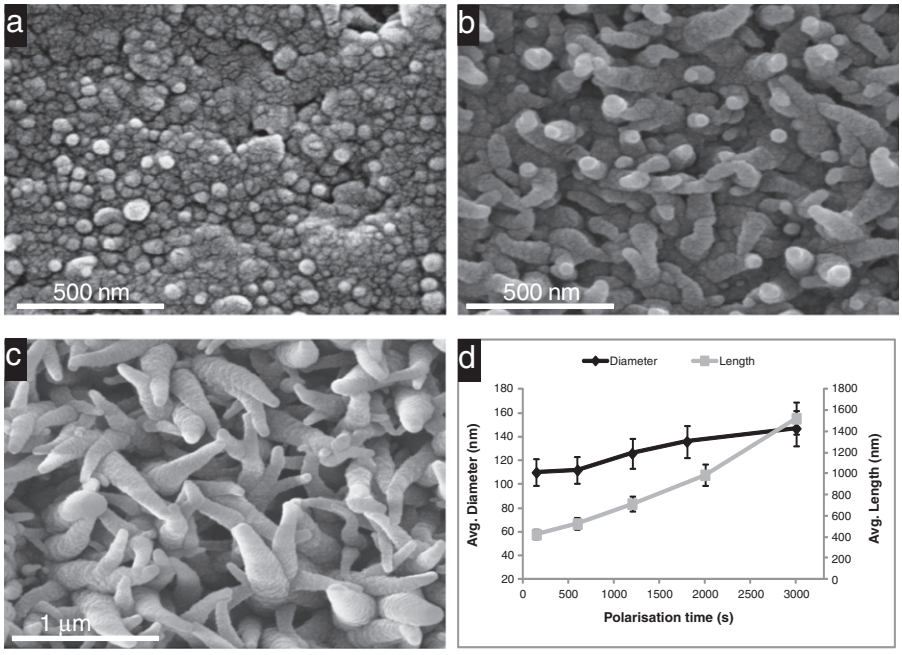

Fig. 2. FE-SEM micrographs of PPyEtCN nanowires at different growth stages (a) 1 min (b) 5 min and (c) 60 min. Average nanowire diameter and length as a function of time (d). Nanowires grown under the conditions given in Section 2.

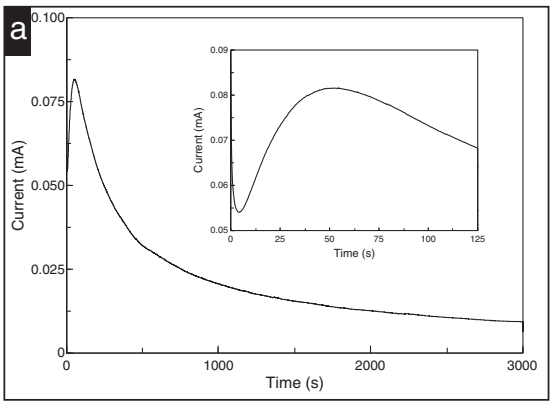

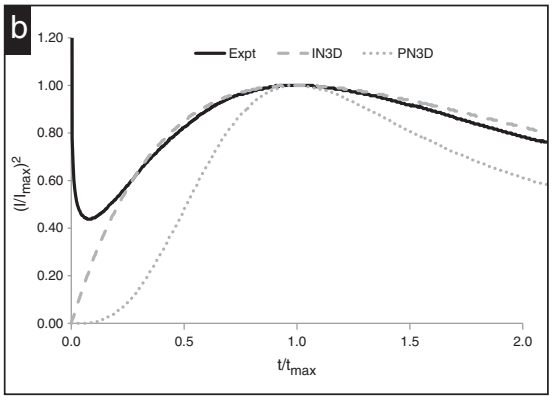

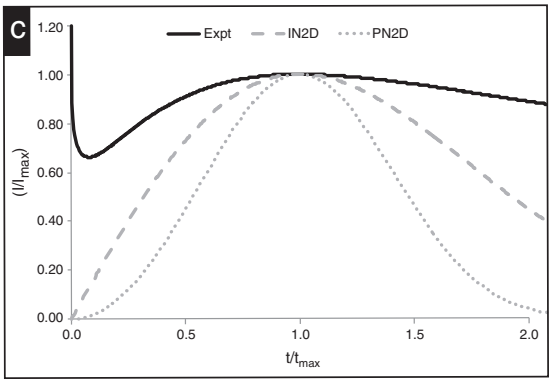

Fig. 3. A typical current-time transient for nanowire growth (a). Dimensionless plots of $(I/I_{max})^2$ or (I/I_{max}) vs t/t_{max} compared with (b) 3-D instantaneous nucleation (IN3-D) and progressive nucleation (PN3-D) (c) 2-D instantaneous nucleation (IN2-D) and progressive nucleation (PN2-D).

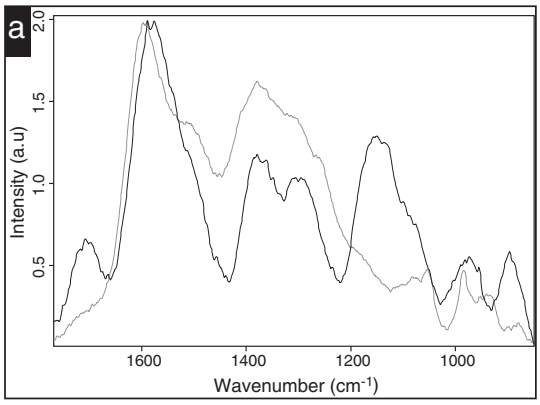

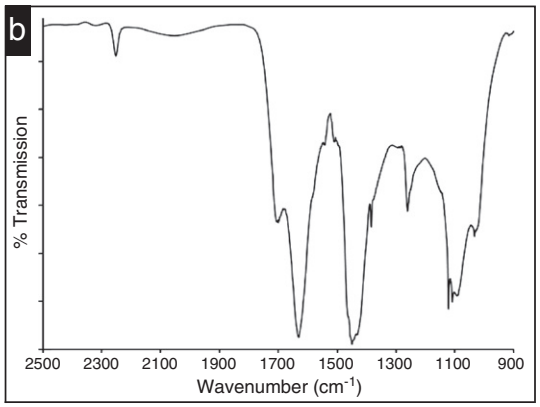

Fig. 5. (a) Raman spectra for bulk PPy (grey) and PPyEtCN nanowire film (black) and (b) FTIR spectrum of PPyEtCN nanowires in KBr disk.

polymer. It appears the polymer nucleates on the surface and grows to give a bulk-like layer. However, 1-D growth along the z-axis is eventually favoured giving the wires extended lengths above the base layer. A TEM micrograph of a single nanowire (Fig. 4(b)) shows a uniform contrast over the entire length, indicating a homogeneous solid structure. The tapering effect, which is common for the longer wires, is also clearly evident.

Direct evidence for the presence of the cyano group is obtained from the FTIR spectrum in which the characteristic $\nu(C\equiv N)$ band at 2246 cm^{-1} is clearly observed (Fig. 5(a)). The Raman spectra of a PPy film and the PPyEtCN nanowires (Fig. 5(b)) show that the PPyEtCN retains the characteristic bands associated with PPy. The band at 1155 cm^{-1} is associated with the CH_2CH_2CN moiety. The most intense band in the PPy spectrum at 1595 cm^{-1} is shifted to 1582 cm^{-1} for the PPyEtCN nanowires. This band is assigned as arising from the $\nu(C=C)$ modes of both oxidised and neutral pyrrole units [20]. This shift to a lower wavenumber is indicative of a reduction in the amount of oxidised units in the nanowires compared to PPy. Furthermore, while

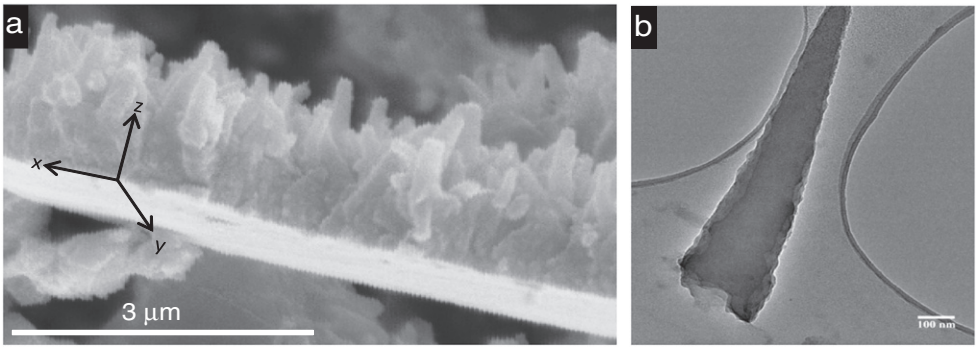

Fig. 4. (a) SEM image of a cross section of a nanowire film showing the base layer of bulk polymer and (b) TEM image of an individual nanowire removed from the electrode surface.

PPy exhibits bands due to the bipolaron and polaron species at 940 and 980 cm^{-1} respectively, only the latter is distinguishable in the PPyEtCN spectrum. The ratio of the intensity of the $\nu(C=C)$ band to that of the skeletal band at 1503 cm^{-1} gives a measurement of the relative amounts of conjugation in the two polymers [21]. The ratios were determined to be approximately 2.7 and 2 for the PPy and PPyEtCN systems respectively, indicating the lower degree of conjugation in the PPyEtCN film. This finding is consistent with the presence of a band at approximately 1705 cm^{-1} in both the Raman and FTIR spectra which is indicative of a carbonyl stretching mode. Aradilla *et al.* observed a $\nu(C=O)$ band in the FTIR of bulk PPyEtCN [22,23]. They proposed that this signal arose from the conversion of C—H moieties to carbonyls at the β positions of the pyrrole rings disrupting the conjugation of the polymer chains.

4. Conclusions

A one step method for the formation of novel PPyEtCN nanowire films was developed. Experiments, using vibrational spectroscopy, confirmed that the CH_2CH_2CN group remains intact during the electropolymerisation and the data is consistent with the conjugation length in the PPyEtCN nanowires being relatively short. The initial growth of the nanowires follows a 3-D instantaneous nucleation and growth, leading to a uniform polymer film with a near homogeneous nanowire length.

Acknowledgements

We would like to thank Anne Shanahan in DIT and Dr. Patrick Carolan in Tyndall for the Raman and TEM analyses. This work was supported by the Environmental Protection Agency Ireland through the STRIVE programme and by Science Foundation Ireland through the Research Frontiers Programme 08/RFP/MTR1423 and the National Access Programme at the Tyndall National Institute.

References

[1] U. Johanson, M. Marandi, T. Tamm, J. Tamm, Electrochimica Acta 50 (2005) 1523.
[2] P.M. Dziewoński, M. Grzeszczuk, The Journal of Physical Chemistry. B 114 (2010) 7158.
[3] P.M. George, A.W. Lyckman, D.A. LaVan, A. Hegde, Y. Leung, R. Avasare, C. Testa, P.M. Alexander, R. Langer, M. Sur, Biomaterials 26 (2005) 3511.
[4] G. Nie, Y. Zhang, Q. Guo, S. Zhang, Sensors and Actuators B: Chemical 139 (2009) 592.
[5] H. Peng, C. Soeller, N. Vigar, P.A. Kilmartin, M.B. Cannell, G.A. Bowmaker, R.P. Cooney, J. Travas-Sejdic, Biosensors & Bioelectronics 20 (2005) 1821.
[6] X. Li, J. Xia, S. Zhang, Analytica Chimica Acta 622 (2008) 104.
[7] I. Hafaid, S. Chebil, H. Korri-Youssoufi, F. Bessueille, A. Errachid, Z. Sassi, Z. Ali, A. Abdelghani, N. Jaffrezic-Renault, Sensors and Actuators B: Chemical 144 (2010) 323.
[8] O. Ouerghi, A. Senillou, N. Jaffrezic-Renault, C. Martelet, H. Ben Ouada, S. Cosnier, Journal of Electroanalytical Chemistry 501 (2001) 62.
[9] H.-J. Um, M. Kim, S.-H. Lee, J. Min, H. Kim, Y.-W. Choi, Y.-H. Kim, Talanta 84 (2011) 330.
[10] G. Fabregat, E. Córdova-Mateo, E. Armelin, O. Bertran, C. Alemán, Journal of Physical Chemistry C 115 (2011) 14933.
[11] J. Zang, C.M. Li, S.-J. Bao, X. Cui, Q. Bao, C.Q. Sun, Macromolecules 41 (2008) 7053.
[12] C. Debiemme-Chouvy, Electrochemistry Communications 11 (2009) 298.
[13] Y.-Z. Long, M.M. Li, C. Gu, M. Wan, J.-L. Duvail, Z. Liu, Z. Fan, Progress in Polymer Science 36 (2011) 1415.
[14] C.J. Roy, L. Leprince, A. De Boulard, J. Landoulsi, V. Callegari, A.M. Jonas, S. Demoustier-Champagne, Electrochimica Acta 56 (2011) 3641.
[15] M. Lin, M.-S. Cho, W.-S. Choe, J.-B. Yoo, Y. Lee, Biosensors & Bioelectronics 26 (2010) 940.
[16] J. Wang, Y. Xu, F. Yan, J. Zhu, J. Wang, Journal of Power Sources 196 (2011) 2373.
[17] S. Asavapiriyanont, G.K. Chandler, G.A. Gunawardena, D. Pletcher, Journal of Electroanalytical Chemistry and Interfacial Electrochemistry 177 (1984) 229.
[18] A. Hamnett, A.R. Hillman, Journal of the Electrochemical Society 135 (1988) 2517.
[19] J.A. Harrison, H.R. Thirsk, in: A.J. Bard (Ed.), Electroanalytical Chemistry, Vol. 5, Marcel Dekker, New York, 1971, p. 67.
[20] F. Chen, G. Shi, M. Fu, L. Qu, X. Hong, Synthetic Metals 132 (2003) 125.
[21] S. Gupta, Journal of Raman Spectroscopy 39 (2008) 1343.
[22] D. Aradilla, F. Estrany, E. Armelin, R. Oliver, J.I. Iribarren, C. Alemán, Macromolecular Chemistry and Physics 211 (2010) 1663.
[23] D. Aradilla, J. Torras, C. Alemán, The Journal of Physical Chemistry B 115 (2011) 2882.

Macromolecules

Article

pubs.acs.org/Macromolecules

Electrochemical Deposition of Hollow N-Substituted Polypyrrole Microtubes from an Acoustically Formed Emulsion

Conor P. McCarthy,*[,†] Niall B. McGuinness,[†] Patrick B. Carolan,[‡] Catherine M. Fox,[†] Bernadette E. Alcock-Earley,[†] Carmel B. Breslin,[†] and A. Denise Rooney[†]

[†]Department of Chemistry, National University of Ireland Maynooth, Maynooth, Co. Kildare, Ireland

[‡]Materials Chemistry and Analysis Group, Tyndall National Institute, Co. Cork, Ireland

Supporting Information

ABSTRACT: We outline an electrodeposition procedure from an emulsion to fabricate novel vertically aligned open and closed-pore microstructures of poly(*N*-(2-cyanoethyl)-pyrrole) (PPyEtCN) at an electrode surface. Adsorbed toluene droplets were employed as soft templates to direct polymer growth. The microstructures developed only in the presence of both ClO_4^- and $H_2PO_4^-$ doping ions due to a slower rate of polymer propagation in this electrolyte. Two sonication methods (probe and bath) were used to form the emulsion, producing significantly different microstructure morphologies. Control over microtube diameter can be achieved by simply altering the emulsion sonication time or the amount of toluene added to form the emulsion. Electrochemical characterization indicated the PPyEtCN microtube morphology had an increased electrochemical response compared to its bulk counterpart. TEM analysis of individual closed-pore microtubes identified a hollow interior at the base within which the toluene droplet was encapsulated. This cavity may be used to entrap other compounds making these materials useful in a range of applications. The methodology was also applied to form microstructures of poly(3,4-ethylenedioxythiophene) and polypyrrole.

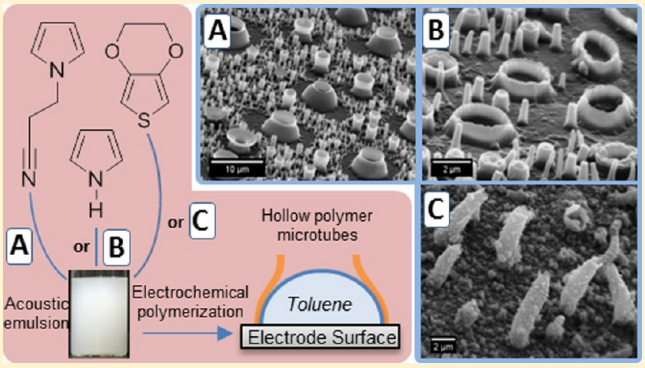

INTRODUCTION

There has been extensive research focusing on methods to control the growth of conducting polymers, as many studies have illustrated that their physical properties are a consequence of their morphology.[1,2] Hollow nano/micro-structured conducting polymeric materials are a rapidly developing research topic due to the significant range of applications for which they are suited, including drug delivery, sensing, separation, encapsulation, catalysis, and as nanoreactors.[3−7] Polypyrrole (PPy) is one of the most extensively studied conducting polymers as it is facile to prepare and has a range of useful properties which include fast redox activity,[8] good ion exchange capabilities,[9] and biocompatibility.[10] Much recent attention has focused on the design and fabrication of PPy into hollow open-pore nano/microtubes[11−14] or hollow closed-pore nano/microspheres[15,16] as these structures have potential application in controlled drug delivery systems. A number of authors, with particular reference to the work of Shi and co-workers, have developed electrodeposition methods to form hollow open tubular PPy structures anchored to substrate materials, which allows greater control over their use.[6,17−20] Furthermore, the permeability of conducting polymers can be altered as a function of applied potential or pH,[21] and this property has been exploited to encapsulate and subsequently release guest species from within PPy microcontainers.[22]

While the nano/micro morphologies of conducting polymers have been comprehensively studied, very little work has been performed with their covalently functionalized counterparts. The development of functionalized conducting polymers in controlled morphologies was highlighted as an important future research area by Shi and co-workers in their review on nanostructured conducting polymers.[23] In our previous work, we developed an electrochemical template-free procedure to form a novel poly(N-(2-cyanoethyl)pyrrole) (PPyEtCN) film in a nanowire morphology.[24] A number of other studies have been reported using electrochemical or chemical approaches to form microstructures of N-functionalized PPy. Examples of note include the electrodeposition of poly(*N*-methylpyrrole) (PPyMe) microstructures in a "doughnut" morphology using a H_2 bubble template carried out by Teixeira-Dias et al.[25] and the development of PPyEtCN and PPyMe microspheres through chemical oxidation on polystyrene core particles by Alemán and co-workers.[26,27] Electrodes modified with covalently functionalized conducting polymers have been utilized in sensor applications as the moieties at the substituted position enable supramolecular interactions with other molecules. For example, PPyEtCN modified electrodes have been used to immobilize

Received: December 4, 2012
Revised: January 20, 2013
Published: February 1, 2013

specific antibodies for the fabrication of biosensors[28] and in the electrochemical sensing of dopamine.[29] Alternatively, the functional group can be chemically modified in order to covalently attach a wide range of species to the polymer surface which include carbon nanotubes,[30] biomolecules,[31] or fluorinated alkyl chains.[32]

There is a growing interest in preparing PPy nano/microstructures employing facile template-free or soft-template electrochemical approaches.[33−35] The advantage of these methodologies is that the steps to construct and then subsequently dissolve the hard templates are not required. Furthermore, the morphology of the polymer formed can be controlled by simply altering the electrochemical conditions. Previously, a number of authors have reported using nano/micro monomer droplets to deposit conducting polymers on electrode surfaces.[20,36,37] However, these methodologies require very high concentrations of monomer and the modification of the electrode surface or the addition of a surfactant. Interestingly, Mazur and co-workers have developed an elegant interfacial chemical oxidation polymerization method using either organic or aqueous solvent microdroplets to entrap either hydrophobic[38] or hydrophilic[16] compounds within PPy microvessels. Herein, we report the first application of this solvent microdroplet method in an electrochemical polymerization reaction.

Using adsorbed toluene droplets as soft templates in conjunction with the mixed electrolyte cosolvent system we have previously employed for the template-free electrodeposition of PPyEtCN nanowires, a novel means has been developed to electrochemically fabricate PPy-based microtubes and microcontainers. This article, to the best of our knowledge, is the first report of the electrochemical deposition of microscale tubular structures of PPyEtCN, in which the tubes are anchored to an electrode surface. Although we have chosen PPyEtCN for these studies, our system can be used to design similar structures for other monomers in which an organic/aqueous based solvent system may be employed.

EXPERIMENTAL SECTION

Preparation of Emulsion. All chemicals were purchased from Sigma-Aldrich and were of analytical grade. *N*-(2-Cyanoethyl)pyrrole (PyEtCN) was distilled under vacuum and stored under nitrogen at −40 °C. In a typical experiment $LiClO_4$ (20 mM) and $(NH_4)H_2PO_4$ (100 mM) were dissolved in a water:ethanol (7:3) solution. Toluene (80 μL) and PyEtCN (56 mM) were added to 10 mL of this solution by a micropipet. This suspension was shaken vigorously and then sonicated using a probe sonicator (Bandelin Sonoplus HD2200, MS72 tip) for 1 min at 20% of maximum power, or the suspension was stirred vigorously and then sonicated in an ultrasonic bath (Fisher Scientific FB 15048) for 1 min.

Polymerization. Electrochemical experiments were performed using a Solatron 1285 potentiostat at room temperature. A standard three-electrode cell was employed using a platinum mesh as an auxiliary electrode, while the working electrode was a glassy carbon rod embedded in a Teflon holder using an epoxy resin. All potentials were measured against a saturated calomel electrode (SCE) reference. Electrode surfaces were prepared by mechanical polishing on emery paper using 6 and 1 μm diamond suspensions lubricated with water, then sonicated in ethanol between each polishing, and finally sonicated in ethanol and water, respectively. Before polymerization the electrodes were left to sit in the emulsion for 5 min to allow the toluene to adsorb to the surface. In a typical experiment an oxidative potential of 0.95 V was applied for 3 min; the polymers were then washed with ethanol and water and dried by air flow before further characterization.

Characterization. SEM analysis was performed using a Hitachi S-3200-N with a tungsten filament electron source, and the resulting images were analyzed using ImageJ software. Before analysis samples were dried using a N_2 flow and then sputter-coated under argon using an Au/Pd target. A thickness monitor was employed to obtain a coating of 15 nm. TEM was performed using a JEOL 2100 with a LaB6 filament operating at 200 kV. Samples were prepared by removing the polymer from the substrate using a surgical blade and then sonicating in ethanol for 10 min. For light microscopy, the emulsions were prepared with the addition of a red dye (Sudan IV, 0.005% wt toluene) which was added to the toluene before its addition to the emulsion solution. This allowed the droplets to be more easily identified. Several drops of this solution were pipetted onto a glass slide, and images were recorded using an Olympus BX161 optical microscopy with Cell^F analysis software. Contact angle experiments employed a static water droplet of 1 μL using an OCA 20 from Dataphysics Instruments. For FTIR characterization samples were made into KBr disks, and spectra were recorded using a PerkinElmer 2000 spectrometer.

RESULTS AND DISCUSSION

When sufficient energy was applied to the toluene/water/ethanol system, through ultrasonication, it was possible to create a homogeneous dispersion of toluene microdroplets within the continuous phase. This turbidity could be maintained for several hours without the need for any surfactants or stabilizers. This is a key factor in utilizing this system as a soft template method, as the absence of stabilizing agents leaves the toluene microdroplets available to adsorb to solid surfaces.[39] The electrochemical polymerization mixture, $LiClO_4$ (20 mM), $(NH_4)H_2PO_4$ (100 mM), PyEtCN (56 mM), and toluene (80 μL) in 10 mL of water/ethanol (7:3), was emulsified using two methods (Scheme 1). The mixture

Scheme 1. (A) Multiphasic Starting Solution of Toluene with H_2O/EtOH/PyEtCN; Resultant Emulsions from (B) Shaking and Probe Sonication and (C) Stirring and Bath Sonication; (D) Resulting Solution of H_2O/EtOH/PyEtCN in the Absence of Toluene

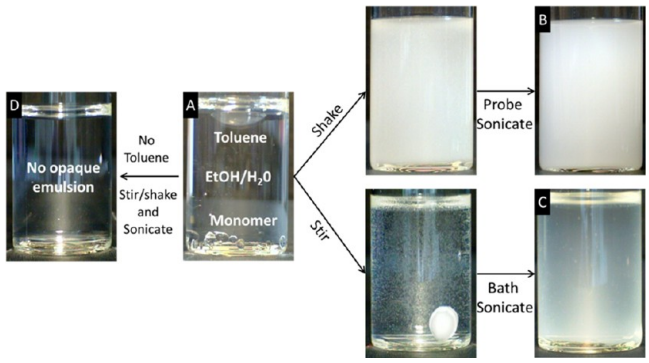

was either shaken vigorously and then sonicated for 1 min using an ultrasonic probe or stirred vigorously for 5 min and then sonicated for 1 min using an ultrasonic bath (Schemes 1B and 1C, respectively). In both cases the solution went from a transparent multiphasic system to an opaque emulsion. However, the emulsion formed using the ultrasonic probe was much more opaque and possessed a longer period of stability than that formed employing the ultrasonic bath. Previous studies, regarding the formation of emulsions, have shown that the use of an ultrasonic probe compared to an ultrasonic bath results in more stable emulsions consisting of smaller sized oil droplets.[40] In the absence of toluene no

dx.doi.org/10.1021/ma302493e | Macromolecules 2013, 46, 1008−1016

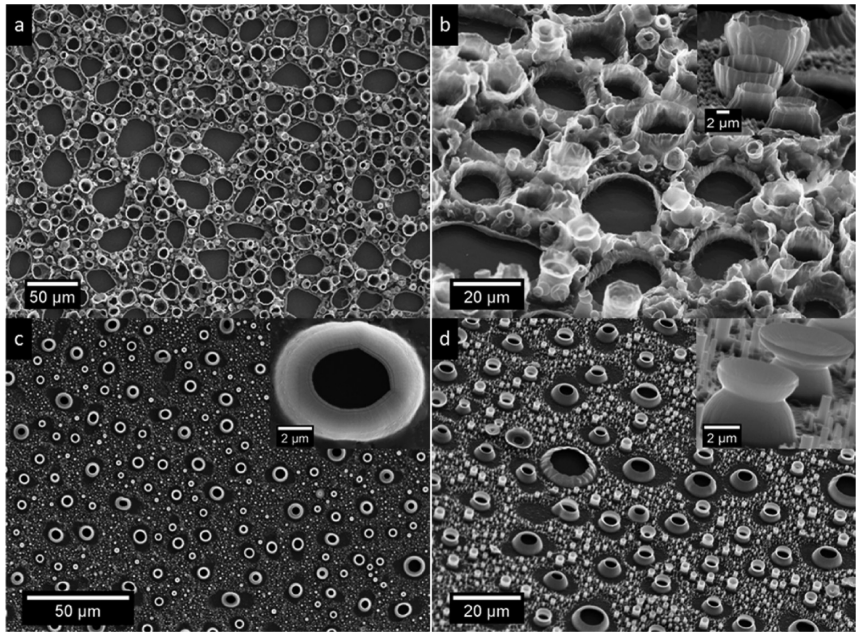

Figure 1. SEM micrographs of PPyEtCN microstructures deposited at 0.95 V from 10 mL of (a, b) water and (c, d) water/ethanol (7:3). Emulsion contained PyEtCN (56 mM), $LiClO_4$ (20 mM), $(NH_4)H_2PO_4$ (100 mM), and toluene (80 μL) with 1 min sonication by probe.

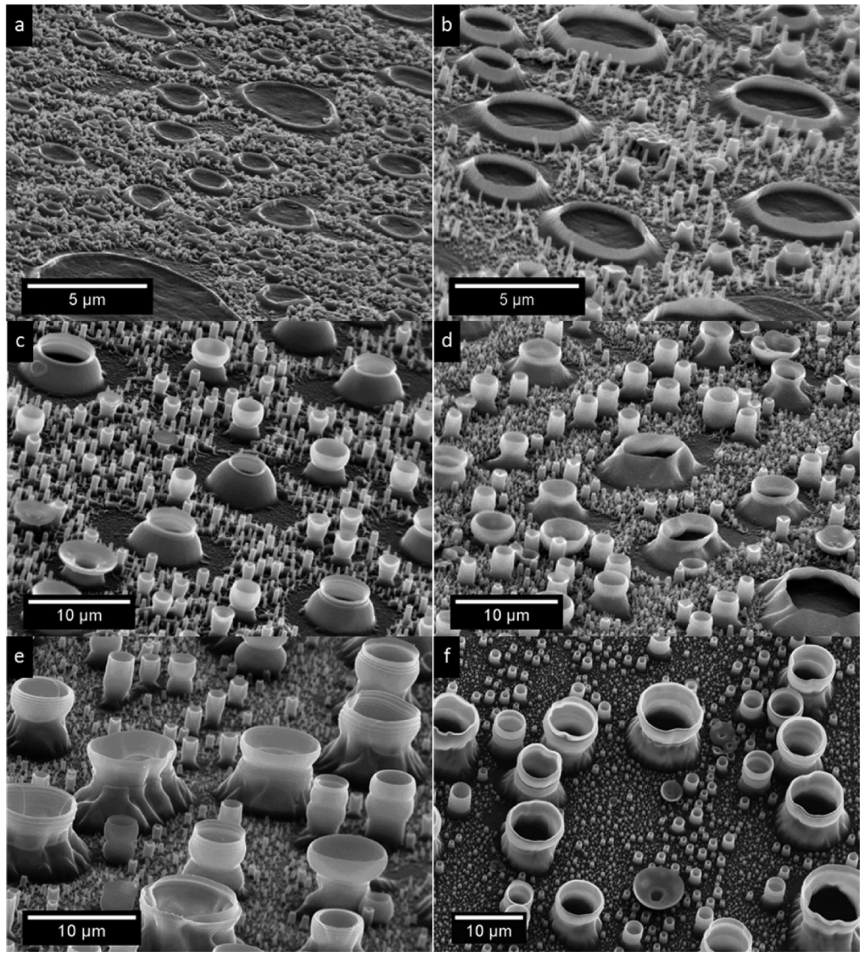

Figure 2. SEM micrographs of PPyEtCN microstructures deposited at (a) 0.85, (b) 0.90, (c) 0.95, (d) 1.00, (e) 1.10, and (f) 1.20 V for 3 min. Emulsion contained PyEtCN (56 mM), $LiClO_4$ (20 mM), $(NH_4)H_2PO_4$ (100 mM), and toluene (80 μL) in 10 mL of water/ethanol (7:3) with 1 min sonication by probe.

dx.doi.org/10.1021/ma302493e | *Macromolecules* 2013, 46, 1008−1016

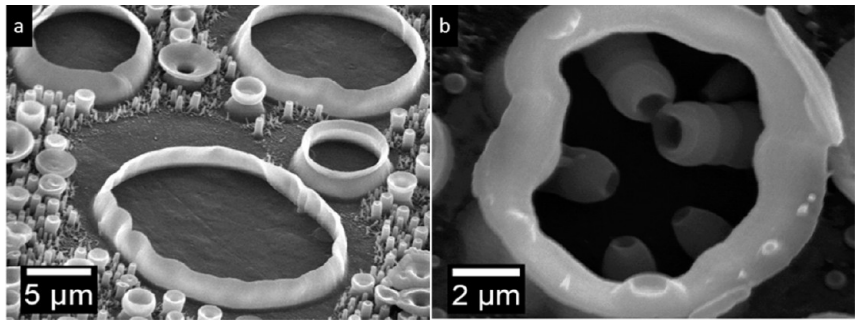

Figure 3. SEM micrograph of PPyEtCN microstructures deposited at 0.95 V for (a) 5 min and (b) 30 min. Emulsion contained PyEtCN (56 mM), $LiClO_4$ (20 mM), $(NH_4)H_2PO_4$ (100 mM), and toluene (80 μL) in 10 mL of water/ethanol (7:3) with 45 s sonication by probe.

opaque emulsion (droplets with diameter >0.1 μm) was formed (Scheme 1D). When the microdroplets adsorbed on an electrode surface, it was then possible to use them as templates for an electrochemical anodic polymerization of PyEtCN into a range of microstructures.

Interestingly, PyEtCN polymerized from a toluene/water emulsion in the absence of ethanol produced incomplete films. The formation of microtubes occurred, but there were large areas (20−50 μm in diameter) across the electrode surface which had total absence of polymer growth (Figure 1a). Moreover, as Figure 1b illustrates, the tubes formed in a highly irregular fashion with varying heights and diameters. A homogeneous distribution of microtubes was only formed when ethanol was added to the system as a cosolvent, as seen in Figure 1c,d. Here, the tubes possess a smooth exterior and have a uniform size distribution. It is also clear that the structures had an empty cavity in the center and were hollow through to the substrate surface (Figure 1c (inset)). Confirmation that the cyano group was still intact after polymerization was obtained by the presence of the characteristic $\nu(C{\equiv}N)$ band at 2251 cm^{-1} in the FTIR spectrum recorded of the polymer film (see Supporting Information Figure 1).

In a typical polymerization experiment the emulsion was formed using the ultrasonic probe, and it was observed that microtubes were produced between the range of oxidation potentials studied (0.85−1.30 V); below this potential no growth was obtained. It was also possible to electrodeposit the microtubes on different substrates such as Au, Pt, and indium−tin oxide. Furthermore, the orientation of the electrode within the cell did not negatively affect microtube growth or their coverage over the electrode surface. Regardless of applied potential, it was the adsorbed toluene droplets which influenced growth to create a tubular morphology. However, the applied electrical potential determined the rate at which the tubes formed and this was found to influence the shape of the hollow tube structure (Figure 2). At a relatively low potential (0.85 V, Figure 2a) platelike structures were formed which had very little vertical growth; this has also been seen by other researchers.[19] As the potential was increased from 0.90 to 1.00 V in 50 mV increments (Figures 2b, 2c, and 2d respectively), the final morphology resembled a more bowl-like structure, as the polymer took the shape of the adsorbed toluene droplet to a greater extent. Furthermore, the polymer growth extended in a vertical direction, and the tubes increased in height; this has also been observed for other PPy microtube systems.[17,19] At higher oxidation potentials of 1.10 and 1.20 V (Figures 2e and 2f) the tubes had increased substantially in height but were also observed to have an increase in diameter at their openings.

Upon inspection of the PPyEtCN microtubule SEM micrographs, it can be seen that the areas immediately surrounding the microtubes showed very little polymerization (Figure 3a). In the toluene/water emulsion chemical oxidation experiments carried out by Mazur and co-workers, it was clear that most of the pyrrole monomer resided inside the toluene droplets, as polymerization only occurred at the surface of the droplets and not in the bulk solution.[38] In the present system, the microtubes formed preferentially in large numbers over the electrode surface as the main structures. However, away from these sites a thin layer of bulk polymer observed. On the basis of these observations, it was apparent that a proportion of the PyEtCN monomer was contained within the toluene droplets, with some monomer remaining free in solution. As the duration of sonication time was increased, the average diameter of the tubes decreased. This observation is consistent with the known literature regarding droplet size as a function of sonication time,[40] and it allows a means of controlling the diameters of the tubes. Interestingly, for prolonged periods of growth (30 min) a second stage of microtube nucleation was observed, yielding smaller tubes developing within the larger tubes (Figure 3b). Growth of these smaller microtubes always evolved from the inner walls of the bigger microtubes and was never observed occurring from the base center. This indicated that the toluene droplets had adhered strongly to the substrate throughout the polymerization process and prohibited further growth at these sites. It also highlighted the stability of the emulsion prepared by this method.

A schematic illustrating the proposed mechanism of microtube formation is displayed in Scheme 2. Here the toluene droplet can be seen adsorbed to the electrode surface,

Scheme 2. Formation Mechanism of PPyEtCN Microtubes

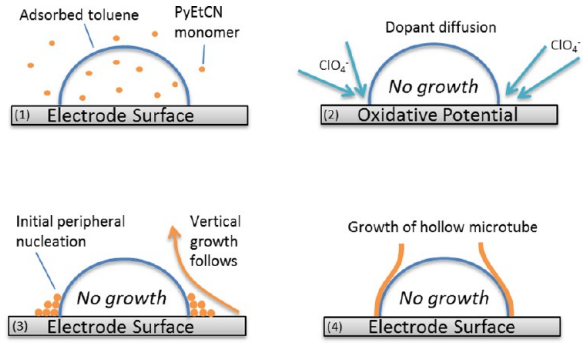

dx.doi.org/10.1021/ma302493e | Macromolecules 2013, 46, 1008−1016

containing some monomer which is distributed between the continuous phase of the emulsion and the toluene droplet (1). Once an oxidative potential is applied, dopant from the surrounding bulk solution diffuses toward the adsorbed droplet (2). Growth proceeds favorably at the surface of the droplet because a high electric field originates here due to edge effects.[20] In addition, at this interface both monomer and dopant are present in sufficient quantities to enable polymerization to proceed (3). Finally, polymer growth mimics the shape of the original droplet leaving a hollow interior (4).

The diameters of the toluene emulsion droplets and polymer microtubes were compared to confirm that the addition of the toluene was responsible for the microtube morphology. A typical emulsion was formed, and several drops were placed on a glass slide and allowed to adsorb for 5 min, before imaging was performed using an optical microscope (Figure 4a).

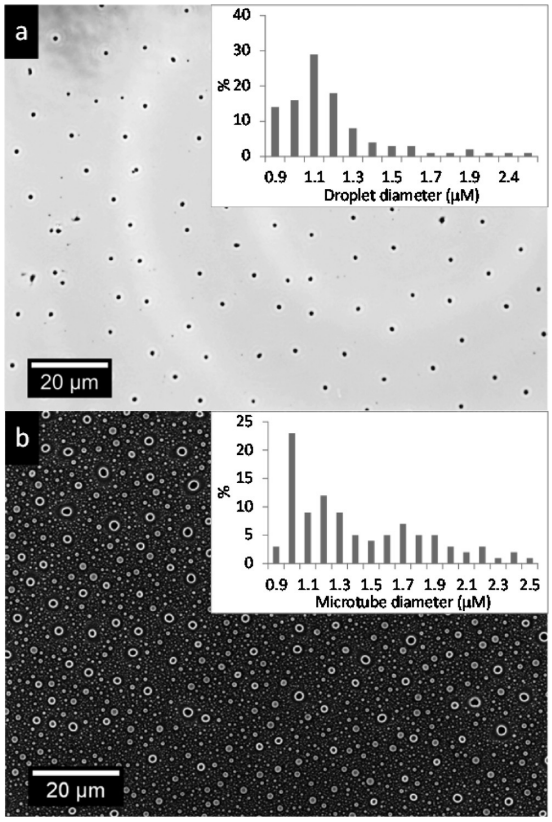

Figure 4. (a) Optical microscope and (b) SEM micrographs of emulsion droplets and polymer microstructures, respectively, with inset of diameter vs percentage of droplets/microtubes. Emulsion contained PyEtCN (56 mM), $LiClO_4$ (20 mM), $(NH_4)H_2PO_4$ (100 mM), and toluene (80 μL) in 10 mL of water/ethanol (7:3) with 1 min sonication by probe.

Similarly, an SEM micrograph was recorded of a polymer film formed from an identical emulsion (Figure 4b). The diameters of the droplets and polymer microtubes were then measured, and the distribution of their sizes is given in Figure 4a (inset) and 4b (inset), respectively. Given the significant difference in resolution between the microscopes used, there was still a good correlation between the droplet size and the microtube diameter. The average diameter of the adsorbed toluene droplet was 1.00 μm while the average diameter of the microtubes was 1.44 μm. Considering the typical thickness of the microtube walls was ~200 nm, these values are consistent with each other. These results confirmed that the toluene droplets do in fact act as the templates for the microtube formation.

The electrolyte mixture ($LiClO_4$ (20 mM)/$(NH_4)H_2PO_4$ (100 mM)) was chosen as previous studies regarding nanowire formation have indicated that this type of system promotes the growth of PPy nanowires in the direction perpendicular to the electrode surface.[24,35,41] However, to the best of our knowledge, this is the first report utilizing this type of electrolyte system to form hollow PPy-based microstructures. It has been proposed that the role of the HPO_4^{2-} or $H_2PO_4^-$ anions during electrochemical deposition of PPy nanowires is to control the vertical growth by acting as a scaffolding agent through H-bonding between the PPy chains.[35] However, interestingly, Debiemme-Chouvy determined that during the electrochemical deposition of PPy nanowires from $NaClO_4$ (1 mM)/Na_2HPO_4 (200 mM) solution the ClO_4^- anion was preferentially incorporated into the polymer to balance the positive charges on the polymer chains.[41] She proposed that when amphoteric HPO_4^{2-} anions are in close proximity to the propagating polymer they become protonated by the H^+ cations which are expelled during polymer formation. This would produce phosphoric acid which is uncharged (pK_a of H_3PO_4 is 2.6) and therefore would not partake in doping of the polymer backbone. A similar effect was observed in the present system as $H_2PO_4^{2-}$ did not efficiently support polymerization, as shown in Figure 5a, curve 1. Here, the polymer growth profile in a $(NH_4)H_2PO_4$ (100 mM) emulsion containing no $LiClO_4$ is shown; upon application of the oxidizing potential the current density remained very small and dropped as a function of time. The SEM recorded at the end of the process showed no evidence of polymer formation. In contrast, when $LiClO_4$ (20 mM) was added to the same polymerization mixture, the growth profile (Figure 5a, curve 2) displayed a significantly larger current density, indicating an electrochemical reaction was taking place. The first part of the growth curve followed the increase in current density observed for electrolyte systems containing solely $LiClO_4$ (Figure 5a, curve 3). However, at ca. 20 s the curve reached a maximum and the rate of polymerization decreased down to a plateau at ca. 80 s, which is typical of systems containing a hydrogen phosphate electrolyte.[41] The SEM recorded of this electrode after 300 s of growth showed the polymer microtubular structures (Figure 5c). Additionally, nucleation of the polymer occurred around each toluene droplet simultaneously, as the sides of each tube were observed to be identical in height. Analysis using EDX indicated that the ClO_4^- was the preferred dopant as the microtubes were found to contain approximately equal amounts of phosphorus/chlorine despite the 5:1 ratio of phosphorus/chlorine in the electrolyte mixture (see Supporting Information Figure 2). When polymerization was performed using only $LiClO_4$ (20 mM) as the electrolyte, a much more rapid polymerization was observed in the growth profile (Figure 5a, curve 3), resulting in bulk polymer forming around the adsorbed toluene droplets (Figure 5b). This identified that reaction conditions which led to a fast rate of polymerization were not favorable for producing vertical polymer growth, perpendicular from the electrode surface.

Using a mixed $LiClO_4$/$(NH_4)H_2PO_4$ electrolyte system provided control over the rate of the polymerization. A number of reports have shown that controlling the kinetics of polymerization, during electrochemical deposition, is the key to growing conducting polymers in an ordered morphology. In

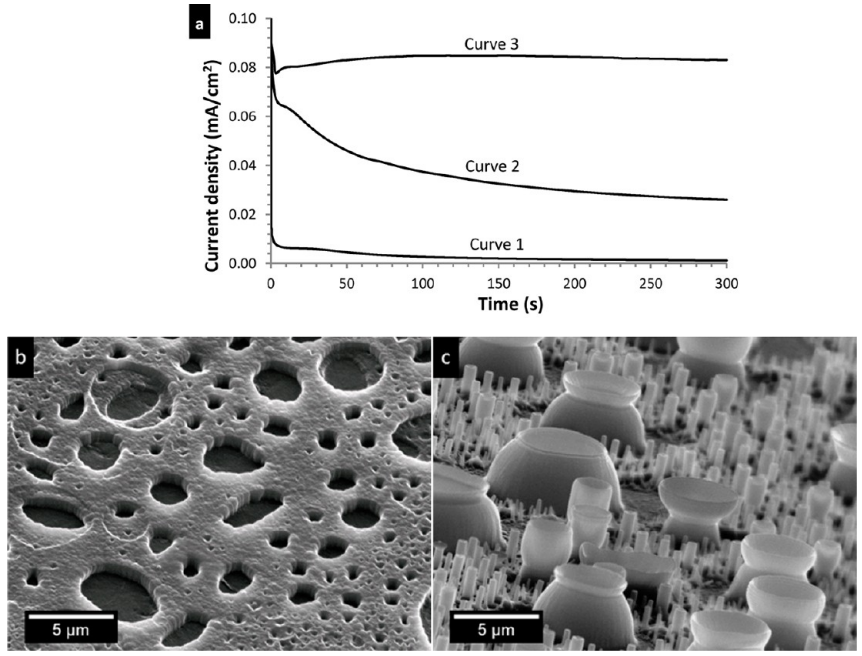

Figure 5. (a) Polarization profile of PPyEtCN polymers deposited from an emulsion containing PyEtCN (56 mM) and toluene (80 μL) in 10 mL water/ethanol (7:3) with 1 min sonication by probe. Electrolytes: curve 1, $(NH_4)H_2PO_4$ (100 mM); curve 2, $LiClO_4$ (20 mM) with $(NH_4)H_2PO_4$ (100 mM); and curve 3, $LiClO_4$ (20 mM). Oblique-angle view SEM micrographs b and c of resulting polymers from (a), curve 3 and curve 2, respectively.

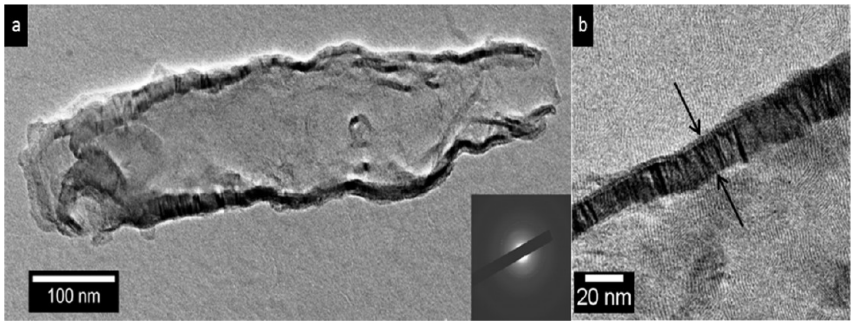

Figure 6. (a) TEM micrograph of individual PPyEtCN tube and (b) magnification of exterior wall area of tube. Emulsion contained PyEtCN (56 mM), $LiClO_4$ (20 mM), $(NH_4)H_2PO_4$ (100 mM), and toluene (80 μL) in 10 mL of water/ethanol (7:3) with 1 min sonication by probe.

these studies the applied current density was reduced in a stepwise fashion to allow for fast initial nucleation followed by slow propagation, yielding uniformly orientated conducting polymer nanowires/tubes.[20,42] In the present system it is clear from the growth curve (Figure 5a, curve 2) that the initial stage of the polymerization was also rapid. However, this initial fast growth rate was not maintained due to the presence of $H_2PO_4^-$. We propose that the role of the $H_2PO_4^-$ ion was to prevent an increase in H^+ ion concentration close to the polymer surface as the polymer propagated. Studies have shown that the rate of polymerization of pyrrole increases under acidic conditions.[43] TEM micrographs recorded of individual tubes show that the hollow cavity extends the entire length of the structure (Figure 6a). It also confirmed that the tube morphology remained intact despite being removed from the surface and sonicated, indicating high structural stability. High-magnification TEM analysis of the outer walls showed that there was dense packing of polymer surrounding the hollow interior (Figure 6b). The high density of the polymer in the tube walls most likely arises due to the combination of the slow rate of polymer propagation combined with the preferential polymerization at the droplet surface. The electron diffraction pattern, which was a diffusive ring, identified the microtubes as having an amorphous structure (Figure 6a inset).

Water contact angle measurements carried out on both the bulk and microtubule PPyEtCN films resulted in average values of 19° and 38°, respectively, indicating that both films had superhydrophilic properties. This has previously been shown for N-substituted PPy films containing a polar functional group.[44] Cyclic voltammograms were recorded of both a PPyEtCN microtubule film and a bulk PPyEtCN film grown in the absence of toluene (Figure 7). As can be observed, the PPyEtCN microstructures (black line) have an increased electrochemical response compared to a bulk polymer (gray line) as indicated by the stronger anodic and cathodic peaks. It is likely that this arises due to the greater number of available redox sites in the microtube film. In addition, the oxidation peak occurs at approximately 0.69 and 0.57 V for bulk and microtube morphologies, respectively. This shift to lower overpotentials when the microtubes are present is consistent with the tubular film possessing higher porosity, allowing easier

dx.doi.org/10.1021/ma302493e | *Macromolecules* 2013, 46, 1008−1016

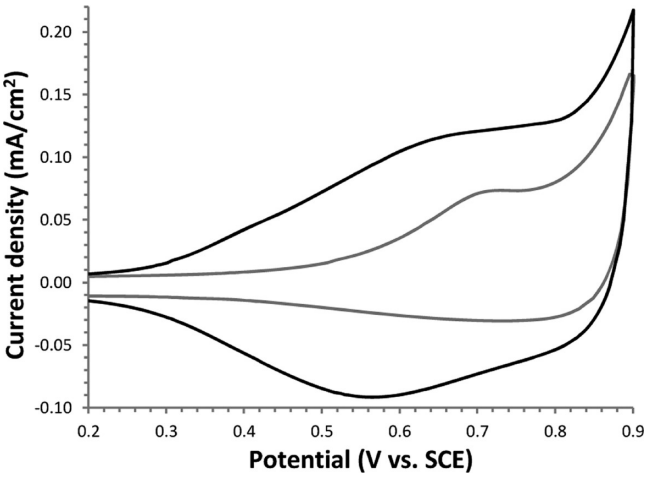

Figure 7. Cyclic voltammograms performed in $LiClO_4$ (100 mM) between 0.20 and 0.85 V for PPyEtCN microtubes (black line) and bulk PPyEtCN (gray line). Emulsion contained PyEtCN (56 mM), $LiClO_4$ (20 mM), and $(NH_4)H_2PO_4$ (100 mM) in 10 mL of water/ethanol (7:3) with 1 min sonication by probe. In the case of the PPyEtCN microtubes toluene (80 μL) was added to form the emulsion.

movement of dopants in and out of the polymer compared to its bulk counterpart.

When the polymerization of PyEtCN was carried out from an emulsion formed using a bath sonicator, inspection of the resulting film (Figure 8) revealed interesting morphology differences compared to the films formed from probe sonicator emulsions (Figure 1). It can be seen from an early stage SEM recorded after 5 min at an applied potential of 0.85 V that the microstructures originally form in an open-tube morphology (Figure 8a). However, as polymerization continues, the opening of the tubes grow toward the center and taper completely closed (Figure 8b). TEM analysis was performed on the smaller and thinner walled microcontainers which the electron beam could penetrate, and it is apparent that a cavity remains near the base of the structure (Figure 8c). As we have discussed previously, since the toluene is strongly adsorbed to the electrode surface, polymerization proceeds to close over the toluene droplet. This makes these materials a potential candidate for entrapping hydrophobic compounds within a conducting polymer microcontainer, with the advantage of being anchored to an electrode surface.

To investigate the versatility of the methodology developed to grow PPyEtCN microstructures, studies were carried out using pyrrole and 3,4-ethylenedioxythiophene. These monomers have differing solubilities in water corresponding to 2.7×10^{-2}, 2.6×10^{-1}, and 7.8×10^{-3} mol/L at 25 °C for PyEtCN, pyrrole, and 3,4-ethylenedioythiophene, respectively.[45] Electropolymerization from the emulsions formed upon probe sonication of both pyrrole and 3,4-ethylenedioxythiophene resulted in the formation of hollow polymer microstructures on the electrode surface (Figure 9). There are some noticeable differences in the morphologies of the resultant polymers; however, this can be expected due to the different characteristic properties of each monomer, particularly their solubilities in water and ease of oxidation. These will affect the partition of the monomer between the continuous and dispersed phase of the emulsion and the rate of polymerization at a given applied potential, respectively. Therefore, this surfactant-free electrochemical procedure which couples acoustic emulsification with a toluene template approach can be used to form microstructures of a range of conducting polymers, regardless of the differing water solubilities of their monomer analogues. In addition, it was observed during the studies on PyEtCN that when the polymerization mixture was exposed to longer acoustic excitation times that the emulsion changed from being opaque to transparent. Separation back to the original multiphasic system was not observed over several days. This indicates the formation of a nanoemulsion and further studies

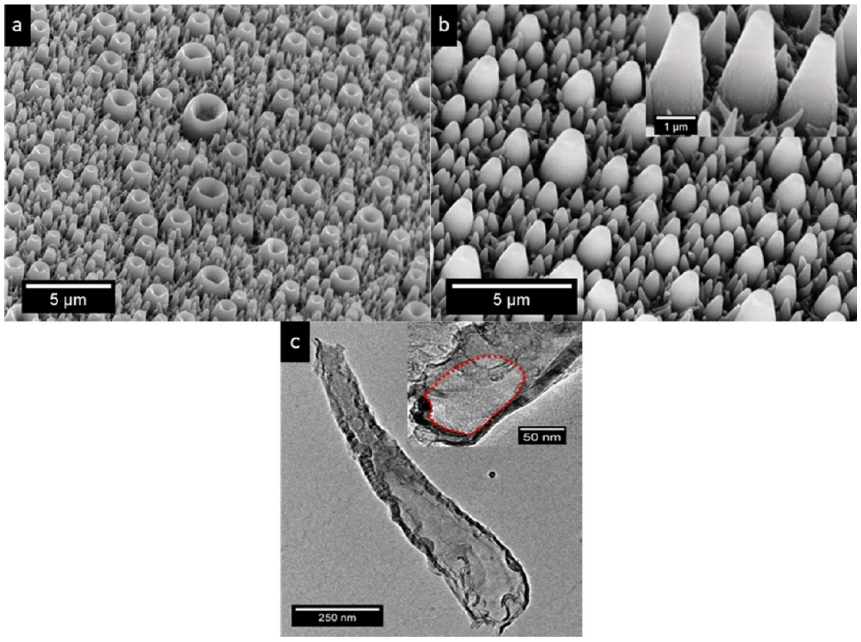

Figure 8. SEM micrographs of PPyEtCN polymers grown at 0.85 V for (a) 5 min, (b) 30 min, and (c) corresponding TEM; inset magnification of base area of tube with hollow cavity highlighted in red. Emulsion contained PyEtCN (75 mM), $LiClO_4$ (20 mM), $(NH_4)H_2PO_4$ (100 mM), and toluene (60 μL) in 10 mL of water/ethanol (7:3) with 1 min sonication by bath.

dx.doi.org/10.1021/ma302493e | *Macromolecules* 2013, 46, 1008−1016

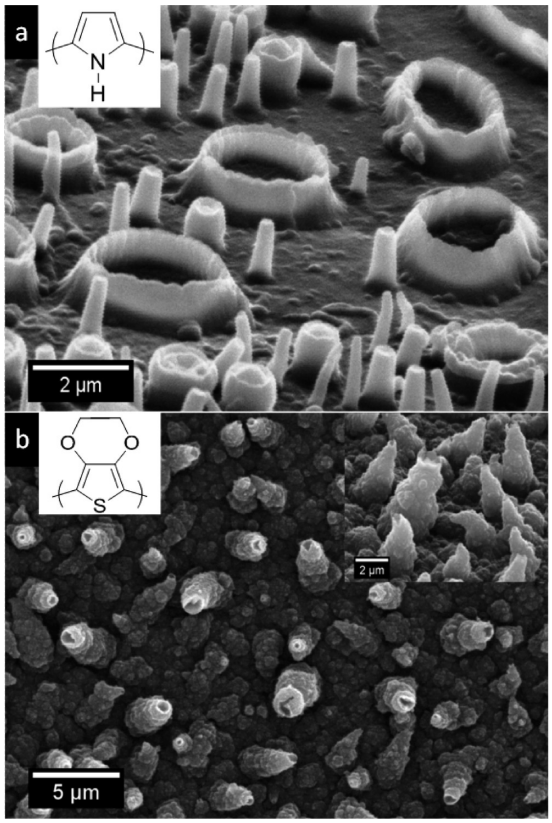

Figure 9. SEM micrograph of microstructures deposited at 0.85 and 1.05 V for (a) polypyrrole and (b) poly(3,4-ethylenedioxythiophene), respectively. Emulsion contained corresponding monomer (38 μL), $LiClO_4$ (20 mM), and toluene (80 μL) in 10 mL of water/ethanol (7:3) with 45 s sonication by probe. The pyrrole solution contained $(NH_4)H_2PO_4$ (300 mM) and the poly(3,4-ethylenedioxythiophene) solution contained $(NH_4)H_2PO_4$ (100 mM).

will now be carried out using this system to investigate the possibility of growing hollow nanotubes of PPyEtCN and other monomers.

CONCLUSIONS

We have developed a facile means of growing novel N-substituted polypyrrole (PPyEtCN) hollow microtubes and microcontainers attached at an electrode surface. A toluene soft template approach, which has previously been used in chemical oxidation methodology, has been successfully adapted to an electrochemical polymerization procedure. The method of sonication, applied potential, and electrolyte mixture have been shown to have a significant effect on the morphology of the final structures. The polymerization growth profiles indicate that the role of the mixed electrolyte system ($LiClO_4$ and $(NH_4)H_2PO_4$) is to allow fast polymer nucleation followed by slow propagation, leading to the formation of vertically aligned structures. The microtube films displayed an increased electrochemical response compared to the bulk films and possessed superhydrophilic properties. Toluene microdroplets have been entrapped within the microcontainers, and so this methodology has the potential to entrap species close to the electrode surface. Furthermore, the procedure described within has also been proven to form microstructures for both pyrrole and 3,4-ethylenedioythiophene. Therefore, it should be applicable for growing a range of microstructures for other conducting polymers.

ASSOCIATED CONTENT

Supporting Information

FTIR spectra for PPyEtCN, PPy, and poly(3,4-ethylenedioythiophene) microtube films; EDX data of PPyEtCN microtube films. This material is available free of charge via the Internet at http://pubs.acs.org.

AUTHOR INFORMATION

Corresponding Author

*E-mail conor.p.mccarthy@nuim.ie.

Author Contributions

The manuscript was written through contributions of all authors. All authors have given approval to the final version of the manuscript.

Notes

The authors declare no competing financial interest.

ACKNOWLEDGMENTS

The authors thank Noel Williams for his technical expertise as well as Dr. Jennifer McManus and Urszula Migas for performing all light microscopy experiments. This project is funded as part of the Science, Technology, Research and Innovation for the Environment (STRIVE) Programme 2007–2013 (Awards 2007-DRP-1-S5 and 2009-ET-MS-8-S2). The programme is financed by the Irish Government under the National Development Plan 2007–2013, and it is administered on behalf of the DECLG by the Environmental Protection Agency (EPA). The authors acknowledge the support of the Tyndall National Institute. This support was provided through the Science Foundation Ireland-funded National Access Programme (Project NAP 353).

REFERENCES

(1) Long, Y.-Z.; Li, M.-M.; Gu, C.; Wan, M.; Duvail, J.-L.; Liu, Z.; Fan, Z. *Prog. Polym. Sci.* **2011**, *36*, 1415–1442.
(2) Uemura, T.; Kadowaki, Y.; Yanai, N.; Kitagawa, S. *Chem. Mater.* **2009**, *21*, 4096–4098.
(3) Wang, Y.; Angelatos, A. S.; Caruso, F. *Chem. Mater.* **2008**, *20*, 848–858.
(4) Fickert, J.; Makowski, M.; Kappl, M.; Landfester, K.; Crespy, D. *Macromolecules* **2012**, *45*, 6324–6332.
(5) Li, G.; Li, Y.; Li, Y.; Peng, H.; Chen, K. *Macromolecules* **2011**, *44*, 9319–9323.
(6) Bajpai, V.; He, P.; Dai, L. *Adv. Funct. Mater.* **2004**, *14*, 145–151.
(7) Zhou, C.; Han, J.; Guo, R. *Macromolecules* **2009**, *42*, 1252–1257.
(8) Johanson, U.; Marandi, M.; Tamm, T.; Tamm, J. *Electrochim. Acta* **2005**, *50*, 1523–1528.
(9) Dziewoński, P. M.; Grzeszczuk, M. *J. Phys. Chem. B* **2010**, *114*, 7158–7171.
(10) George, P. M.; Lyckman, A. W.; LaVan, D. A.; Hegde, A.; Leung, Y.; Avasare, R.; Testa, C.; Alexander, P. M.; Langer, R.; Sur, M. *Biomaterials* **2005**, *26*, 3511–3519.
(11) Gao, W.; Sattayasamitsathit, S.; Uygun, A.; Pei, A.; Ponedal, A.; Wang, J. *Nanoscale* **2012**, *4*, 2447–2453.
(12) Surdo, S.; Strambini, L. M.; Malitesta, C.; Mazzotta, E.; Barillaro, G. *Electrochem. Commun.* **2012**, *14*, 1–4.
(13) Cui, Y.; Wen, Z.; Liang, X.; Lu, Y.; Jin, J.; Wu, M.; Wu, X. *Energy Environ. Sci.* **2012**, *5*, 7893–7897.
(14) Roy, C. J.; Chorine, N.; De Geest, B. G.; De Smedt, S.; Jonas, A. M.; Demoustier-Champagne, S. *Chem. Mater.* **2012**, *24*, 1562–1567.
(15) Mangeney, C.; Bousalem, S.; Connan, C.; Vaulay, M.-J.; Bernard, S.; Chehimi, M. M. *Langmuir* **2006**, *22*, 10163–10169.
(16) Kijewska, K.; Blanchard, G. J.; Szlachetko, J.; Stolarski, J.; Kisiel, A.; Michalska, A.; Maksymiuk, K.; Pisarek, M.; Majewski, P.; Krysiński, P.; Mazur, M. *Chem.–Eur. J.* **2012**, *18*, 310–320.

(17) Qu, L.; Shi, G.; Yuan, J.; Han, G.; Chen, F. E. *J. Electroanal. Chem.* **2004**, *561*, 149−156.
(18) Qu, L.; Shi, G.; Chen, F. E.; Zhang, J. *Macromolecules* **2003**, *36*, 1063−1067.
(19) Qu, L.; Shi, G. *J. Polym. Sci., Polym. Chem.* **2004**, *42*, 3170−3177.
(20) Huang, J.; Quan, B.; Liu, M.; Wei, Z.; Jiang, L. *Macromol. Rapid Commun.* **2008**, *29*, 1335−1340.
(21) Skotheim, T. A.; Reynolds, J. R. *Handbook of Conducting Polymers*; CRC Press: Boca Raton, FL, 2007.
(22) Parakhonskiy, B.; Andreeva, D.; Mohwald, H.; Shchukin, D. G. *Langmuir* **2009**, *25*, 4780−4786.
(23) Li, C.; Bai, H.; Shi, G. *Chem. Soc. Rev.* **2009**, *38*, 2397−2409.
(24) McCarthy, C. P.; McGuinness, N. B.; Alcock-Earley, B. E.; Breslin, C. B.; Rooney, A. D. *Electrochem. Commun.* **2012**, *20*, 79−82.
(25) Teixeira-Dias, B.; Alemán, C.; Estrany, F.; Azambuja, D. S.; Armelin, E. *Electrochim. Acta* **2011**, *56*, 5836−5843.
(26) Fabregat, G.; Alemán, C.; Casas, M. T.; Armelin, E. *J. Phys. Chem. B* **2012**, *116*, 5064−5070.
(27) Martí, M.; Fabregat, G.; Estrany, F.; Alemán, C.; Armelin, E. *J. Mater. Chem.* **2010**, *20*, 10652−10660.
(28) Um, H.-J.; Kim, M.; Lee, S.-H.; Min, J.; Kim, H.; Choi, Y.-W.; Kim, Y.-H. *Talanta* **2011**, *84*, 330−334.
(29) Fabregat, G.; Córdova-Mateo, E.; Armelin, E.; Bertran, O.; Alemán, C. *J. Phys. Chem. C* **2011**, *115*, 14933−14941.
(30) Sravendra, R.; Niranjan, K.; Jae Whan, C.; Young, H. K. *Nanotechnology* **2008**, *19*, 495707.
(31) Kwon, O. S.; Park, S. J.; Jang, J. *Biomaterials* **2010**, *31*, 4740−4747.
(32) Shida, N.; Ishiguro, Y.; Atobe, M.; Fuchigami, T.; Inagi, S. *ACS Macro Lett.* **2012**, *1*, 656−659.
(33) Wang, J.; Xu, Y.; Yan, F.; Zhu, J.; Wang, J. *J. Power Sources* **2011**, *196*, 2373−2379.
(34) Al-Mashat, L.; Debiemme-Chouvy, C.; Borensztajn, S.; Wlodarski, W. *J. Phys. Chem. C* **2012**, *116*, 13388−13394.
(35) Zang, J.; Li, C. M.; Bao, S.-J.; Cui, X.; Bao, Q.; Sun, C. Q. *Macromolecules* **2008**, *41*, 7053−7057.
(36) Gao, Y.; Zhao, L.; Li, C.; Shi, G. *Polymer* **2006**, *47*, 4953−4958.
(37) Gao, Y.; Zhao, L.; Bai, H.; Chen, Q.; Shi, G. *J. Electroanal. Chem.* **2006**, *597*, 13−18.
(38) Kępińska, D.; Blanchard, G. J.; Krysiński, P.; Stolarski, J.; Kijewska, K.; Mazur, M. *Langmuir* **2011**, *27*, 12720−12729.
(39) Mazur, M. *Langmuir* **2008**, *24*, 10414−10420.
(40) Lad, V. N.; Murthy, Z. V. P. *Ind. Eng. Chem. Res.* **2012**, *51*, 4222−4229.
(41) Catherine, D.-C. *Electrochem. Commun.* **2009**, *11*, 298−301.
(42) Liang, L.; Liu, J.; Windisch, J. C. F.; Exarhos, G. J.; Lin, Y. *Angew. Chem., Int. Ed.* **2002**, *41*, 3665−3668.
(43) Zhou, M.; Heinze, J. *J. Phys. Chem. B* **1999**, *103*, 8443−8450.
(44) Weiss, Z.; Mandler, D.; Shustak, G.; Domb, A. J. *J. Polym. Sci., Polym. Chem.* **2004**, *42*, 1658−1667.
(45) Scifinder. Substance experimental properties.